University College London

Computer Modelling of Hydrogenation Reactions in the Organic Solid State

Thesis submitted for the degree of Doctor of Engineering (EngD)

by

Simon N. Austin

Supervised by

Dr Robert G. Bell

University College London

Department of Chemistry

September 2018

Declaration

I, Simon N. Austin, confirm that the work presented in this thesis is my own. Where information has been derived from other sources, I confirm that this has been indicated in the thesis.

Simon Austin

September 2018

Abstract

1,4-bis(phenylethynyl)benzene, also known as DEB, is a hydrogen getter molecule that is used in industry to prevent the potential catastrophic build up of hydrogen by removing it from the system. This thesis aimed to computationally study the melting point of the DEB molecule along with its mobility after hydrogenation. Another aim was to compare the DEB molecule against a similar, previously well studied molecule – diphenylacetylene. The technique that was utilised to perform these solid state simulations was molecular dynamics (MD) based on interatomic potentials. The Consistent Valence Forcefield (also known as cvff) was shown to be the most appropriate force field to be used for the calculations in this study. The melting point 'envelope' for DEB was calculated to be 400.15 – 473.15 K which was in good agreement with previously published experimental data. Diffusion coefficients were calculated and used to illustrate that the fully hydrogenated DEB molecule (1,4-bis(phenylethyl)benzene) was faster than the virgin DEB molecule when the system consisted of varying concentrations of both molecules. The conclusions drawn from the diphenylacetylene study compared favourably with those drawn from the DEB study. The melting point 'envelope' of diphenylacetylene was in good agreement with the literature, whilst the hydrogenated molecule moved faster than its unhydrogenated counterpart. These results advocate cvff as an appropriate force field to be used in the molecular dynamic simulations of DEB for future research. The result of the faster hydrogenated DEB molecule provides a platform for further investigation into the mobility of the system.

Acknowledgements

First of all, I would like to thank my supervisor, Dr Robert G Bell, for providing me with the opportunity to carry out this research as well as the generous support and guidance throughout the years. I am very grateful for all the help and the friendly atmosphere during our meetings.

Also, I would like to thank all the members of Rooms G27, 230 and 105, for all their help, lively discussions and laughter when most needed. I would also like to acknowledge the use of the UCL Legion High Performance Computing Facility (Legion@UCL) and UCL Grace High Performance Computing Facility (Grace@UCL), and associated support services, in the completion of this work. I would like to thank EPSRC and the Atomic Weapons Establishment (AWE) for the funding and also the latter for their guidance

Finally, I want to especially thank my family and friends for all the constant love, support, encouragement and motivation throughout this EngD. This thesis would not have been possible without them.

I would like to dedicate this work to my aunt, Sue, who sadly passed away 3 days before the completion of this thesis.

Table of Contents

List of Conferences

- Poster Presentation: S. N. Austin and R. G. Bell.

  CCP5 Summer School. Manchester 2014

- Oral Presentation: S. N. Austin and R. G. Bell.

  M3S CDT Annual Industry Day. London 2014

- Poster Presentation: S. N. Austin and R. G. Bell

  Nuclear, Analytical & Materials Science Exchange Convention. Aldermaston 2015

- Poster Presentation: S. N. Austin and R. G. Bell

  CCP5 AGM. Lancaster 2015

- Poster Presentation: S. N. Austin and R. G. Bell.

  M3S CDT Annual Industry Day. London 2015

- Poster Presentation: S. N. Austin and R. G. Bell

  RSC 36th Solid State Christmas Group Meeting. Loughborough 2016

- Oral Presentation: S. N. Austin and R. G. Bell.

  M3 CDT Annual Industry Day. London 2017

Table of Figures

Chapter 1: Introduction

This section gives a brief history of hydrogenation and introduces the concept of hydrogen ‘getters’ and their role. It will also look at previous experimental and computational work that has been carried out in this area as well as introducing the research aims for this EngD thesis.

1.1 Introduction to Hydrogenation and Hydrogen Getters

Hydrogenation is one of the fundamental processes in chemistry, since its first use in 1823 by Johann Wolfgang Döbereiner in his lamp by catalysing the addition of hydrogen to oxygen using platinum.[1] However most people regard the “father of hydrogenation” to be Paul Sabatier who, in 1897, discovered the Sabatier reaction, and developed heterogeneous catalytic hydrogenation by passing vapours of the organic compound along with the hydrogen gas over a heated catalyst at a suitable temperature.[2] His work with hydrogenation led to him sharing the 1912 Nobel Prize for Chemistry with Victor Grignard for “his method of hydrogenating organic compounds in the presence of finely disintegrated metals whereby the progress of organic chemistry has been greatly advanced in recent years".[3] A vast number of hydrogenation reactions require a transition metal catalyst for practical purposes,[4] where the most popular metals being used include palladium[5–7], platinum[8,9], rhodium[10–12], nickel[13,14] and ruthenium[15,16] although several methods have utilised copper,[17,18] iridium[19] and cobalt.[20] One of the useful and interesting aspects of hydrogenation is the ability to control it with the use of different metal catalysts and conditions. This is evident in the use of the Lindlar Catalyst which is able to partially hydrogenate alkynes to alkenes without

hydrogenating it fully to an alkane[5]. Another example of the power of using transition metal catalysts in hydrogenation is the use of Raney nickel[13] which facilitates the reduction of benzene to cyclohexane, a reaction which is otherwise very hard to achieve. Hydrogenation of unsaturated bonds is not only useful in creating desirable biological and chemical compounds but also in the removal of hydrogen from unwanted places such as nuclear weapons, hydrogen generators and Gallium Arsenide (GaAs) Devices used in light-emission devices. A build-up of hydrogen in a sealed container can lead to multiple complications including the corrosion of nuclear materials, deterioration of electrical components and even explosion hazards.[21–24]

So-called hydrogen getters are materials that prevent this build-up of H_2 gas and thus prevent any damage. Traditionally, the main type of hydrogen getters were noble metals catalysts, usually platinum or palladium, that were combined with molecular sieves and, using oxygen, converted the hazardous hydrogen into water.[21] The primary problem with this system was that oxygen is needed which is not ideal in a closed sealed container that lacks the necessary gas.[21] Another problem was that the hydrides formed from platinum and palladium were stable when the environment lacked oxygen but were particularly pyrophoric when exposed to the atmosphere.[21] More recently, new hydrogen getters have been manufactured which consist of an alkyne (which is a highly unsaturated chain) with bulky aromatic groups on either side of the unsaturated hydrocarbon, that have a strong binding interaction with transition metal surfaces.[24,25] This organic compound is then blended with an activated carbon-supported palladium catalyst to form small pellets. The most common examples are 1,4-diphenylbutadiyne (DPB) (**Figure 1.1**) and the industrially

named DEB, which refers to 1,4-bis(phenylethynyl)benzene (**Figure 1.2**), which the majority of this thesis is based on.[25]

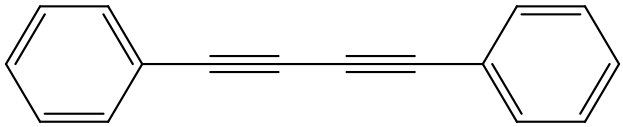

Figure 1.1 - 1,4-diphenylbutadiyne (DPB)

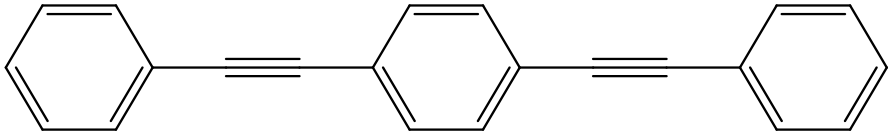

Figure 1.2 - 1,4-bis(phenylethynyl)benzene (most commonly known as DEB)

The role of the palladium catalyst is to break the molecular hydrogen into atomic hydrogen so that the DEB and DPB molecules can take up the gas, as the getters themselves are unable to interact with molecular hydrogen.[22] The activated carbon, which is supported on the Pd, has a very large surface area and thus spreads the catalyst throughout the pellets.[22] **Figure 1.3** shows an image of the Pd on the carbon support.

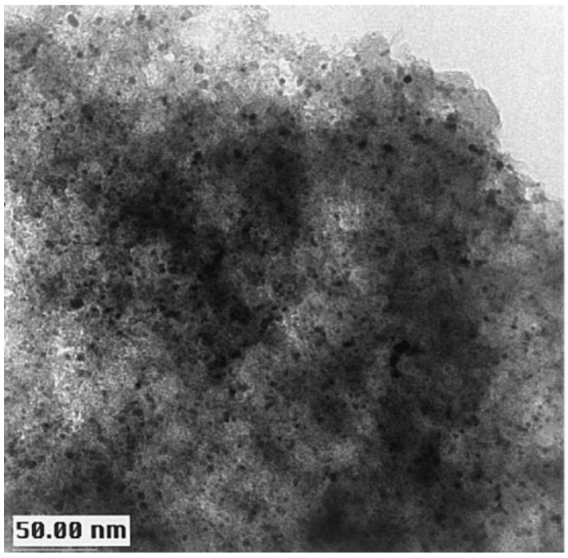

Figure 1.3 – TEM picture of carbon-supported palladium (~5 nm in diameter, black spots)[26] (Figure taken from reference 26)

1.2 Synthesis of DEB

There are many different reaction paths that can be followed in order to make 1,4-bis(phenylethynyl)benzene but the most successful one is the Sonogashira cross-coupling reaction between phenylacetylene and 1,4-diiodobenzene.[27] Sanechika *et al.* recorded a yield of 100% for this reaction using $Pd(PPh_3)_4$ and copper(I) iodide as the catalyst, triethylamine as the base and a temperature of 89°C for 30 minutes **(Figure 1.4)**.[28]

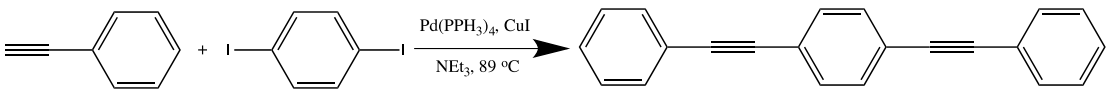

Figure 1.4 - Reaction pathway for the synthesis of 1,4-bis(phenylethynyl)benzene

1.3 Literature Review

This section will cover the previous work, both experimental and computational, that has been carried out on both of the organic hydrogen getters mentioned – DPB and DEB.

1.3.1 Experimental Studies on Organic Hydrogen Getters

A variety of experiments have been carried out on these hydrogen getters due to their industrial importance.[26] Two of the main areas that have been investigated are the kinetics of the hydrogen uptake by the molecules and their aging aspects.

In 2006, Pri-Bar *et al.* investigated the mechanism by which the reaction of hydrogen with DEB took place under low pressures.[29] The experiment involved, at first, mixing the organic molecule with the Pd/C in a 2:1 wt.% and then subjecting it to hydrogen gas in a sealed container.[29] The getter was not exposed to its full capacity of hydrogen at once, but rather several sequential portions of the gas, with each portion containing 10% of its theoretical maximum capacity.[29] They discovered that the reaction took place in two separate steps; at first a slow activation step and then a quicker propagation step.[29] Pri-Bar *et al.* suggested that the slower step was due to the time needed for the Pd/C to become activated and that the catalyst's preparation method could be instrumental at this stage.[29] The pre-treatment of Pd/C has been studied previously, with authors noting that the size and dispersion of the Pd particles can greatly affect their activity and selectivity.[30] They then went on to explore different preparation methods and their hypothesis was correct, as when the transition metal catalyst was treated with hydrogen before being mixed with DEB, the initiation step was practically non-

existent (**Figure 1.5**, white squares), due to the oxide layer being removed from the palladium particles.[29] However, if the catalyst was exposed to oxygen, either by not reacting it with hydrogen (**Figure 1.5**, black circles) or by reacting it with evaporated THF which further oxidized it (**Figure 1.5**, white circles), then the initiation step was much longer which implies it's a lot slower.[29,31] The final test, which produced the largest initiation step, was mixing the DEB/catalyst prepared by THF evaporation with CO gas before adding hydrogen to the container (**Figure 1.5**, black squares).[29,31] The CO poisoned the catalyst and hence it could not be as readily activated. The following figure (**Figure 1.5**) is a summary of these results.

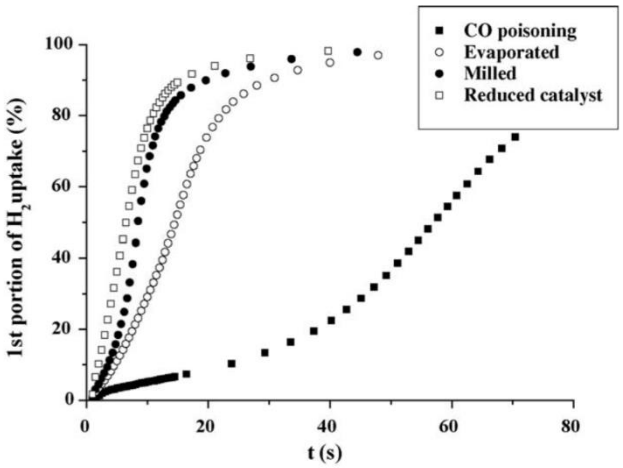

Figure 1.5 - Hydrogen uptake at the initiation step as a function of time, after the Pd/C catalyst has been prepared using different methods[29] (Figure taken from reference)

Next, they investigated the propagation step of the reaction and reached the conclusion that there are three main products of the DEB molecules reacting with hydrogen. These were 8H-DEB which is the fully saturated version of DEB (1,5-bis(phenylethyl) benzene), 6H-DEB (1-(2-

Phenylethyl)-4-[(E)-2-phenylvinyl]benzene) and 4H-DEB (the trans compound is known as 1,4-distyrylbenzene and the syn compound is known as 1-(2-phenylethyl)-4-(phenylethynyl)benzene) .[29] The 8H- 6H- and 4H- notation is the nomenclature given to describe the number of hydrogen atoms added to each DEB molecule through hydrogenation. 8H-DEB is described in greater detail later in the thesis but below are pictures of the partially hydrogenated 6H-DEB and 4H-DEB (**Figures 1.6** and **1.7**). There are 2 E-Z isomers for 6H-DEB whilst there are 3 E-Z isomers for 4H-DEB along with one configuration where one of the two alkyne bonds remains and the other is fully hydrogenated.

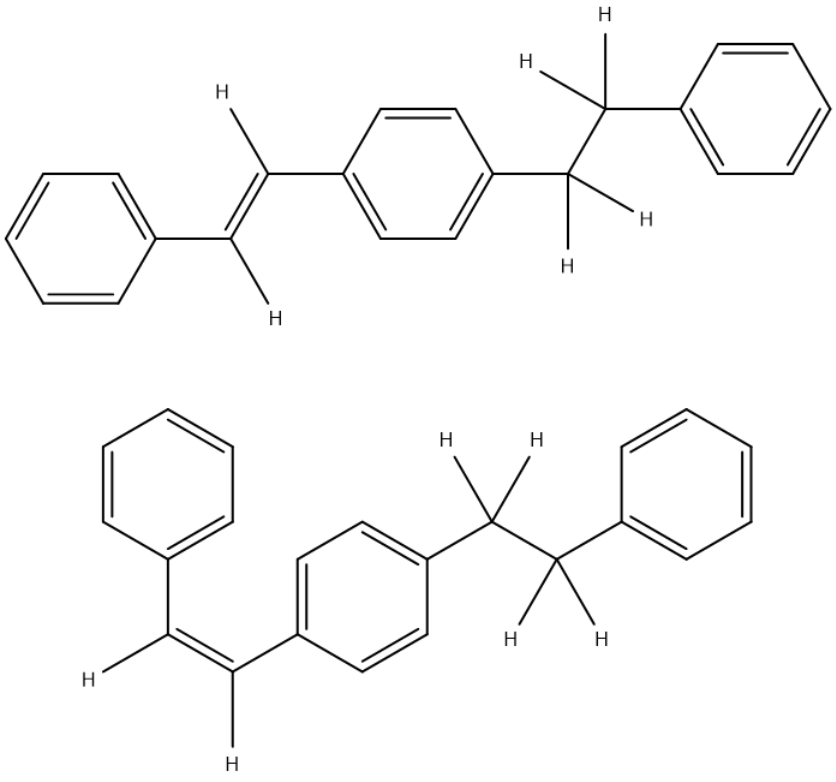

Figure 1.6 - The two possible configurations of 6H-DEB

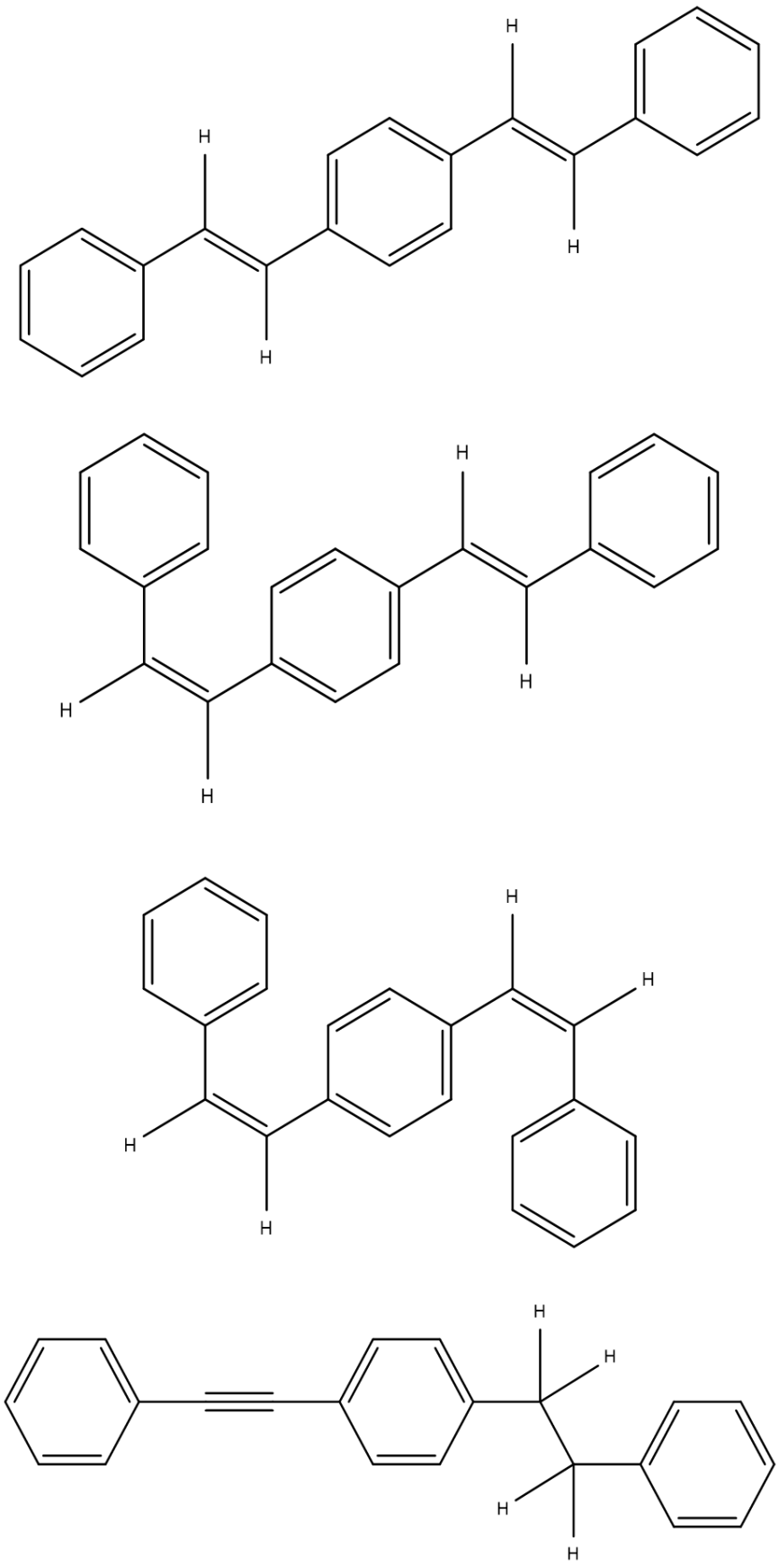

Figure 1.7 – The four possible configurations of 4H-DEB

At higher pressures, of around 150 Torr, 8H-DEB was the main product but as the pressure was slowly lowered to around 12 Torr this shifted to a 1:1 ratio of 8H-DEB:4H-DEB.[29] As the pressure continues to fall, partially saturated 6H-DEB and 4H-DEB are formed until at very low pressure, 4H-DEB is the only product.[29] The relevance of this is that it demonstrates the mobility of the hydrogen gas. At high pressures, the organic molecules surrounding the catalyst become fully saturated and hence hydrogen mobility is retarded.[29] At lower pressures however, the uptake of hydrogen is lower and hence hydrogen mobility can occur resulting in the partially saturated DEB molecules, and allowing hydrogen to be transported to less accessible getter molecules.[29] To further support this migration effect, Pri-Bar *et al.* conducted an experiment where the distribution of the products were compared following partial hydrogenation at 12 Torr.[29] The experiment was carried out three times using three different hydrogen doses, 4%, 10% and 13% of the theoretical maximum hydrogen capacity of DEB.[29] After the experiment was completed one of two procedures were undertaken, half of the reduced samples were immediately dissolved and analysed by Gas Chromatography-Mass Spectrometry and the other half were dissolved and analysed 40 days later.[29] The results concluded migration of hydrogen did occur in all three samples, which were analysed after 40 days, and in fact showed a decrease of 8H-DEB and an increase in 4H-DEB concentrations.[29] This confirmed that hydrogen migration occurred from 8H-/6H-DEB to 4H-DEB over longer timescales.[32]

The experimental research that has been presented so far has been concerned with the hydrogen uptake of the getter molecules. In 2013, Dinh *et al.* decided to investigate the aging aspects of 1,4-bis(phenylethnyl)benzene

(DEB) getters.[22] Aging refers to the changes in uptake capacity of the DEB pellet as a function of temperature and time.[22] The main aim of the experiment was to consider several aging mechanisms of the getters and the effect of aging on hydrogen uptake, and more significantly concentrating on three areas: (i) the surface segregation of the organic DEB, (ii) the clustering of palladium particles, and (iii) poisoning of the Pd catalyst.[22] In order to study these effects, DEB was mixed with palladium on an activated carbon support and was stored in pellets in groups at varying temperatures (45 ^{o}C, 60 ^{o}C and 75 ^{o}C) and storage conditions (such as N_2-filled vacuum containers and laboratory atmospheric conditions) for an extended time period to accelerate the aging process, and then every few months a set of pellets were removed for testing.[22] Dinh *et al.* used microscopy techniques such as TEM and HRTEM (High Resolution Transition Electron Microscopy) in order to monitor the condition of the catalyst, in case of any clustering together of the Pd nano-particles resulting from being stored at higher temperatures.[22] A comparison was also made of the hydrogen uptake capacity of the DEB pellets between those stored for an extended time at room temperature in laboratory atmosphere and those that were heated for a short time under a dynamic vacuum immediately before measurements were taken.[22] The pellets used were 75 wt.% DEB and 25 wt.% catalyst (5 wt.% Pd on activated carbon) and were stored at ~21 °C until they were needed for the experiment.[22] The pellets were stored for 7 years under laboratory atmospheric conditions until being placed in a nitrogen-filled vacuum containers and stored in ovens set at 45 °C, 60 °C and 75 °C where they remained until testing.[22] **Figure 1.8** shows an image of the apparatus used to measure the hydrogen uptake from the DEB

pellets (on the left hand side) along with a graph depicting the typical information that can be obtained from the setup (on the right hand side).[22] The graph in **Figure 1.8** shows a straight line (in red) when there were no getter molecules present, as the pressure merely rises as time passes.[22] The black line shows what occurs when DEB pellets were added, with the pressure being lower as time elapses due to DEB "gettering" the hydrogen, however the pressure soon rises as the DEB molecules become saturated and can no longer remove the hydrogen from the chamber.[22]

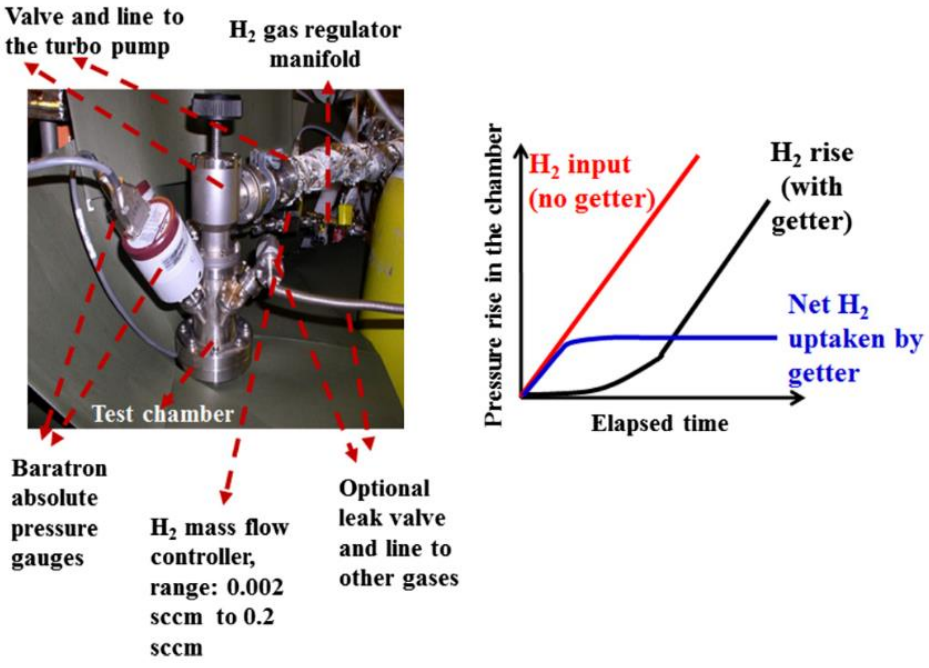

Figure 1.8 - On the left, the experimental setup used to measure hydrogen uptake of the getter pellets; and on the right a graph showing typical information gained from the experiment[22] (Figure taken from reference)

Dinh *et al.* took several pictures to show the various states of the pellets. In **Figure 1.9**, both an optical picture and three SEM images are

shown depicting a fully unsaturated DEB pellet.[22] They observed that the crystallites, both saturated and unsaturated, were in fact white and the only reason for the black colour was the activated carbon support.[22] **Figure 1.9** shows four optical images of DEB pellets after 7 and 12 months of being heated in the ovens.[22] The observations made were firstly, that the pellets were porous which facilitates gas diffusion through them and secondly, that all pellets that were contained in nitrogen-filled containers were visibly lighter in colour than those kept in laboratory conditions and the pellets heated to 75 °C were much lighter than those at 45 °C and 60 °C although some lightening was still seen at the lower temperatures.[22] The only possible explanation for this was that the DEB molecules, which are the only white structures in the pellets, must diffuse to the surface upon heating.[22]

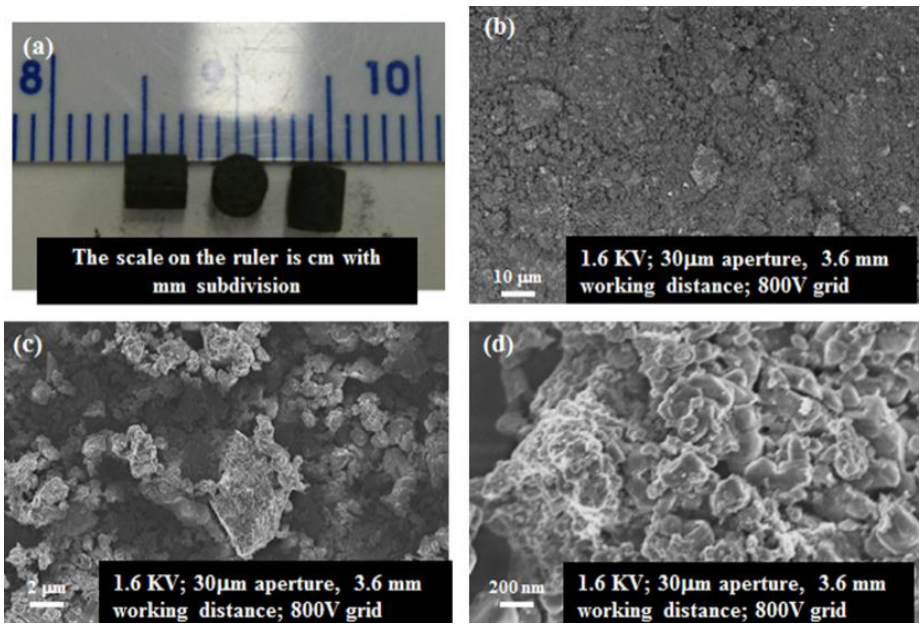

Figure 1.9 - Optical picture (a) and three SEM images (b,c and d) of a fully unsaturated DEB pellet[22] (Figure taken from reference)

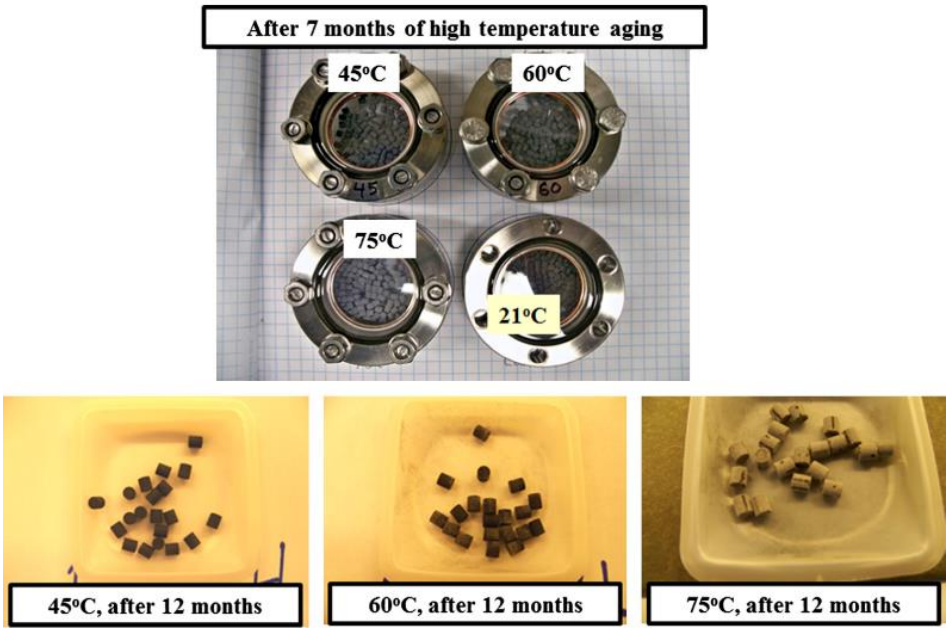

Figure 1.10 - Optical pictures of DEB pellets after 7 months and 12 months of oven aging[22] (Figure taken from reference)

Higher magnification images were then taken of pellets after 12 months at room temperature, 45 °C, 60 °C and 75 °C (**Figure 1.10**). The higher magnification highlights that not only do the DEB molecules diffuse to the surface of the pellets, but in fact they form larger crystallites at higher temperatures.[22] After 12 months, the difference in size in crystallites is negligible between 45 °C and 60 °C but much more distinct at 75 °C and after 20.5 months the lightening (or equivalently the density of DEB crystallites) on the surfaces was visibly more noticeable than at 12 months, however the crystal size did not appear to have increased.[22] The evidence for this and to confirm that the lightening of the pellets was due to DEB diffusing to the surface, the authors scraped crystals off the surface of DEB pellets that were stored at 75 °C and examined them using ^{1}H NMR.[22] The spectrum produced

from the white crystals was identical to that produced from DEB crystals from the manufacturer.[22]

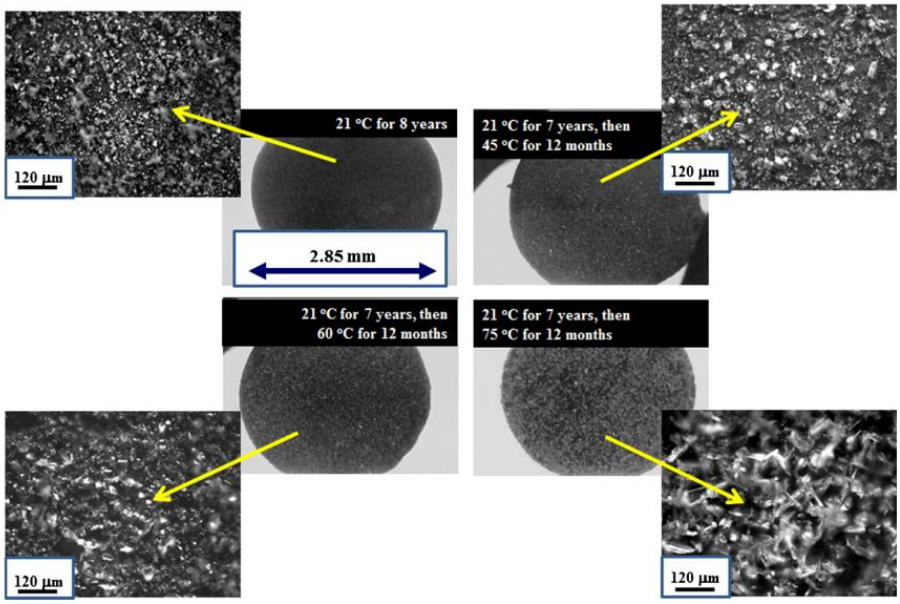

Figure 1.11 - SEM images of the pellets stored at room temperature, 45 °C, 60 °C and 75 °C after 12 months of aging, at a higher magnification[22] (Figure taken from reference)

The clustering of Pd nano-particles could severely affect the uptake of hydrogen by the getters, and so this was tested by using data from three batches that were given to AWE (the Atomic Weapon Establishment, in the UK) in 1992, 1998 and 2008.[22] There seemed to be a connection between the size of the palladium particles and their uptake capacity, so HRTEM was used in order to determine the size of the particles.[22] The results showed that the 1992 batch had a significant number of larger Pd particles, and an average size of 4.41 nm which was shown by its uptake of approximately 60%.[22] The 1998 and 2008 batches however showed no signs of the large palladium particles, and had average sizes of 2.85 nm and 4.04 nm respectively, which was also demonstrated by their uptakes of 65% and >90% respectively,

proving that larger palladium particles significantly altered the getter's uptake capacity.[22] The size of the particles was not known at the time of their formation, and hence it was not possible to deduce whether it was a result of particles clustering together or a manufacturing issue.[22] **Figure 1.12** demonstrates how this diffusion-aggregation may cause a drop in the hydrogen uptake capacity of the getter.[22]

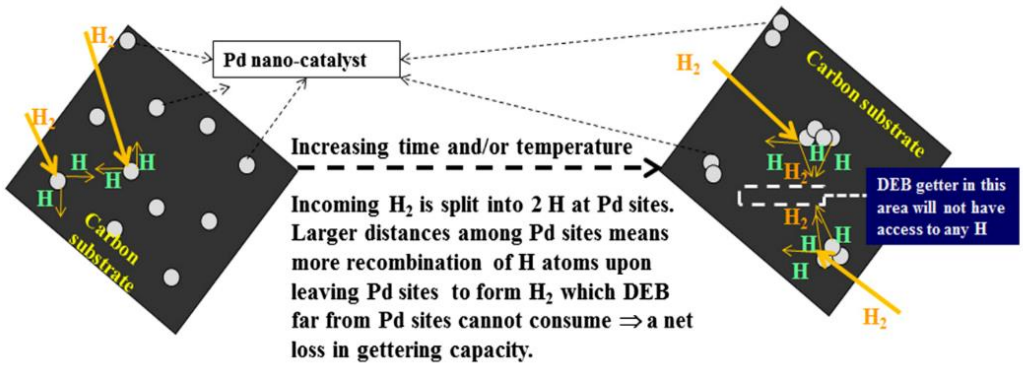

Figure 1.12 - Depiction of the potential diffusion-aggregation of catalysts in DEB pellets[22] (Figure taken from reference)

Dinh *et al.* carried out further investigations into the possibility of this aging mechanism by taking HRTEM images of palladium sites and size distributions from more regions and different temperatures of the pellets.[22] The experiment looked at the comparison between an unsaturated DEB pellet stored at 21 °C and two unsaturated DEB pellets kept at 75 °C for 12 months, and the results showed that there was not a great amount of difference between the particle sizes and hence temperature does not seem to play a significant role in the palladium particle sizes.[22] Using the knowledge that the average Pd particle size is ~3.5 nm, the average weight of each Pd nano-

catalyst is ~8.6 x 10^{-23} kg and the weight of a DEB molecule is ~4.6 x 10^{-25} kg, they predicted the mobility of the Pd nano-catalysts to be ~200 times slower than that of a DEB molecule, meaning that the activation energy barrier for the diffusion-aggregation of Pd nano-catalysts should be much greater than that for surface segregation of DEB molecules.[22] This implied that the surface segregation of DEB molecules should be much more dominant that the diffusion-aggregation of Pd nano-catalysts in the aging of DEB pellets.[22]

Figure 1.13 shows the plots of hydrogen uptake vs. time for uptake experiments carried out at 40 °C for 20 virgin DEB pellets that had previously been stored 45 °C, 60 °C and 75 °C in dry nitrogen for 127 days before the experiment.[22] It is evident from the graphs that the uptake rates up to 75% theoretical capacity for all three temperatures are identical and after this the uptakes begin to drop towards zero as demonstrated by graph (b).[22] As it approaches the saturation uptake capacity however, the rates of uptake and maximum capacity vary randomly from one investigation to the other.[22] No measurable decreases in the maximum uptake capacity of the pellets were observed at higher temperatures and the random values observed were explained by non-uniformity in the pellets themselves when they were manufactured.[22] This helped Dinh *et al.* come to the conclusion that the visible DEB segregation on the surface of the pellets for samples stored at higher temperatures did not have a great effect on the uptake capacity of the getter pellets.[22] The reasons they gave were that due to the high mobility of the DEB molecules, the additional local heat along with the heat due to the hydrogenation reaction itself leads to diffusion of unsaturated DEB molecules towards the catalyst surface.[22] Another option could be that atomic hydrogen

diffuses away from the Pd catalyst on the activated carbon to reach the DEB molecules that have segregated on the surface of the pellet, however there is no definite theoretical or experimental evidence of this.[22]

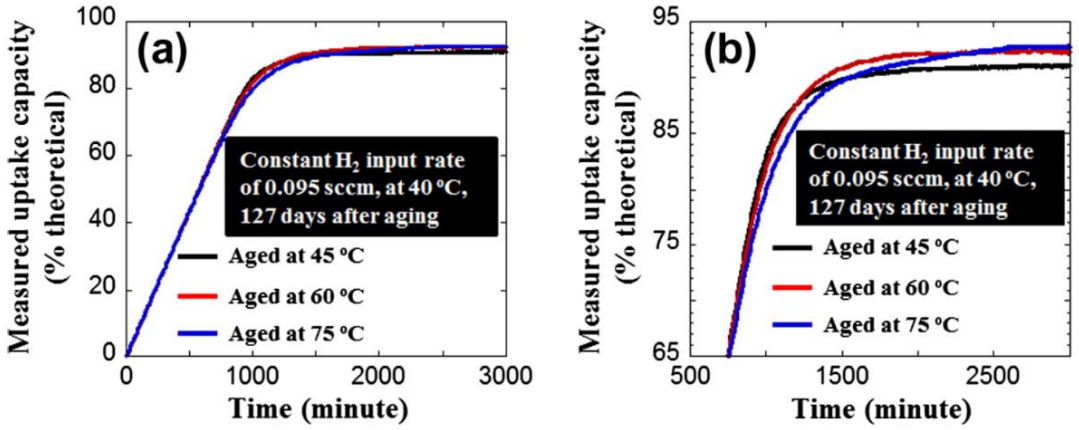

Figure 1.13 - Hydrogen uptake vs. time plots for uptake experiments carried out at 40 °C for 20 virgin DEB pellets at different temperatures, having been stored for 127 days in dry-nitrogen. (b) is a zoomed in portion of (a) between 65% and 95% theoretical uptake capacity[22] (Figure taken from reference)

The porosity of the DEB pellets at room temperature in laboratory atmospheres is thought to potentially lead to poisoning of the Pd catalyst surface by CO_2, CO and other contaminants, causing the catalyst surface to become dirty and thus lose its effectiveness and affect its overall uptake capacity.[22,33–36] Dinh *et al.* had a theory that the pellets stored in nitrogen-filled containers at higher temperatures may have a better chance to desorb some of the contaminants and thus would have a higher efficiency than those kept at room temperature.[22] In order to test this theory, they set up nine experiments using unsaturated DEB pellets that were stored at room temperature over a period of 8 years.[22] These experiments were split into three sets of three experiments. The first three experiments took virgin DEB

pellets out of the standard room temperature air-filled container and transferred them to the hydrogen uptake chamber where they were pumped out by 10^{-4} Pa for a day prior to hydrogen exposure at 40 °C.[22] The second set of three experiments consisted of removing the unsaturated pellets from the air-filled container and heating them under a dynamic vacuum at 75 °C for 48 hours and then cooling them before being exposed to hydrogen at 40 °C.[22] The final three experiments involved following the same procedure as the second set of experiments (i.e. heated at 75 °C under dynamic vacuum for 48 hours), but then being cooled to room temperature, before being exposed to dry air for 24 hours and then exposed to hydrogen at 40 °C.[22] The results, shown in **Figure 1.14**, demonstrate that the pellets which were vacuum-heated at 75 °C for 48 hours had a higher measured uptake capacity.[22]

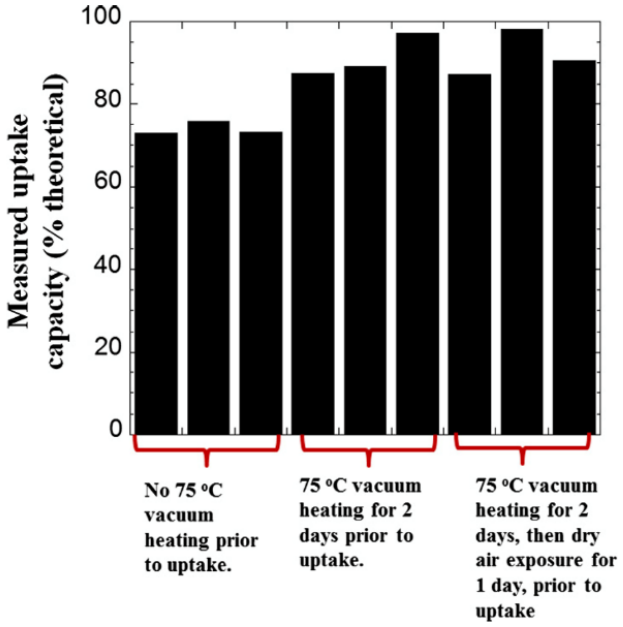

Figure 1.14 - Comparison of uptake capacities for virgin DEB getters exposed to air for many years and then treated with various conditions[22] (Figure taken from reference)

Mass-spectra from the species that were desorbed from the DEB pellets showed no particular differences between room temperature and 75 °C, except for H_2O and CO_2.[22] It was seen that H_2O desorbed more completely at higher temperatures and the majority of CO_2 was removed at 75 °C.[22] Therefore they concluded that the pellets which were heated at 75 °C had a higher uptake capacity due to structural changes in the composite as a result of the heating, perhaps even just opening more pores in the getter's network via a distribution of DEB molecules.[22] Another possibility was a desorption of the H_2O multilayer, which formed on the surface of the pellets over many years of storage, and which may open up some more pores.[22]

1.3.2 Computational Studies on Organic Hydrogen Getters

There has not been a great deal of computational work on DEB but there have been a handful of studies looking at 1,4-diphenylbutadiene (DPB). This work has included both density functional theory (DFT) and force field calculations, the majority of which were carried out by Maiti, Gee, Maxwell and Saab. In 2006, Maiti *et al.* used DFT to study the binding energies of various molecules onto Pd (1 1 0) and (1 1 1) surfaces.[37] The values of interest concerning this area of work were the binding energies of dissociated H_2 and DPB onto the surfaces, which were 16.5 kcal mol^{-1} on (1 1 0) compared to 19.3 kcal mol^{-1} on (1 1 1) for the dissociated H_2 whilst DPB had a binding energy of 66.0 kcal mol^{-1} on Pd (1 1 0) and 41.0 kcal mol^{-1} on (1 1 1).[37] **Figure 1.15** shows the DPB molecule bound to both surfaces.

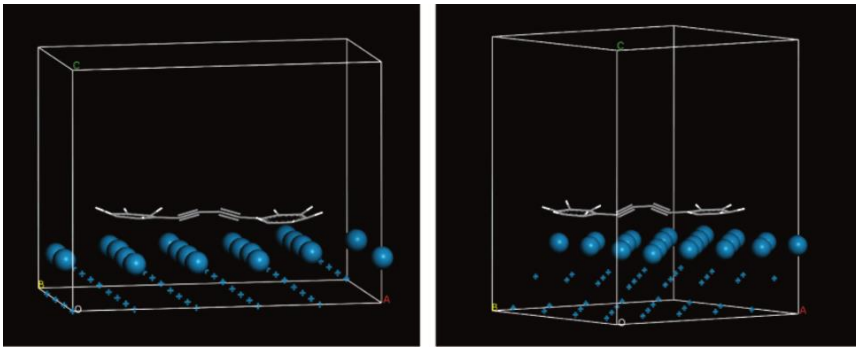

Figure 1.15 - A DPB molecule bound to Pd (1 1 0) on the left and Pd (1 1 1) on the right hand side[37] (Figure taken from reference)

The heat of reaction (at 0 K) for hydrogen insertion into DPB (i.e. the alkyne into the alkene) was also calculated, giving an identical result of –43.1 kcal mol^{-1} on both surfaces, meaning that the reaction is the same for both surfaces.[37]

Maiti also conducted further calculations with Dinh *et al.* to investigate the kinetics of hydrogen uptake.[25] This time, a combination of DFT and force fields were used, as DFT does not calculate Van der Waals forces well, and the COMPASS force field (Condensed-phase Optimized Molecular Potentials for Atomistic Simulation Studies) was chosen to carry out part of the investigation, as it includes Lennard-Jones potential terms to represent Van de Waal forces.[25,38] The main results of the investigation were: a) the sublimation energy was calculated to be 28.2 kcal mol^{-1} which was in good agreement with the experimental value of 29.2 kcal mol^{-1} [23] for the heat of vaporization of unsaturated DPB; b) the dissociation energy for H_2 was –9.7 kcal mol^{-1} and thus exothermic, which agreed with the previous calculation ;[37] c) as more H was adsorbed onto the metal surface, it slowly became less energetically favourable, due to the catalyst becoming more saturated; d) desorption of a H radical into the gas phase was severely energetically

unfavourable, with a value of 52.6 kcal mol^{-1} and finally e) H radical spillover would stay in the vicinity of the metal particles and so the getter must bind to the palladium and uptake the H in this manner.[25,37]

Sharma *et al.* used a combination of experimental and computational techniques to investigate a variety of properties of DEB. Firstly effusion thermogravimetry, differential scanning calorimetry (DSC), x-ray diffraction (XRD), and Fourier Transform Infrared (FTIR) was used to examine the equilibrium vapor pressures, melting points, and structures of DEB from a virgin state through a fully hydrogenated state.[39] The relative thermodynamic stability of each species during hydrogenation reactions was then calculated using Density Functional Theory (DFT).[39] The conclusions drawn from this study were; firstly, there was no continuous rate of change with regards to equilibrium vapor pressures across the different hydrogenation levels however 8H-DEB was the most volatile species.[39] Next, the melting points were calculated using DSC, with virgin DEB having a melting point of 455.9 K and 8H-DEB having the lowest melting point of 366.3 K.[39] XRD was then used to explore the d-stacking distances which is informative with regards to the orientation of benzene rings in DEB and its hydrogenated products, with a "T-shaped type" configuration, where one ring is at a right angle to another, being the preferred configuration for Virgin and 8H-DEB.[39] It was also determined that collective CH bond dipole interactions in the hydrogenated DEB crystal structures, play a significant role in the overall volatility of the DEB series.[39] The DFT calculations confirmed the aforementioned experimental results as well as showing, through energetic calculations, that the hydrogenation reaction is highly favourable and exothermic.[39] Molecular configurations for

the various DEB species were optimized along with the bulk crystal structure of Virgin DEB, with the bulk density calculated as 0.99 g/cm^3.[39]

1.4 Research Aims and Overview

As previously mentioned, hydrogen getters play an important role in the prevention of hydrogen build up and thus are important molecules to study further, especially for industrial purposes. The main objectives of this thesis are to:

- Find and validate a suitable force field and understand their applicability to a standard getter system.
- Investigate the interface between unhydrogenated / hydrogenated mixtures and the effect of temperature on the mixing process.
- Investigate the relative diffusivities of the saturated and unsaturated molecules and how these are affected by temperature and relative proportions of the molecules.

Chapter 2 will introduce the computational methods, namely molecular dynamics, used in this thesis. Chapter 3 will present a summary of the comparison of four force fields, with the most suitable candidate being chosen to use to calculate thermodynamic properties of DEB.

In Chapter 4, molecular dynamics have been used again to study the melting point 'envelope' for DEB using two different techniques – firstly the removal of molecules from a crystal structure and secondly, the creation of slabs. These two techniques had to be used as, in molecular dynamics, simply heating up the system does not allow nucleation to occur and thus the melting

point is overestimated. It is important to investigate the effect of temperature on the system as it is useful for understanding the dynamics of the getter molecules, at the melting point and above, and helps understand the effect on catalytic activity. In Chapter 5, the mixture of saturated and unsaturated DEB is investigated, and the effect of temperature and the concentration of hydrogenation will be discussed through the use of diffusion coefficients. This is useful to gain a better insight in to the mobility of the DEB molecules at varying conditions, and whether the hydrogenated molecules are mobile which could also help explain the hydrogenation mechanism. Chapter 6 will look at the closely related diphenylacetylene molecule and the same investigations that were undertaken on DEB are carried out to explore any trends and comparisons between the molecules. This investigation helps ensure the accuracy and validity of the DEB calculations.

Finally, Chapter 7 will summarise the findings of this study and draw conclusions about the getter system as well as explore future possibilities.

Chapter 2: Methodology

This chapter will look at the theory and methodology used to obtain the results of this investigation. The molecular dynamics computational method was used along with interatomic potentials to perform the simulations. DL_POLY was the molecular dynamics package used through the study.

2.1 Molecular Dynamics

Molecular Dynamics (MD) is a method by which Newton's equations of motions are numerically solved to study the microscopic behaviour of interacting particles in a system. MD is a technique that allows the inclusion of time into the system and so the positions and velocities of particles in the system can be analysed over a time period.[40,41] A typical algorithm followed in an MD calculation can be seen below (**Figure 2.1**). In comparison to quantum mechanics (QM) methods, MD allows for simulations of large systems to be performed over long timescales without great computational expense which makes it a valuable and widely-used methodology.[42] The second of Newton's three laws of motion is the one which is utilised to determine the aforementioned positions and velocities of particles in the system. Newton's second law of motion states that the rate of change of momentum is equal to the force acting on the particle,[43] which can be written in equation form as:

$$\mathrm{F} = m\mathrm{a} \qquad \textbf{Eq. 2.1}$$

Where F is the force acting upon the particle, *m* is the mass of the particle and a is the acceleration of the particle. **Eq. 2.1** can be expressed as:

$$\frac{d^2x}{dt^2} = \frac{F_x}{m} \qquad \textbf{Eq. 2.2}$$

which can be arranged to:

$$m\frac{d^2x}{dt^2} = F_x \qquad \textbf{Eq. 2.3}$$

The second derivative, $\frac{d^2x}{dt^2}$, is the acceleration (i.e. change of velocity) of the particle along the x-axis and so it follows that if the force acting everywhere and at all times is known then solving **Eq. 2.3** will give the trajectory.[43]

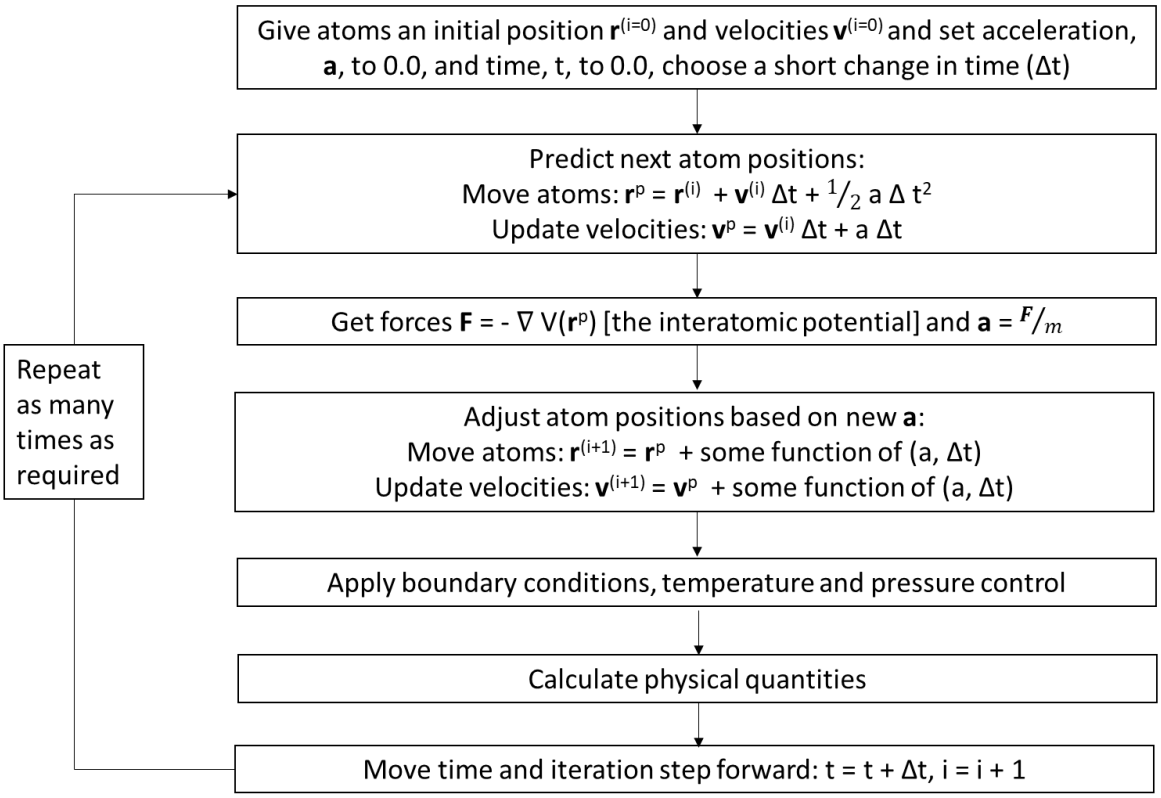

Figure 2.1 - Typical algorithm used during an MD simulation. drawn in Powerpoint)

The classical equations of motion are expressed through the following equations.

$$\frac{d\boldsymbol{r}(t)}{dt} = \frac{\boldsymbol{p}(t)}{m} = \boldsymbol{v}(t) \qquad \textbf{Eq. 2.4}$$

$$\frac{d\boldsymbol{p}(t)}{dt} = \boldsymbol{F}(\boldsymbol{r}) \qquad \textbf{Eq. 2.5}$$

$$\frac{d\boldsymbol{v}(t)}{dt} = \frac{\boldsymbol{F}(t)}{m} \qquad \textbf{Eq. 2.6}$$

$\boldsymbol{p}$ is the particle's momentum ($\boldsymbol{p}$=m**v**(t); **v**(t) is the particle's velocity), and t is time. To define the particle trajectory dependent on the external force-field ***F(r)***, we need to integrate **Eqs. 2.4**, **2.5** and **2.6**, giving the position **r**(t), and momentum $\boldsymbol{p}$(t) at each time.

For a moving particle that is under a constant force, such that **F**(r) = F, the evolution of a particle's momentum and position with time is given by:

$$\boldsymbol{p}(t) = Ft + \boldsymbol{p}_0 \qquad \textbf{Eq. 2.7}$$

$$\boldsymbol{r}(t) = \frac{F}{2m}t^2 + \frac{\boldsymbol{p}_o}{m}t + \boldsymbol{r}_0 \qquad \textbf{Eq. 2.8}$$

where $\boldsymbol{p}_0$ and $\boldsymbol{r}_0$ are the particle's initial position and momentum. Thus, the knowledge of these initial terms is what defines the particle's trajectory.

Realistically, a simulation is a system of N interacting particles where the force acting on a particle changes with changing particle position, i.e. the force is the gradient of the potential $\boldsymbol{F} = -\nabla V\ (r_1, r_2, \ldots, r_N)$, where $-\nabla V$ is

the negative gradient of the overall potential. To describe the motion of N interacting particles, a set of N equations are used:

$$m\frac{d^2\boldsymbol{r}}{dt^2} = \boldsymbol{F}_i(r_1, r_2, \ldots, r_n) i = 1, N \qquad \textbf{Eq. 2.9}$$

with the equations of motion for each of the N particles being

$$m\frac{d\boldsymbol{r}_i}{dt} = \frac{\boldsymbol{p}_i}{m} \qquad \textbf{Eq. 2.10}$$

$$\frac{d\boldsymbol{p}_i}{dt} = \boldsymbol{F}_i \qquad \textbf{\textit{Eq. 2.11}}$$

The force acting on the particles has a complicated form and thus equation 2.7 cannot be analytically solved. Instead, to solve these differential equations, a finite difference approach is utilised by breaking down the calculation into short time steps (Δt). At every time step, the forces acting on the particles is calculated and then combined with the current positions and velocities to yield new positions and velocities. Then the particle is moved to the new position and the forces are recalculated. The force acting on a particle is assumed to be constant during each time step. This procedure is repeated for a set simulation time to generate a dynamical trajectory, which is describing the time evolution of $\boldsymbol{r}_i$ and $\boldsymbol{p}_i$ for each particle on a time grid:

$$\{\boldsymbol{r_i}(\boldsymbol{t_0}), \boldsymbol{r_i}(\boldsymbol{t_0} + \Delta\boldsymbol{t}), \boldsymbol{r_i}(\boldsymbol{t_0} + \boldsymbol{2}\Delta\boldsymbol{t}), \ldots\} \qquad \textbf{Eq. 2.12}$$

$$\{\boldsymbol{p}_i(t_0), \boldsymbol{p}_i(t_0 + \Delta t), \boldsymbol{p}_i(t_0 + 2\Delta t), \ldots\} \qquad \textbf{Eq. 2.13}$$

Therefore, MD computes the microscopic dynamics of a system, in terms of a trajectory for each individual particle in the system. MD is a deterministic technique, meaning output is fully determined by the parameter

values and the initial conditions; with the initial set of positions and momenta, you can completely define the time evolution.

2.1.1 Finite Difference Method Algorithms

As previously mentioned, a finite difference method is required to integrate the equations of motion in order to calculate the force and this is carried out by algorithms. The idea behind a finite difference method is that the integration is broken down into steps, separated by fixed time Δt. All algorithms used for this integration assume that positions, velocities and accelerations can be approximated as a Taylor expansion series:

$$\boldsymbol{r}(t+\Delta t) = \boldsymbol{r}(t) + \Delta t\boldsymbol{v}(t) + \frac{1}{2}\Delta t^2\boldsymbol{a}(t) + \frac{1}{6}\Delta t^3\boldsymbol{b}(t) + \frac{1}{24}\Delta t^4\boldsymbol{c}(t) + \ldots \quad \textbf{Eq. 2.14}$$

Differentiation of **Eq. 2.14** gives the first derivative of the positions with respect to time, which is velocity ($\boldsymbol{v}$):

$$\boldsymbol{v}(t+\Delta t) = \boldsymbol{v}(t) + \Delta t\boldsymbol{a}(t) + \frac{1}{2}\Delta t^2\boldsymbol{b}(t) + \frac{1}{6}\Delta t^3\boldsymbol{c}(t) + \ldots \quad \textbf{Eq. 2.15}$$

Differentiation of **Eq. 2.15** gives the second derivative, which is acceleration ($\boldsymbol{a}$):

$$\boldsymbol{a}(t+\Delta t) = \boldsymbol{a}(t) + \Delta t\boldsymbol{b}(t) + \frac{1}{2}\Delta t^2\boldsymbol{c}(t) + \ldots \quad \textbf{Eq. 2.16}$$

Differentiation of **Eq. 2.16** gives the third derivative:

$$\boldsymbol{b}(t+\Delta t) = \boldsymbol{b}(t) + \Delta t\boldsymbol{c}(t) + \ldots \quad \textbf{Eq. 2.17}$$

Differentiation of **Eq. 2.17** would give the fourth derivative and so on.

Common algorithms used in molecular dynamics will now be looked at.

2.1.1.1 Verlet Algorithm

The most widely used method of integrating the equations of motion in molecular dynamics is the Verlet algorithm.[44] The Verlet algorithm takes the positions and accelerations at the current time, t, and only the positions of from the previous step $\boldsymbol{r}(t-\Delta t)$. This then allows the new positions, $\boldsymbol{r}(t-\Delta t)$, at $t+\Delta t$ to be calculated. At present time, t, velocities can be related to the accelerations and positions at previous ($\boldsymbol{r}(t-\Delta t)$) and new ($\boldsymbol{r}(t+\Delta t)$) steps:

$$\boldsymbol{r}(t+\Delta t)=\boldsymbol{r}(t)+\Delta t\boldsymbol{v}(t)+\frac{1}{2}\Delta t^2\boldsymbol{a}(t)+\ldots \qquad \textbf{Eq. 2.18}$$

$$\boldsymbol{r}(t-\Delta t)=\boldsymbol{r}(t)-\Delta t\boldsymbol{v}(t)+\frac{1}{2}\Delta t^2\boldsymbol{a}(t)-\ldots \qquad \textbf{Eq. 2.19}$$

The addition of **Eq. 2.18** and **Eq 2.19** then yields:

$$\boldsymbol{r}(t+\Delta t)+\boldsymbol{r}(t-\Delta t)=2\boldsymbol{r}(t)+\Delta t^2\boldsymbol{a}(t) \qquad \textbf{Eq. 2.20}$$

$$\boldsymbol{r}(t+\Delta t)=2\boldsymbol{r}(t)-\boldsymbol{r}(t-\Delta t)+\Delta t^2\boldsymbol{a}(t) \qquad \textbf{Eq. 2.21}$$

It is noticeable from this that velocity is cancelled out in the addition of **Eq. 2.18** and **Eq 2.19** and thus the Verlet algorithm does not explicitly give the velocity. There are two methods that can be used to calculate the velocity. Firstly, one can divide the difference between the next position at time $t+\Delta t$ and the previous position at time $t-\Delta t$ by $2\Delta t$:

$$\boldsymbol{v}(t)=\frac{[\boldsymbol{r}(t+\Delta t)-\boldsymbol{r}(t-\Delta t)]}{2\Delta t} \qquad \textbf{Eq. 2.22}$$

Or the velocities can be calculated for the half step $t+\frac{1}{2}\Delta t$:

$$\mathbf{v}\left(t + \frac{1}{2}\Delta t\right) = \frac{[\boldsymbol{r}(t+\Delta t) - \boldsymbol{r}(t)]}{\Delta t} \qquad \textbf{Eq. 2.23}$$

Thus, it is clear that a disadvantage of the Verlet algorithm is the absence of an explicit velocity term in the equations. Velocities cannot be calculated until the positions have been computed for the next step. The current and previous positions are used to calculate new positions and so at t = 0 there is no previous position which means it has to be calculated another way.

A similar algorithm to the Verlet algorithm, with slight variations, is the leap - frog algorithm

2.1.1.2 Leap-Frog Algorithm

The leap – frog algorithm[45] was used to carry out the molecular dynamics in this thesis and uses the following equations:

$$\boldsymbol{r}(t + \Delta t) = \boldsymbol{r}(t) + \Delta t\mathbf{v}\left(t + \frac{1}{2}\Delta t\right) \qquad \textbf{Eq. 2.24}$$

$$\mathbf{v}\left(t + \frac{1}{2}\Delta t\right) = \mathbf{v}\left(t - \frac{1}{2}\Delta t\right) + \Delta t\boldsymbol{a}(t) \qquad \textbf{Eq. 2.25}$$

The velocities at the previous time, $\mathbf{v}\left(t - \frac{1}{2}\Delta t\right)$, and the accelerations at time t are used to calculate the velocities, $\mathbf{v}\left(t + \frac{1}{2}\Delta t\right)$. The positions at the next step $\boldsymbol{r}(t + \Delta t)$ are then found from these new calculated velocities and the current position $\boldsymbol{r}(t)$. The velocities at time t are calculated from:

$$\mathbf{v}(t) = \frac{1}{2}\left[\mathbf{v}\left(t + \frac{1}{2}\Delta t\right) + \mathbf{v}\left(t - \frac{1}{2}\Delta t\right)\right] \qquad \textbf{Eq. 2.26}$$

The algorithm calculates velocities in such a way that they ‘leap – frog’ over the positions to give values at $t + \frac{1}{2}\Delta t$. Positions then leap – frog over the

velocities to give their new values at $t + \Delta t$. The advantage of the leap – frog algorithm over the Verlet algorithm is that it explicitly includes velocity and does not need to calculate difference between large numbers.

2.1.2 Ensembles

A statistical ensemble is a finite collection of all possible systems that have different microscopic states but the same thermodynamic state. The simplest ensemble is the microcanonical one, *i.e. NVE* ensemble, in which the number of particles (*N*), the cell volume (*V*) and the total energy (*E*) are conserved. However, this ensemble does not represent the majority of real systems; temperature and pressure are required for more realistic simulations. These ensembles are the *NVT* and *NPT* ensembles that are described below.

2.1.2.1 Canonical Ensemble

In the canonical ensemble, usually referred to as the *NVT* ensemble, along with *N* and *V*, temperature *T* is kept constant. The energy of endothermic and exothermic processes is exchanged with a thermostat, that adds or removes energy to the system to maintain the temperature around a specified average.

2.1.2.2 Isobaric-Isothermal ensemble

In this ensemble, temperature, pressure and number of particles is kept constant (*NPT*). This is an extension of the canonical ensemble and is the

most commonly employed ensemble, as chemical reactions are typically carried out under constant pressure conditions. In order to maintain this ensemble a weak coupling to an external pressure bath, known as the Berendsen barostat,[46] was used. This will be discussed further in the following section.

2.1.2.3 Berendsen Barostat and Thermostat

Berendsen *et al.*[46] developed a simple thermostat, where a hypothetical external heat bath of a fixed temperature is coupled to the simulation cell. The practical inference of this is frequent collisions of the simulated particles with light particles forming an ideal gas at the fixed temperature. This is attained by introducing a velocity scaling factor (λ), with a value of λ such that the change of temperature with time is proportional to the temperature difference between external bath and simulation cell.

$$\frac{dT(t)}{dt} = \frac{1}{\tau}\left(T_0 - T(t)\right) \qquad \textbf{Eq. 2.27}$$

The barostat also maintains the pressure of the system by a weak coupling of the system to an external pressure bath. The principle of least local perturbation is used to do this.

It should be noted here that the *NPT* ensemble was used for all MD simulations in this body of work, specifically the implementing of the Berendsen barostat and thermostat. There are other barostats and thermostats available such as the Nose-Hoover; where an additional degree

of freedom in the determination of E accounts for the effect of the external bath on the system.[47]

2.2 Molecular Mechanics and Interatomic Potentials

Quantum mechanical calculations offer a rigorous description of the molecule modelled from both a structural and electronic point of view.[48] Molecular dynamics on the other hand, is based on empirical observations of interatomic interactions. In the case of MD, the nuclear motion is considered while implying a fixed electron distribution associated with each atom, *i.e.* a charge. Thus, a model has been developed where molecules are represented as a collection of spheres joined together by springs. Therefore, classical physics and simple potential energy functions can be used, and large systems and long simulation times can be computed, with MD runs that result in good statistical data.

Bonding information must therefore be provided rather than being assigned as a result of solving the electronic Schrodinger's equation. This information is contained within a force field; it is composed of bonded and non-bonded interactions. The sum of the bonded and non-bonded interactions for a single particle yields the total energy, with the negative differential of that total energy with respect to particle position returning the force on that particle.

$$U_{total} = U_b + U_\theta + U_d + U_{id} + U_{nb} \qquad \textbf{Eq. 2.28}$$

where $U_b + U_\theta + U_d + U_{id}$ are the bonded terms; specifically, the bond, angle, proper and improper dihedral functions, *i.e.* the intramolecular terms. U_{nb} is

the non-bonded term made up of intermolecular interactions, namely the electrostatic and van der Waals interactions.

2.2.1 Bonded Interactions

Bonded interactions are described by the bonded terms of a force field, and is made up of the bonds, angles and dihedral energies.

2.2.1.1 Two Body Harmonic Bond Stretching Potential

A simple harmonic oscillator approximation is applied when considering the bond between two particles. The potential energy of bond stretching is described by:

$$U_b(\boldsymbol{r}) = \frac{1}{2} k_b (r - r_0)^2 \qquad \textbf{Eq. 2.29}$$

where k_b is a harmonic spring constant between the two particles and where $\boldsymbol{r}$ is the bond length and r_0 is an ideal bond length such that $(r - r_0)^2$ is the squared distance of bond length from the ideal value.

2.2.1.2 Two Body Morse Bond Stretching Potential

Another potential which can be used when considering the bond between two particles is the Morse potential, named after physicist Philip M. Morse.[49] It is a better representation of the vibrational structure of the molecule than the harmonic potetnial mentioned above and accounts for the anharmonicity of real bonds. The potential energy of bond stretching is described by:

$$V(r) = D_e(1 - e^{-a(r-r_e)})^2 \quad \textbf{Eq. 2.30}$$

where *r* is the distance between the atoms, r_e is the equilibrium bond distance, D_e is the potential well depth and *a* is the potential well width.

2.2.1.3 Three Body Harmonic Angle Bending Potential

The three-body angular bond potential describes the angular vibrational motion occurring between three atoms and is traditionally treated the same way as a bond length, described by a harmonic bending potential.

$$U_\theta(\boldsymbol{r}) = \frac{1}{2}k_\theta(\theta - \theta_0)^2 \quad \textbf{Eq. 2.31}$$

where k_θ is a harmonic spring constant, the current angle is θ and θ_0 is the ideal angle such that the potential energy increases as the angle deviates from that ideal.

2.2.1.4 Four Body Dihedral Angle Potentials

The harmonic description is only valid for small deformations 2- and 3-body terms only; dihedral terms are required to describe the 4 body terms present in molecules of more than 3 atomic spheres.

For the torsional potential, a periodic function provides a better description:

$$U_\Phi(\mathbf{r}) = k_\Phi[1 + \cos(m\Phi - \delta_0)] \quad \textbf{Eq. 2.32}$$

Where k_Φ is a force constant proportional to the barrier to rotation, m is the periodicity – indicating the number of minima in the function and δ is a phase angle that determines which torsional angle Φ that corresponds to a

minimum (the optimum value). A depiction of a proper dihedral angle is in **Figure 2.2**.

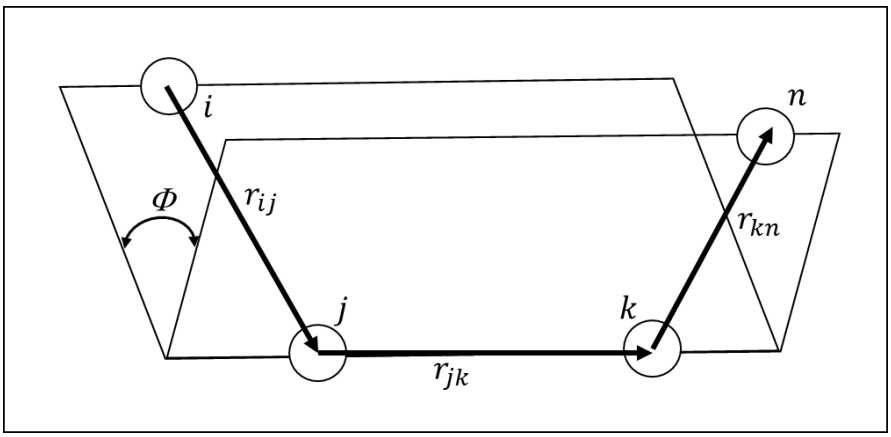

Figure 2.2 - A graphical representation of a proper dihedral angle, from reference.[50]

Whilst a proper dihedral follows the sequence of 4 atoms in a single line, $i-j-k-n$, in **Figure 2.2**, an improper torsional angle lies between the plane containing atoms $i-j-k$ and atoms $j-k-n$, shown in **Figure 2.3**.

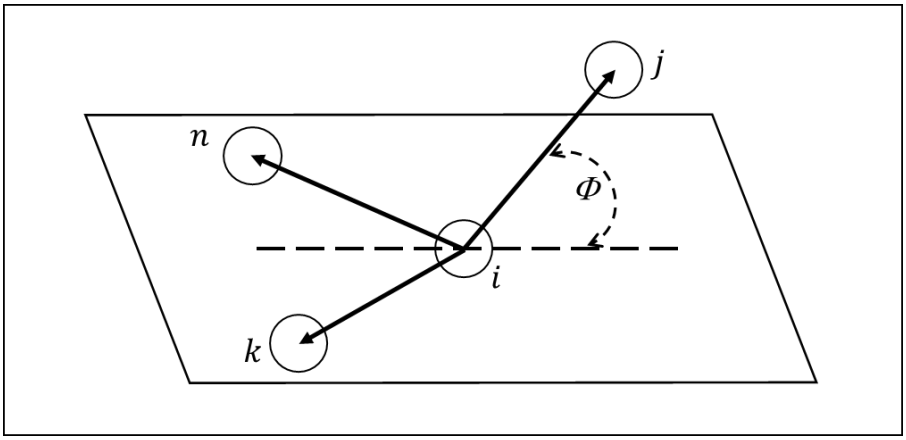

Figure 2.3 - A graphical representation of an improper dihedral angle, with associated vectors.

Improper torsional angles are used to maintain planar groups such as carbon rings, and chirality on a tetrahedral group, ensuring that structures do not flip or pucker. Here, a harmonic potential may be used:

$$U_{\Phi}(\mathbf{r}) = \frac{1}{2} k_{\Phi}(\Phi - \Phi_0)^2 \qquad \textbf{Eq. 2.32}$$

2.2.2 Non-Bonded Interactions

For interactions that are not defined by the connectivity of bonds in the molecules, the terms are instead dependent on the distance between particles or atoms. These interactions can be considered to consist of two parts: Van der Waals and electrostatic or coulombic interactions.

2.2.2.1 Van der Waals Interactions

Often referred to as the combination of attractive and repulsive forces between two non-bonded atoms, the interaction can be described by the simple 6-12, also called Lennard-Jones (L-J),[51] or a Buckingham potential,[52] to name a couple. Most commonly used, despite the relative simplicity is the 6-12 Lennard-Jones potential that does not require the calculating of large numbers of square roots and exponentials, which would be computationally expensive. It depends only on two parameters and is expressed as:

$$U_{LJ}(\mathbf{r}) = \epsilon_{ij} \left[\left(\frac{\sigma_{ij}}{r_{ij}} \right)^{12} - 2 \left(\frac{\sigma_{ij}}{r_{ij}} \right)^{6} \right] \qquad \textbf{Eq. 2.33}$$

where ϵ_{ij} is the minimum of the potential of the interaction between atoms i and j, σ_{ij} the collision diameter (the separation at which the energy is zero) and r_{ij} is the separation distance. London dispersion-attraction forces are described by the r^{-6} term, whilst short range repulsions are accounted for by the r^{-12} term. At short distances the repulsive term dominates this potential.

As the distance increases the potential goes to zero, so typically a cut-off distance is used to shorten the potential to zero quicker, making the calculation more computationally efficient. As a molecular crystal is being studied in this thesis, this potential is very important as the crystal properties are dictated by the weak nature of these intermolecular forces.

2.2.2.2 Electrostatic Interactions

Atoms that are highly electronegative attract electrons more than less electronegative atoms, and this gives rise to an uneven distribution of the charge in a molecule. The electrostatic interactions are usually calculated using partial charges on the atom centres with the energy calculated using Coulomb's law:

$$U_{el}(\mathbf{r}) = \sum \frac{q_i q_j}{D r_{ij}} \qquad \textbf{Eq. 2.34}$$

where q_i and q_j are the charges of atoms i and j, separated by distance r_{ij}, and D equates to:

$$D = 4\pi\epsilon_0 \qquad \textbf{Eq. 2.35}$$

ϵ_0 is the free space permittivity. The electrostatic term becomes less accurate for highly polarisable ions or groups, and this is when polarisable force-fields would be required.

A closer look at specific force fields and their potentials is outlined in Chapter 3.

2.3 Periodic Boundary Conditions

It is important that the system size chosen for these simulations is a balance between: explicitly representing a large enough system of the particles in bulk, and the size and computational cost of the simulation. Thus, an approach to minimise the computational cost of simulations of bulk periodic structures is to utilise periodic boundary conditions (PBC). Essentially, PBC allows for a simulation to be carried out using a small number of particles in such a way that the particles experience forces as if they were in a bulk system. If one takes a cubic box of particles as an example, then in a 2D array a central square box would be surrounded by 8 neighbouring square boxes. If a particle moves out of one side of the box, an identical particle simultaneously enters the box from the opposite side. This is represented graphically in **Figure 2.4**.

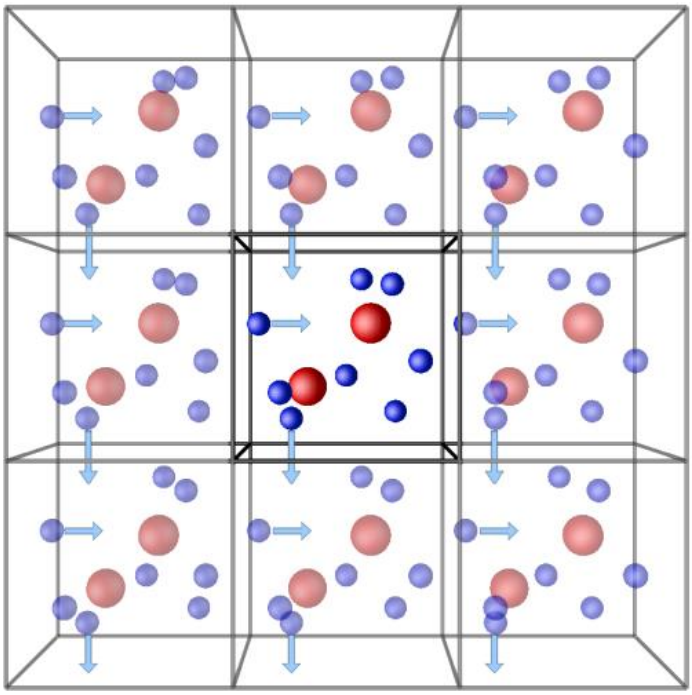

Figure 2.4 - A graphical representation of PBC, from reference.[53] It shows that as one blue atom leaves the centre of the box, another simultaneously enters the central box from the opposite side.

Another important point is that in an MD simulation, a particle may interact with another particle in a neighbouring cell (which is an image of a particle within the unit cell), if it is within the maximum inter-atomic distance r_{cut}. It will then ignore the equivalent particle in the simulation box as it is too far away. In other cases, the interaction comes from a particle in the simulation cell itself. This is known as the minimum image convention, as the interaction is always calculated with the closest image. Thus, the rule is that r_{cut} cannot be larger than the half width of the simulation cell, *i.e.* $r_{cut} < \frac{L}{2}$ (where L is the width of the simulation cell) to ensure that the cut-off radius only allows a particle to interact with one image of any given atom.

2.4 Performing a Simulation

2.4.1 Computer Codes and HPC

There a wide variety of computer codes that can be utilised to run molecular dynamics simulations depending on the target atoms/molecules and the potentials used. The DL_POLY package[54] was utilised throughout this thesis and in particular DL_POLY 4.[55,56]

HPC, or High Performance Computing, was used to carry out the simulations as they deliver a greater performance than running the simulations on a desktop. The HPC clusters utilised in this project were the Research Computing Services of UCL, namely Legion and Grace.

2.4.2 Creating the INPUT File

In some simulations, it was not possible or worthwhile using the crystal structure to create the atom configuration input file for the calculation and thus the program PACKMOL was used. An example when this was used is when looking at melted systems and a specific density was required for the system rather than a crystal structure. PACKMOL[57] is used to pack the molecules within spatial regions with the desired density and in such a way that the distance between any pair of particles is larger than a threshold tolerance, also specified. Further detail into the packing strategy is provided in a publication.[58] In essence, the molecules are packed within spatial regions with the desired characteristics, in such a way that atoms from different molecules keep a safe pairwise distance.[57] This is important as atoms that became too close or molecules that overlapped would then cause the calculation to crash. A program known as DL_FIELD[59] was utilised to create the CONFIG and FIELD files (where CONFIG is the file containing the dimensions of the unit cell, the key for periodic boundary conditions and the atomic labels and coordinates and FIELD is the file that contains the force field information defining the nature of the molecular forces).

Chapter 3: Force Field Validation and Thermochemical Properties of DEB

3.1 Force Field Validation

This chapter will look at the investigation that was carried out to find the most appropriate force field to use for the molecular dynamics calculations. Four force fields were chosen for the comparison of the optimization of the DEB crystal structure, identified by Li *et al.* in 1998.[60] The force fields chosen were the consistent-valence force field (cvff),[61] Dreiding,[62] Optimized Potentials for Liquid Simulations (OPLS)[63] and Assisted Model Building with Energy Refinement (AMBER).[64] The force field calculations were run using the General Utility Lattice Program (GULP).[65–71] A list of the force field parameters used in this investigation can be found in Appendix A. Force fields have been chosen to be used over DFT as DFT is computationally more expensive and so is limited to a smaller simulation size. Also, DFT does not accurately take into account the van der Waals forces which play an important role, despite recent improvements and additions.[72,73] GULP, a computationally cheaper program, was thus used for minimisation calculations which paved the way for molecular dynamics (MD) simulation later in the thesis.[74]

Following a general introduction to each of the force fields, a discussion of the results will be presented, with the best force field ultimately being chosen. This chosen force field was then used to carry out molecular dynamics calculations which allowed thermochemical properties such as

enthalpy of vaporization and density to be calculated. These calculations were carried out using the DL_POLY code mentioned in Chapter 2.

A brief description of each force field used will now be given. The consistent valence force field (cvff) is a force field that has the following shortened functional form:

$$V_{total} = \sum_{b} D_b \left[1 - e^{-a(b-b_0)}\right] + \sum_{\theta} H_\theta \, (\theta - \theta_0)^2 + \sum_{\varphi} H_\varphi \, [1 + scos\,(n\varphi)] + \sum_{\chi} H_\chi \, \chi^2 + \sum \varepsilon \left[(\frac{r^*}{r})^{12} - 2\left(\frac{r^*}{r}\right)^6 \right] + \sum \frac{q_i q_i}{\varepsilon r_{ij}}$$

Eq 3.1

The equation above shows the energy terms for the bond lengths, bond angles, torsion angles, out-of-plane angles, van der Waals interactions and Columbic interactions respectively, as described previously in Chapter 2. It is noticeable that primarily, a Morse potential is used to describe the bond-stretching term despite being computationally more expensive than the harmonic form. The creators of cvff's reasoning behind this was that the number of bonding interactions is negligible to the number of nonbonding interactions and thus the extra cost is insignificant.[61] Harmonic potentials are available for the bond-stretching term but only for certain situations. As mentioned earlier, cvff uses the AB form of the LJ potential, detailed in the equation above using the n-exp form, a more mathematically general form, as $\sum e \left[\left(\frac{r^*}{r}\right)^{12} - 2\left(\frac{r^*}{r}\right)^6\right]$.

The Dreiding force field is a generalized force field that was developed by Mayo *et al.* in 1990.[62] The authors describe that the

philosophy behind this force field was considering simple hybridizations to produce general force constant and geometry parameters rather than individual constants and parameters for every combination of atoms.[62]

Jorgensen and Tirado-Rives developed the OPLS force field in 1988.[63] It contains two types of force fields; a united atom force field (UAFF) and an all atom force field (AAFF).[63] The UAFF treats terminal methyl groups and methylene bridges as single groups of atoms, with the carbons and its hydrogen atoms being treated as a single interaction site, that only requires one set of parameters.[63] On the other hand, the AAFF treats every atom separately and provides parameters for all types.[63] This investigation used the all atom approach.

The final force field to be used was the AMBER force field, which has a variety of parameter sets, depending on the molecule and system being investigated. The GAFF (General AMBER Force Field) was used in this investigation, as it was the most suitable for covering all the atom types that were present, in particular small organic molecules.[64]

All of the forcefields mentioned derived their potential parameters from experimental data. Before the potentials could be chosen and assigned, the atom force field types and atom charges needed to be assigned separately for each force field. Materials Studio was used to complete this task for cvff and Dreiding, based on information from the bond increments found in the force field file based on the atom types. These charge values are derived from experimental (usually crystallographic) data and quantum mechanical modelling.MeanwhileOPLS had to be assigned

manually and Amber used the antechamber package.[75] The diagrams (**Figures 3.1** and **3.2**) show the different chemical labels in a DEB molecule used for distinction by the force fields and the crystal structure:

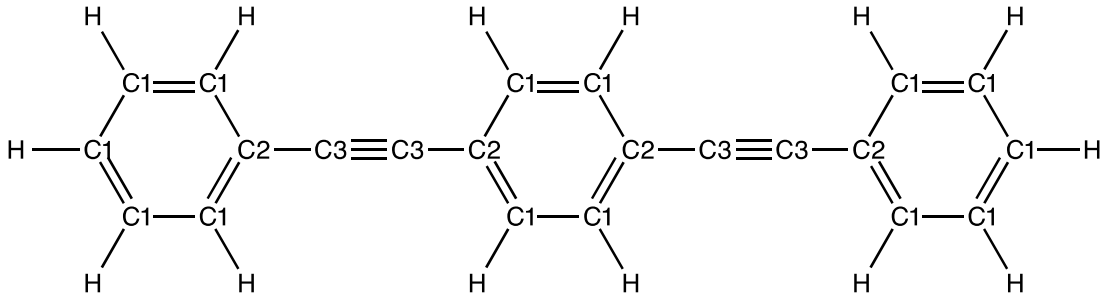

Figure 3.1 - A DEB molecule showing the different atom types recognized by the force fields

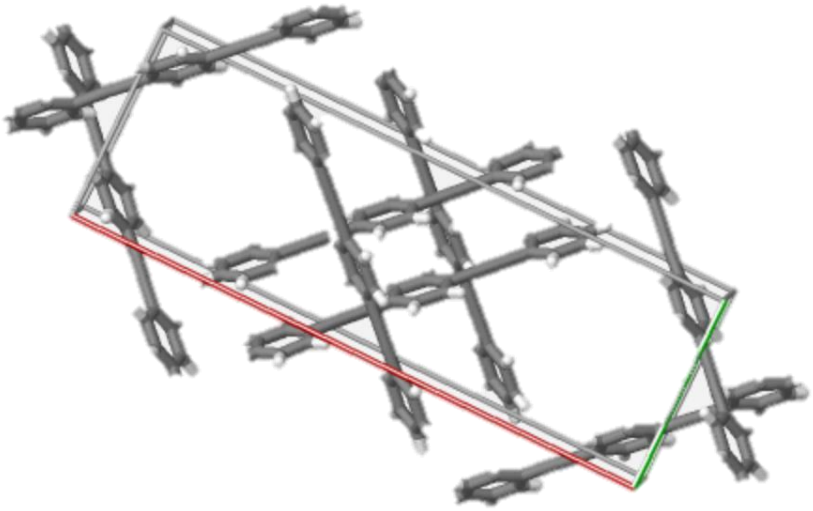

Figure 3.2 - The orthorhombic crystal structure of DEB[60]

In order to ensure the force field was providing accurate and reliable data, i.e. results that were similar to that of the experimental data, another molecule was used to test against it. This molecule had to be similar to DEB in order that similar potentials were used and thus was a valid comparison. The molecule chosen was 2,5-dipropoxy-1,4-bis(phenylethynyl)benzene which shares the three aromatic moieties and the two triple bonds, but also the addition of two propoxy groups on the middle benzene ring. Thomas *et*

al. reported the crystal structure for this molecule in 2009.[76] The diagrams (**Figures 3.3** and **3.4**) show the molecule with its atom labels that were calculated in the same manner described above for DEB and its crystal structure.

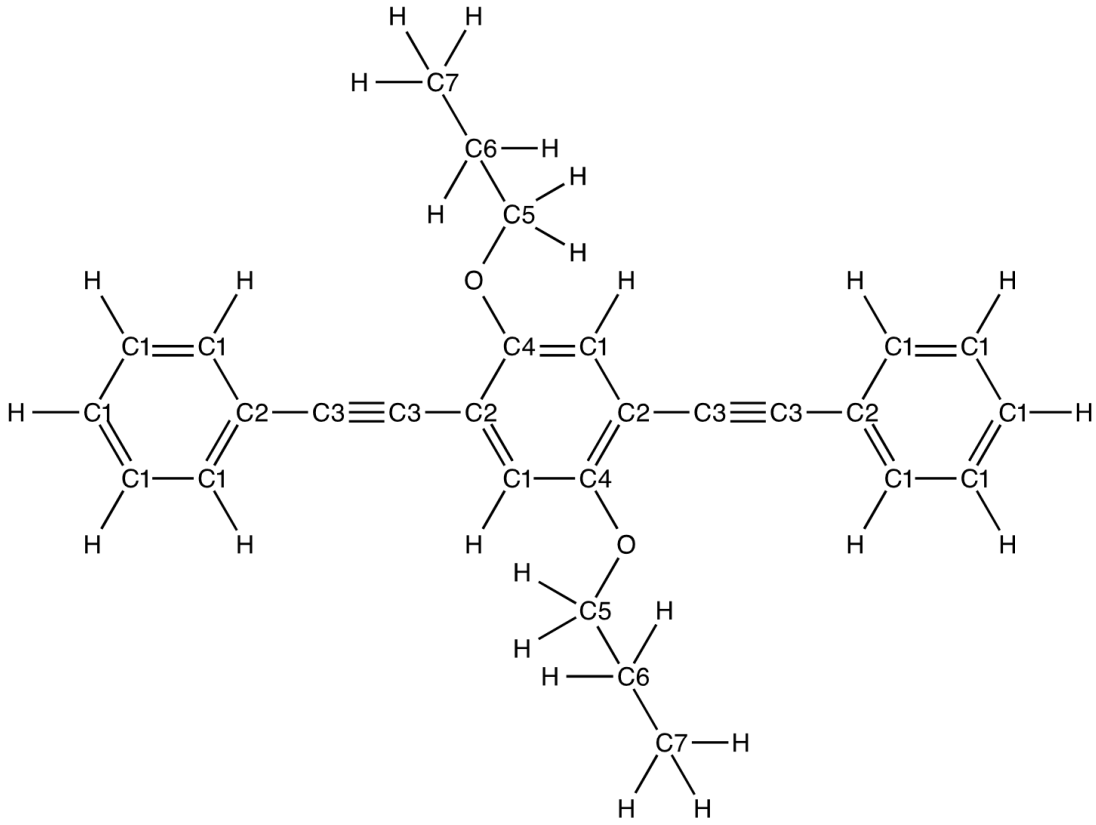

Figure 3.3 - A 2,5-dipropoxy-1,4-bis(phenylethynyl)benzene molecule showing the different atom types recognized by the force fields

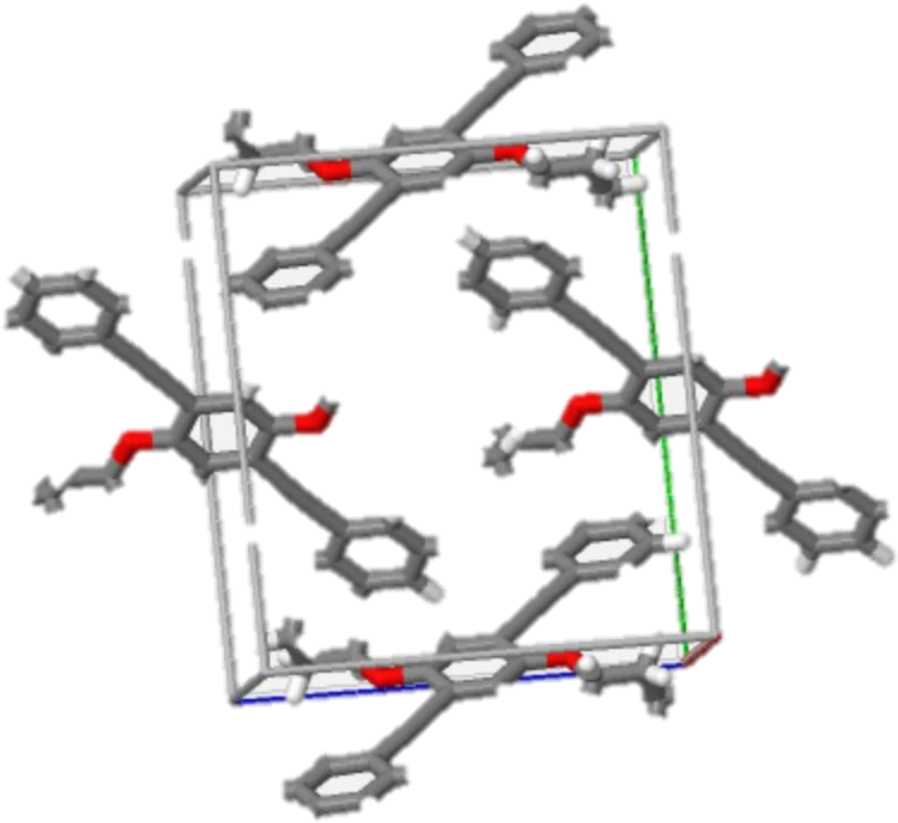

Figure 3.4 - The monoclinic crystal structure of 2,5-dipropoxy-1,4-bis(phenylethynyl)benzene[76]

3.2 Thermochemical Properties for DEB

Once the force fields results were compared and the best performing force field, i.e. the one which most closely replicated the experimental data, was chosen, further molecular dynamic calculations were set up to calculate the density and enthalpy of vaporization. These calculations involved three steps – a pre-equilibration run for 30,000 steps at 1 fs/step using the NVT ensemble. An equilibration run of 30,000 steps at 1 fs/step using the NPT ensemble was then undertaken before a final production run of 50,000 steps at 1 fs/step with the NPT ensemble was completed. The density was calculated using the standard equation for density: $\rho = \frac{m}{V}$, where ρ is the

density, m is the mass of the system and V is the volume. The volume is given in the output and the mass can easily be calculated. The enthalpy of vaporization required greater manipulation of the data, and the equation used was the one given in the study by McQuaid *et al.* in 2006.[77] The equation used was: $\Delta H_V = \frac{E_{CED} \times M}{\rho + (T \times R)}$, where E_{CED} is the cohesive energy density (the amount of energy needed to completely removeca unit volume of molecules from its neighbours), M is the molecular weight, ρ is the density, T is the Temperature (in K), and R is the universal gas constant. An example of the equation in use for phenylacetylene can be seen below:

Energy of Total Simulation = -3.17 x 10^5 kcal mol^{-1} (unit cell)

Number of Molecules = 192

So, $\frac{\text{Energy of Total Simulation}}{\text{Number of Molecules}} = \frac{-3.17 \times 105}{192}$ = -1653.13 kcal

Internal energy for 1 Molecule = -1633.70 kcal (Averaged over the same type of run)

Therefore, cohesive energy per molecule = -1653.13 - -1633.70 =

-19.43 kcal (the intramolecular energy is not included in cohesive energy)

Cohesive energy per unit cell (J mol^{-1}) = cohesive energy per molecule x

192 x 1000 x 4.1868

= -19.43 x 192 x 1000 x 4.1868

= -1.56 x 10^7 J mol^{-1} (unit cell)

Average $\mathcal{V}$ of unit cell = 3.09 x 10^4 $Å^3$ = 3.09 x 10^{20} cm^3.

Volume of mole (unit cell) = volume of unit cell x Avogadro's Constant

= 3.09 x 10^{20} cm^3 x 6.02 x 10^{23} mol^{-1}

= 1.85940 x 10^4 cm^3 mol^{-1}

So, cohesive energy density (E_{CED}) = $\frac{\text{Cohesive energy per unit cell}}{\text{Volume of mole (unit cell)}} = \frac{-1.56 \times 10^7}{1.85940 \times 10^4}$

= -8.40019 x 10^2 J cm^{-3}

So, $\Delta H_V = \frac{E_{CED} \times M}{\rho + (T \times R)} = \frac{-8.40019 \times 0.10213}{1054.58742 + (298.15 \times 8.3144621)}$ = 78.87 kJ mol^{-1}

3.3 Results & Discussion

3.3.1 Force Field Validation

The cell parameters, cell volume, average bond lengths and total lattice energy obtained by each of the four force fields for DEB and its derivative were compared against the experimental values as seen in **Table 3.1** and **Table 3.2**, respectively.

3.3.1.1 cvff

cvff produces accurate results in terms of reproducing the experimental structure of DEB. From table 3.1 it is evident the minimised cell volumes are very close to the experimental value of 2900.27 $Å^3$, obtained for the crystal structure by Li *et al*.[60] The best result is when the Morse potential was used within the cvff and this is to be expected for two reasons. First of all, the Morse potential is more accurate as it represents the true anharmonicity of real bonds, as mentioned earlier. Furthermore, all the bonds in this crystal could be successfully modelled using the Morse potential whereas the harmonic potential did not provide any parameters for the triple bond between the benzene moieties and thus it would not give as

good a result. The harmonic potential for a C=C double bond had to be used instead. This is also seen in the average bond lengths where the Morse potential increased the triple bond length (C3---C3) by as little as 0.38% compared to the 13% increase when using the harmonic potential. The C3---C2 bond is also larger when using harmonic potentials but again this is due to a lack of terms, especially regarding the C3 atom. Another noticeable bond length is that of the C1---H bond which is increased by around 13.7% using both types of potentials. This may be due to overlapping atoms allowing the bonded C and H atoms to drift apart more than expected. The other bond lengths are fairly close to the experimental values, suggesting this force field models the system well. With regards to the cell parameters, both a (- 4.97%) and c (- 2.29%) were decreased whilst b (+ 7.89%) was increased in both instances but there was not a significant difference to the experimental data, as demonstrated in **Figure 3.5**. These differences could be attributed to the force field underestimating the lattice energy of the crystal, which consists of the intermolecular cohesive energy and an intramolecular relaxation energy.[78] The intramolecular parameters, which have been determined experimentally, produce accurate bond lengths however the intermolecular parameters (i.e. van der Waals forces) seem to have varying results depending on the direction of the cell length. All intermolecular forces in a molecular crystal are anisotropic, meaning they are dependent on the relative orientation of the molecules. As noted by Sharma *et al.*, the DEB molecule has no hydrogens on its backbone to interfere with its benzene-benzene π-stacking, meaning the 3-T-shaped configuration can be formed.[39] When this π-stacking occurs along the axis

of the unit cell, as observed in this system along the B axis, and the van Der Waals term poorly represents the π-stacking, differing accuracies are calculated between the cell lengths. As cvff was parameterised using small organic crystals it would be expected to produce good results for this system.

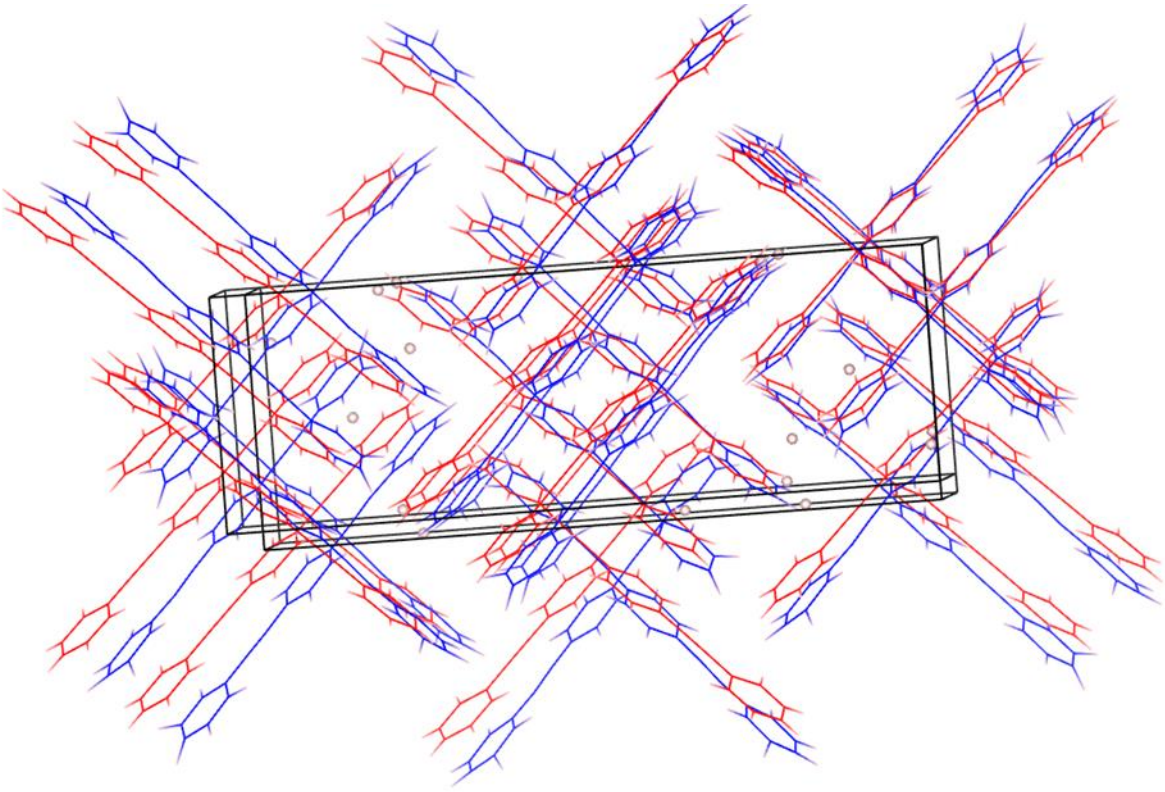

Figure 3.5 – Optimised DEB crystal using the consistent valence forcefield [cvff] (in blue) overlaying the experimental crystal structure of Li *et al.*[60] (in red).

3.3.1.2 Dreiding

The Dreiding force field produced a set of results with varying degrees of accuracy when compared to the experimental data. First of all, the cell parameters for b (+ 3.29%) and c (+ 5.08%) are very close to those of the experimental structure, and despite the a value (4.03%) being slightly

smaller it is not a significant amount, as shown in **Figure 3.6**. Interestingly, the a and b values are similar to those found in cvff (negative and positive difference, respectively) however there is a 7.37% difference between the c values. The volume produced using the Dreiding force field, however, is much larger than the experimental value, approximately 4% larger in fact with a value of 3021.01 $Å^3$, which would suggest this force field would not be a good choice. The average bond lengths also vary in their similarity to the experimental structure. The C1---C1 (+ 1.90%), C3---C3 (- 0.60%) and C2---C1 (+ 0.90%) are reasonable values but the other two bonds have a large discrepancy. This is evident in the C3---C2 bond which is 8.7% shorter and the H---C1 bond which is 7.62% greater than the 1.43 Å and 0.95 Å, respectively, reported for the experimental structure. A possible reason for Dreiding's failure in this system is that it is a generalised force field, meaning the parameters can be used for organic, biological and main-group inorganic molecules.[62] This means that the parameters used are not necessary ideal for the system being dealt with.

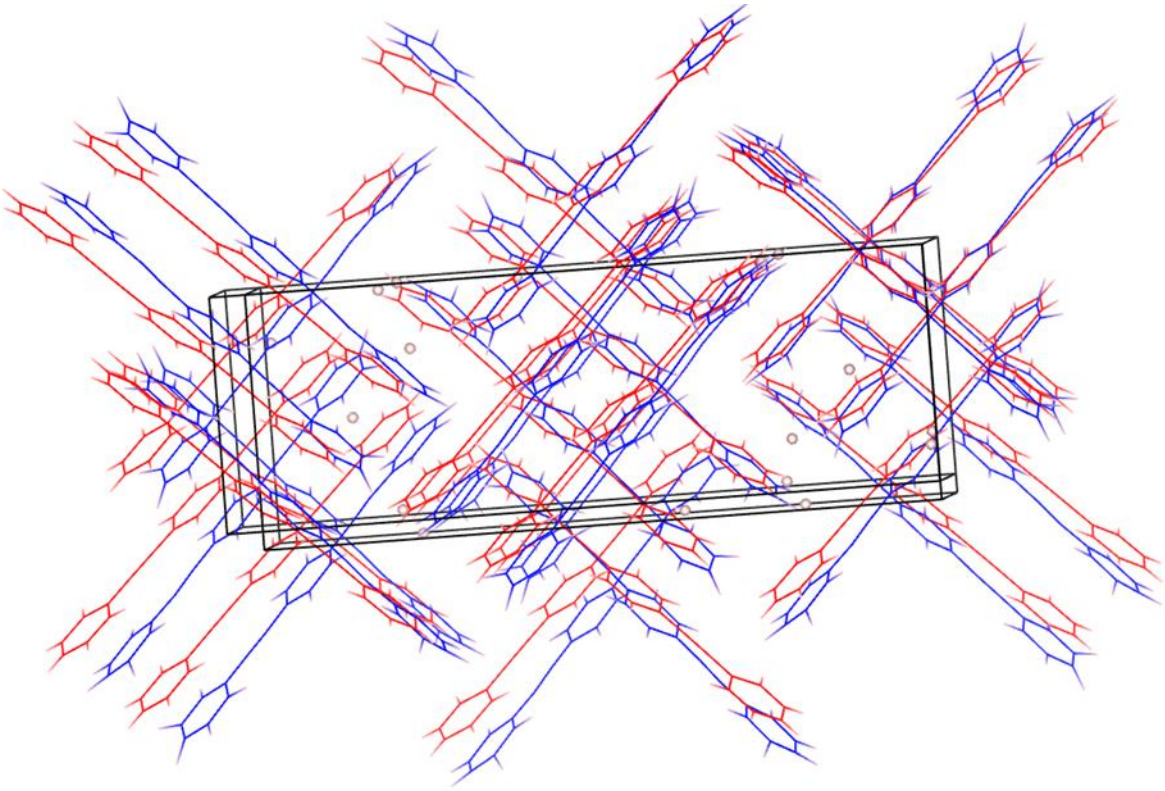

Figure 3.6 - Optimised DEB crystal using Dreiding force field (in blue) overlaying the experimental crystal structure of Li *et al.*[60] (in red).

3.3.1.3 OPLS

The Optimized Potentials for Liquid Simulations (OPLS) force field also produced mixed results. Just like cvff, the a (- 4.45%) and c (- 6.05%) cell parameters are slightly smaller than the experimental structure, whilst the b parameter is the closest to the original value than any other force field, only increasing it by 2.84% as depicted in **Figure 3.7** The volume calculated differed quite significantly with a decrease of 7.68%, which is too large to be overlooked. Just like the Dreiding force field, some of the average bond lengths were reasonably accurate, in particular C2---C1 (+ 0.29%), C3---C3 (0.71%), C1---C1 (+ 1.73%) and C3---C2 (+ 1.71%). The H---C1 bond length is very similar to those given by cvff and thus is similarly around 14% larger

than literature values. This force field may again be not as good as cvff as it too is used mainly for other systems, particularly biological systems. This is seen by the fact that its parameters were optimised to fit experimental properties of liquids. Therefore, although OPLS produced slightly better results than Dreiding, it is not as good as cvff.

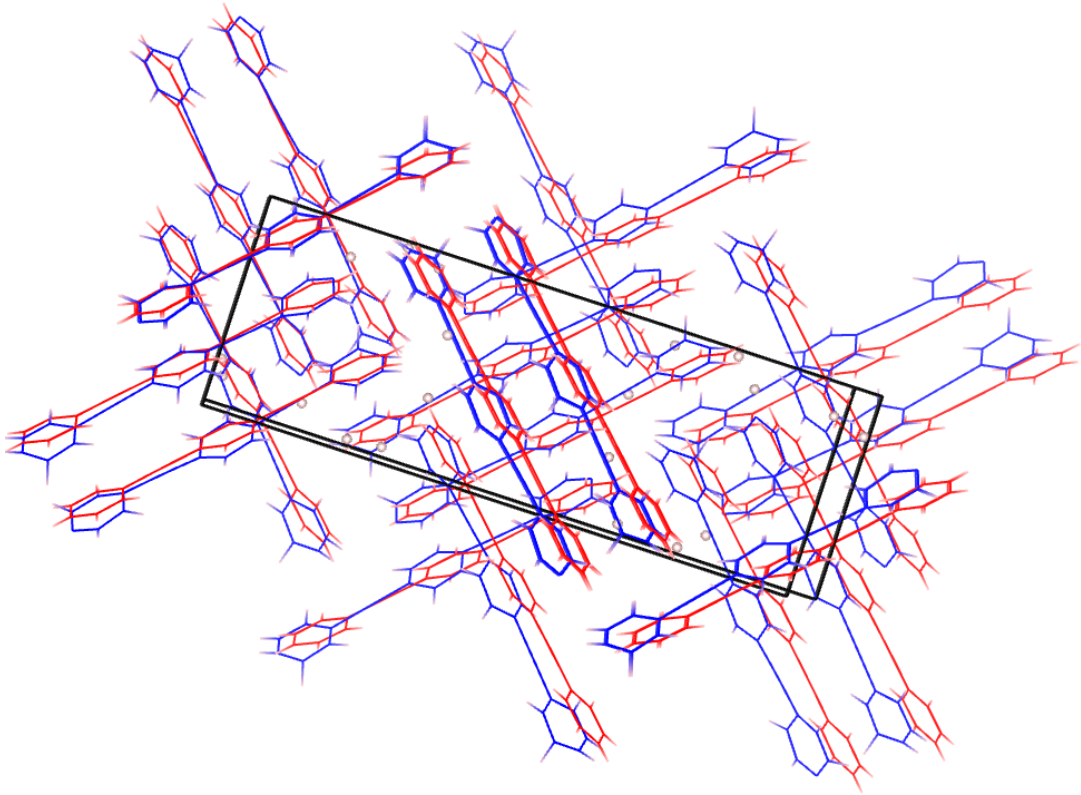

Figure 3.7 - Optimised DEB crystal using OPLS force field (in blue) overlaying the experimental crystal structure of Li *et al.*[60] (in red).

3.3.1.4 AMBER (GAFF)

After cvff, AMBER was probably the most successful force field as its results were fairly close in all aspects to the original values. The c cell parameter value was very close to that of the experimental, being only 0.26% larger with an answer of 11.08 Å^3. The a parameter was slightly smaller (- 6.44%) and the b parameter slightly larger (+ 8.12%) but once

again this is reasonably acceptable, although the volume calculated by GAFF was 1.4% larger than the 2900.27 Å^3 of the experimental crystal structure. **Figure 3.8** illustrates these differences. Despite producing the largest increase in the H---C1 bond length, with a 14.4% increase, of all the force fields, it still gave reasonable results for the other bond lengths. Although this particular AMBER force field is generic, it covers a greater number of possible bonding combinations compared to Dreiding. GAFF is also a force field that has been built over many years and thus has had many changes and additions made it to it which improves its accuracy.

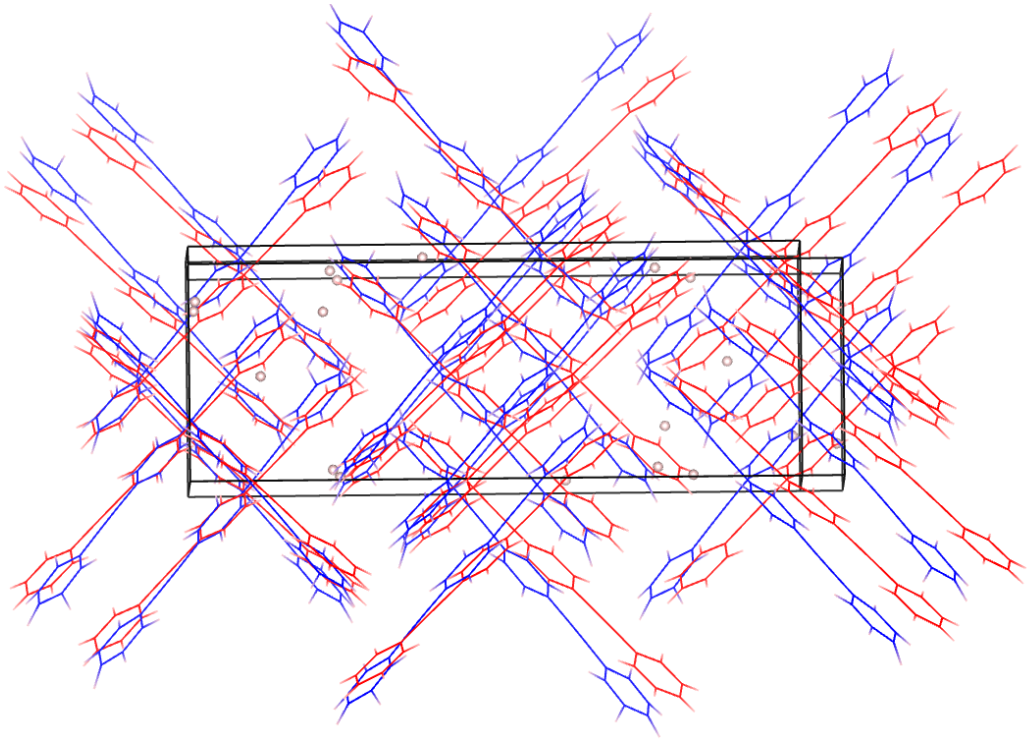

Figure 3.8 - Optimised DEB crystal using AMBER force field (in blue) overlaying the experimental crystal structure of Li *et al.*[60] (in red)3.3.1.5 Summary of force fields for DEB

Overall, cvff was the most accurate force field, especially using the Morse potential, as it reproduced values very similar to that of the crystal structure presented in 1998 by Li *et al*.[60] After cvff, AMBER looked the most

promising with most values accurate and only a few minor errors. Dreiding and OPLS however were the worst for this system as their generic parameters produced a large amount of discrepancies, despite the few accurate results.

3.3.1.6 2,5-dipropoxy-1,4-bis(phenylethynyl)benzene

The values calculated for 2,5-dipropoxy-1,4-bis(phenylethynyl)benzene are shown in **Table 3.2**, using the same force fields as a comparison. This confirms everything discussed above, with cvff once again reproducing results closest to the crystallographic data, most notably the volume which was only smaller by 5.68% when using the harmonic potential and 6.43% when using the Morse potential. Of course, this percentage difference is not ideal, as the Dreiding forcefield for DEB was dismissed earlier, partly due to its 4% increase in volume. However, when compared to the other forcefields cvff still produced the best results: Dreiding (9.23% smaller), Amber (11.14% smaller) and OPLS (20.42% smaller). The cvff (with Morse potential) force field did produce a bond length greater than the experimental value for C4---C1 (+ 14.89%) but as the C4 atom type is not required in the DEB system it is not of great concern. The four carbon bonds involved in both molecules (C1---C1, C2---C1, C3---C2 and C3---C3) were once again in good agreement with the experimental value for 2,5-dipropoxy-1,4-bis(phenylethynyl)benzene, being within ± 2.4% of the literature values. Once again, the bonds involving C3 (the triple bonded carbon) are a lot larger using the harmonic potential due to its lack of parameterisation. An example of this is with the Dreiding C3---C3 bond which it calculated 9.43% smaller than the experimental value. The Dreiding, OPLS and AMBER forcefields reproduced some properties with some degree

of accuracy yet some are not close enough. An example of this is the volume calculated by OPLS, 921.3647 $Å^3$, which is 20.42% smaller than experimental value.

	Experimental	*cvff (Harmonic)*	*Difference (%)*	*cvff (Morse)*	*Difference (%)*	*Dreiding*	*Difference (%)*	*OPLS*	*Difference (%)*	*Amber*	*Difference (%)*
Cell Parameters	a: 28.1212 Å b: 9.3300 Å c: 11.0541 Å α: 90.0000° β: 90.0000° γ: 90.0000°	a: 26.3720 Å b: 10.4319 Å c: 10.7507 Å α: 90.0000° β: 90.0000° γ: 90.0000°	*- 6.227* *+ 11.8* *- 2.74* *0* *0* *0*	a: 26.7240 Å b: 10.0666 Å c: 10.8006 Å α: 90.0000° β: 90.0000° γ: 90.0000°	*- 4.97* *+ 7.89* *- 2.29* *0* *0* *0*	a: 26.9876 Å b: 9.6368 Å c: 11.6160 Å α: 90.0000° β: 90.0000° γ: 90.0000°	*- 4.03* *+ 3.29* *+ 5.08* *0* *0* *0*	a: 26.8691 Å b: 9.5950 Å c: 10.3858 Å α: 90.0000° β: 90.0000° γ: 90.0000°	*- 4.45* *+ 2.84* *- 6.05* *0* *0* *0*	a: 26.2964 Å b: 10.0877 Å c: 11.0833 Å α: 90.0000° β: 90.0000° γ: 90.0000°	*- 6.44* *+ 8.12* *+ 0.26* *0* *0* *0*
Volume (Å^3)	2900.2730	2957.6409	*+ 1.98*	2905.5757	*+ 0.17*	3021.0138	*+ 4.16*	2677.5482	*- 7.68*	2940.0664	*+ 1.37*
Average Bond Lengths (Å)	**C1---C1**: 1.3807 **C2---C1**: 1.4002 **C3---C2**: 1.4297 **C3---C3**: 1.2028 **H---C1**: 0.9500	**C1---C1**: 1.3929 **C2---C1**: 1.3949 **C3---C2**: 1.4753 **C3---C3**: 1.3609 **H---C1**: 1.0797	*+ 0.88* *- 0.38* *+ 3.19* *+ 13.1* *+ 13.7*	**C1---C1**: 1.3986 **C2---C1**: 1.4043 **C3---C2**: 1.4112 **C3---C3**: 1.2075 **H---C1**: 1.0795	*+ 1.30* *+ 0.29* *- 1.29* *+ 0.39* *+ 13.6*	**C1---C1**: 1.4070 **C2---C1**: 1.4128 **C3---C2**: 1.3057 **C3---C3**: 1.1956 **H---C1**: 1.0224	*+ 1.90* *+ 0.90* *- 8.67* *- 0.60* *+ 7.62*	**C1---C1**: 1.4064 **C2---C1**: 1.4042 **C3---C2**: 1.4541 **C3---C3**: 1.2113 **H---C1**: 1.0794	*+ 1.73* *+ 0.29* *+ 1.71* *+ 0.71* *+ 13.6*	**C1---C1**: 1.4028 **C2---C1**: 1.4038 **C3---C2**: 1.4409 **C3---C3**: 1.1910 **H---C1**: 1.0868	*+ 1.60* *+ 0.26* *+ 0.78* *- 0.98* *+ 14.4*
Total Lattice Energy (eV)	----------	16.0220	----------	-1547.1730	----------	3.2627	----------	-0.5248	----------	-6.0700	----------

Table 3.1 – Comparison of the properties of the DEB crystal between experimental[60] and computational calculations with various force fields

	Experimental	*cvff (Harmonic)*	*Difference (%)*	*cvff (Morse)*	*Difference (%)*	*Dreiding*	*Difference (%)*	*OPLS*	*Difference (%)*	*Amber*	*Difference (%)*
Cell Parameters	a: 5.7856 Å b: 14.9764 Å c: 13.3619 Å α: 90.0000° β: 90.1120° γ: 90.0000°	a: 6.1890 Å b: 14.0547 Å c: 12.5595 Å α: 89.5263° β: 91.6096° γ: 90.0988°	*+ 6.97* *- 6.15* *- 6.01* *- 0.53* *+ 1.66* *+ 0.11*	a: 6.463 Å b: 12.7827 Å c: 13.1296 Å α: 92.7494° β: 89.1676° γ: 89.5954°	*+ 11.71* *- 14.65* *- 1.74* *+ 3.05* *- 1.05* *- 0.45*	a: 5.9986 Å b: 13.1814 Å c: 13.3015 Å α: 89.8902° β: 92.597° γ: 90.0307°	*+ 3.68* *- 11.99* *- 0.45* *- 0.12* *+ 2.76* *+ 0.03*	a: 5.5719 Å b: 12.6581 Å c: 13.0881 Å α: 89.9964° β: 93.5132° γ: 90.0052°	*- 3.69* *- 15.48* *- 2.05* *0.00* *+ 3.77* *+ 0.01*	a: 5.6004 Å b: 13.9598 Å c: 13.2053 Å α: 90.0517° β: 95.5182° γ: 90.0098°	*- 3.20* *- 6.79* *- 1.17* *+ 0.06* *+ 6.00* *+ 0.01*
Volume (Å^3)	1157.7725	1092.0134	*- 5.68*	1083.2994	*- 6.43*	1050.9135	*- 9.23*	921.3647	*- 20.42*	1028.7729	*- 11.14*
Average Bond Lengths (Å)	**C1---C1**: 1.3678 **C2---C1**: 1.3833 **C3---C2**: 1.4307 **C3---C3**: 1.1936 **C4---C1**: 1.3790 **C4---C2**: 1.3974 **C6---C5**: 1.5101 **C7---C6**: 1.5045 **O---C4**: 1.3644 **O---C5**: 1.4339 **H---C1**: 0.9612 **H---C5**: 1.0261 **H---C6**: 0.9960 **H---C7**: 1.1033	**C1---C1**: 1.3936 **C2---C1**: 1.3941 **C3---C2**: 1.4758 **C3---C3**: 1.15803 **C4---C1**: 1.3983 **C4---C2**: 1.4037 **C6---C5**: 1.5305 **C7---C6**: 1.5269 **O---C4**: 1.3840 **O---C5**: 1.3797 **H---C1**: 1.0794 **H---C5**: 1.1059 **H---C6**: 1.1061 **H---C7**: 1.1060	*+ 1.89* *+ 0.78* *+ 3.15* *- 2.98* *+ 1.40* *+ 0.45* *+ 1.35* *+ 1.49* *+ 1.44* *- 3.78* *+ 12.30* *+ 7.78* *+ 11.05* *+ 0.24*	**C1---C1**: 1.4006 **C2---C1**: 1.3959 **C3---C2**: 1.4131 **C3---C3**: 1.2101 **C4---C1**: 1.5843 **C4---C2**: 1.3857 **C6---C5**: 1.5216 **C7---C6**: 1.5245 **O---C4**: 1.4351 **O---C5**: 1.432 **H---C1**: 1.0797 **H---C5**: 1.1055 **H---C6**: 1.1044 **H---C7**: 1.1059	*+ 2.40* *+ 0.91* *- 1.23* *+ 1.38* *+ 14.89* *- 0.84* *+ 0.76* *+ 1.33* *+ 5.18* *- 0.13* *+ 12.33* *+ 7.74* *+ 10.88* *+ 0.24*	**C1---C1**: 1.4058 **C2---C1**: 1.4064 **C3---C2**: 1.2958 **C3---C3**: 1.1953 **C4---C1**: 1.409 **C4---C2**: 1.413 **C6---C5**: 1.5316 **C7---C6**: 1.5298 **O---C4**: 1.3549 **O---C5**: 1.4224 **H---C1**: 1.0194 **H---C5**: 1.0904 **H---C6**: 1.0896 **H---C7**: 1.0907	*+ 2.78* *+ 1.67* *- 9.43* *+ 0.14* *+ 2.18* *+ 1.12* *+ 1.42* *+ 1.68* *- 0.70* *- 0.80* *+ 6.05* *+ 6.27* *+ 9.40* *- 1.14*	**C1---C1**: 1.4035 **C2---C1**: 1.4036 **C3---C2**: 1.4599 **C3---C3**: 1.2122 **C4---C1**: 1.4044 **C4---C2**: 1.413 **C6---C5**: 1.5304 **C7---C6**: 1.5326 **O---C4**: 1.3682 **O---C5**: 1.4316 **H---C1**: 1.0793 **H---C5**: 1.0907 **H---C6**: 1.0892 **H---C7**: 1.0917	*+ 2.61* *+ 1.47* *+ 2.04* *+ 1.56* *+ 1.84* *+ 1.12* *+ 1.34* *+ 1.87* *+ 0.28* *- 0.16* *+ 12.29* *+ 6.30* *+ 9.36* *- 1.05*	**C1---C1**: 1.3994 **C2---C1**: 1.3989 **C3---C2**: 1.4381 **C3---C3**: 1.1907 **C4---C1**: 1.4005 **C4---C2**: 1.4049 **C6---C5**: 1.5421 **C7---C6**: 1.5453 **O---C4**: 1.3792 **O---C5**: 1.4452 **H---C1**: 1.0866 **H---C5**: 1.0946 **H---C6**: 1.0919 **H---C7**: 1.094	*+ 2.31* *+ 1.13* *+ 0.52* *- 0.24* *+ 1.56* *+ 0.54* *+ 2.12* *+ 2.71* *+ 1.08* *+ 0.79* *+ 13.05* *+ 6.68* *+ 9.63* *- 0.84*

Table 3.2- Comparison of the properties of the 2,5-dipropoxy-1,4-bis(phenylethynyl)benzene crystal between experimental[76] and computational calculations with various force fields

3.3.2 Thermochemical Properties for DEB

The table below, **Table 3.3**, shows the calculated densities and enthalpies of vaporization for 1,4-bis(phenylethynyl)benzene (DEB) and phenylacetylene, along with the literature values, where available.

	Density		Enthalpy of Vaporization	
	Calculated (g/cm^3)	Experimental (g/cm^3)	Calculated (kJ/mol)	Experimental (kJ/mol)
Phenylacetylene	1.05	1.100[79]	78.87	43.78 ± 0.13[80]
DEB	1.14	1.2[81]	178.52*	135.8*[26]

Table 3.3 - The calculated and experimental values for the densities and enthalpies of vaporization for phenylacetylene and DEB. *Enthalpy of Sublimation given

It is noticeable that, with regards to the density, the calculated values are lower than the values obtained from experiments. This can be explained for phenylacetylene by comparing the conditions under which the values were acquired. The experimental work was carried out at room temperature (298.15 K) where phenylacetylene is a liquid, however a crystal solid structure was used in the calculations. Also, the experiment was carried out at 0.4 GPa[79] (which is approximately 3.9 atm) whereas the calculation was carried out 1 atm. After bearing these matters in mind, the two values are in reasonably good agreement. The calculated DEB value is only 5% lower than the experimental value, which is an acceptable margin of error. The difference in the experimental/computational techniques just mentioned also help explain the vast difference between the calculated and experimental values for the enthalpy of vaporization of phenylacetylene. The enthalpy of vaporization is the enthalpy change required to convert a liquid into a gas, however as previously mentioned this system was a crystalline solid and so this proves

problematic when attempting to calculate the enthalpy of vaporization. Also, unfortunately, there is no literature data for the enthalpy of vaporization for DEB so far.

3.4 Conclusion

Overall the investigation was a success. The four force fields in question – cvff, Dreiding, OPLS and Amber – all minimised the crystal structure with varying accuracy. cvff was the most accurate, especially when using the Morse potential, and is a suitable force field to use throughout the rest of this thesis. The other force fields did produce some promising results for certain parameters and bond lengths but there was a large discrepancy between some calculated values and those given in literature. This is due to the systems they were created for, *e.g.* biological or liquid.

The second part of the investigation looked at using the cvff force field to explore the thermochemical properties of DEB and phenylacetylene. In both instances the density was calculated accurately, giving good agreement with experimental values. With regards to the enthalpy of vaporization, there were discrepancies with the literature values but as discussed this was due to the conditions under which the calculations were made.

Chapter 4: Melting Point ‘Envelope’ for DEB

This chapter will describe the investigation carried out to determine a melting point ‘envelope’ for the DEB crystal. The melting point ‘envelope’ is the temperature range within which melting is expected to occur. This is important to study to further understand how the DEB molecules are affected by greater temperatures and to understand their movements and behaviours once the melting point has been reached. This is vital to understand in real life applications as this could affect their properties and thus efficiency. It is important to note that the system could not simply be subjected to increasing temperatures until the crystal structure broke down as this would provide an overestimation of the melting temperature, caused by a phenomenon known as superheating.[82] In order for an accurate calculation toto be performed two methods were utilised – one involving removing percentages of molecules from the system and a second method involving creating slabs of molecules with empty space in between. Accurate and efficient melting point molecular dynamics calculations are still complex tasks[83] so these two methods were chosen as these were considered relatively simpler methods. Another method which could have been utilised is a free-energy calculation however this rigorous method is generally more complicated to apply and more computationally expensive.[83] The main difference between the removal of molecules method and the ‘slab’ technique was that the latter exposed a surface, which will be discussed further, later in the chapter.

4.1 Methodology

Molecular dynamics (the DL_POLY software package) was once again used along with the consistent-valence force field (cvff) which was found to be most appropriate force field in Chapter 3. The melting point 'range' was compared to the experimentally determined value of 449.15 K – 451.15 K.[39,84,85] The aforementioned methods used to investigate the melting point 'envelope' will now be discussed in further detail.

4.1.1 Removal of Molecules from System

The first method used to test the melting temperature involved removing various percentages of whole DEB molecules from the system. The percentages chosen were 0% (as a control), 10% (14 molecules), 15% (21 molecules) and 20% (28 molecules). These systems will be named D0, D10, D15 and D20 respectively for clarity. The reasoning behind removing some of the molecules is to create a defect in the system which eliminates the free energy barrier to the formation of a solid-liquid interface.[86] These defects, or voids, allow the formation of solid-liquid interfaces which lowers, if not eliminates, the free energy barrier for the conversion of solid to liquid. The location and distribution of these voids in the system has been shown not to affect the melting point predictions[82] and so the molecules to be removed could be chosen randomly. These randomly removed molecules were chosen by a random number generator and then removed from the DL_POLY CONFIG file. This method was carried out in 3 stages. The first stage involved evaluating the 'new' systems (after the molecules had been removed) at 373.15 K, 423.15 K and 473.15 K. The calculations were carried out for 330

ps using the NPT ensemble. After this, the system with no molecules removed was simulated at two higher temperatures - 523.15 K and 573.15 K, again for 330 ps. Finally, the D10 and D20 systems were run again for 1 ns at two lower temperatures 273.15 K and 323.15 K. Mean square displacement (MSDs) and radial distribution functions (RDFs) were produced to analyse the data. When analysing the results, it is important to ensure that the crystal is actually melting rather than minimising to an amorphous phase, where the crystal has lost its long-range order but still exhibits the properties of a solid.

4.1.2 Slab Technique

The slab technique method comprised of two parts – a melting part and a freezing part. The melting aspect would help find the upper temperature of the 'envelope' whereas the freezing part would help identify the lower temperature.

4.1.2.1 Slab Technique - Melting Method

The second method used to test for the upper temperature for the 'envelope' involved creating slabs of molecules that were separated by empty space that the molecules can melt into (**Figure 4.1a**). A melting point range is utilised as it is harder to pinpoint an actual melting 'point' using calculations as these larger DEB molecules take longer to break their intermolecular bonds and so is not always obvious when the crystal has melted. The creation of the slabs was achieved by keeping the cartesian coordinates of the molecules the same and doubling the cell parameters, leading to 2D slabs separated by a vacuum. This in effect created a surface which allowed the molecules at the solid-vacuum interface to first gain rotational freedom and then mobility,

ultimately leading to a crystal-to-liquid transition.[87] Each cell parameter was doubled separately in order to ensure the results were as accurate as possible. These new parameter values were a = 72.24 Å, b = 75.05 Å and c = 81.83 Å. The calculations used the NVT ensemble and were carried out for 2 ns. The temperatures tested were 273.15 K, 323.15 K, 373.15 K, 423.15 K, 473.15 K, 523.15 K and 573.15 K. Once again, MSDs and RDFs were used to analyse the data.

4.1.2.2 Slab Technique – Freezing Method

To find the lower melting point for the melting point range, calculated as 455 K by Sharma *et al.* in 2017 using the differential scanning calorimetry technique [39] and the 452 K reported by Nigrey in 2000.[24] The same slab technique was used as before with a few modifications. For a start, a CONFIG file produced from the end of a melting calculation was used as the starting CONFIG file while investigating the lower temperature. This was to ensure that the system was in a liquid state before the freezing phase could occur. **Figure 4.1b** shows a visualisation of the liquid system at the beginning. Also slightly different temperatures were tested – 500.15 K down to 300.15 K in 25 K intervals. This was to ensure the most accurate lower melting point could be found, as 50 K intervals may be too large and overlook the point of freezing. Once again, the calculation was run for 2 ns using the NVT ensemble with MSDs and RDFs being used as analysing tools.

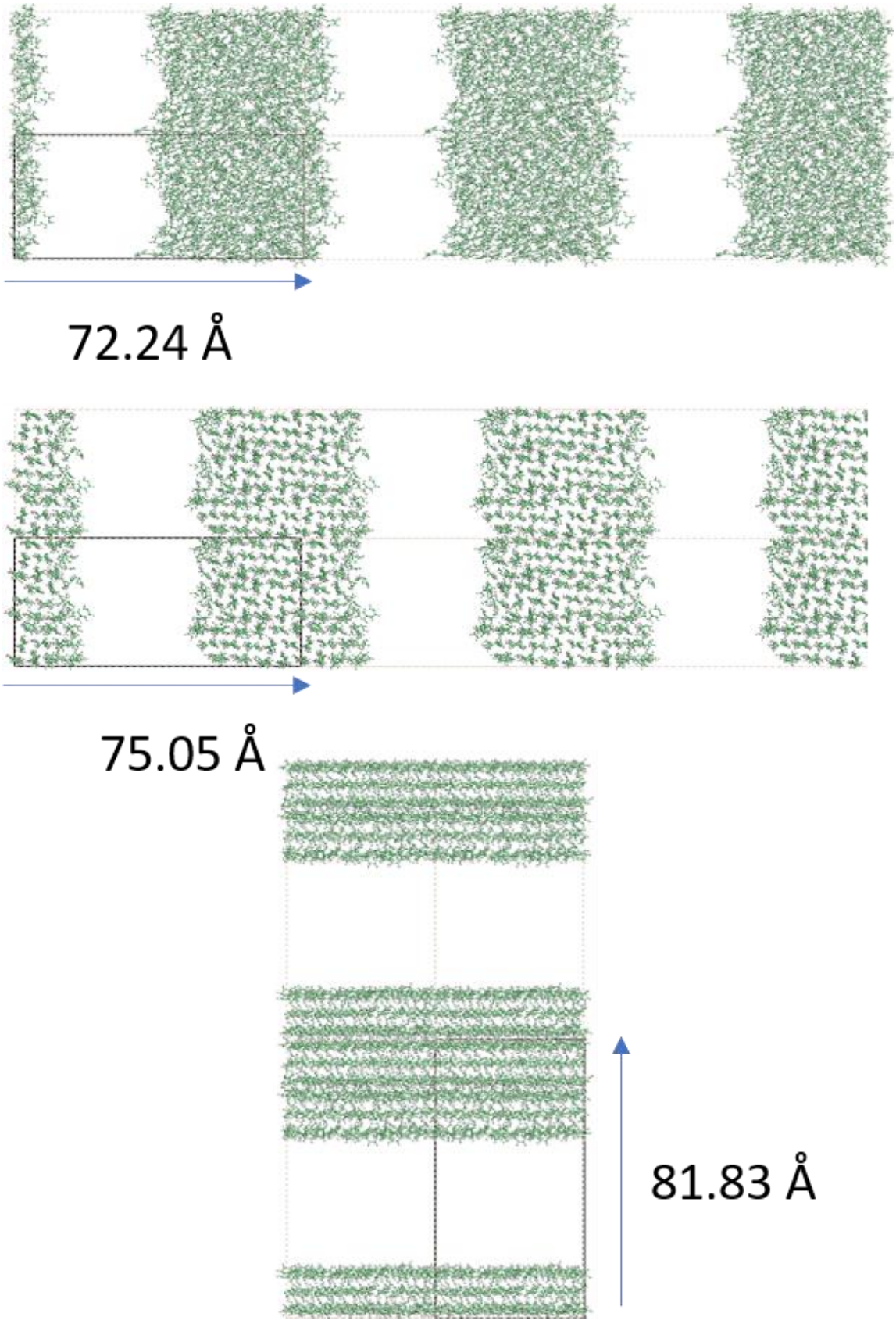

Figure 4.1a - Picture showing the slabs of molecules (in green) with the vacuum in between along with the doubled parameters (top - a; middle – b, and bottom - c).

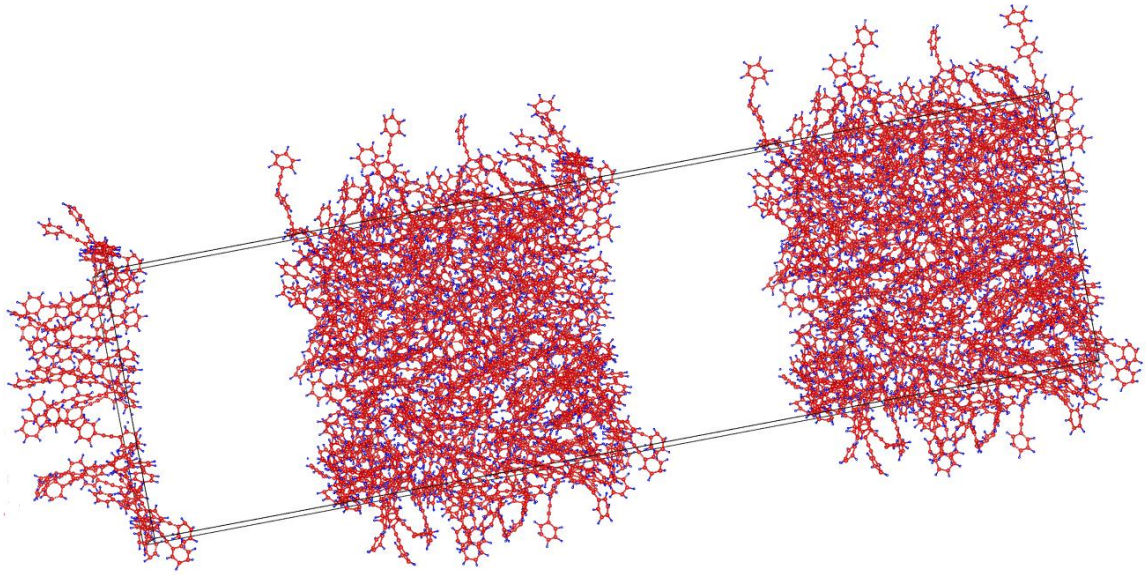

Figure 4.1b – Image showing the DEB system in its liquid state (i.e. after being melted at 573.15 K). This liquid state was used as the starting structure for the freezing phase calculations using the slab technique.

4.2 Results and Discussion

Mean square displacement (MSD) and radial distribution function (RDF) graphs were made to characterise diffusivity of the DEB molecules as well as the short and medium range order and thus from this, assess if melting (and later, freezing) had occurred. MSDs measure the average distance a molecule (or group of molecules) diffuse over time. If melting has occurred, the molecules exhibit long range motion in three dimensions as they would be part of a liquid, as opposed to the solid crystalline structure they began in. The MSDs used for this investigation were all-atom MSDs. RDFs measure the probability of finding a molecule (or group of molecules) at a certain distance away from the reference atoms. In this case, the sp carbon atoms (CT, if using force field notation) were used to compile the inter-molecular RDFs (**Figure 4.2**). If melting had occurred, these distances would increase as the molecules

drifted further apart, again as they would now be part of a liquid. This is due to the loss of longer range order and would result in the peaks of the RDF losing intensity before completely disappearing.

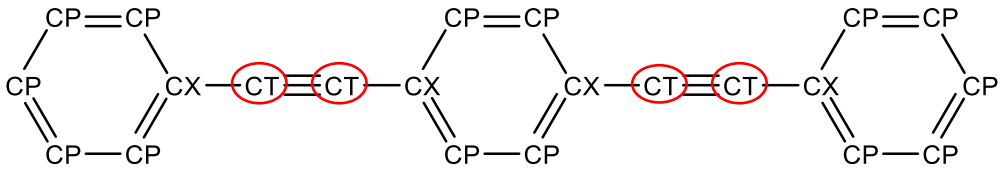

Figure 4.2 – DEB molecule with the atom names used by the constant valence force field. The atoms highlighted in red were the ones used to calculate the RDFs

4.2.1 Removal of Molecules – Melting Method

This section will look at the results obtained from the removal of varying percentages of DEB molecules from the simulation box. Here, firstly, are the results from the calculation run at 330ps.

Looking at the graphs below, **Figures 4.3 – 4.12**, the first noticeable point is that there is some evidence of melting occurring as the number of molecules removed increases. With reference to the RDFs (**Figure 4.3a**), as the simulation is run from D0 to D20, it is clear there is a large peak at ~5 Å that shows the nearest neighbour and is present throughout all temperatures and percentages of removed molecules. The next closest neighbour is approximately 10 Å away and clearly loses intensity as more molecules are removed (D0 ~1.6, D10 ~ 1.4, D15 ~1.25 and D20 ~ 1). This suggests there is some loss of long-range order, which is an indication of melting (or amorphisation). This is further supported by the two smaller peaks at ~13 Å and ~15 Å that are visible at D0 have completely disappeared by the D20

system. **Figure 4.3b** shows the RDF of the DEB crystal at 0K, i.e pre production run. It is noticeable that, as one would expect, there is a greater deal of order in the crystal structure at 0K as there is no movement from the molecules, not even vibrational. Further evidence is supplied by the MSD (**Figure 4.4**), which shows no long-range diffusion when 0% of the DEB molecules were removed from the box at any temperature, and thus no melting has occurred. **Figure 4.5** shows images of the simulation for 0% removal at 473.15 K and there are no signs of molecules having moved at all, with the molecules keeping their order in the cell throughout the calculation.

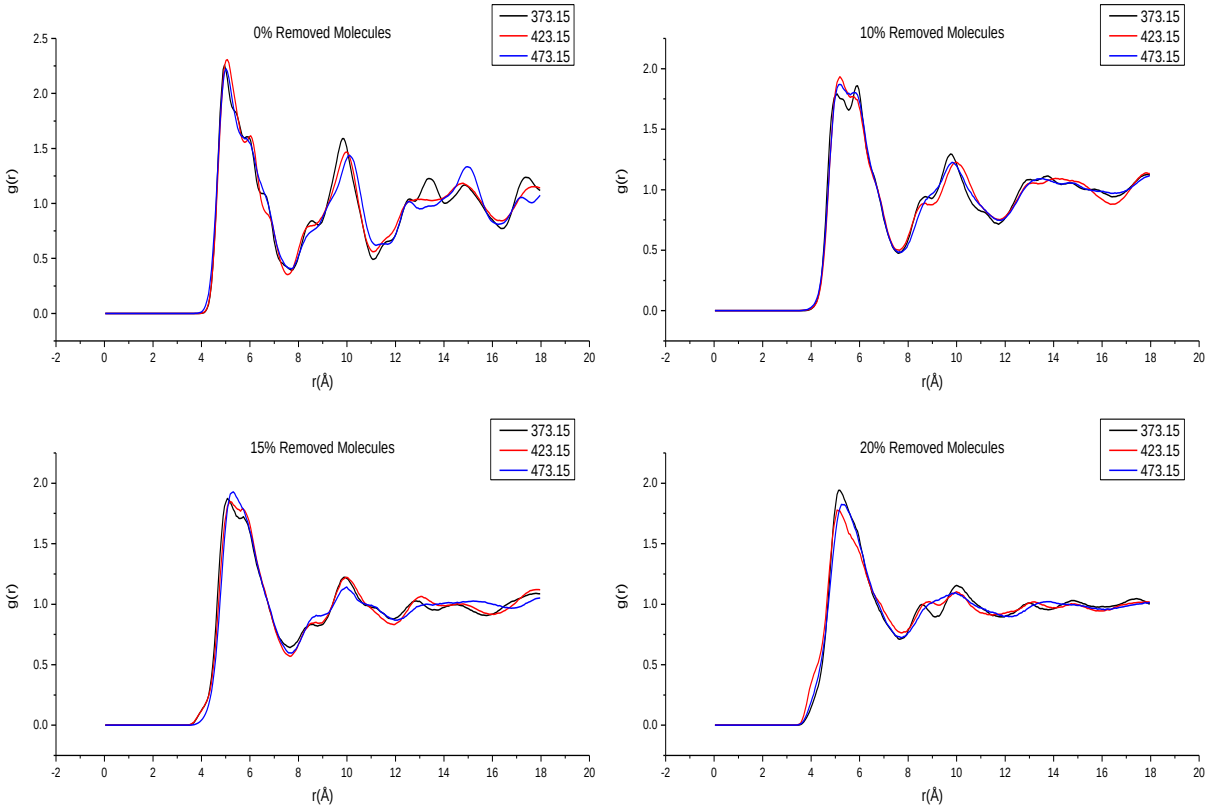

Figure 4.3a - Intermolecular CT-CT RDFs for the various percentages of molecules removed from the box at 373.15, 423.15 and 473.15 K

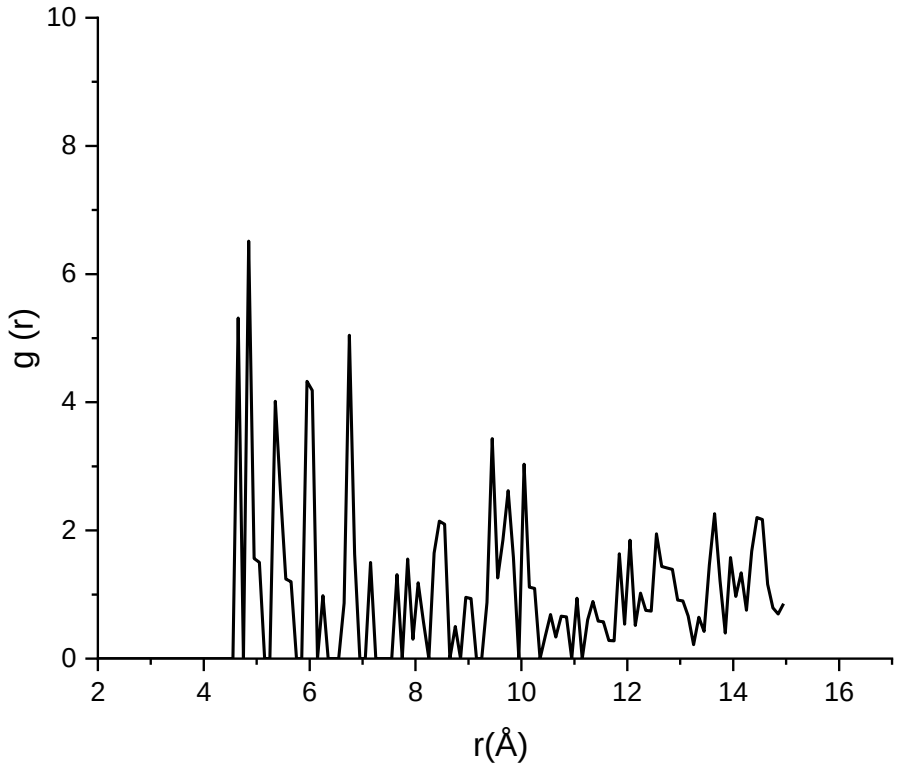

Figure 4.3b - Intermolecular CT-CT RDF for the DEB crystal at 0K.

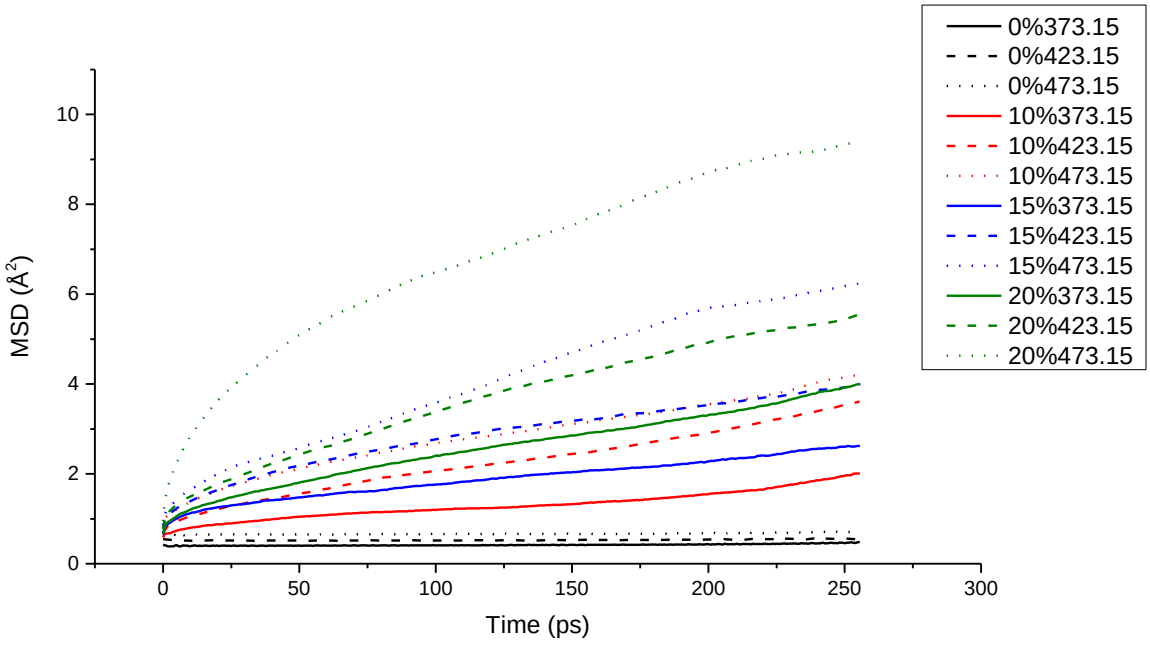

Figure 4.4 - All-atom MSD for the various percentages of molecules removed from the box at 373.15, 423.15 and 473.15 K

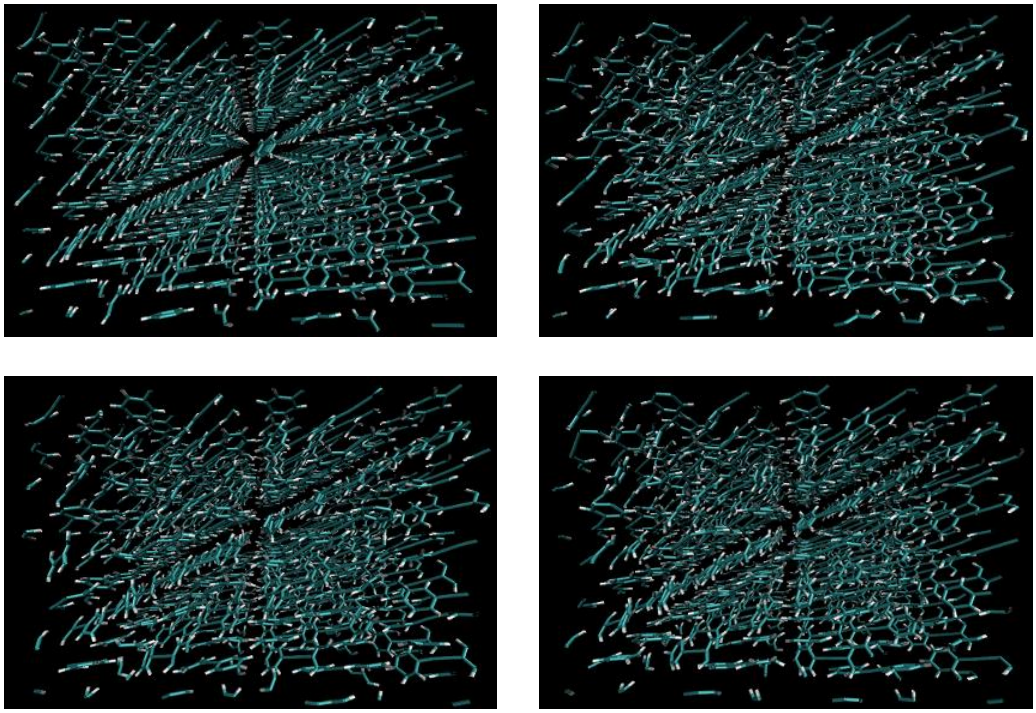

Figure 4.5 - Images of 0% removed DEB molecules at 473.15 K - Top Left: 0 ps, Top Right: 110 ps, Bottom Left: 220 ps, Bottom Right: 330 ps

The simulation that appears to have produced the most long-range diffusion of DEB molecules was when the simulation was run at 473.15 K with 20% of the molecules removed, giving an MSD of around 8.5 $Å^2$ over the 250 ps period. The initial sharp increase in gradient is due to thermal displacement, as the cell is becoming minimised and thus the atoms are moving slightly. However, after this initial 50 – 100 ps region, the MSD continues to increase suggesting long-range diffusion of the molecules is taking place. This is to be expected, as with 28 molecules removed, there is more room for the remaining DEB molecules to move around and this can be seen in **Figure 4.6**, which shows screenshots from the simulation. There is evidence of melting occurring for the higher temperatures for D20 (the green lines). At D10 and D15, the previously mentioned indicators of melting occur at the highest temperature (473.15 K) yet there is not conclusive evidence

whether there is melting actually occurring. There is some loss of order but that could mean the crystal has become amorphized rather than actually melting.

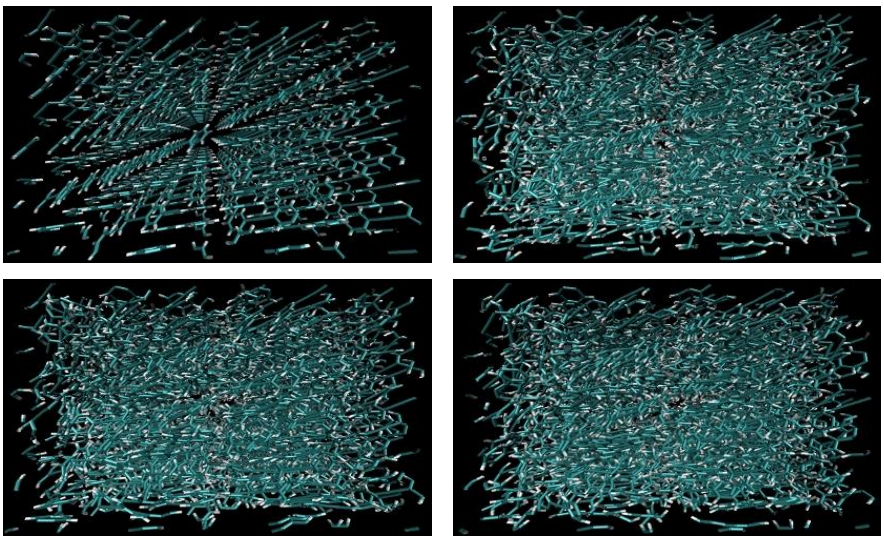

Figure 4.6 - Images of 20% removed DEB molecules at 473.15 K - Top Left: 0 ps, Top Right: 110 ps, Bottom Left: 220 ps, Bottom Right: 330 ps

To ensure that there was definitely no melting when 0% of the molecules were removed, the simulation was run at two higher temperatures – 523.15 K and 573.15 K:

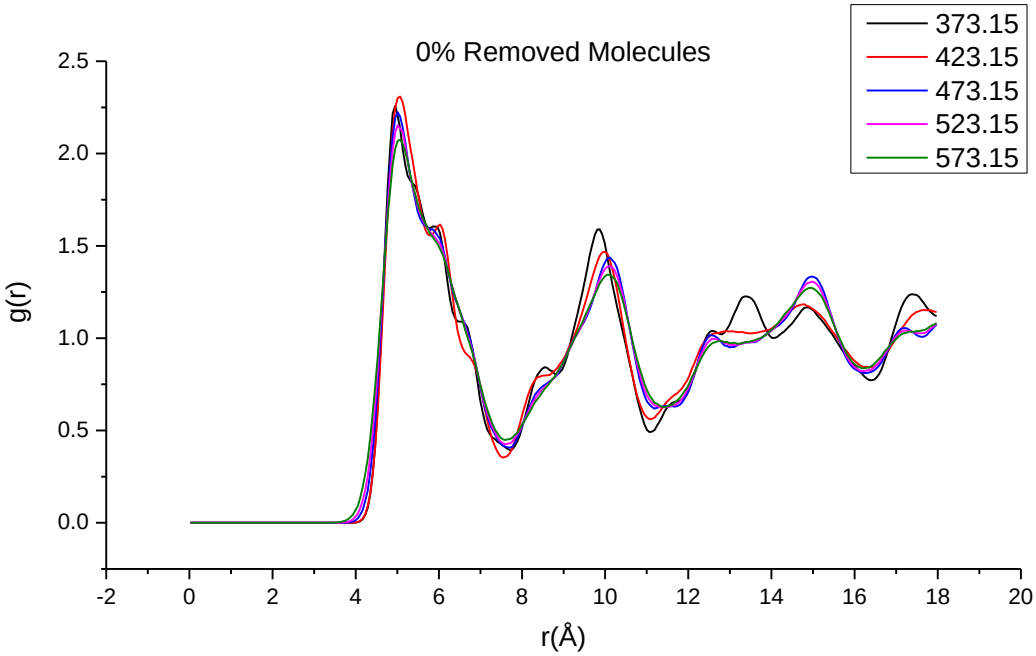

Figure 4.7 – Intermolecular CT-CT RDF for 0% of molecules removed from the box with two higher temperatures – 523.15 K and 573.15 K

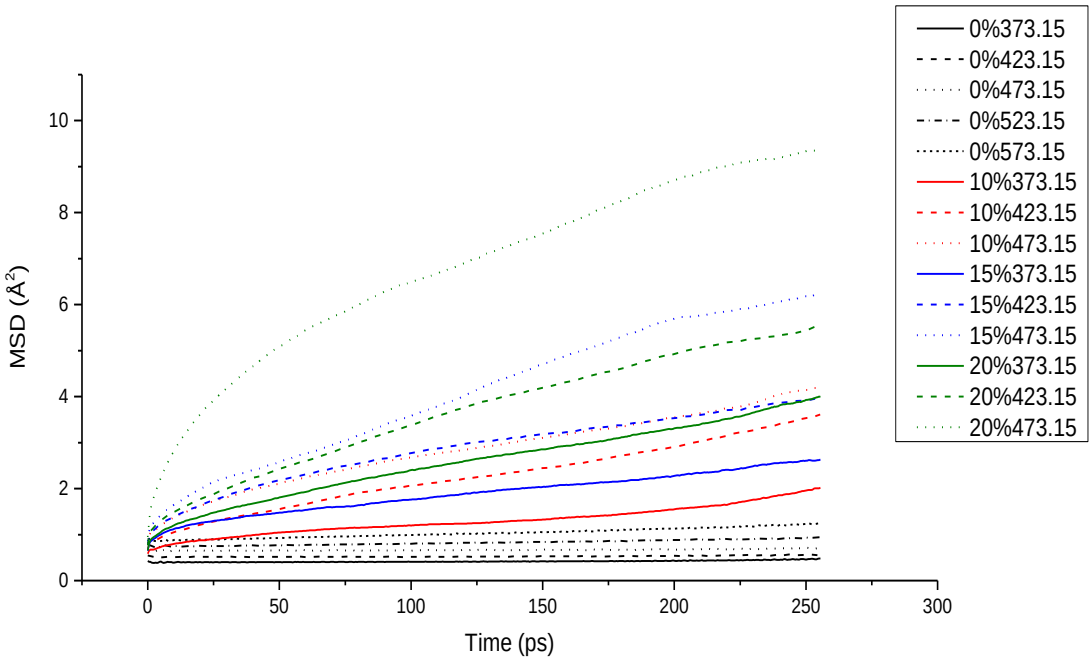

Figure 4.8 - All-atom MSD for the various percentages of molecules removed from the box at 373.15 K, 423.15 K and 473.15 K, with two higher temperatures (523.15 and 573.15 K) being used for 0% of molecules removed.

There is strong evidence, from both the RDF (**Figure 4.7**) and MSD (black lines in **Figure 4.8**) that there is still no melting occurring when 0% of the DEB molecules were removed. The peaks in the RDF suggest there is still medium and long range order, from 5 Å to 18 Å, and there are similar intensities at each temperature, implying the DEB molecules remain the same distance apart as the temperature increases. The slight decrease in intensity at around 13 Å is probably due to some loss of order caused by increased thermal vibration rather than any signs of melting. No melting occurring at 0% removed molecules is to be expected, as with the molecules packed tightly the liquid phase cannot nucleate. As discussed earlier, the melting of the crystal occurred for the higher temperatures when 20% of the molecules were removed and possibly at the higher temperature when 10% and 15% of the molecules were removed. Both the 10% and 20% simulations were run again at two lower temperatures (273.15 K and 323.15 K) to compare with the values given at the higher temperatures. Also, it was important to confirm that melting was actually taking place due to the increase of temperature rather than just cell minimization and molecular vibrations occurring. Also, the calculation was run for longer – 1ns. Below are the graphs displaying the results from these calculations:

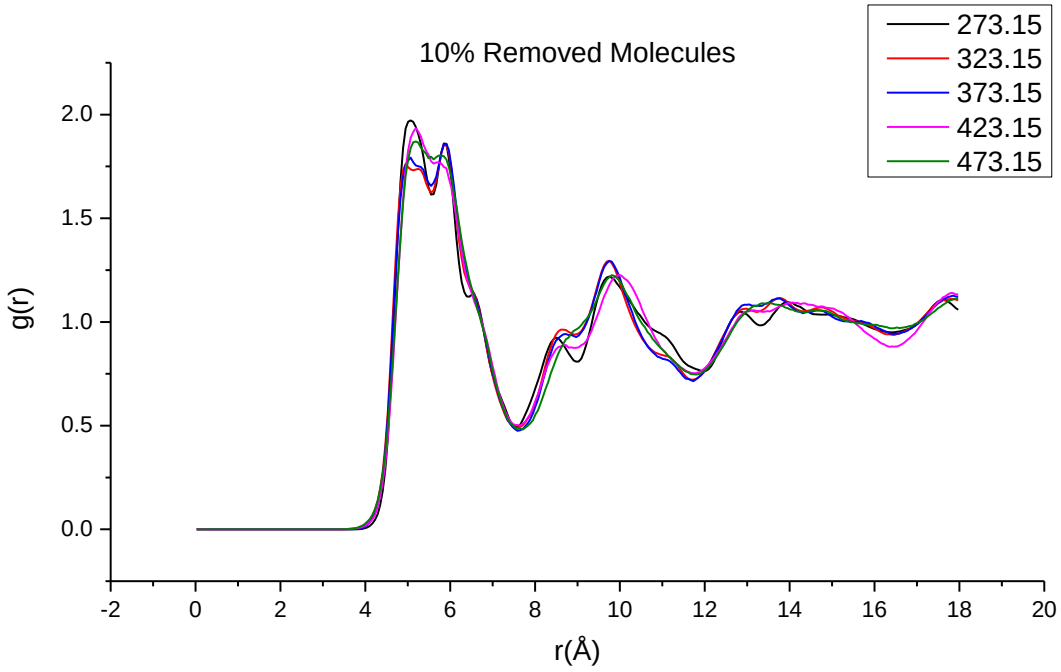

Figure 4.9 - Intermolecular CT-CT RDF for D10 at 273.15 K, 323.15 K, 373.15 K, 423.15 K and 473.15 K

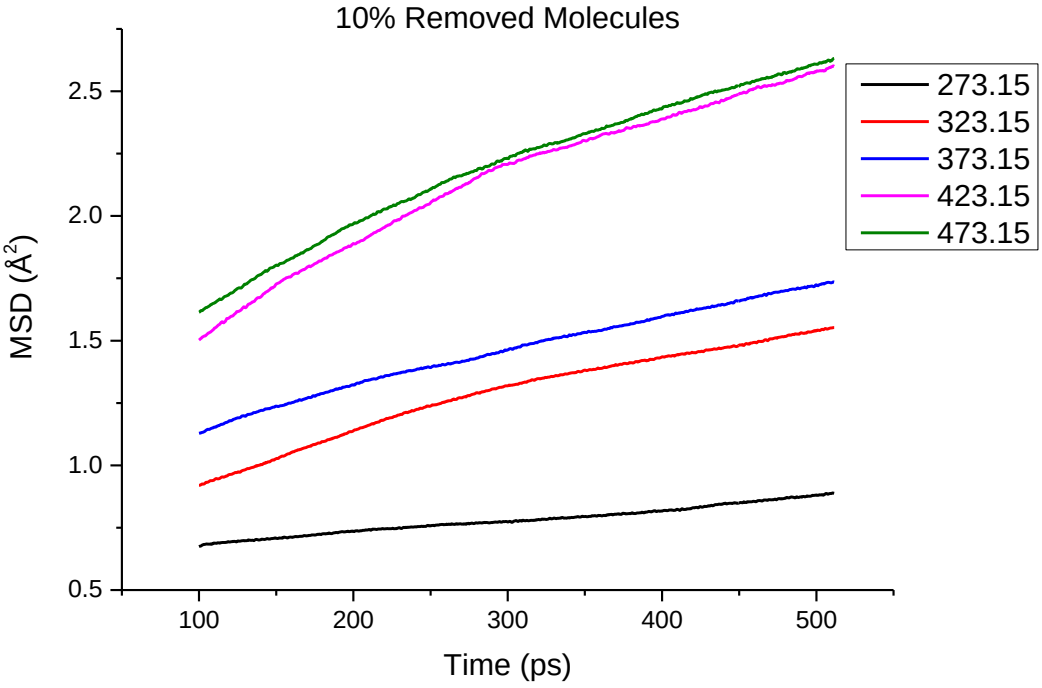

Figure 4.10 - All-atom MSD for D10 at 273.15 K, 323.15 K, 373.15 K, 423.15 K and 473.15 K

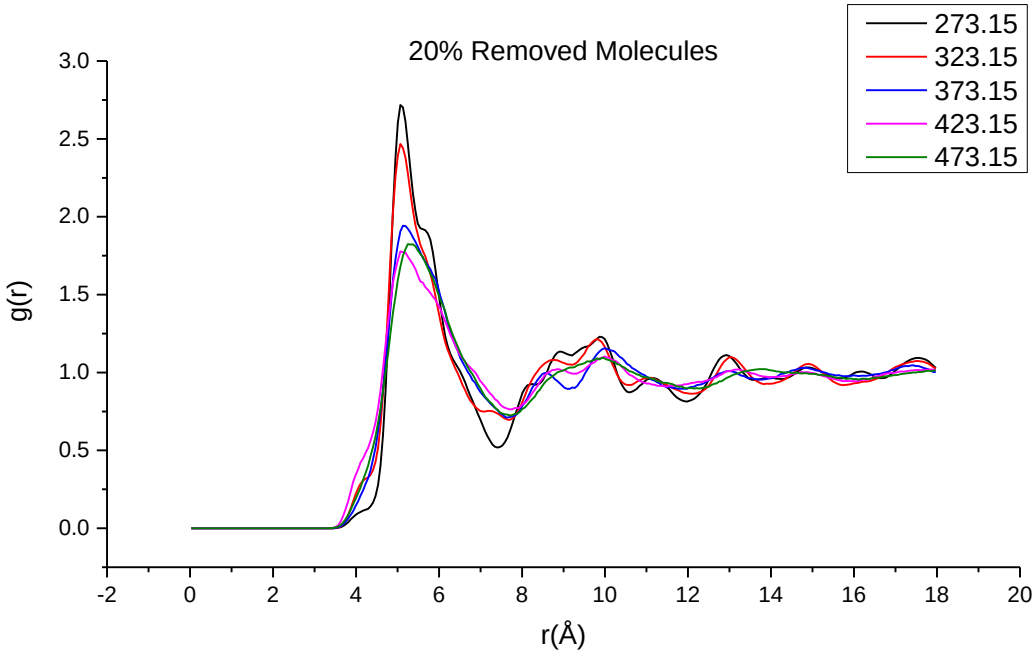

Figure 4.11 - Intermolecular CT-CT RDF for D20 at 273.15 K, 323.15 K, 373.15 K, 423.15 K and 473.15 K

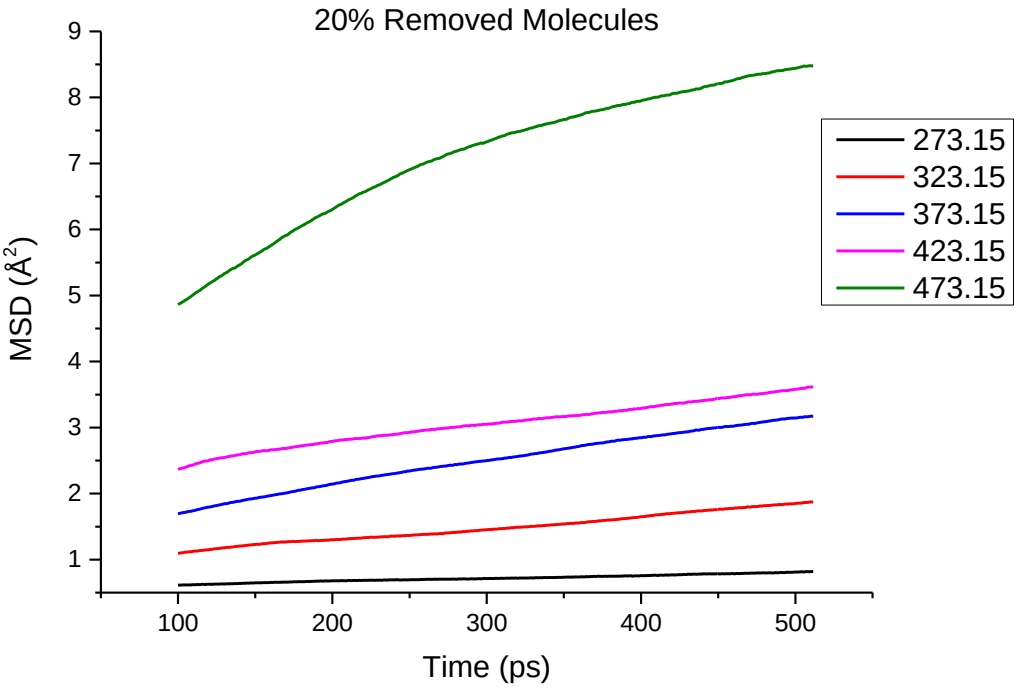

Figure 4.12 - All-atom MSD for D20 at 273.15 K, 323.15 K, 373.15 K, 423.15 K and 473.15 K

For D10, the peaks of the RDF at approximately 5.5 Å /6 Å show a little difference across the varying temperatures but it is not until 473.15K that the two peaks decrease in intensity showing that the molecules that were in the vicinity of each other start to break their intermolecular bonds and drift apart, showing that melting is begging to occur in the system However, there are no major differences between the lines representing the different temperatures, making it difficult to say for certain if melting has occurred. On the other hand, the MSD gives some interesting results. There is a mean square difference of 2.5 $Å^2$ at both 423.15 K and 473.15 K, indicating there is a small amount of long-range diffusion. This value is very small, making it difficult to decisively say that the crystal has melted. **Table 4.1** shows the diffusion coefficients calculated from the MSDs and, despite their small values, show the mobility of the molecules increasing almost two-fold from 3.48 x 10^{-32} m^2 s^{-1} for 373.15 K to 6.30 x 10^{-32} m^2 s^{-1} for 473.15 K.

The RDF for D20 (**Figure 4.11**) is very helpful as it clearly shows a small drop in the g(r) (the probability of finding a particle at a distance r from another tagged particle) of around 1.0 at the shoulder peak section at the 5 Å for 373.15 K, 423.15 K and 473.15 K. The intensity of the other peaks also decreases as the temperature increases, with the line at 473.15 K becoming almost completely linear. The loss of long-range order suggests the structure is no longer present and a viscous liquid has resulted. When looking at these three temperatures on the MSD graph, it is evident that there are signs of melting for all of them, however on closer inspection, the gradient for 373.15 K is very small and is almost linear, thus it is difficult to confirm melting has occurred. The two higher temperatures, of 423.15 K and 473.15 K, show a

greater gradient and thus melting, with MSDs of 2.5 Å and 8.5 Å respectively. Once again, **Table 4.1** shows the calculated diffusion coefficients and evidently at 473.15 K the mobility of the molecules is greater, with a coefficient of 20.86 x 10^{-32} m^2 s^{-1}, which is almost 5 times greater than that of 323.15 K (4.4 x 10^{-32} m^2 s^{-1}).

Therefore, this method of removing various percentages of molecules from the simulation gives an upper melting point of 423.15 - 473.15 K.

	Diffusion Coefficients (m^2 s^{-1}) [all values are x 10^{-32}]	
Temperature (K)	**10% Removed Molecules**	**20% Removed Molecules**
273.15	1.13	1.16
323.15	3.48	4.44
373.15	3.68	8.74
423.15	5.88	6.77
473.15	6.30	20.86

Table 4.1 – Diffusion Coefficients for 10% and 20% removed molecules for 1 ns production run

4.2.2 Slab Technique – Melting Method

To investigate the results obtained from the removal of molecules technique, the slab technique was used to measure the melting point 'envelope'. As described in the methodology, this involves increasing the size of one of the cell parameters, creating an alternating pattern of layers of molecules and a vacuum, each of the same width as the original cell dimension. In this investigation, each cell parameter was doubled in separate simulations, and the results are described below.

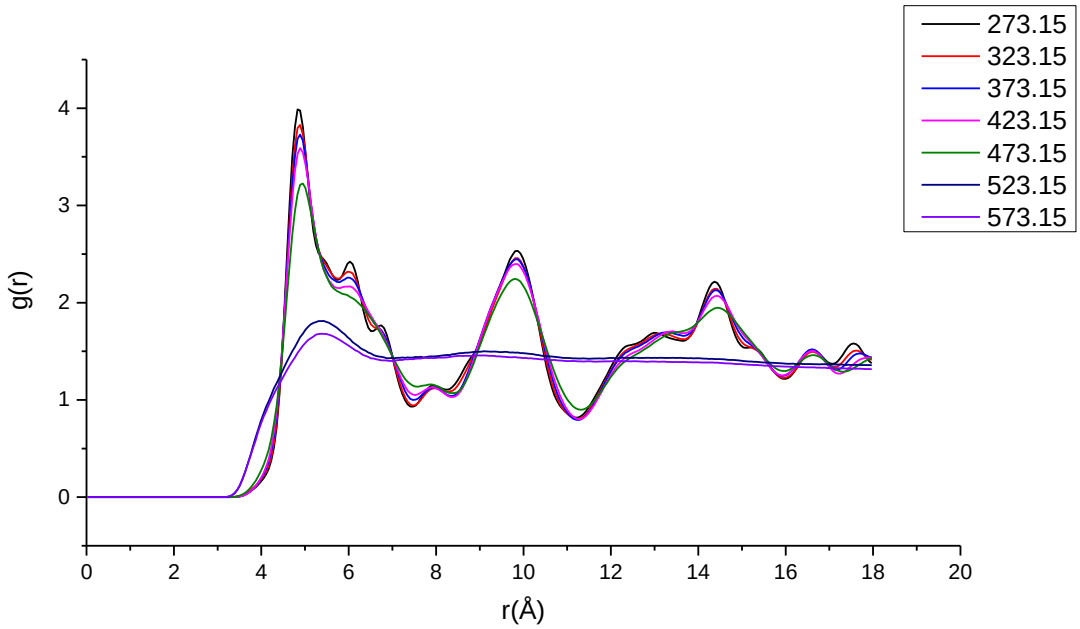

Figure 4.13 - Intermolecular CT-CT RDF when the a parameter is doubled at various temperatures.

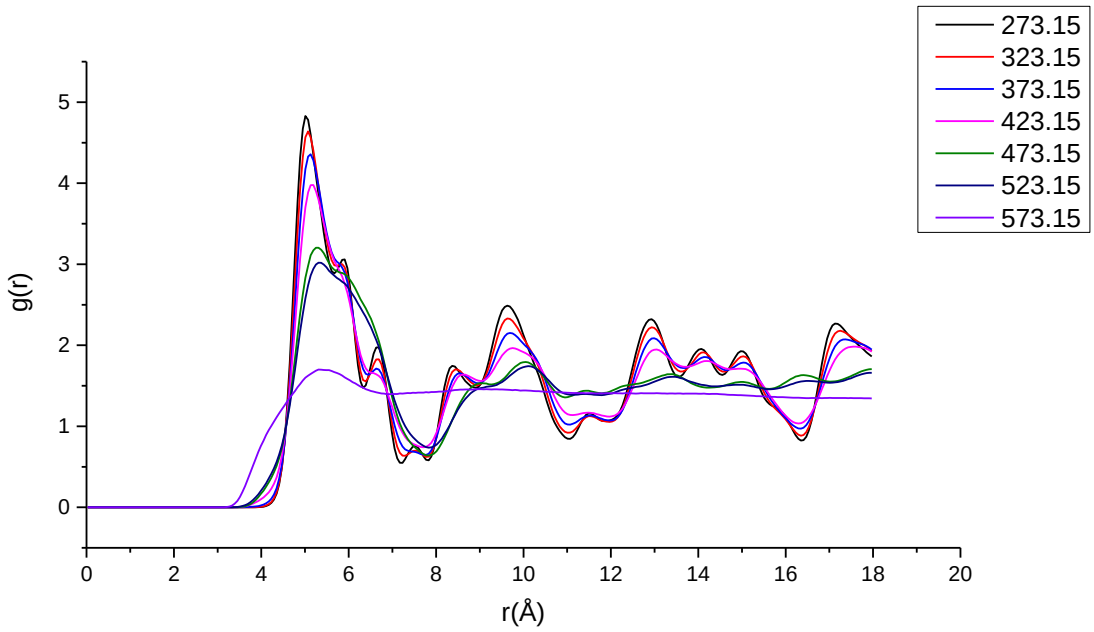

Figure 4.14 - Intermolecular CT-CT RDF when the b parameter is doubled at various temperatures.

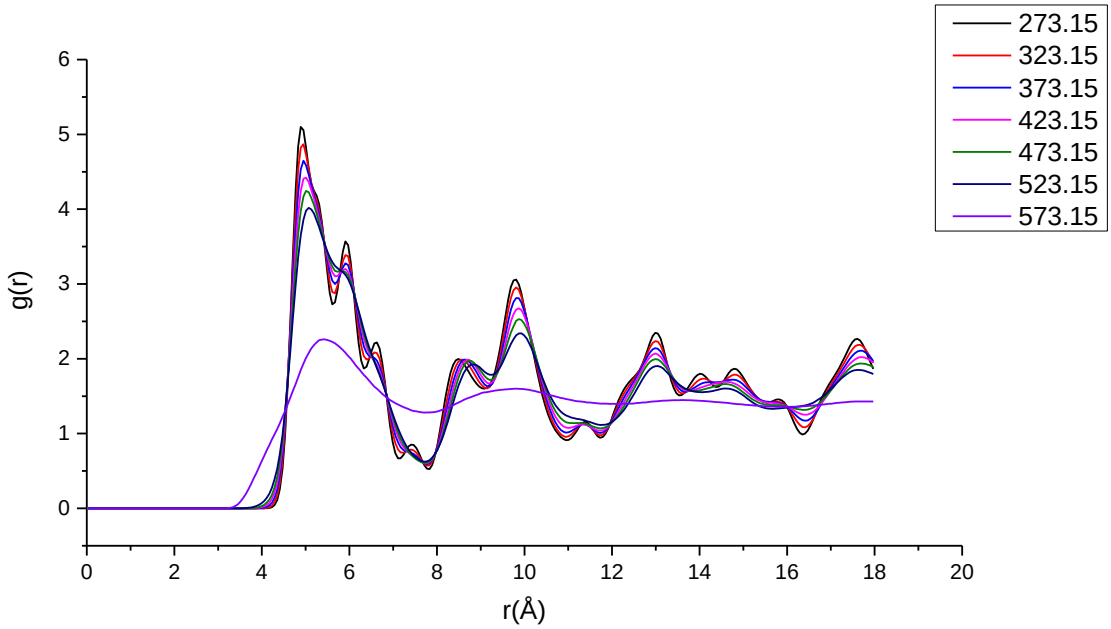

Figure 4.15 - Intermolecular CT-CT RDF when the c parameter is doubled at various temperatures.

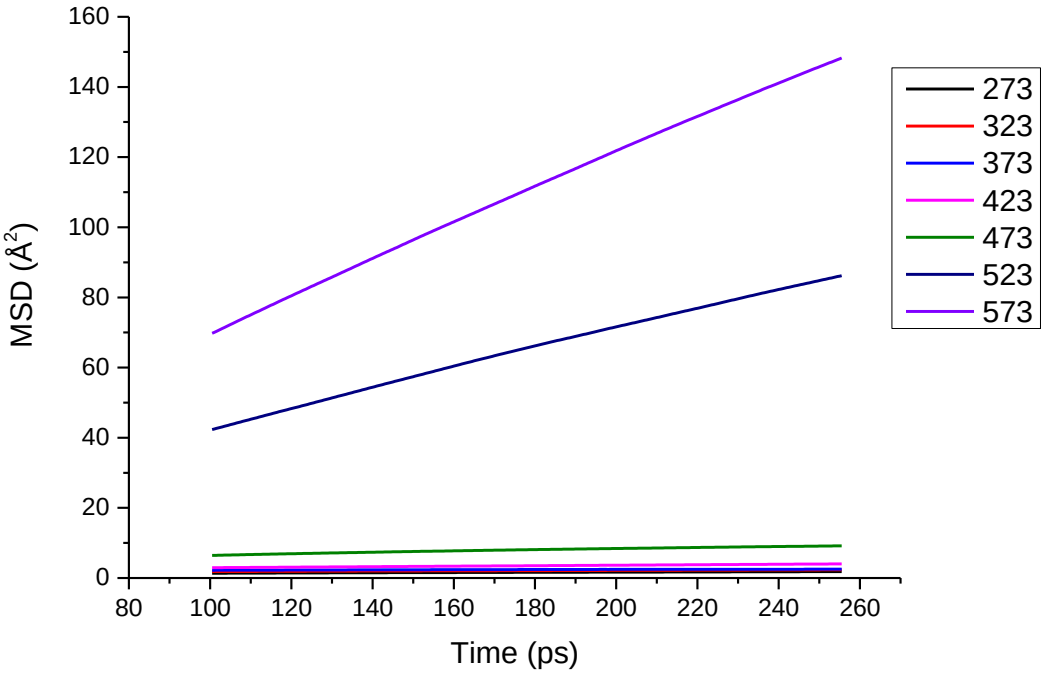

Figure 4.16 - All-atom MSD when the a parameter is doubled at various temperatures.

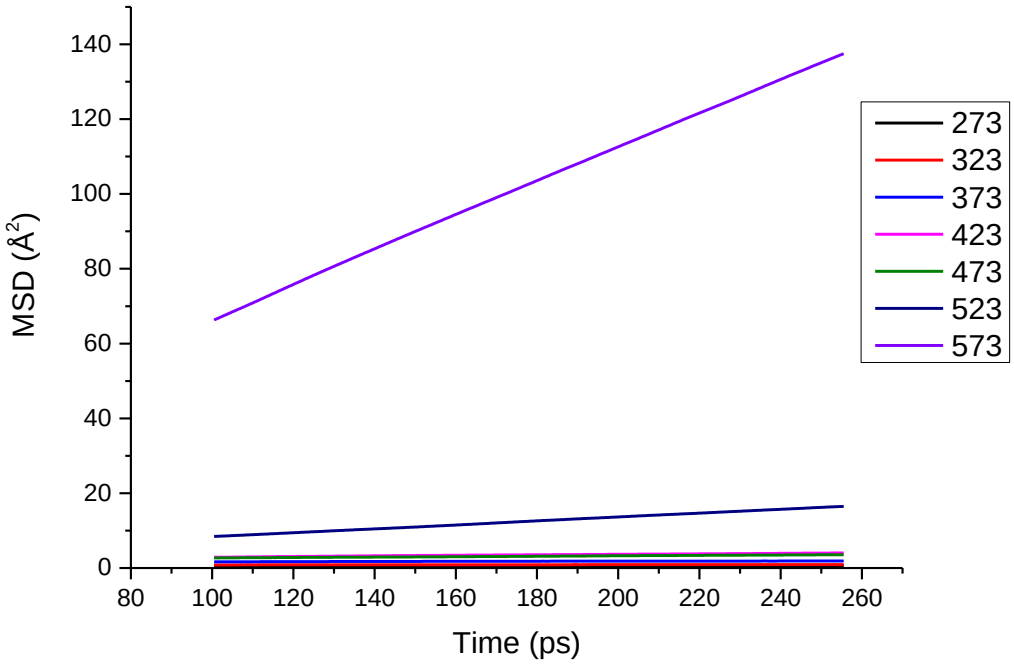

Figure 4.17 - All-atom MSD when the b parameter is doubled at various temperatures.

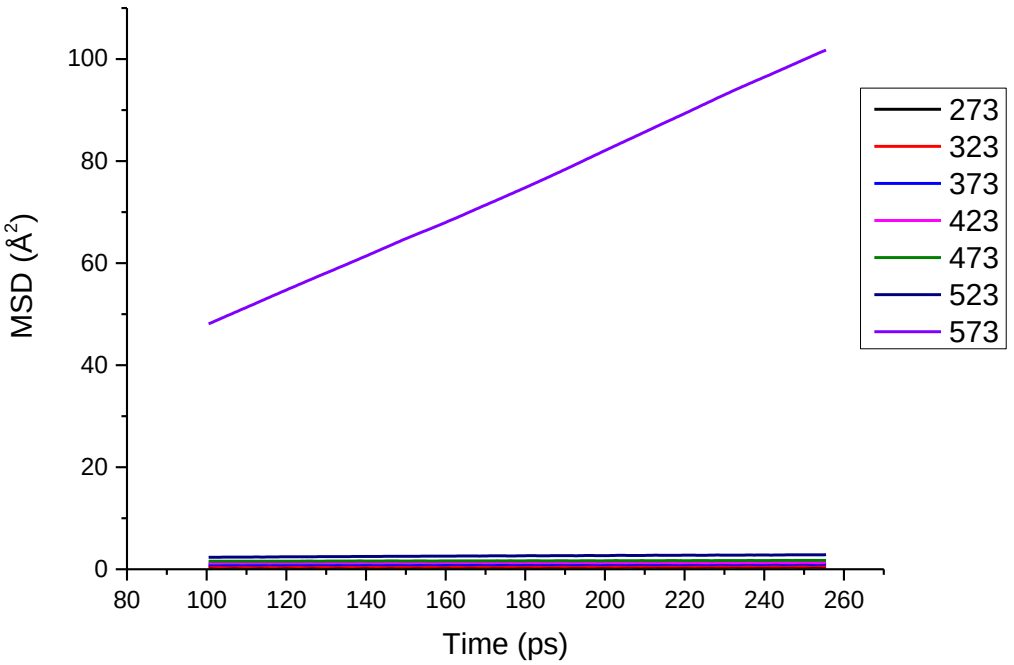

Figure 4.18 - All-atom MSD when the c parameter is doubled at various temperatures.

Table 4.2 shows the diffusion coefficients calculated from the MSDs of the doubled parameters.

	Diffusion Coefficients ($m^2 s^{-1}$) [all values are x 10^{-32}]		
Temperature (K)	**Double a Parameter**	**Double b Parameter**	**Double c Parameter**
273.15	1.76	0.04	0.18
323.15	2.69	0.55	0.38
373.15	2.83	1.26	0.41
423.15	6.45	6.58	0.72
473.15	16.07	5.29	1.01
523.15	263.30	48.71	2.85
573.15	471.35	425.00	323.24

Table 4.2 -Diffusion Coefficients for each doubled parameter over the various temperatures

The first noticeable difference between these RDFs and the ones produced from using the void method is that there is a visible difference between each temperature. When the a parameter is doubled, the peak at 5 Å slowly decreases between 273.15 K and 423.15 K, suggesting the molecules in the crystal are slowly beginning to move over these temperatures. The difference in intensity of the peaks at 5 Å for 423.15 K and 473.15 K is slightly larger than the lower temperatures, suggesting this is when the crystal begins to melt in earnest. The peaks are no longer as intense suggesting that both medium- and long-range order has been lost. When the temperature reaches 523.15 K the system appears to be a liquid as the peaks have reduced significantly to an almost linear plot and the small peak at 6 Å has completely disappeared. This RDF plot is one that would be expected for a liquid. When b was doubled, there appears to be 3 stages of melting. Between 273.15 K and 423.15 K, the peak at 5 Å steadily decreases, just as in the doubling of a, with a small peak at 6 Å still apparent. Again, the size of the peak decreases more as the simulation heats up to 473.15 K, with the aforementioned temperature and 523.15 K being close together with the peak

at 6 Å disappearing. The rest of the RDFs for these two temperatures also provide a more featureless plot, compared to the lower temperatures, suggesting the value of g(r) is constant. At 573.15 K only the first peak at 5 Å is visible, suggesting the crystal has completely melted. The final RDF, for when the C parameter is doubled, gives some interesting results. The RDFs for 273.15 K to 523.15 K do not show any significant signs of melting, just the slight decrease in peak size that has been observed in the other two cases. It is not until the highest temperature, of 573.15 K, that melting occurs, with only two peaks at 5 Å and approximately 9 Å remaining on the RDF. The difference in melting temperatures observed between the three parameters can be attributed to the orthorhombic crystal shape exhibited by 1,4-bis(phenylethynyl)benzene and the cohesive forces that exist between the molecules. The doubling of the parameters also partially exposes molecules on the a and b cell lengths which would have an effect on melting temperature. Also, when the c parameter is doubled, the molecules are positioned in such a way their benzene rings are stacked on top of each other, causing π-π interactions to be the strongest cohesion force present, which in turn makes removal of a molecule from the surface harder. The extra energy required to remove a molecule from the surface results in the system only melting at the highest temperature of 573.15 K. This is in contrast to when the b and a parameters are doubled. In these instances, the surfaces created have molecules where the intermolecular interactions are weaker as the molecules are not stacked, meaning lower temperatures are required for the systems to melt.

The MSDs produced from these results confirm the observations made in the RDFs above. For double a, the two highest temperatures have large MSDs, showing that the system is in a liquid state, with significantly larger diffusion coefficients (of 263.30 x 10^{-32} m^2 s^{-1} and 471.35 x 10^{-32} m^2 s^{-1}, respectively), than at lower temperatures. However, when looking at the bottom of the graph, it is evident that there is a gradient for the line representing 473.15 K (green line), with a diffusion coefficient of 16.07 x 10^{-32} m^2 s^{-1} showing this is where melting begins. When b was doubled, 573.15 K again produced the largest MSD showing the molecules have a high diffusivity (demonstrated by the 425 x 10^{-32} m^2 s^{-1} diffusion coefficient) by this temperature. Once again towards the bottom of the graph, both 523.15 K and 473.15 K do have slight gradients, suggesting melting is under way. The rest of the temperatures produce almost completely linear plots, with the diffusion coefficient supporting this with values from 0.04 x 10^{-32} m^2 s^{-1} to 1.26 x 10^{-32} m^2 s^{-1} suggesting no melting is happening. Finally, when c was doubled it is clear that no temperatures produced any melting except for at 573.15 K. The diffusion coefficient provides evidence of this as the value for 573.15 K (323.24 x 10^{-32} m^2 s^{-1}) is approximately 113 times greater than that for 523.15 K (2.85 x 10^{-32} m^2 s^{-1}). The rest of the temperature plots are pretty much linear, suggesting no long-range diffusion and thus no melting.

With the results from the previous method of removing molecules from the box and this method of creating slabs by doubling the cell parameters, it is reasonable to state that the upper boundary for the melting point ‘envelope’ is 473.15 K. This in itself is not accurate, as a lower limit calculation is needed to give a melting point range.

4.2.3 Slab Technique – Freezing Point

In order to find the lower boundary for the melting point 'envelope' the same slab technique that was used to find the upper melting point was used again. The temperatures tested were 25 K intervals from 500.15 K down to 300.15 K. The results obtained are now discussed with the use of RDFs and MSDs once again.

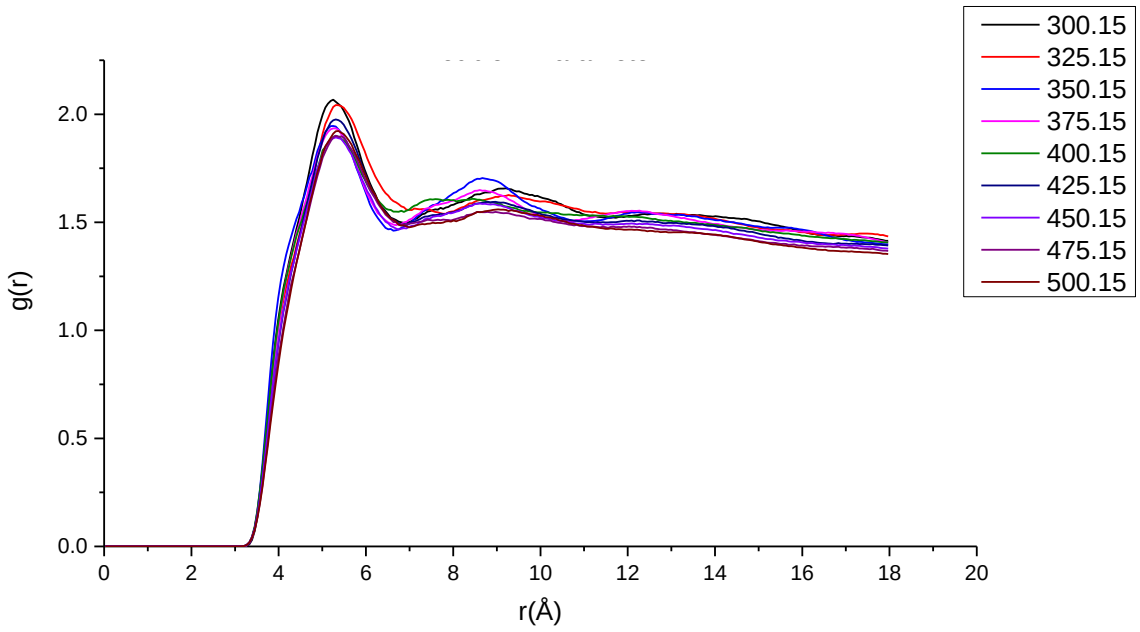

Figure 4.19 - Intermolecular CT-CT RDF when a parameter is doubled, using temperatures ranging from 500.15 K down to 300.15K

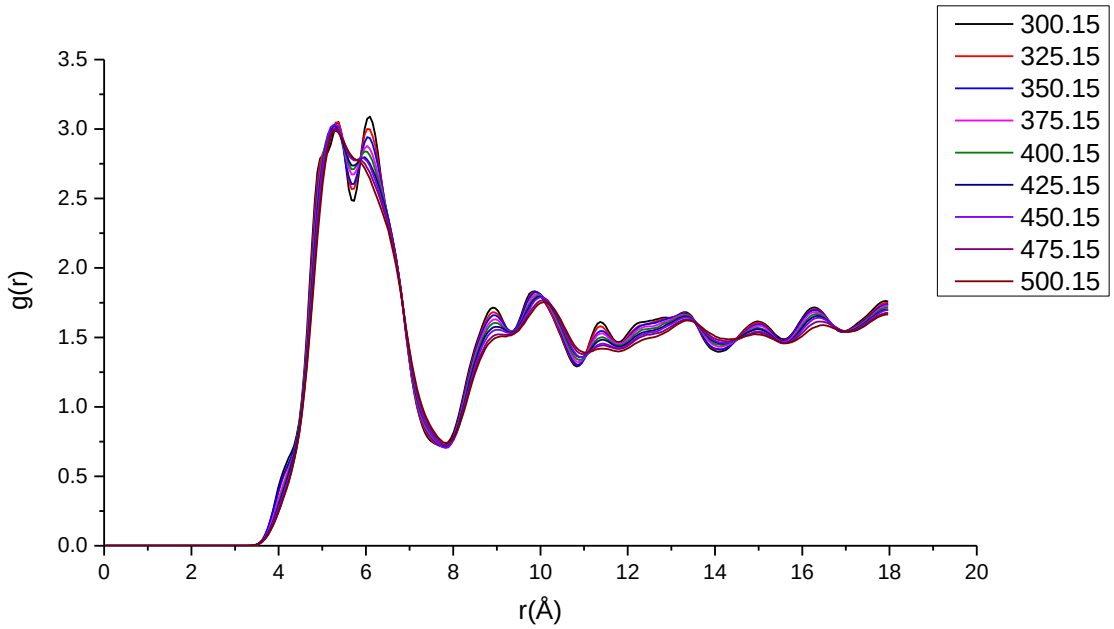

Figure 4.20 - Intermolecular CT-CT RDF when b parameter is doubled, using temperatures ranging from 500.15 K down to 300.15K

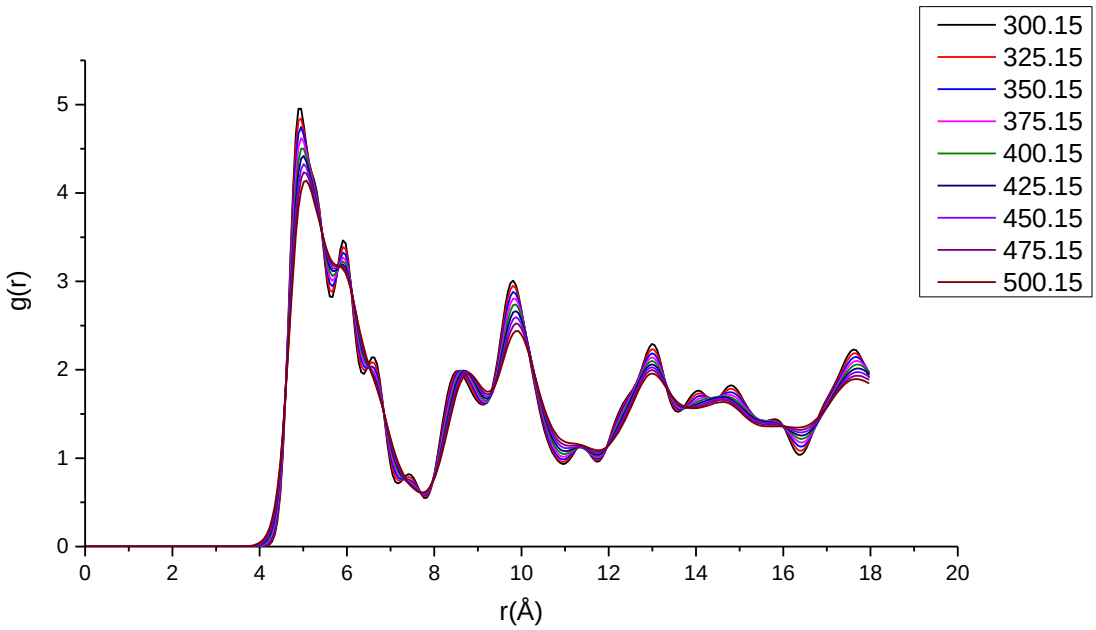

Figure 4.21 - Intermolecular CT-CT RDF when c parameter is doubled, using temperatures ranging from 500.15 K down to 300.15K

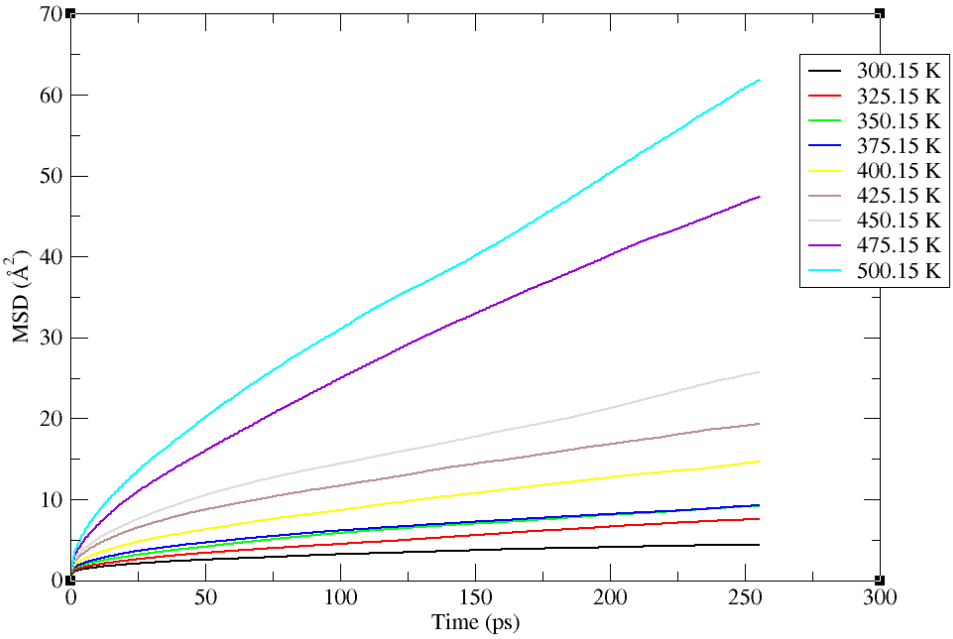

Figure 4.22 - All-atom MSD when a parameter is doubled, using temperatures ranging from 500.15 K down to 300.15K

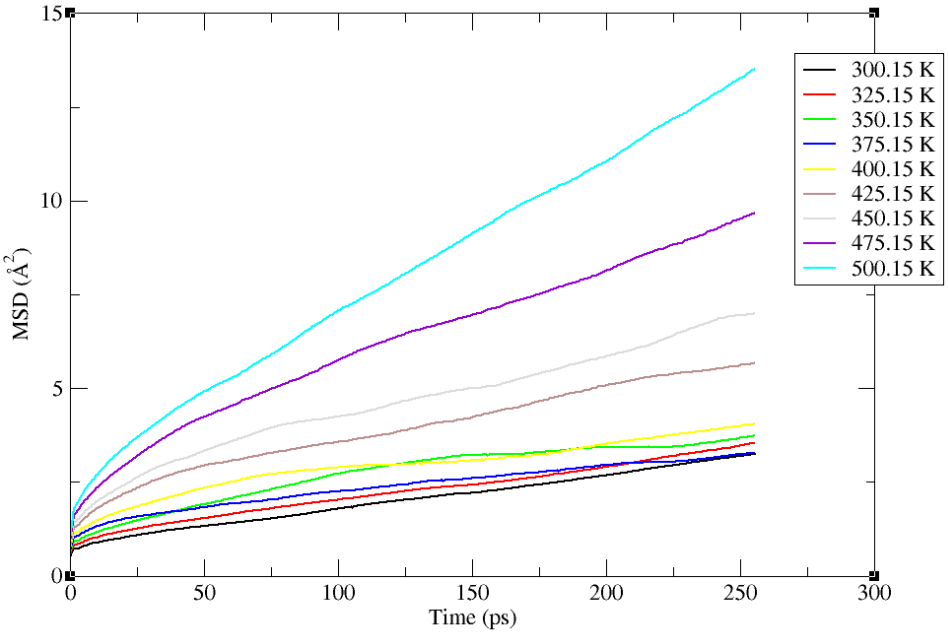

Figure 4.23 - All-atom MSD when b parameter is doubled, using temperatures ranging from 500.15 K down to 300.15K

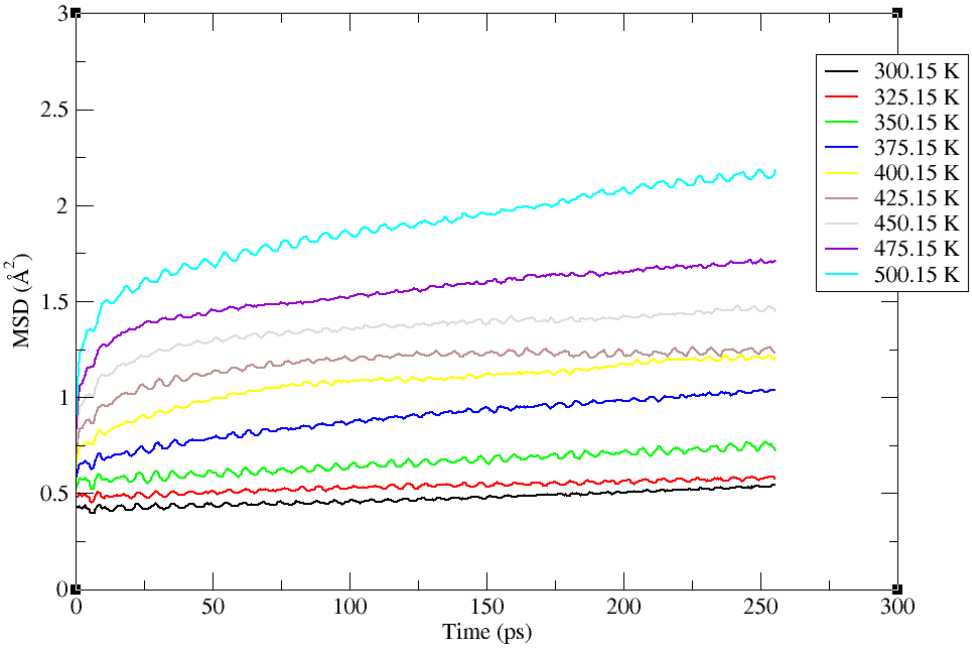

Figure 4.24 - All-atom MSD when c parameter is doubled, using temperatures ranging from 500.15 K down to 300.15K

It is difficult to see any freezing occurring in both the RDFs and MSDs. The RDFs produced for all the scenarios give very little information, with all temperatures showing the same peaks. However it is interesting to note that the intensity of these peaks differs as the temperature changes. As the temperature decreases the intensity of the peaks at 5 Å increases, suggesting there is a greater assembly of molecules as the system approaches freezing point. Another interesting observation is the splitting of the first peak at around 5 Å in the double b parameter, compared to the RDF of the melting calculation for the same system, as well as a further split also observed at the peak at around 10 Å. This increased splitting could possibly be caused by the presence of pairs, where more than two atoms are sharing parts of the second-nearest neighbour shell as well as molecular vibrations.[88,89] This is perhaps due to the short range order displayed in amorphous solids, such as

the ones produced by the freezing of the DEB liquid system. The MSDs provide a more useful technique in finding the lower boundary for the melting point. Firstly, when the a parameter was doubled the two highest temperatures (500.15 K and 475.15 K) do not show any signs of freezing with both plots still showing signs of a positive gradient and thus molecules are diffusing. At 450.15 K, the gradients begin to decrease; suggesting freezing is beginning to start. This pattern of the plots becoming gradually more linear continues as the temperature decreases. The positive gradients for the lines when the b parameter is doubled are not as steep as for the doubling of a however they are still present especially at the higher temperatures. It is again at around 425.15/450.15 K that the lines begin to plateau and thus the molecules are not moving around as much as before, suggesting this is the temperature freezing occurs. Finally, doubling c produced interesting results, just as it did during the melting investigation, with all the plots being linear, suggesting the crystal freezes at all the temperatures tested. The reason for this may be due to the same reason as before, with the orientation of the molecules playing a big role in the melting and freezing of the crystal.

4.3 Conclusion

Overall this investigation was a success, providing a melting point 'envelope' of 400.15 – 473.15 K which is in good agreement with the value of 449.15 K – 455.9 K stated by several experimental sources.[39,84,85] A melting point 'envelope' was calculated as due to the viscous nature of the melted DEB, a range would better encapsulate the start of the crystal melting to a fully liquid system. The value of 455.9 K reported by *Sharma et al*'s differential scanning calorimetry (DSC) experiment[39] is approximately 17 K lower than

the upper boundary of 473.15 K and 55 K greater than the lower boundary of 400.15 K calculated during this study. There are two possible causes for this discrepancy; firstly, the parameters used to calculate the melting point differs between the two techniques. The calculated melting point is dependent on the number of voids in the system and thus its density whereas DSC uses heat capacity. DSC establishes a relationship between temperature and specific physical properties of substances and is the only method for direct determination of the enthalpy associated with the process of interest.[90] This results in a better prediction for melting point compared to the use of density alone. Also, the short simulation time may have had an effect on the cooling rate of the system and so extending the simulation duration, which would decrease the cooling rate, could provide a more reliable estimate of the lower boundary. As crystal nucleation is a rare event, a longer simulation time could be more advantageous as the longer the simulation is running the greater the possibility that crystal nucleation will occur. Out of the methods used, the slab technique, which created a surface, was slightly more accurate although the removal of molecules, or creating a void, did provide a reasonable estimation of the upper boundary. One of the problems experienced with void method was deciding the percentage of molecules to remove as removing too many DEB molecules would result in the crystal melting at a lower temperature than expected, whereas not removing enough molecules resulted in the crystal not melting at all. In order to provide a better estimation of the melting point using the void method, a smaller incrementation of molecules removed should be implemented which would allow the ideal number of voids created to be established.

Using RDFs and MSDs was an effective method for analysing the results and depicting if the crystal had melted or not. The only instance that this method was not as effective as hoped for was the freezing aspect of the investigation, as the system did not freeze back into a crystal and formed an amorphous structure instead. This made it harder to compare the RDFs between the structures and to identify when the freezing phase occurred therefore further analysis techniques could be explored

Chapter 5: Mixtures of Unhydrogenated- and Hydrogenated-DEB

This chapter reports molecular dynamics simulations involving various mixtures of hydrogenated (8H) [1,4-bis(phenylethyl) benzene] and unhydrogenated (0H) DEB [1,4-bis(phenylethynyl) benzene]. Diffusion coefficients will be calculated in order to gain a better understanding of the DEB molecules' mobility once hydrogenation has occurred. A deeper understanding of the mobility of both unhydrogenated and hydrogenated molecules is useful, as it can provide insight into how the hydrogenation process occurs within a getter/catalyst pellet under reaction conditions. These calculations were run at several temperatures ranging from 350 K to 550 K in 25 K intervals in order to investigate the effect of temperature on the molecules during the hydrogenation. The hydrogenation reaction occurs between 323 K and 330 K[26,91] and, as the reaction is exothermic, localised heating can occur which can increase the temperature at the reaction sites.

5.1 Methodology

The initial configurations were constructed using the PACKMOL software,[57] which efficiently packs molecules in defined regions of space ensuring that short range repulsive interactions do not disrupt the simulations.[58] The coordinates of one molecule of each type, the number of molecules of each type and the spatial constraints that each type of molecule must satisfy are required for a successful packing of the system. In this instance the coordinates of one unhydrogenated DEB molecule and one

hydrogenated DEB molecule were input into the PACKMOL program, with the instruction that there must be 240 molecules in total, packed into in a cubic cell with side lengths of 85 Å. This size of 85 Å was chosen through a trial and error approach. If the size of the cell was too small then the molecules would be packed on top of each other resulting in the packing process failing. Conversely if the cell was too large there would be too few interactions between the molecules making subsequent NPT equilibration less efficient. 85 Å allowed the molecules enough room to be packed into the cell whilst avoiding overcrowding. These 240 molecules were split into 0H:8H ratios (i.e 10:90, 20:80, etc.); where 10:90 means 10% of the 240 molecules (24) were unhydrogenated-DEB and 90% (216) were hydrogenated-DEB. Similarly to the previous chapter a notation system will be employed; H (for hydrogenated) and U (for unhydrogenated) will be used along with the percentage of that species in the system. For example, the 10:90 system mentioned above will be discussed using U10 and H90 as the two species. DL_POLY 4, using the cvff force field, was used to run NPT simulations with a 250 ps equilibration time followed by a 1 ns production run. Volume vs time graphs were plotted to ensure that the volume of the cell had stabilised before continuing with the production time. The simulations were run at various temperatures from 350 K to 550 K in 25 K intervals.

MSDs were used as analysis tools To investigate the mobility of the DEB molecules further, diffusion coefficients were calculated using the equation (1):

$$MSD = q_i Dt \qquad \textbf{Eq.5.1}$$

where MSD is the gradient of the slope of the MSD, q_i is a numerical constant that depends on the dimensionality of the system (which is 6 for 3-dimensional diffusion), D is the diffusion coefficient (in $m^2 s^{-1}$) and t is the time (in seconds).

The diffusion coefficient was calculated over four time ranges of a single production run to gain a better understanding of the mobility of the species throughout the simulation. The first time range (0.5 – 999.5 ps) covered the whole simulation, the second (0.5 – 500.5 ps) covered the start and the third & fourth ranges (200.5 – 500.5 ps and 250.5 – 750.5 ps) covered two mid-ranges of the simulation. The time ranges studied are listed below, along with an example of both the MSDs produced from the run and a fit to the MSD with the four gradients (**Figures 5.1a and 5.1b**):

- 0.5 – 999.5 ps
- 0.5 – 500.5 ps
- 200.5 – 500.5 ps
- 250.5 – 750.5 ps

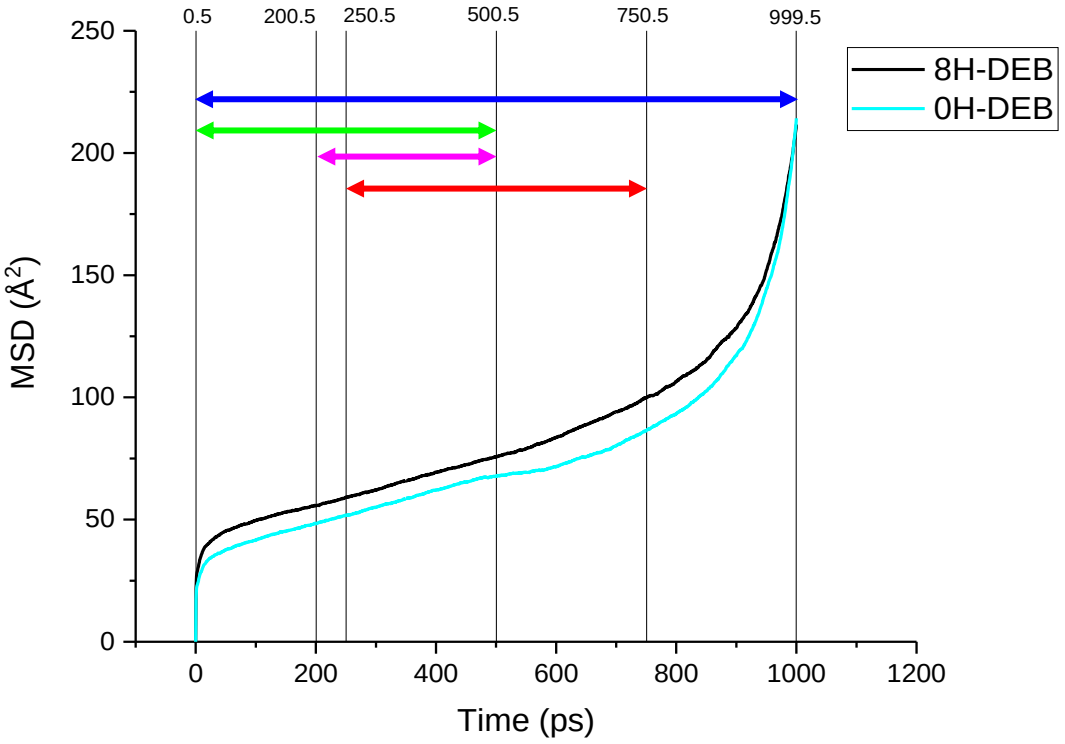

Figure 5.1a – Total MSDs for 50:50 ratio of 0H:8H for 0-1000ps at 475 K, also illustrating the four time ranges..

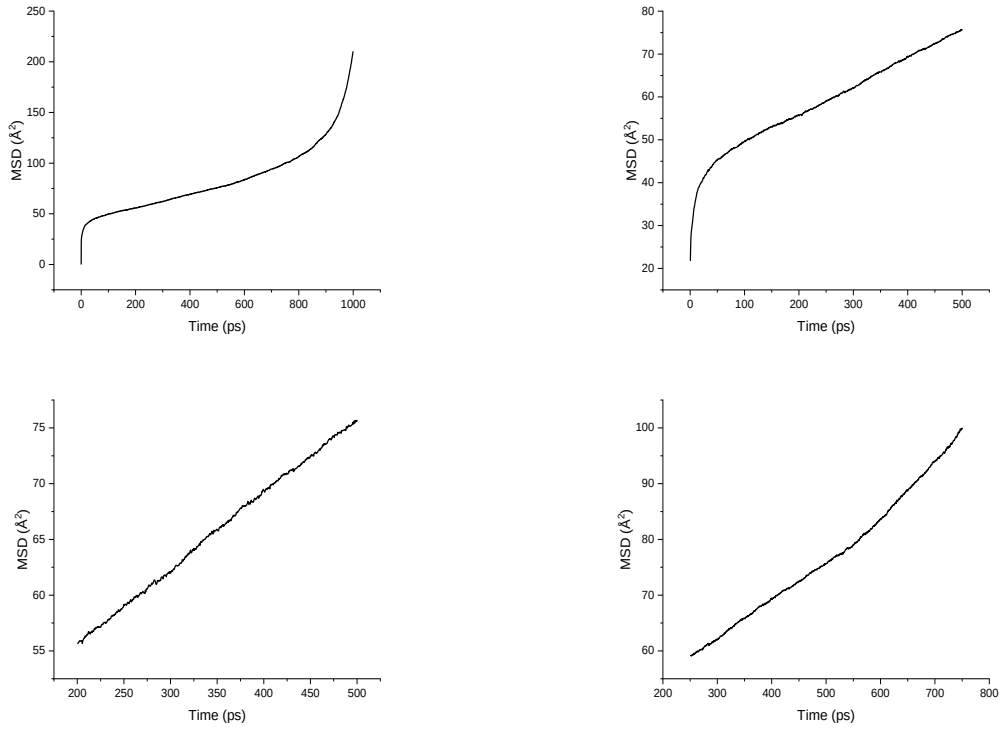

Figure 5.1b – The four time ranges MSDs (shown above in Figure 5.1a) for 50:50 ratio of 0H:8H [top left: 0.5 – 999.5 ps; top right 0.5 – 500.5 ps; bottom left: 200.5 – 500.5 ps; bottom right 250.5 – 750.5 ps] at 475 K.

5.2 Results and Discussion

As with the previous chapter, MSDs were produced from the trajectory files of the calculation and they will be discussed now before moving on to the diffusion coefficients. Due to the large volume of data and to prevent the graphs from becoming too complex, only certain 0H:8H ratios and temperatures will be shown.

The first two graphs (**Figures 5.2** and **5.3**) show the effects of different ratios of 0H:8H and temperature on the individual atom types (c2 for the hydrogenated species and ct for the unhydrogenated species). Looking at

Figure 5.2, the first noticeable point from the three ratios shown is that as the percentage of c2 increases (*i.e.* an increase of hydrogenated-DEB), the MSD also increases which suggests that the average mobility increases as the proportion of hydrogenated molecules increases. This can be seen in the 14 $Å^2$ increase from 70H to 90H at 550 K at *t*= 880 ps. The reason for this is owing to the 8H-DEB molecule being more flexible in comparison to the 0H-DEB molecule due to the removal of the triple bond through the process of hydrogenation. A larger percentage of more conformationally flexible molecules in the system would increase mobility. Also noticeable from **Figure 5.2** is the effect of temperature on the system. 80H at 550 K (the solid pink line) has a greater MSD of around 7 $Å^2$ than 90H at 525K (the dotted blue line) despite having 10% less hydrogenated-DEB.

Figure 5.3, which shows a comparison of the ct atom type, depicts the opposite to its c2 counterpart and shows that as the percentage of 0H-DEB increases, the mobility of the molecule decreases. This can be seen by 10U at 550 K having a greater MSD than 20U at 550 K which in turn has a greater MSD than 30U at 550 K. This suggest that as the concentration of 8H-DEB increases, the diffusivity of both 0H-DEB and 8H-DEB increases. The greater the proportion of unhydrogenated-DEB, the harder it is for the molecules to move. Temperature is once again important as 30U at 550 K has a greater MSD than 10U at 500 K and 20U at both 500 and 525 K. The kink observed at approximately 500 ps for 550 K of the 10:90 ratio is due to the fewer number of molecules at this ratio and hence statistical uncertainty.

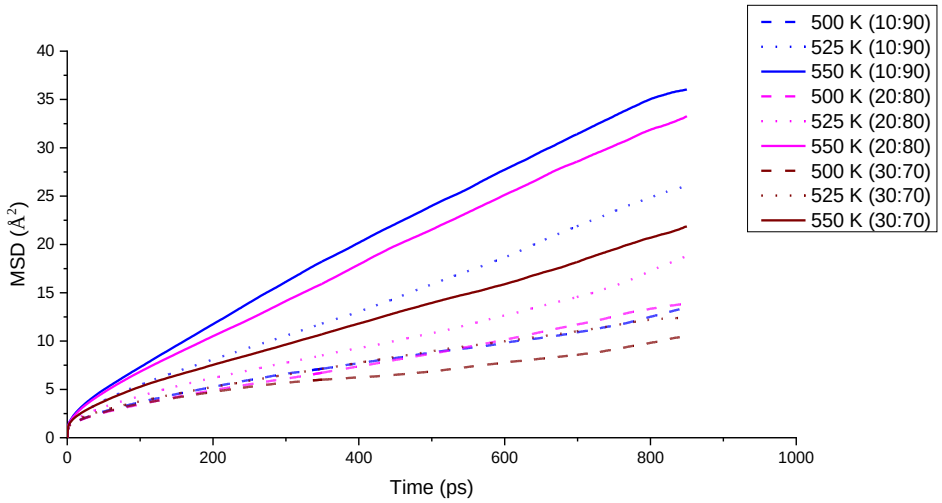

Figure 5.2 - MSDs for the c2 atom type (8H-DEB) at the ratios of 0H:8H - 10:90, 20:80 and 30:70.

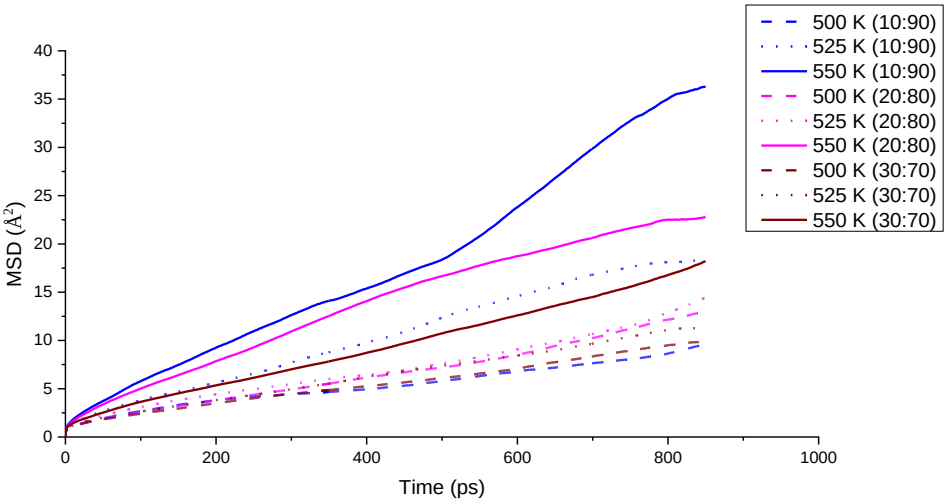

Figure 5.3 - MSDs for the ct atom type (8H-DEB) at the ratios of 0H:8H - 10:90, 20:80 and 30:70.

Figures 5.4 and **5.5** show a comparison of the two atom types (c2 and ct) at the two extremes of composition (i.e. 10:90 and 90:10).

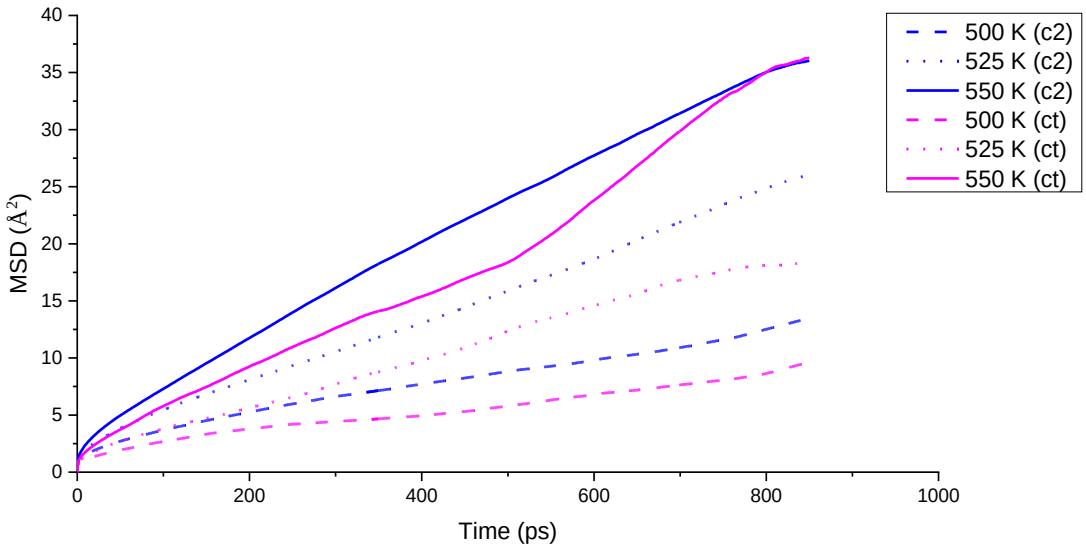

Figure 5.4 - Comparison of the two atom types (c2 - hydrogenated, ct - unhydrogenated) in the 0H:8H ratio of 10:90.

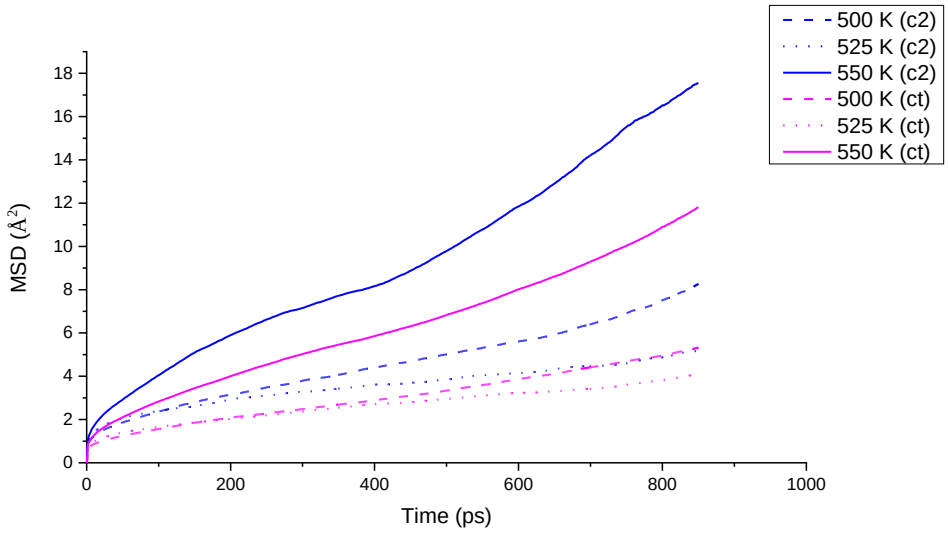

Figure 5.5 - Comparison of the two atom types (c2 - hydrogenated, ct - unhydrogenated) in the 0H:8H ratio of 90:10.

The first noticeable thing is that the MSDs represented by blue lines (for the c2 atom type) are greater than those for the ct atom types (pink lines) in both systems. That implies the hydrogenated-DEB is more mobile than the unhydrogenated-DEB whether there is a large concentration of it (as in U10:H90) or a small concentration (as in U90:H10). This is again due to its

conformational flexibility enabling it to diffuse more easily, even at lower concentrations. Figure 5.6 illustrates the optimised molecular configuration for [1,4-bis(phenylethyl) benzene as establishedby Sharma *et al*.[39], illustrating the presence of the two aliphatic C_2H_4 groups with the molecule,

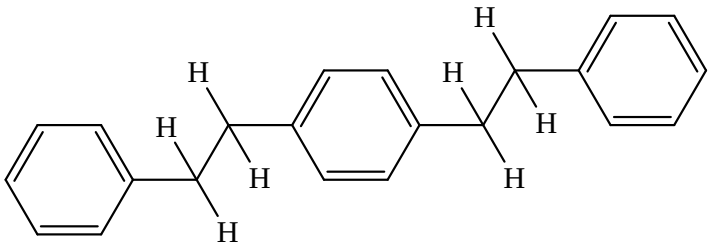

Figure 5.6 – Optimised molecular configuration for [1,4-bis(phenylethyl) benzene] showing its conformational flexibility compared to [1,4-bis(phenylethynyl) benzene]

Also visible from the two figures is that both atom types have a greater mobility in the 10:90 system compared to the 90:10 system. An example of this is in the comparison of both systems at 525 K: c2 has an MSD of 26.1 $Å^2$ and ct has an MSD of 18.4 $Å^2$ in 10:90 system but these numbers drop dramatically to 5.3 $Å^2$ and 4.1 $Å^2$, for c2 and ct respectively, in the 90:10 system. This is further evidence that with more of the flexible molecules present, both the hydrogenated- and unhydrogenated-DEB molecules have greater mobility. This is further shown in **Figures 5.6** and **5.7** which take a further look at the individual atom types in systems with opposite ratios (*i.e.* when the ratio is 30:70 and 70:30).

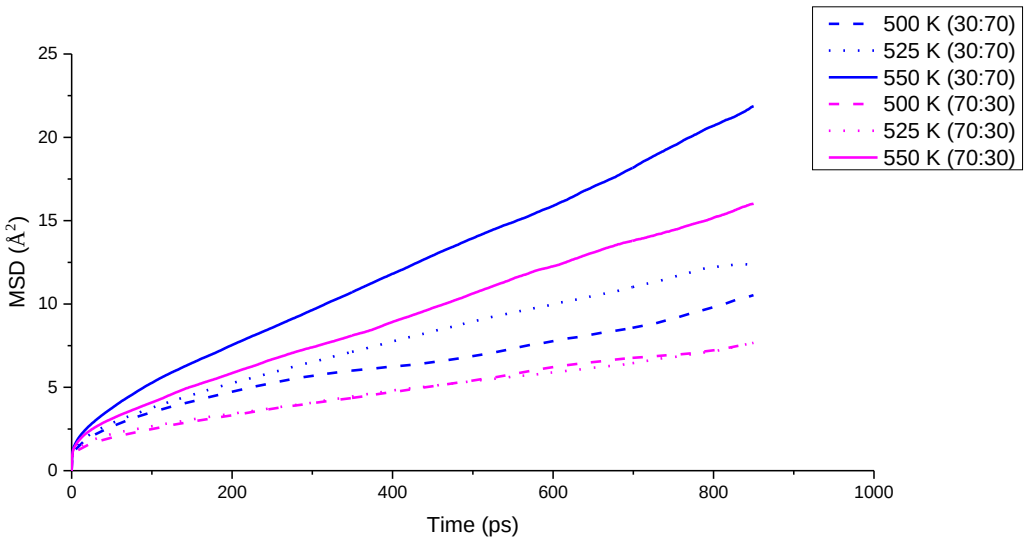

Figure 5.7 - Comparison for the c2 atom type when there is 70% (30:70) and 30% (70:30) of it in the system.

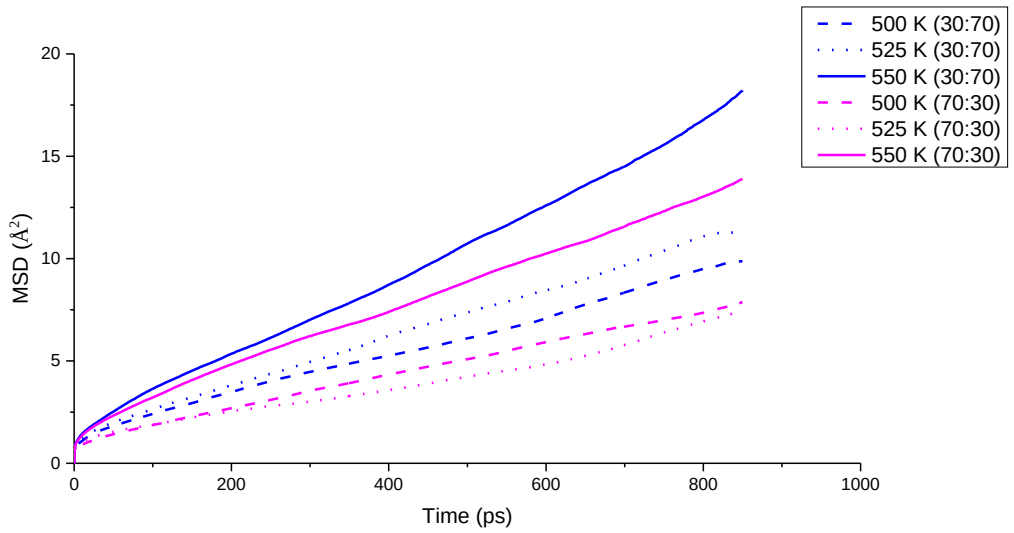

Figure 5.8 - Comparison for the ct atom type when there is 30% (30:70) and 70% (70:30) of it in the system.

From **Figures 5.7** and **5.8** it is evident that the high temperature of 550 K causes both atom types to show the greatest mobility in both systems. Furthermore, when 500 and 525 K are considered, the pattern of both

molecules having greater mobility when there is a greater concentration of hydrogenated-DEB is seen (the two dotted blue lines in both graphs).

For clarity, only the RDFs for the 10:90 ratio will now be looked at (**Figures 5.9**, **5.10** and **5.11**), with the RDFs for the other ratios being found in Appendix B.

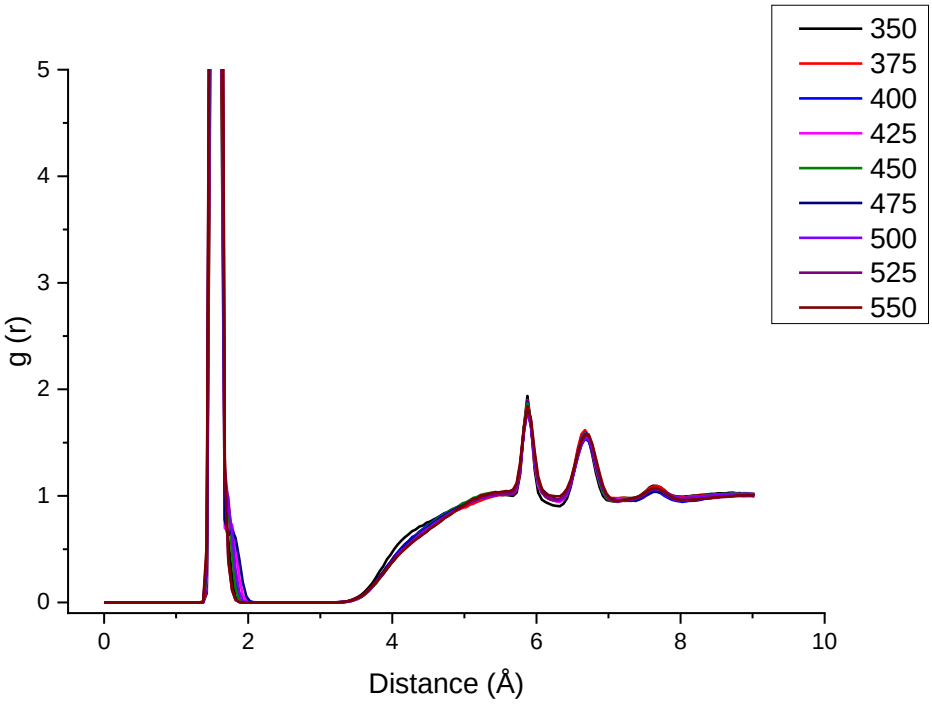

Figure 5.9 – RDFs for c2-c2 interactions in the 10:90 (0H:8H) ratio for all temperatures, in K

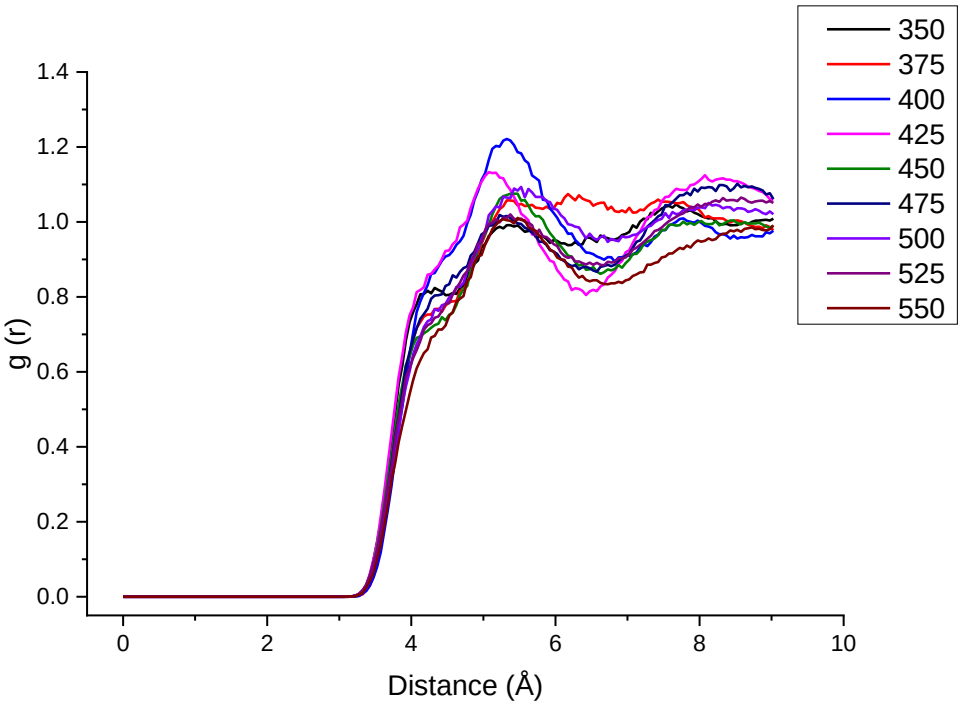

Figure 5.10 - RDFs for ct-c2 interactions in the 10:90 (0H:8H) ratio for all temperatures, in K

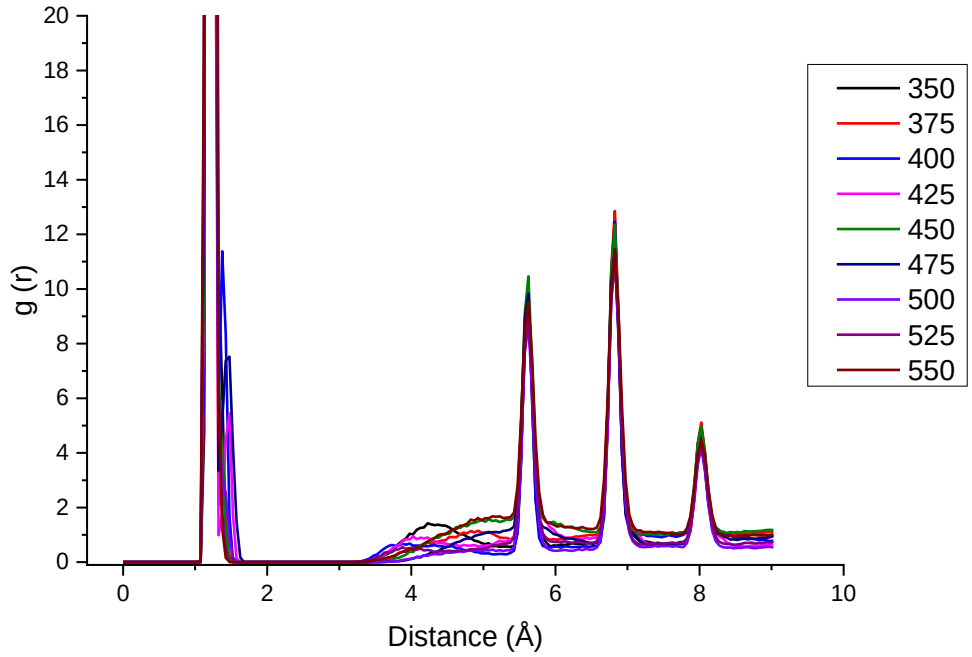

Figure 5.11 - RDFs for ct-ct interactions in the 10:90 (0H:8H) ratio for all temperatures, in K

The largest peaks in **Figures 5.9** and **5.11** are due to the intramolecular C-C and C≡C distances, respectively. The RDFs seen in these two figures have been magnified in order to see the lower intensity peaks. In both instances their closest neighbours are well defined at approximately 6 Å and 7 Å for c2 and 5.5 Å, 7 Å and 8 Å for ct at all temperatures. As there is a lower proportion of the unhydrogenated DEB in the U10:H90 system, the intramolecular C≡C distances are sharper in the RDF. The intramolecular c2-c2 peaks in figure 5.9 are also broader due to the greater flexibility of the molecule, though they do not show any significant broadening with temperature, within the range studied. The most interesting RDF is **Figure 5.10**, which shows the intensity of the peak at 5.5 Å decreasing as the temperature increases, suggesting the 0H and 8H molecules diffuse away from each other more frequently.

5.2.1 Diffusion Coefficients

This next part of the results and discussion section will look at the diffusion coefficients calculated from the MSDs discussed above. As previously mentioned, the diffusion coefficient was calculated over four time ranges of the MSD. The reason for this was to see if the diffusion changed during the simulation. **Figures 5.12**, **5.13, 5.14** and **5.15** show the diffusion coefficients vs temperature for the two atom types in the 10:90 and 90:10 systems.

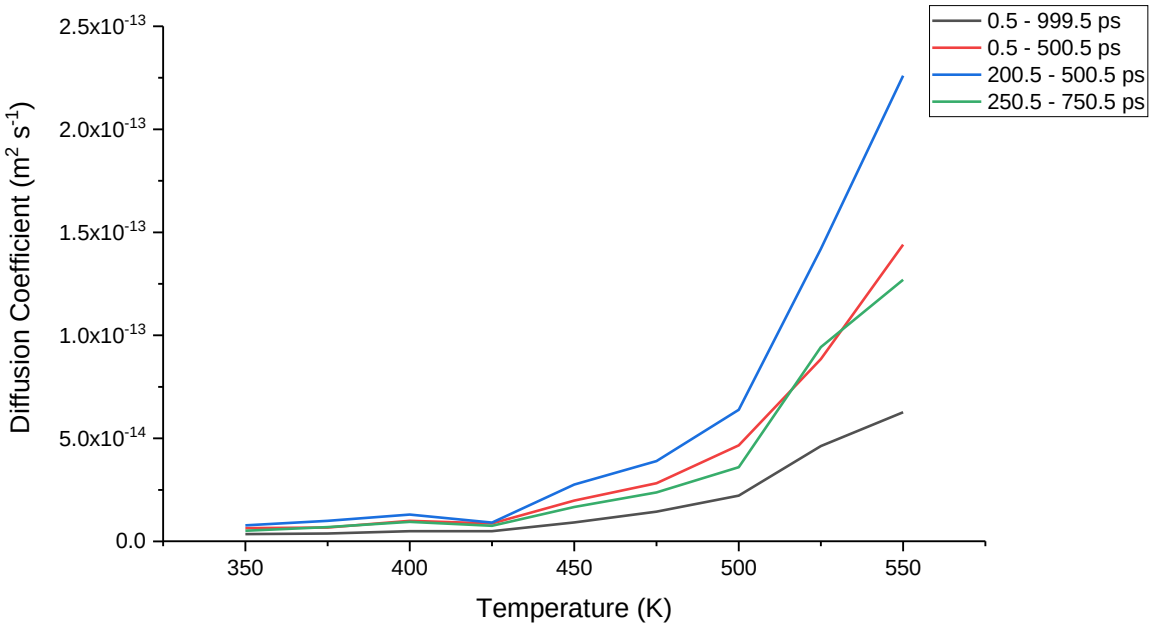

Figure 5.12 - Diffusion Coefficient vs Temperature for the c2 atom type at various time ranges of the MSD: 0.5 - 999.5 ps, 0.5 - 500.5 ps, 200.5 - 500.5 ps and 250.5 - 750.5 ps for 10:90.

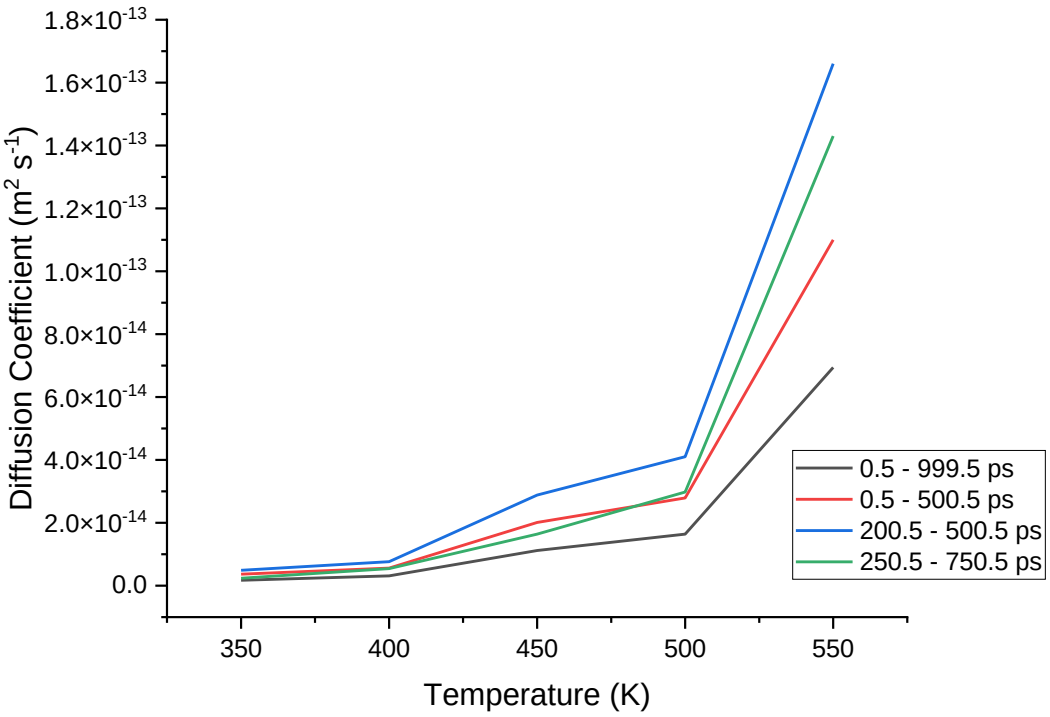

Figure 5.13 - Diffusion Coefficient vs Temperature for the ct atom type at various time ranges of the MSD: 0.5 - 999.5 ps, 0.5 - 500.5 ps, 200.5 - 500.5 ps and 250.5 - 750.5 ps for 10:90.

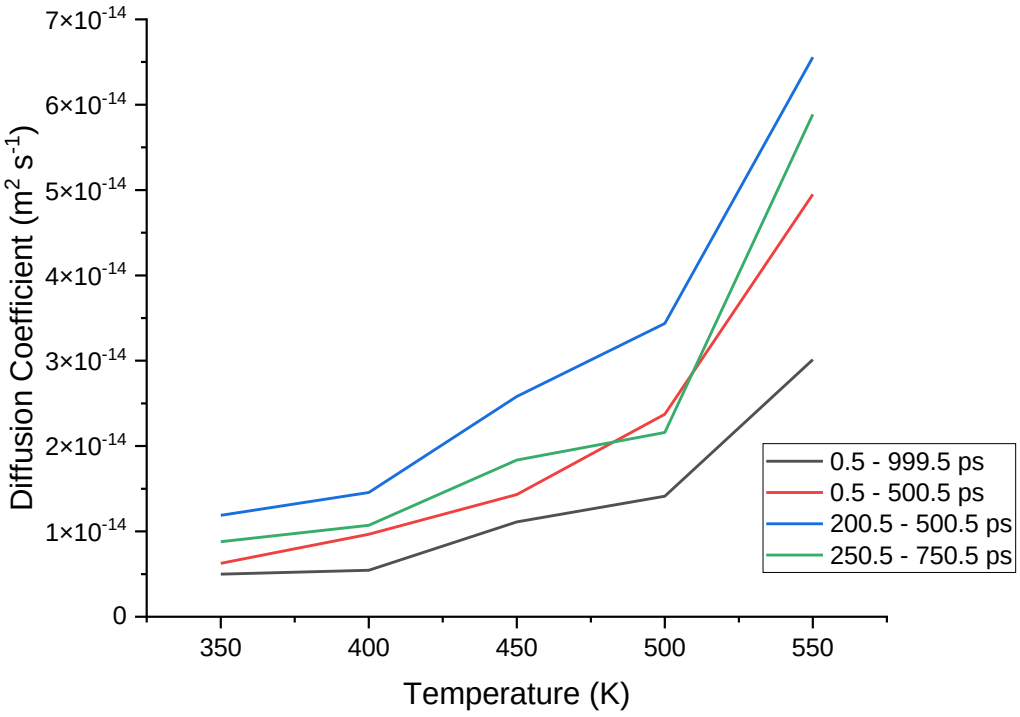

Figure 5.14 - Diffusion Coefficient vs Temperature for the c2 atom type at various time ranges of the MSD: 0.5 - 999.5 ps, 0.5 - 500.5 ps, 200.5 - 500.5 ps and 250.5 - 750.5 ps for 90:10.

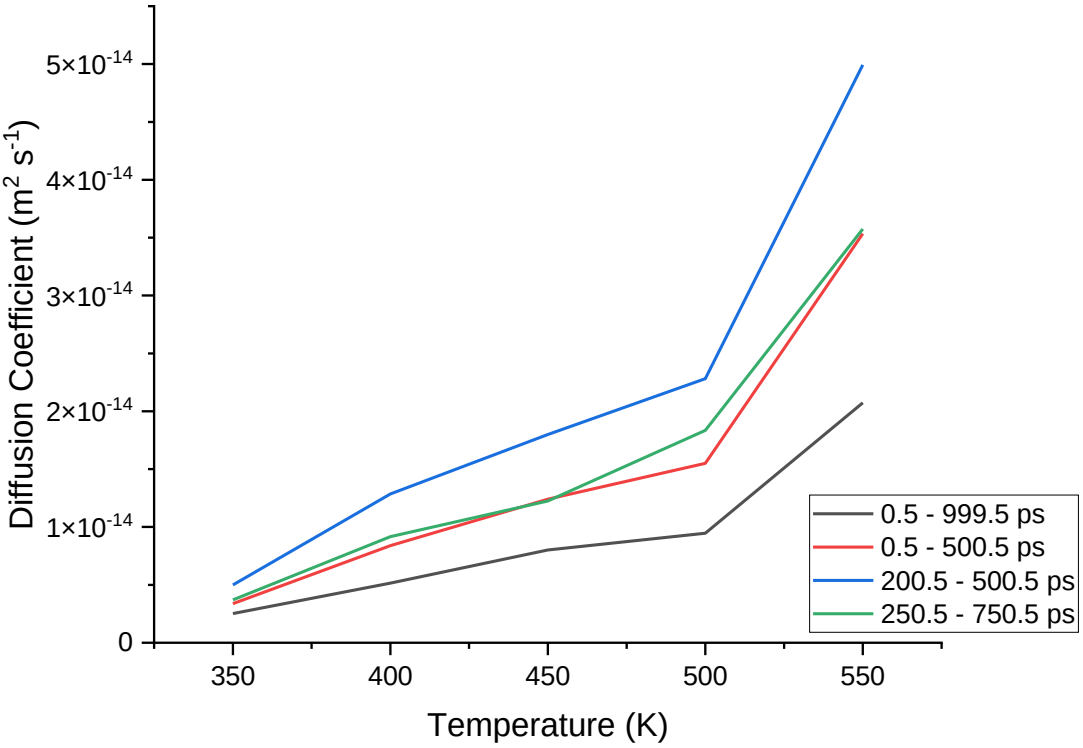

Figure 5.15 - Diffusion Coefficient vs Temperature for the ct atom type at various time ranges of the MSD: 0.5 - 999.5 ps, 0.5 - 500.5 ps, 200.5 - 500.5 ps and 250.5 - 750.5 ps for 90:10.

The 250.5 – 750.5 ps range (green line) was the range chosen to study in more detail as it gave coefficients in between the two extremes (blue and black lines) in both sets of ratios. **Table 5.1** shows chosen diffusion coefficients from the 250.5 – 750.5 ps for all the different ratios of 0H:8H. As already established in this chapter the ct atom types (unhydrogenated-DEB) always have less mobility than their c2 counterparts and thus the data for the ct atom type has been omitted. Also, for the purpose of clarity and illustration, only 5 of the 9 temperatures tested are shown in the table. All the diffusion coefficients for all temperatures, all ratios and both atom types can be found in Appendix B. The table illustrates that the c2 diffusivity increases as the

concentration of 8H-DEB and the temperature increases. When considering the temperature, the impact it has on diffusivity can be clearly seen in the dramatic increase from 350 K to 450 K and then to 550 K for all the ratios. When looking at the different ratios it is clear, once again, that the more c2 atom types (8H-DEB) the higher the diffusivity. This can be seen by 10:90 at 550 K (so 90H) being at least twice as large as the diffusivity at the same temperature but in the 90:10 system (10H).

Diffusivity increases as temperature increases

Diffusion Coefficients (m^2s^{-1}) [all values are x 10^{-15}]									
Temperature (K)	U10:H90	U20:H80	U30:H70	U40:H60	U50:H50	U60:H40	U70:H30	U80:H20	U90:H10
350	5.18	4.25	4.56	4.63	7.45	2.41	6.50	3.59	8.7
400	9.51	9.65	11.3	8.17	9.67	18.7	5.73	7.00	10.7
450	16.7	19.6	18.1	21.3	12.4	20.5	14.2	13.5	18.4
500	36	46.6	24.7	24.3	18.4	31.1	22.9	17.3	21.6
550	127	120	71	69.7	60.2	58.2	53.7	44.1	58.9

Diffusivity increases as concentration of c2 increases (8H-DEB)

Table 5.1 - Table showing the diffusion coefficients for each of the 0H:8H percentages for the 250.5 – 750.5 ps time range of the MSD

5.3 Conclusion

Overall, the investigation provided an insight into the mobility of both the hydrogenated and hydrogenated species of DEB at various temperatures and ratios with a mixture. The primary objective was to investigate the mobility and diffusivity of the two types of molecule (unhydrogenated- and hydrogenated-DEB) and this has been accomplished. It is clear from the MSDs and the diffusion coefficients calculated from them that the c2 atom type (*i.e.* 8H-DEB) has greater mobility than its 0H-DEB counterpart due to its conformational flexibility. The concentration of each molecule in the system also plays an important role, as the systems with larger concentrations of 8H-DEB provided greater mobility and diffusivity for both types of molecules. This may give an insight in to the hydrogenation of the molecules in the DEB pellet. Perhaps the fully hydrogenated-DEB (8H-DEB) diffuses away (due to its greater diffusivity) and allows the unhydrogenated-DEB (0H-DEB) to move in and pick up the atomic hydrogen.

Other stages of hydrogenation (such as 4H or 2H/6H) could be investigated in the future to gain a deeper understanding of what happens to the mobility of the DEB molecules through various stages of hydrogenation and temperature but the various isomers of these different concentrations of hydrogenations could cause problems.

Chapter 6: Diphenylacetylene

This chapter will look at diphenylacetylene (DPA) which is a molecule with similarity to 1,4-bis(phenylethynyl)benzene (DEB). It has the two benzene rings connected by single-triple-single carbon bonds. This similarity makes it a good molecule to run the same melting point 'envelope' and mixing calculations that were used for DEB in the previous two chapters in order to obtain some comparisons and further validate the DEB simulations. The experimental value of the melting point for DPA that was used for comparisons was the 332 K reported by Tkachenko *et al*.[92]

Diphenylacetylene has a monoclinic crystal structure with unit cell parameters of; **a** = 15.28 Å **b** = 5.72 Å and **c** =12.75 Å and angles; **α**=**γ**=90° and **β**=113.76°.[93,94] An image of the unit cell can be seen in **Figure 6.1**.

DPA is widely used as a building block in organic synthesis and as a ligand in organometallic chemistry. Two methods used to produce DPA will now be described: firstly, benzil is condensed with hydrazine hydrate to form benzil dihydrazone which is then oxidised with mercury(II) oxide to form diphenylacetylene (**Figure 6.2**).[95] The second method involves the bromination of trans-stilbene to form stilbene dibromide which is then subjected to dehydrohalogenation to form the diphenylacetylene (**Figure 6.3**).[96]

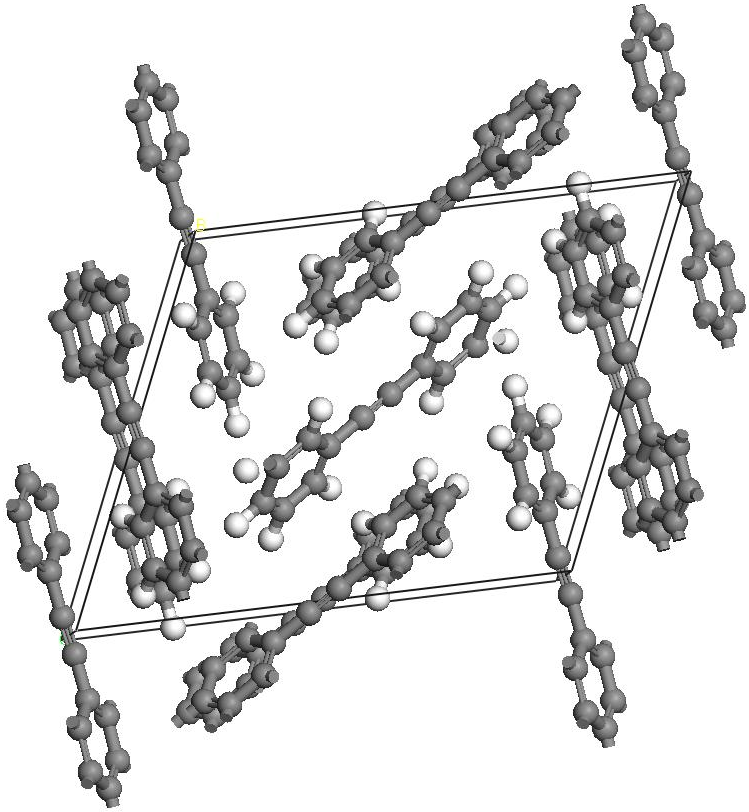

Figure 6.1 – Unit cell of diphenylacetylene

.

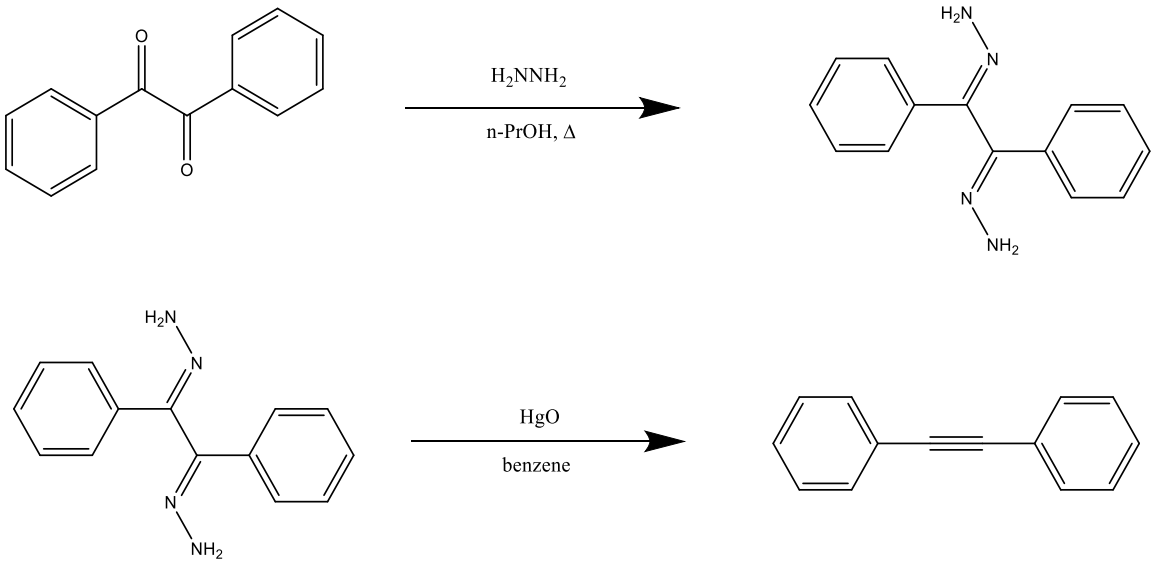

Figure 6.2 - Synthesis of diphenylacetylene from benzil

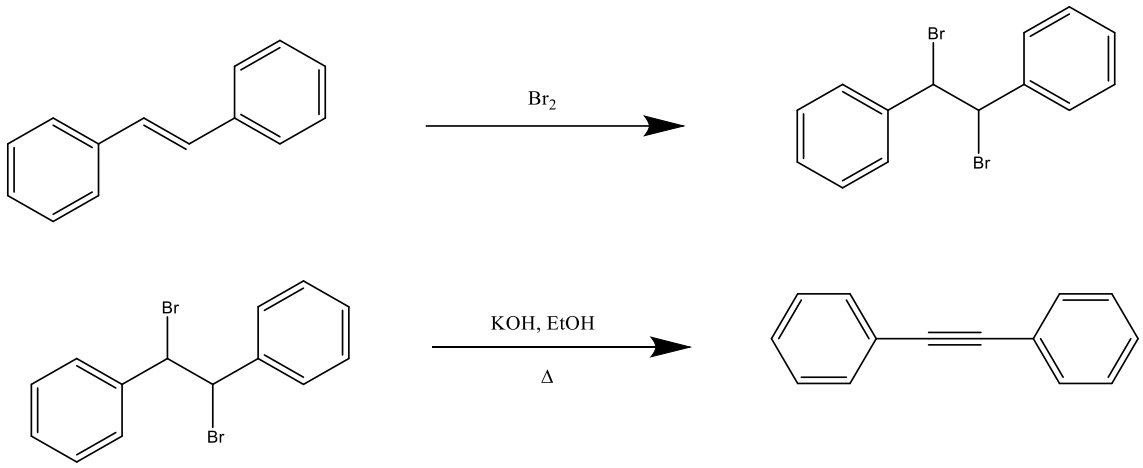

Figure 6.3 - Synthesis of diphenylacetylene from trans-stilbene

6.1 Methodology

The same force field, cvff, that was used for the DEB calculations was used on diphenylacetylene and the atom types used for the unhydrogenated- and hydrogenated-DPA can be seen in **Figures 6.4** and **6.5** respectively.

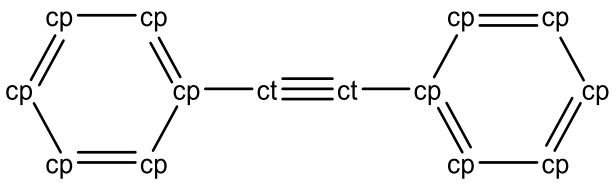

Figure 6.4 - Unhydrogenated-diphenylacetylene molecule with the atom types for the cvff forcefield

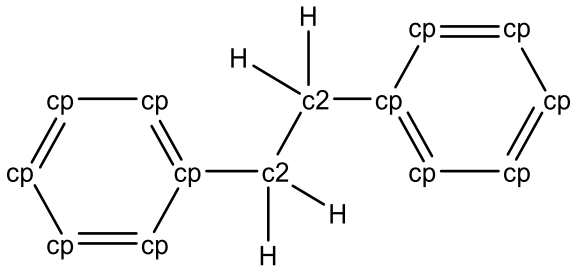

Figure 6.5 - Hydrogenated-diphenylacetylene molecule with the atom types for the cvff forcefield

For the melting point envelope simulations, a method involving the removal of molecules, similarly to Chapter 4, was utilised. This method was chosen over the slab technique discussed in Chapter 4 as we have shown it yields reliable results and is less computationally expensive. The melting point temperature range can be calculated from the same system of molecules whereas the slab technique involves creating two separate simulations – the melting point (for the upper boundary) and the freezing point (for the lower boundary). For reasons of computational efficiency, the removal of molecules technique was the most appropriate as it provides accurate results in a shorter period of time. The crystal structure of diphenylacetylene[93,97] was used to create a 4x4x4 supercell with cell parameters of **a** = 45.84 Å **b** = 17.15 Å and **c** =38.26 Å with 625 molecules in total. From this structure 10% (63 molecules), 20% (126 molecules) and 30% (189 molecules) were removed and NPT calculations run with a 250 ps equilibration run, followed by a 825 ps production run. The calculations were carried out at 325 K, 350 K, 400 K, 450 K and 500 K. For analysis, MSDs and RDFs were produced.

For the mixing of the unhydrogenated (0H)- and hydrogenated (4H)-DPA section, a total of 360 molecules were split into the same ratios used in Chapter 5, *i.e.* 4H:0H – 10:90, 20:80, 30:70, 40:60, 50:50, 60:40, 70:30, 80:20

and 90:10. PACKMOL was used to create a starting configuration for the molecules. NPT calculations were run with a 75 ps equilibration run followed by a 1 ns production run, at 300 K, 350 K, 400 K, 450 K and 500 K. MSDs and RDFs were generated from the trajectories and diffusion coefficients calculated using equation 5.1. U-DPA will refer to unhydrogenated-DPA and H-DPA will refer to hydrogenated-DPA.

6.2. Results and Discussion

6.2.1 Melting Point 'Envelope'

For the MSDs, the y-axis was magnified as some of the higher temperature runs (especially with 20% and 30% removal of molecules) created large MSDs which tend to dwarf those of the lower temperatures. The first graphs to be considered will be the MSDs and RDFs for 10% removal (**Figures 6.6** and **6.7**).

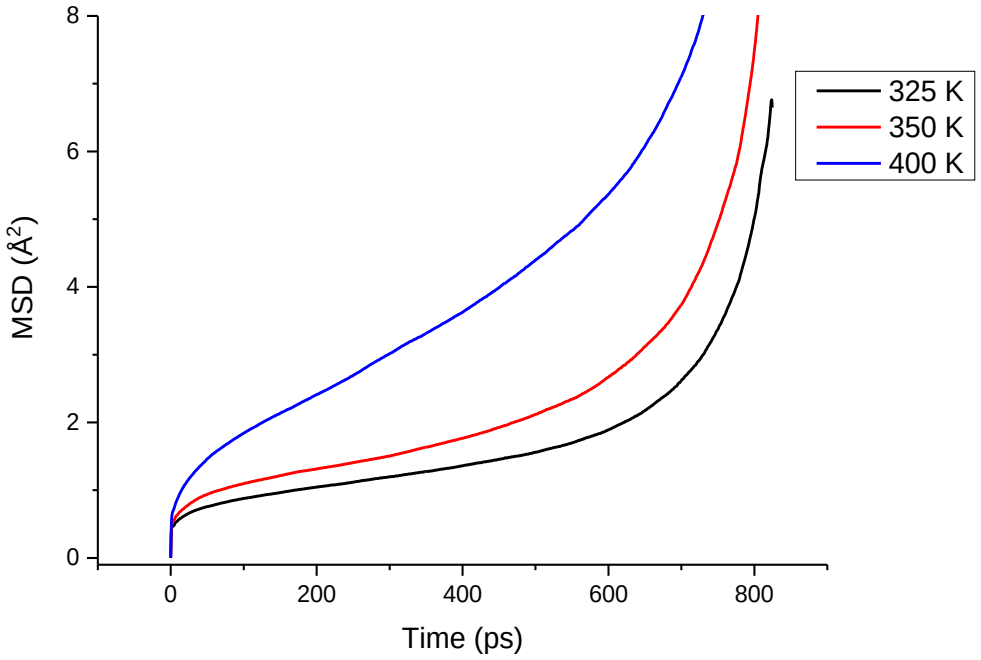

Figure 6.6 - ct MSDs for DPA system with 10% of the molecules removed

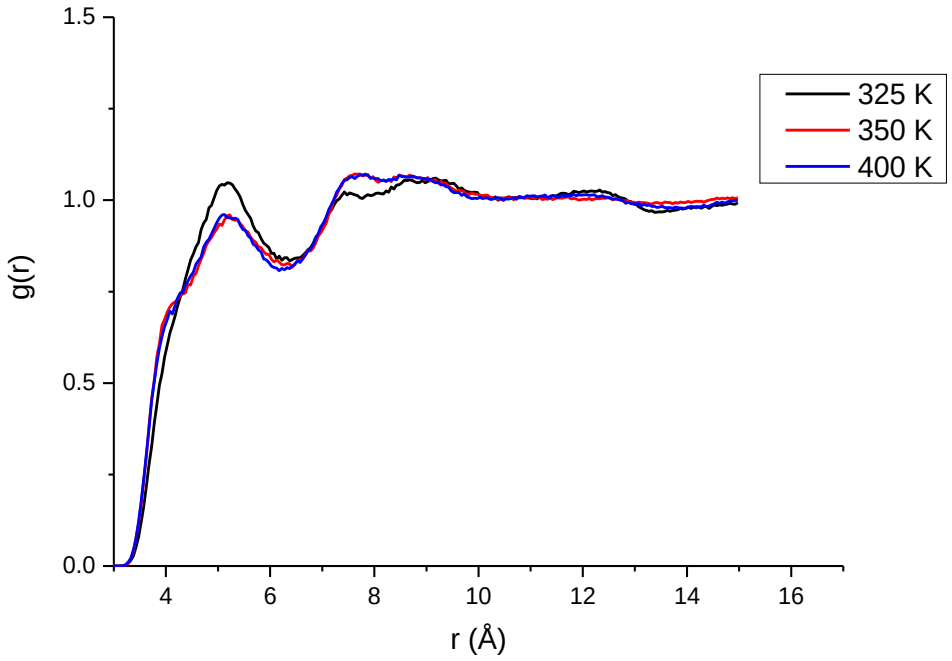

Figure 6.7 – Intermolecular ct-ct RDF for DPA system with 10% of the molecules removed.

The first noticeable point from **Figure 6.6** is that the MSD for 400 K is much greater than those for 325 K and 350 K, indicating greater mobility of the molecules at that temperature. This would suggest that melting is already under way at this temperature. There is slight movement at 325 K, but this could be due to the cell still minimizing and hence moving the molecules. For clarity, **Figure 6.7** starts at 3 Å as the large peaks seen below this are due to intramolecular interactions between the triple bonded carbons. The RDF (**Figure 6.7**) shows there is some short-range order at all temperatures however the peak at ~5 Å, its closest neighbour, does become less intense as the temperature increases suggesting order is being lost in the system. It is interesting to note that in comparison to DEB, for the same percentage of removed molecules, the MSD for DPA is approximately three times greater than that of DEB at the same temperatures. This is to be expected due to the smaller size and more conformational flexibility of DPA allowing the molecule to have greater mobility and diffusivity. As the DPA molecules are smaller, the van der Waals interactions in the cell will be less than those seen in the DEB, which would also result in a lower melting point. The almost acceleration observed at around 800 ps is not observed for DEB however this may be due to the cell still minimizing slightly during the production run. The next two graphs (**Figures 6.8** and **6.9**) show the system with 20% of the molecules removed at the three temperatures already shown and two higher ones (450 K and 500 K).

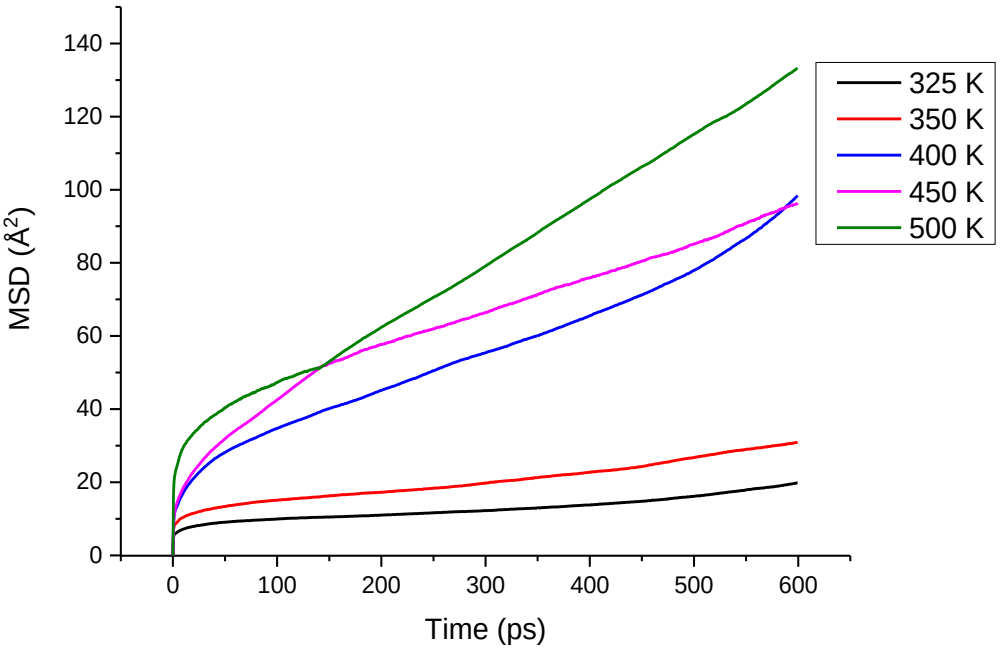

Figure 6.8a - ct-ct MSD for DPA system with 20% of the molecules removed

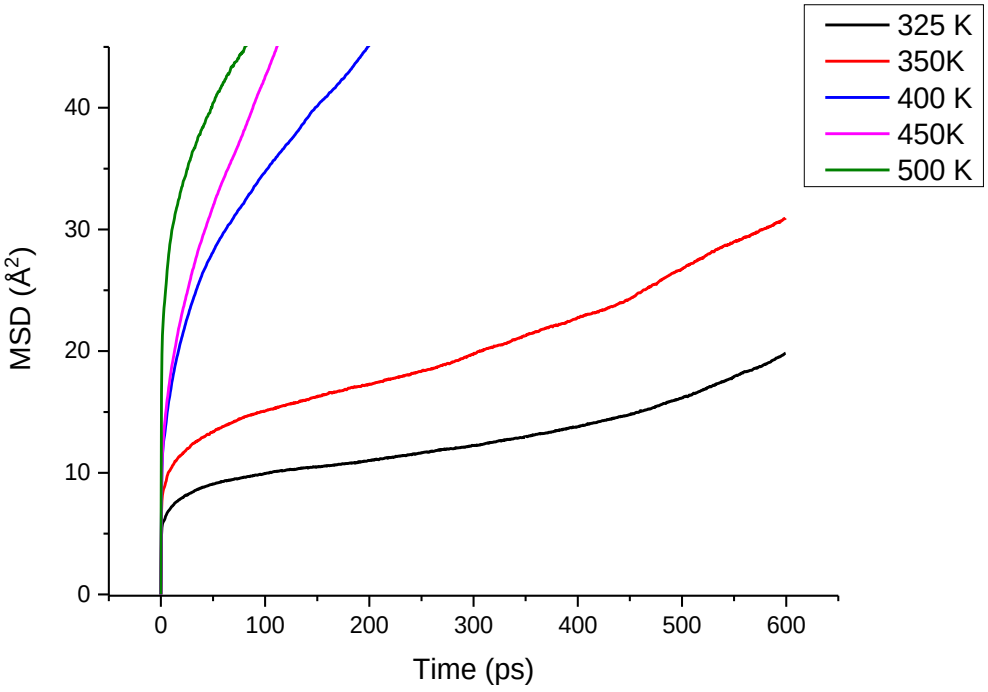

Figure 6.8b - A magnification of 6.8a, for a more detailed look at the lower temperatures

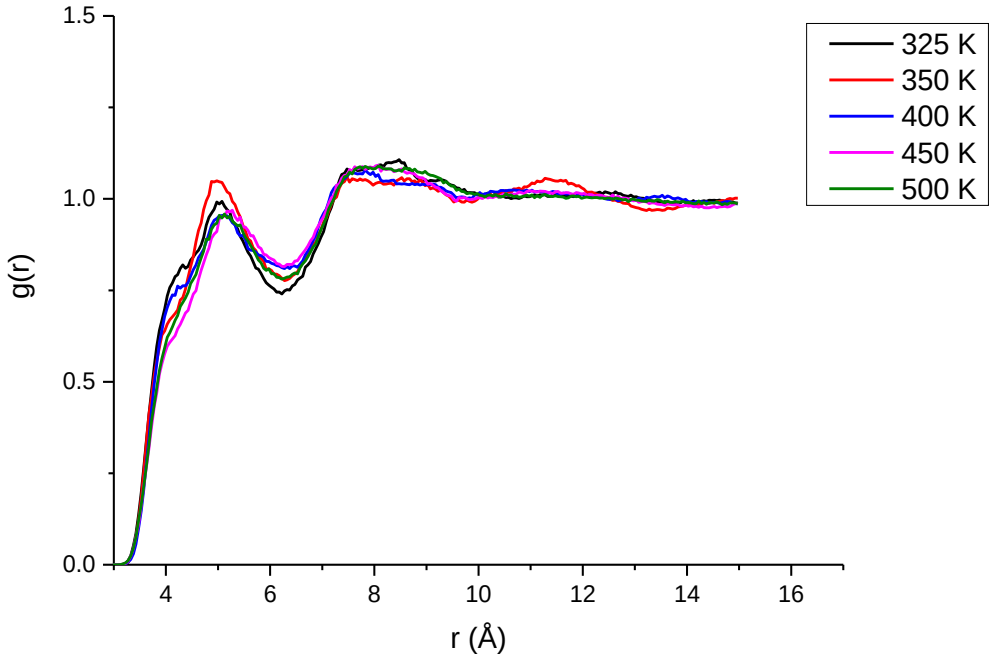

Figure 6.9 – Intermolecular ct-ct RDF for DPA system with 20% of the molecules removed

Figure 6.8 once again shows that at the higher temperatures of 400 K, 450 K and 500 K there is significant bulk molecular diffusion being observed with the MSD. This again suggests that the system is more fluid at this point. This indicates that melting is beginning to occur between 350 K and 400 K. 325 K (the black line) does show evidence of movement amongst the molecules but as previously mentioned this could be due to molecular vibrations possibly combined with further cell minimization. The almost vertical MSDs observed at the start of the 400 K, 450 K and 500 K appears to show instant melting however this is not the case. The cause for these sharp increases look to be artefacts of the minimization phase. 20% removal of molecules from the system is a significant amount and such a change in cell volume is liable to cause minimization to take longer. Despite the monitoring of the cell volume during minimization it appears that the system had not fully

equilibrated before the production run was started. When one compares even the lowest temperature of the DPA production with that of DEB, it is noticeable that DPA's MSD is approximately five times greater. As mentioned previously, this is due to the size of the molecule along with the fact that with 20% of the molecules removed, there is an even greater space for the molecule to diffuse in to. The RDFs (**Figure 6.9**) was once again started from 3 Å in order to view the intermolecular interactions more clearly. They show some short-range order at 5 Å and as the temperature increases there is some loss of detail in the RDFs over 8 Å suggesting melting is occurring and medium – long range order is being lost. This is demonstrated in the 400 K system (the pink line) as it shows a decrease in the peaks at ~5 Å and 7.5 Å. Finally, 30% removal of molecules will be considered (**Figures 6.10** and **6.11**).

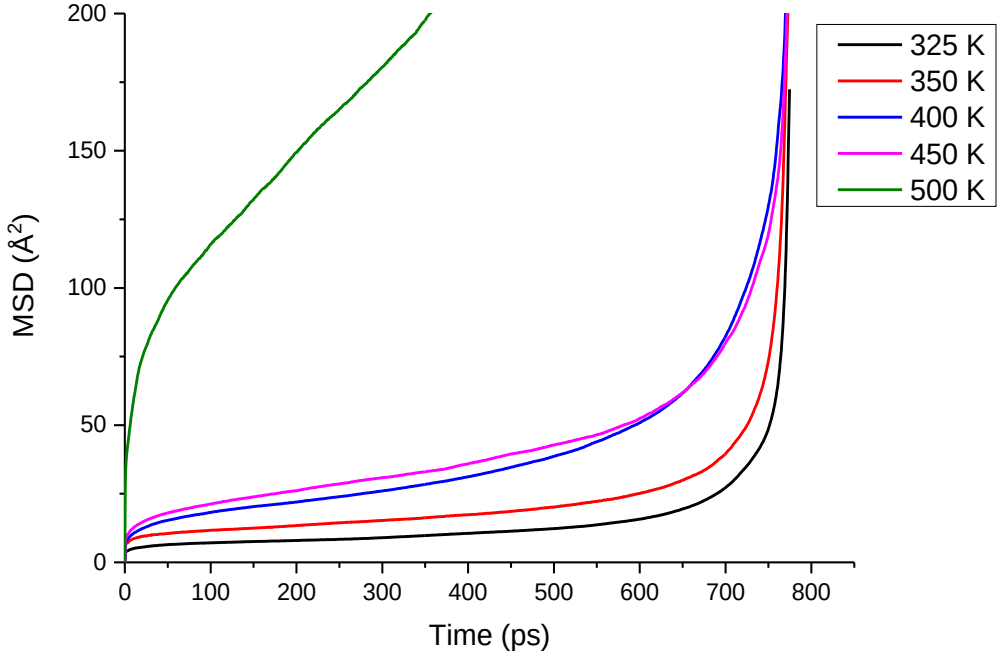

Figure 6.10a - ct-ct MSD for DPA system with 30% of the molecules removed

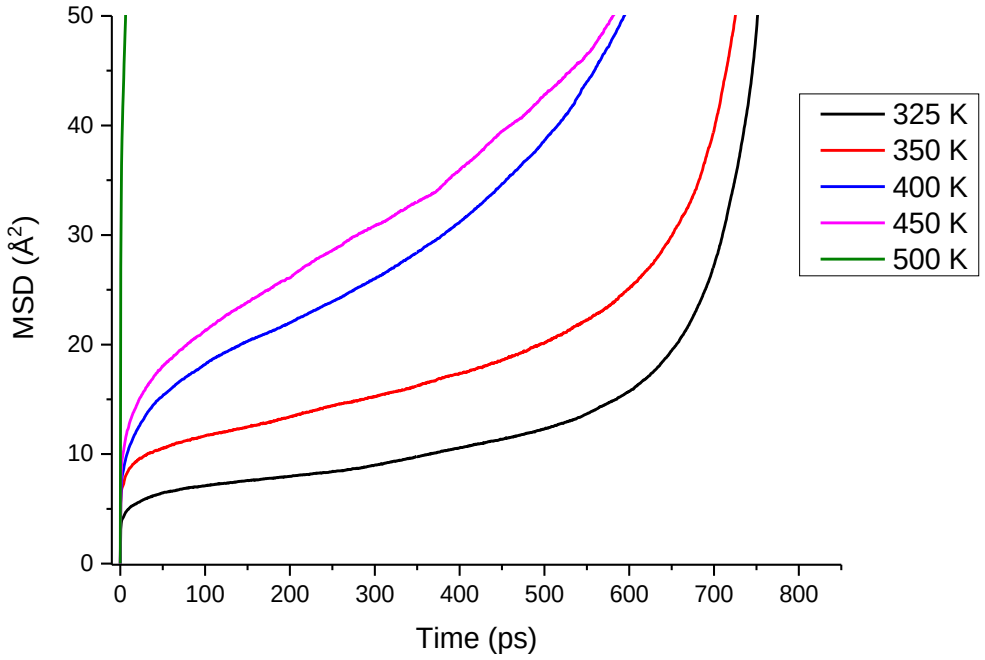

Figure 6.10b - A magnification of 6.10a, for a more detailed look at the lower temperatures

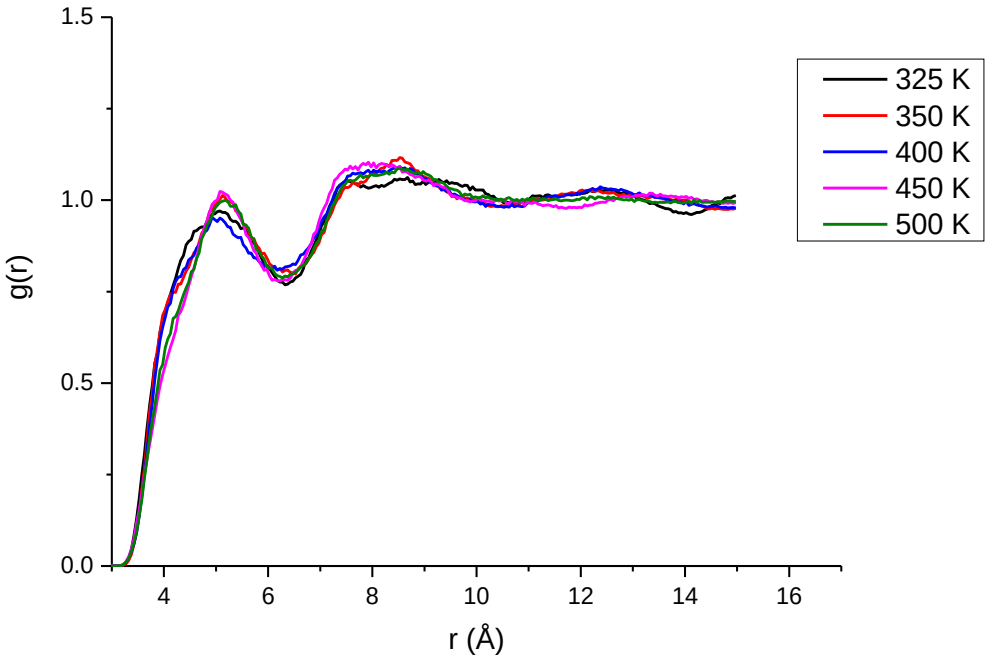

Figure 6.11 – Intermolecular ct-ct RDF for DPA system with 30% of the molecules removed

Figures 6.10 and **6.11** illustrate the same point as the previous MSDs and RDFs with the molecules showing much greater movement from 400 K upwards compared to the lower temperatures. The RDFs show a slight loss of structure which, as previously mentioned, suggests the system is rather viscous.

Using the given data it is reasonable to suggest that the melting point 'envelope' is between 350 K and 400 K which compares favourably with the experimental value of ~335 K.[92,98] One would expect the computational model to overestimate the melting point as by removing molecules, we are still only approximating the way melting could be nucleated, i.e. via a void in the system.

6.2.2 Mixing of Unhydrogenated- and Hydrogenated-DPA

Due to the large amount of data generated, only a few select graphs will be shown – with the others being available Appendix C. The first graphs to be looked at will be the MSDs for the 50:50 ratio (**Figures 6.12** and **6.13**). This ratio has been picked here as there are equal concentrations of both H-DPA and U-DPA and so the main effect on the diffusivity of the molecules is the temperature. Both sets of molecules show the same trends where the MSD increases as the temperature increases. There is practically a horizontal line for 300 K (black line) and this is due to very little molecular diffusion as the melting point for DPA has not yet been reached and so the amorphous system is in a more solid state than other temperatures. At 500 K (green line),

the MSD rises to ~90 Å for H-DPA and ~83 Å for U-DPA. H-DPA has a slightly greater MSD due to the molecules having more conformational flexibility and so likely to exhibit greater diffusivity. The RDFs for the 50:50 ratio at the various temperatures is shown in **Figures 6.14**, **6.15** and **6.16**.

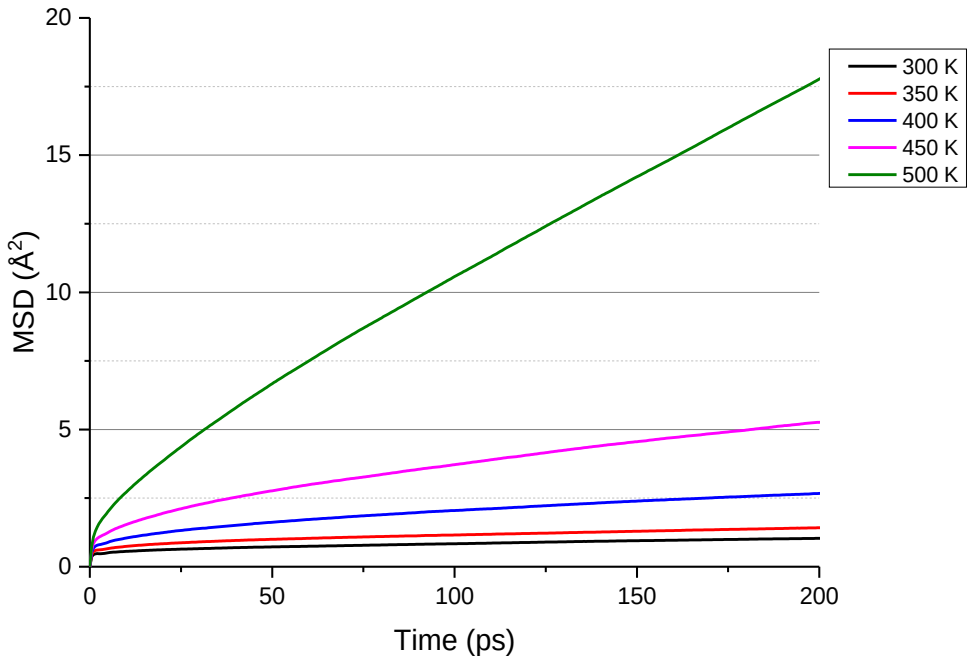

Figure 6.12 - The MSDs for all the 50:50 ratio (4H:0H) at the various temperatures for c2 species

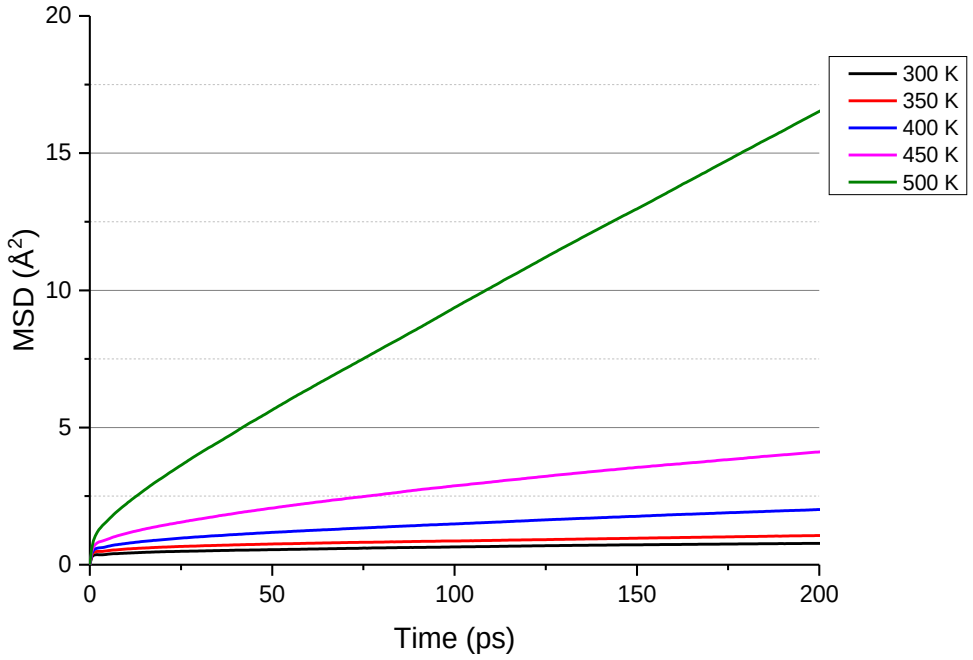

Figure 6.13 - The MSDs for all the 50:50 ratio (4H:0H) at the various temperatures for ct species

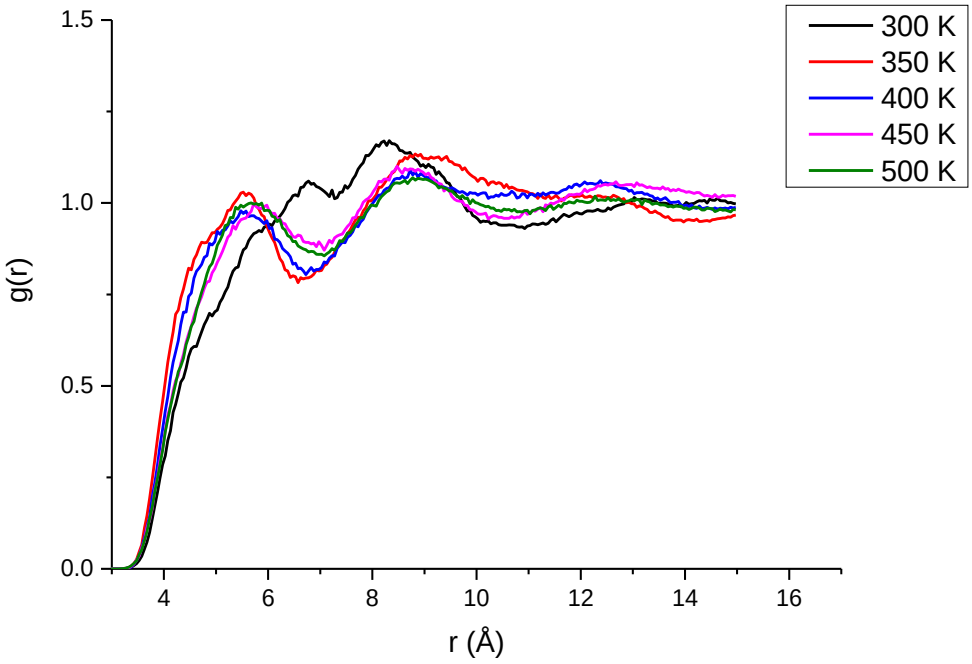

Figure 6.14 - c2-c2 RDFs at the various temperatures for the 50:50 ratio (4H:0H)

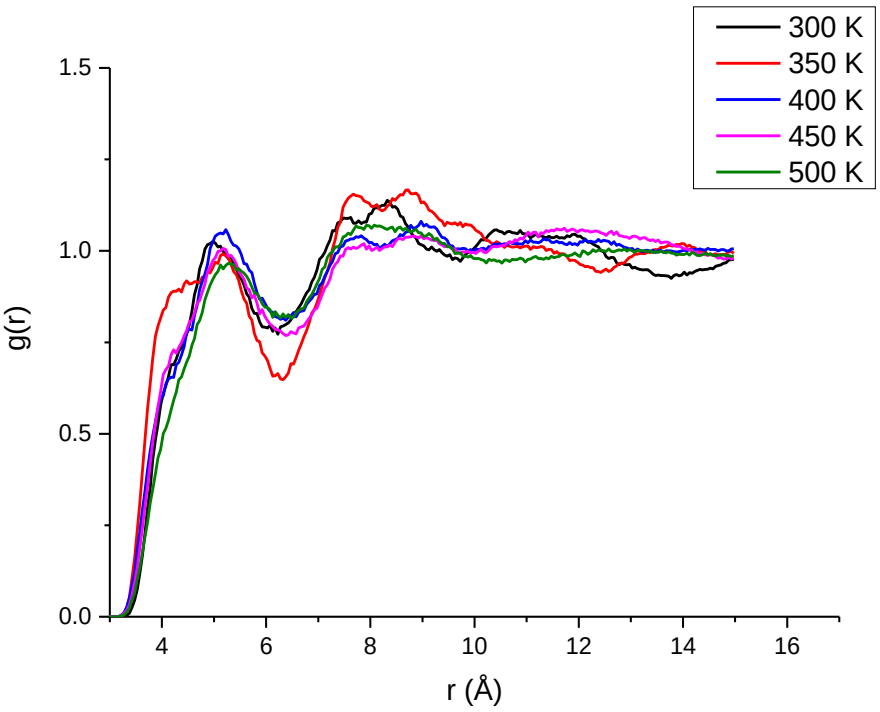

Figure 6.15 - ct-ct RDFs at the various temperatures for the 50:50 ratio (4H:0H)

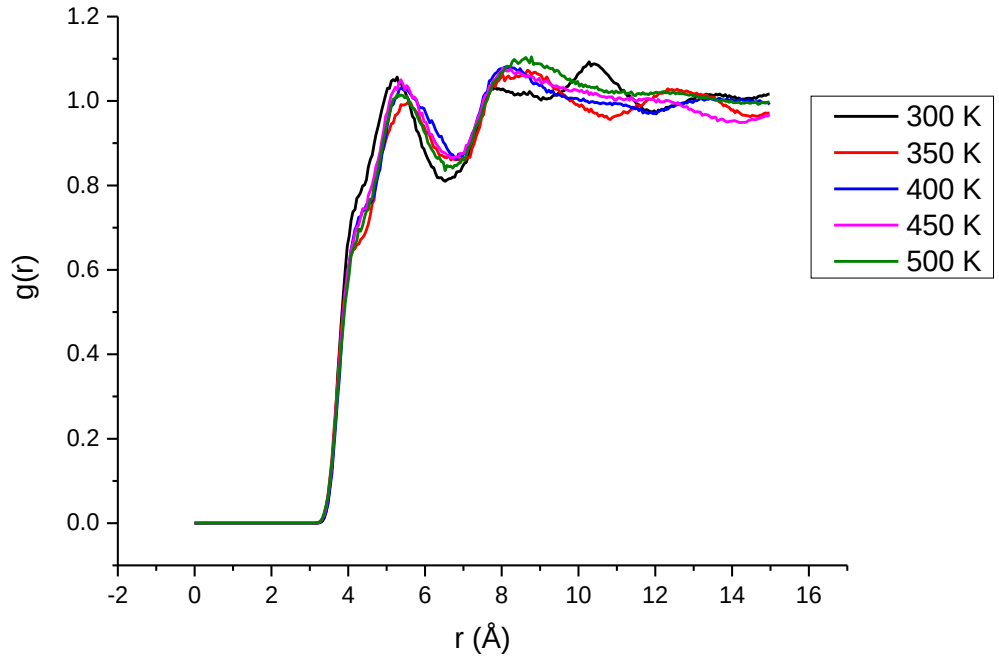

Figure 6.16 - c2-ct RDFs at the various temperatures for the 50:50 ratio (4H:0H)

For **Figures 6.14** and **6.15**, the y-axis has been zoomed in order to see the smaller peaks. The large peaks in both cases (around 1.5 Å for c2-c2 and 1.28 Å for ct -ct) are due to the intramolecular bonds of the atoms. The RDF for c2-c2 (**Figure 6.14**) shows peaks at 5.5 Å and 8.5 Å representing its nearest non-bonded molecules for all temperatures except 300 K which instead has a steadily rising RDF from around 4 Å to 8 Å, which shows it is still in the amorphous configuration. The peaks observed for the nearest neighbours will be described in greater detail shortly. All three RDFs show a qualitative change between 300 K and 350 K and **Figure 6.15** shows the intensity of the peak at ~5.5 Å slightly decreasing as the temperature increases, which indicates diffusivity of the molecules.

The next graphs to be looked at are the MSDs for all the various ratios at 500 K – split into the 2 different atom types (c2 and ct) (**Figures 6.17** and **6.18**).

500 K was chosen as by this point the structure has completely melted and thus should show the greatest diffusivity of the molecules. As an overall trend from the graphs, the MSD increases as the percentage of hydrogenated-DPA (c2) increases and thus the self-diffusion of the molecules. This is evident with the two purple lines (80:20 and 90:10) recording MSDs that are twice as big as the red and black lines (10:90 and 20:80). Similar to the case of DEB, this is due to 4H-DPA molecule being more flexible than its 0H-DPA counterpart. In both **Figures 6.17** and **6.18**, some graphs are out of sequence (i.e. 10:90 and 20:80 for c2 and 90:10 and 80:20 for ct) and this can be explained due to the low number of molecules present in these atom types for

these concentrations which can cause statistical uncertainty. It is noticeable that the MSDs for DPA are approximately 2.5 times greater than those for DEB. This is due to the DPA molecule being smaller in size and therefore able to diffuse more rapidly than its bulkier DEB counterpart. The corresponding RDFs are shown below (**Figures 6.19**, **6.20** and **6.21**).

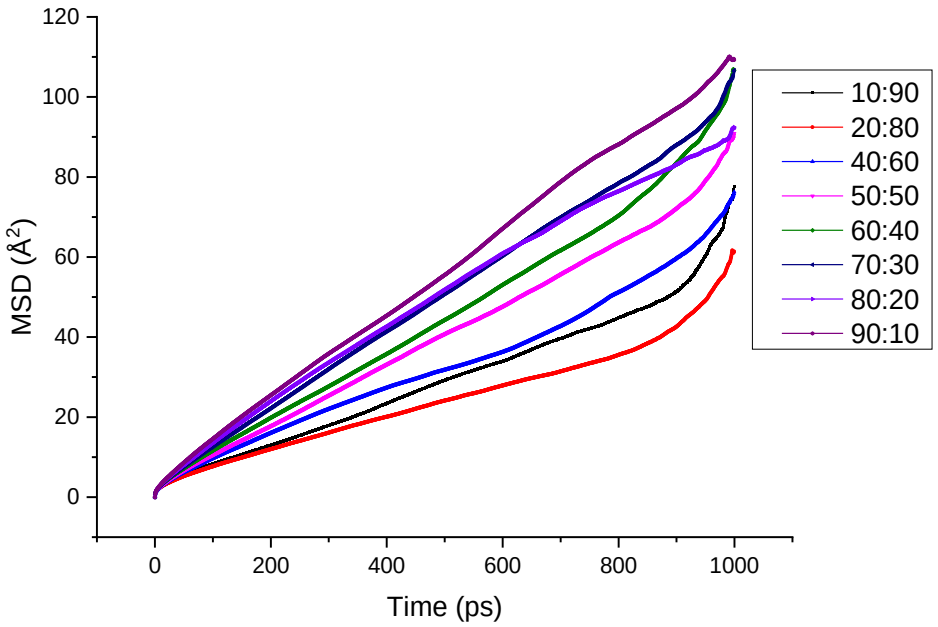

Figure 6.17 - The MSDs for all the various ratios (4H:0H) at 500 K for the c2 atom type

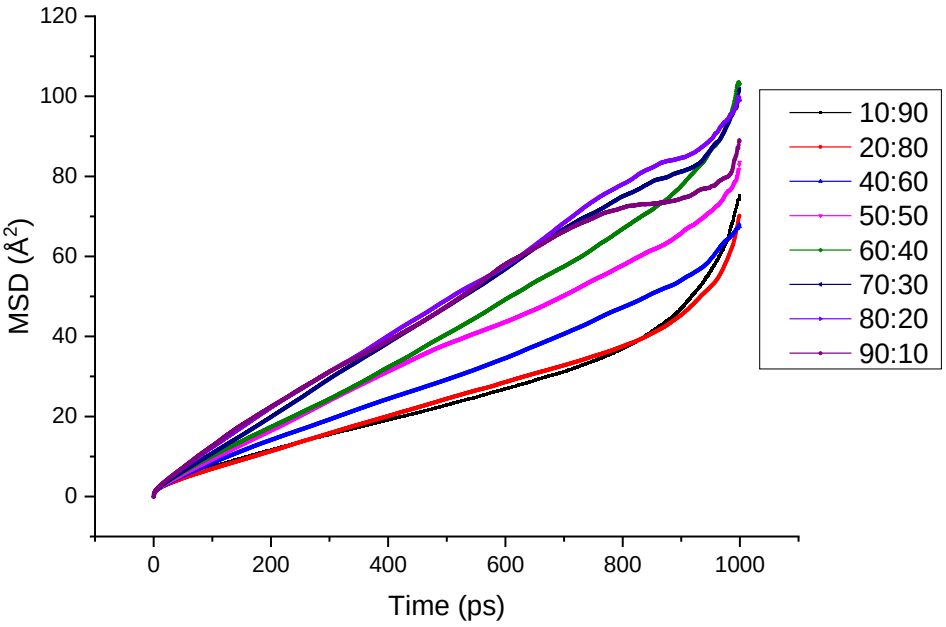

Figure 6.18 - The MSDs for all the various ratios (4H:0H) at 500 K for the ct atom type

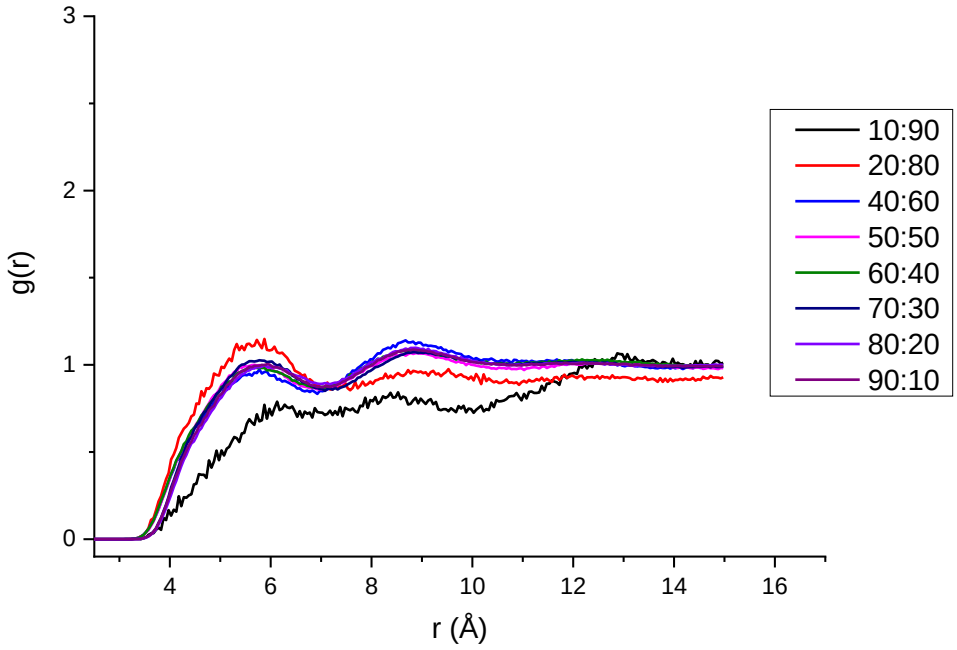

Figure 6.19 - c2-c2 RDFs at 500 K for all the various ratios (4H:0H)

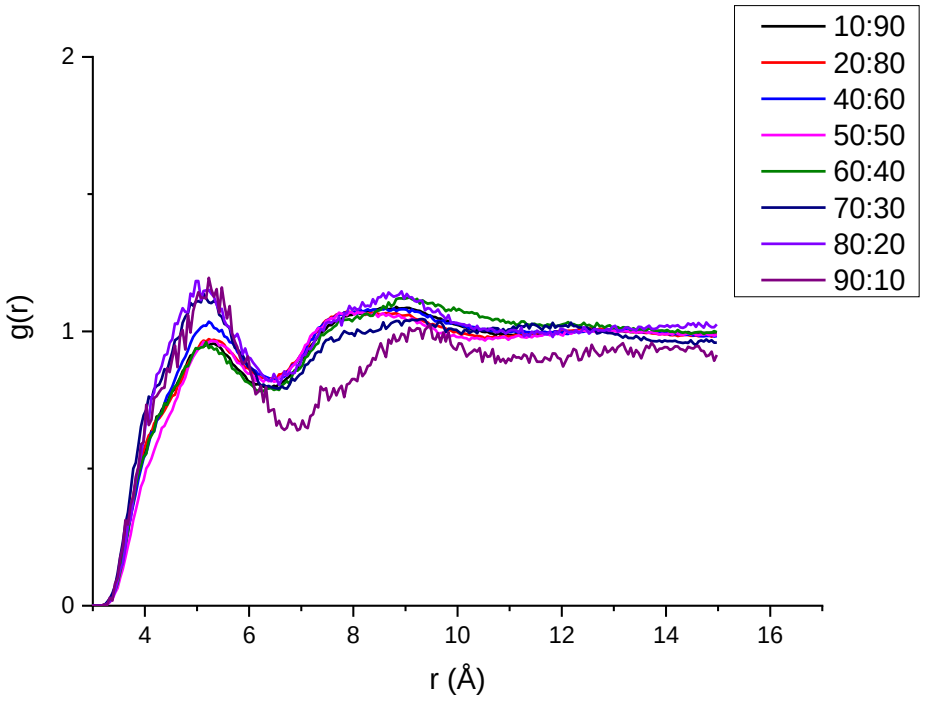

Figure 6.20 – Intermolecular ct-ct RDFs at 500 K for all the various ratios (4H:0H)

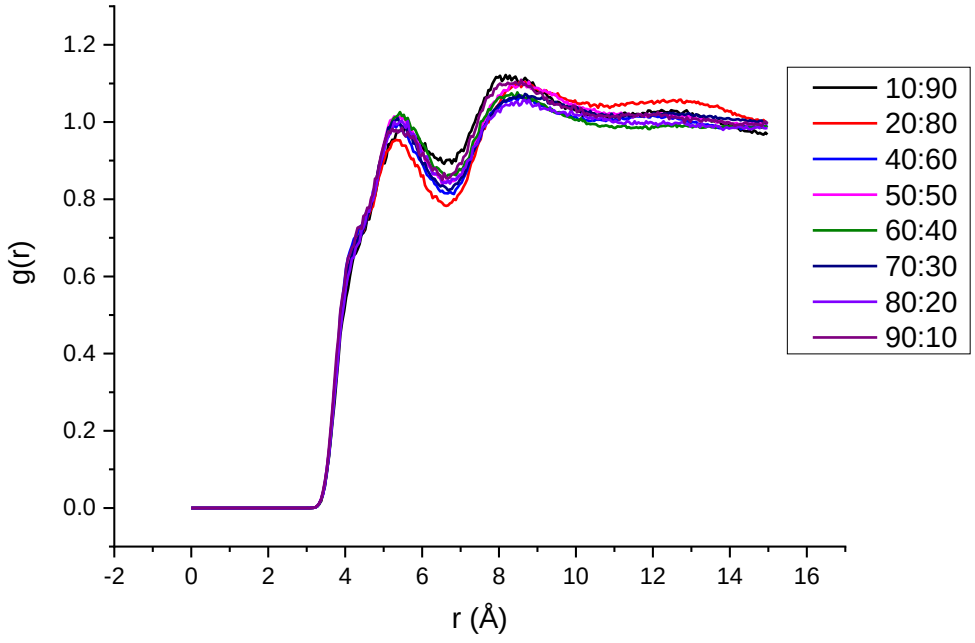

Figure 6.21 - c2-ct RDFs at 500 K for all the various ratios (4H:0H)

Several of the peaks representing the c2-c2 intramolecular bond (1.5 Å) have broadened in **Figure 6.19** however the x-axis was zoomed in on in order to highlight the features at 5.5 Å and 8.5 Å. This broadening is observed in all the RDFs as the temperature increases and so could be due to the high temperature causing the C-C bond to stretch more as the simulation progresses. This can be seen in **Figure 6.22** which shows the change in length of the C-C intramolecular bond throughout the simulation. As previously mentioned, the peaks at approximately 5.5 Å and 8.5 Å are due to neighbouring H-DPA molecules. This can be seen in **Figures 6.23** and **6.24** which illustrates the distance between two isolated H-DPA molecules of the system. The erratic nature of the 10:90 and 20:80 lines (black and red, respectively) in **Figure 6.19** is once again due to the small amount of data available and thus statistical uncertainty.

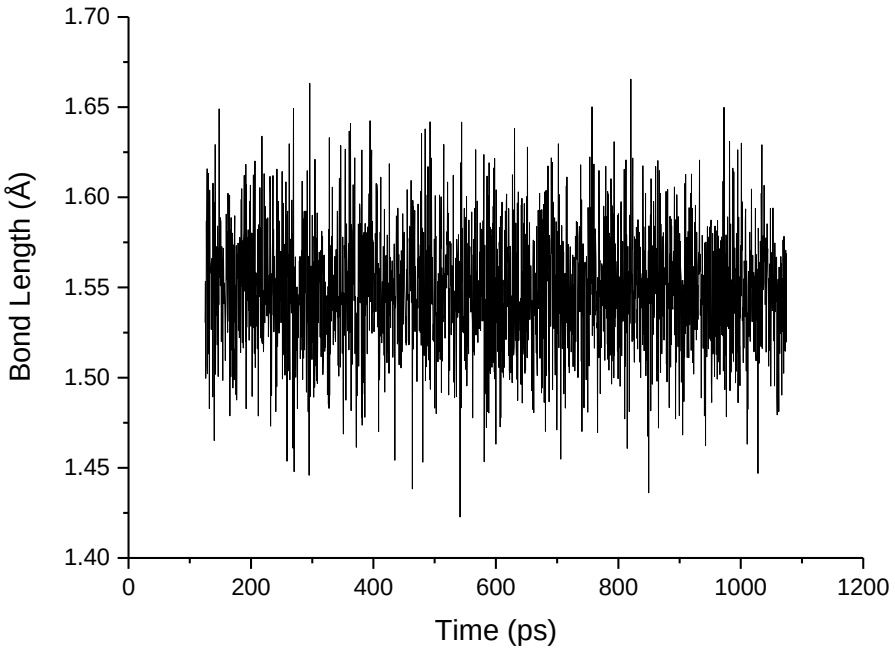

Figure 6.22 - Graph showing the change in length of the C-C bond (c2-c2) throughout the simulation (after equilibration) at 400 K.

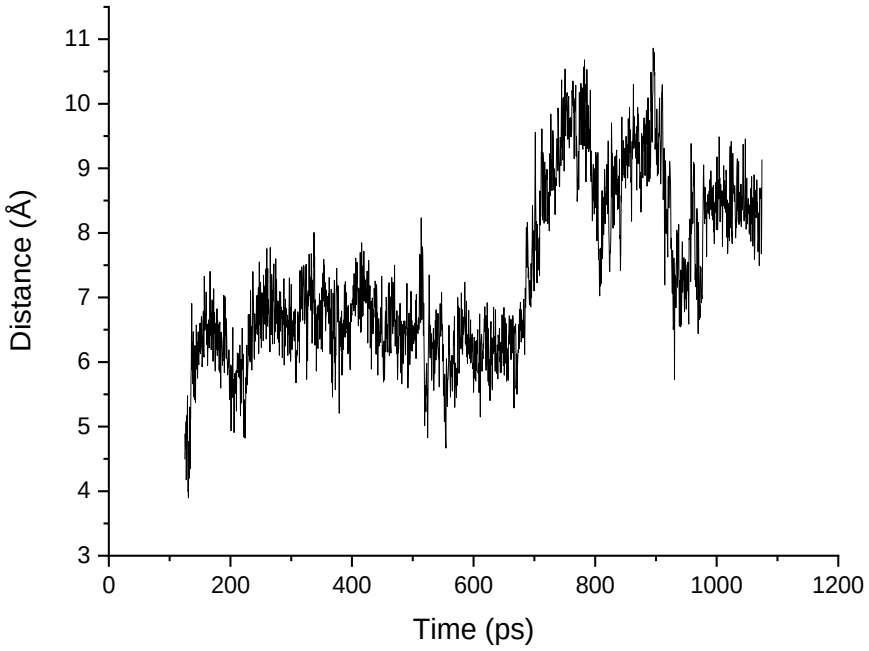

Figure 6.23 - Graph showing the change in intermolecular distance between two c2-c2 atoms throughout the simulation (after equilibration) at 400 K.

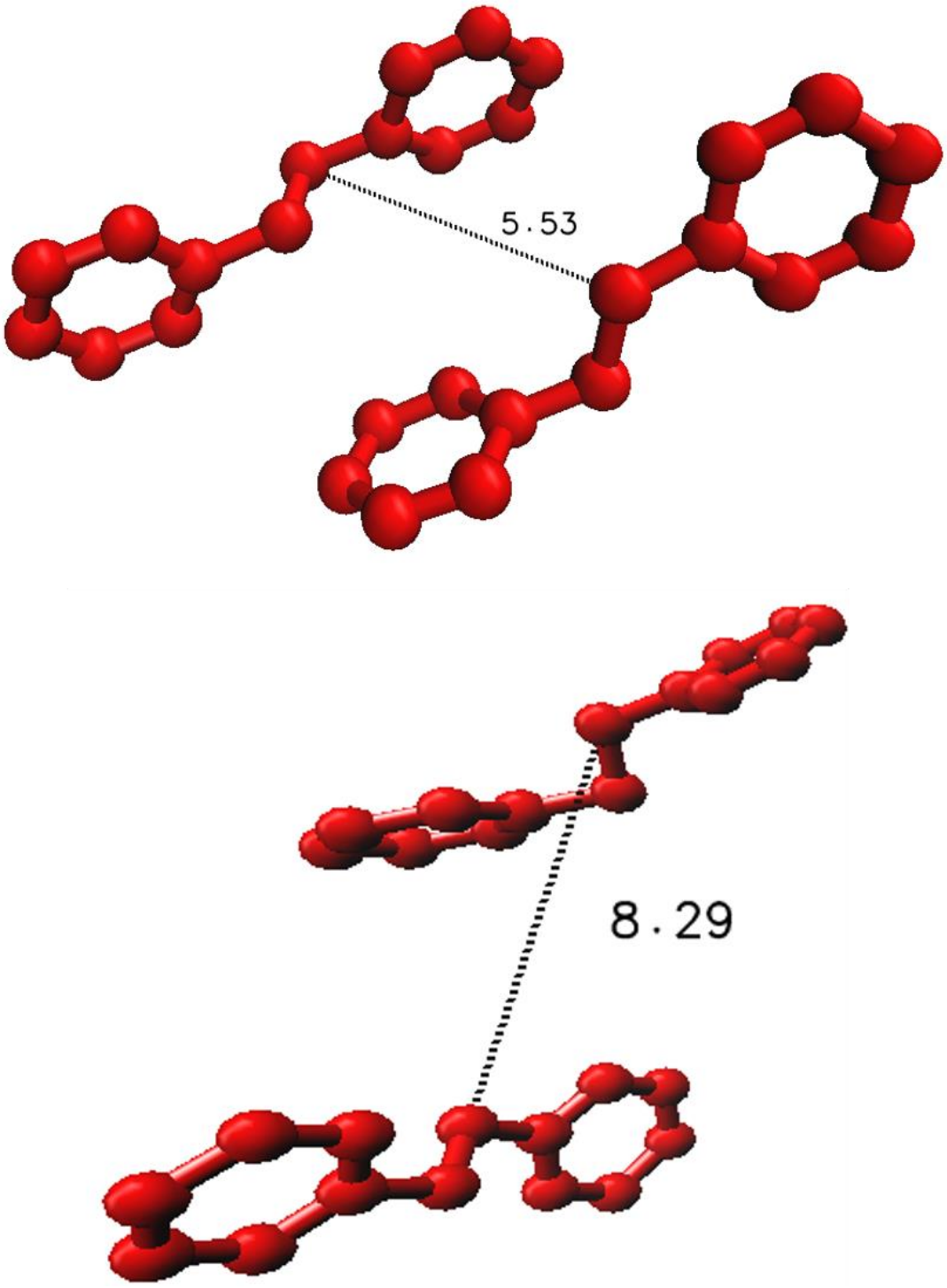

Figure 6.24 - Image demonstrating the change in intermolecular distance between two c2-c2 atoms, corresponding to the peaks in the RDF of ~5.5 Å and 8.5 Å

Broadened peaks in the RDF are seen once again in **Figure 6.20** where the C≡C is at 1.2 Å. Once again, this is due to the temperature and the change in bond length through the simulation can be seen in **Figures 6.25**. There are also neighbouring unhydrogenated-DPA molecules around 5 Å and 8 Å away and this can be observed in **Figures 6.26** and **6.27**. The deep purple line (90:10), in **Figure 6.20**, is also jagged due to the statistical uncertainty mentioned previously.

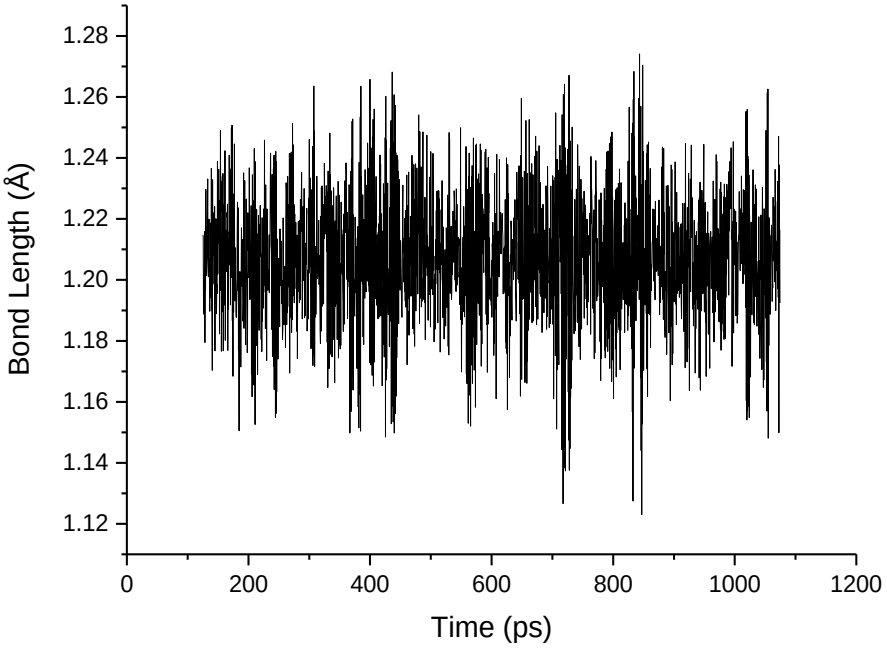

Figure 6.25 - Graph showing the change in length of the C≡C bond (ct-ct) throughout the simulation (after equilibration) at 400 K.

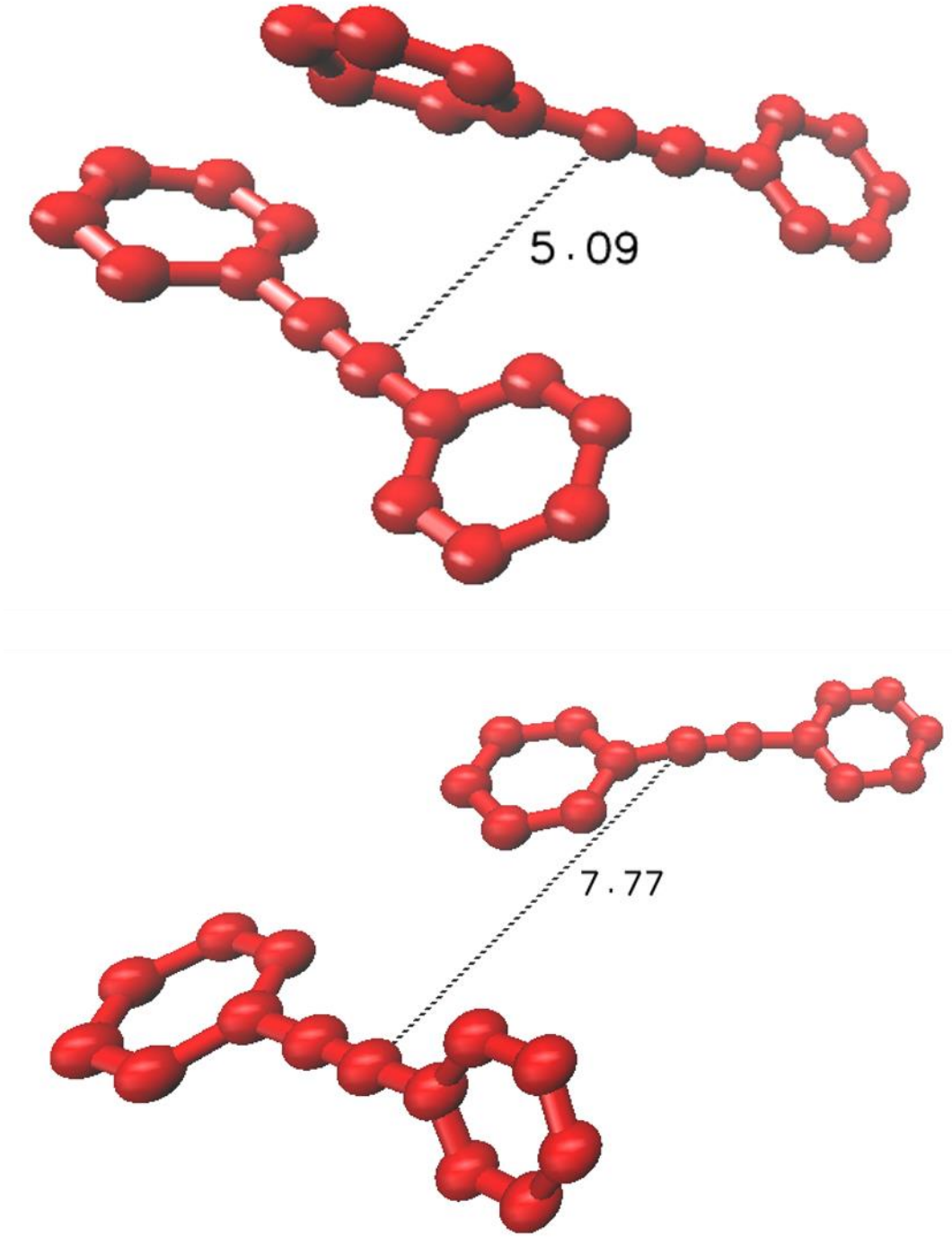

Figure 6.26 – Image demonstrating the change in intermolecular distance between two ct-ct atoms, corresponding to the peaks in the RDF of ~5 Å and 8 Å

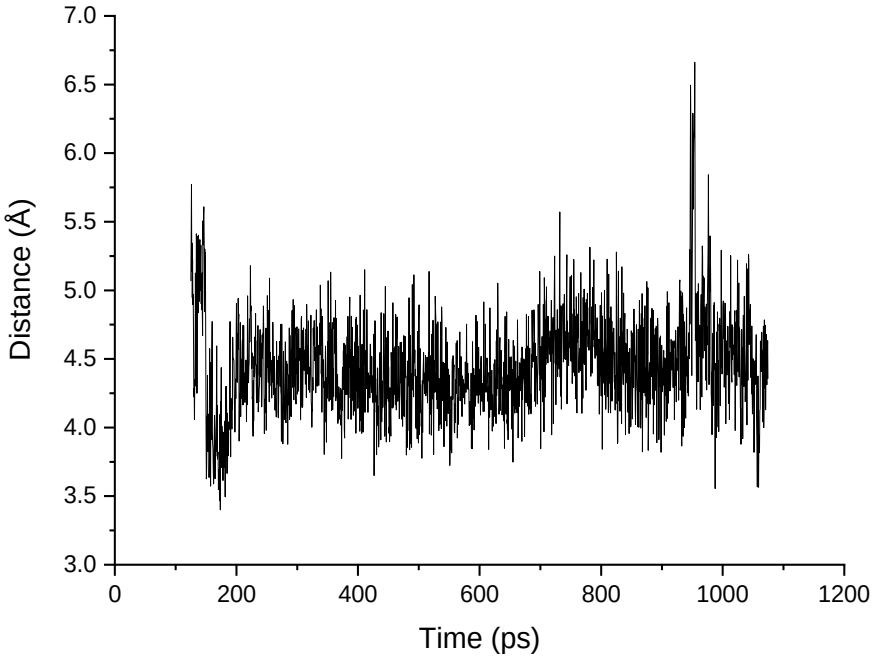

Figure 6.27 - Graph showing the change in intermolecular distance between two ct-ct atoms throughout the simulation (after equilibration) at 400 K.

The final RDF to be considered (**Figure 6.21**) is the one that illustrates the distances between c2 and ct atoms. Two clear peaks are visible at approximately 5 Å and 9 Å showing the distance between H-DPA and U-DPA molecules and once again this can be visualised in **Figures 6.28** and **6.29**.

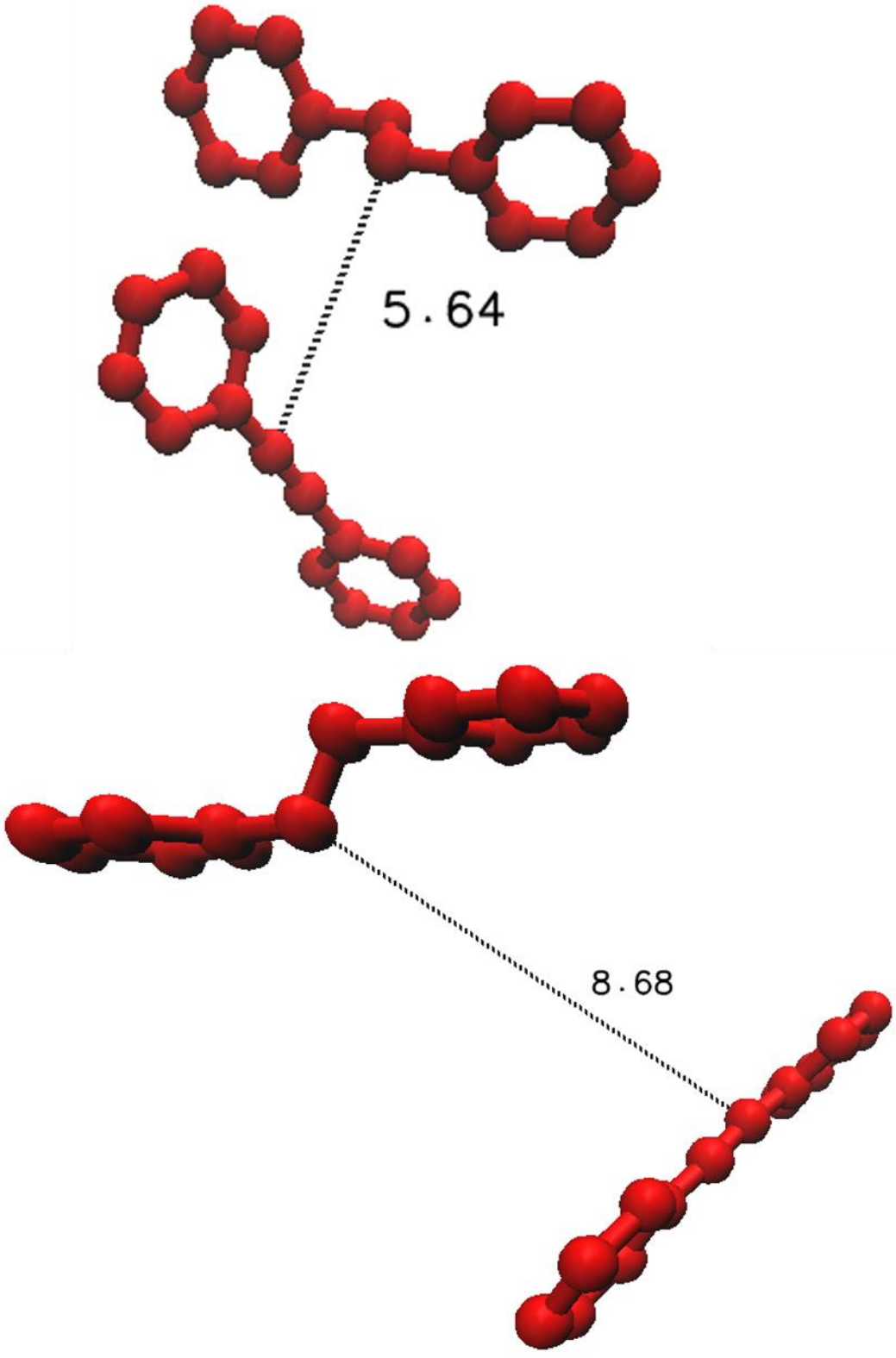

Figure 6.28 - Image demonstrating the change in intermolecular distance between one c2 and one ct atom, corresponding to the peaks in the RDF of ~5 Å and 9 Å.

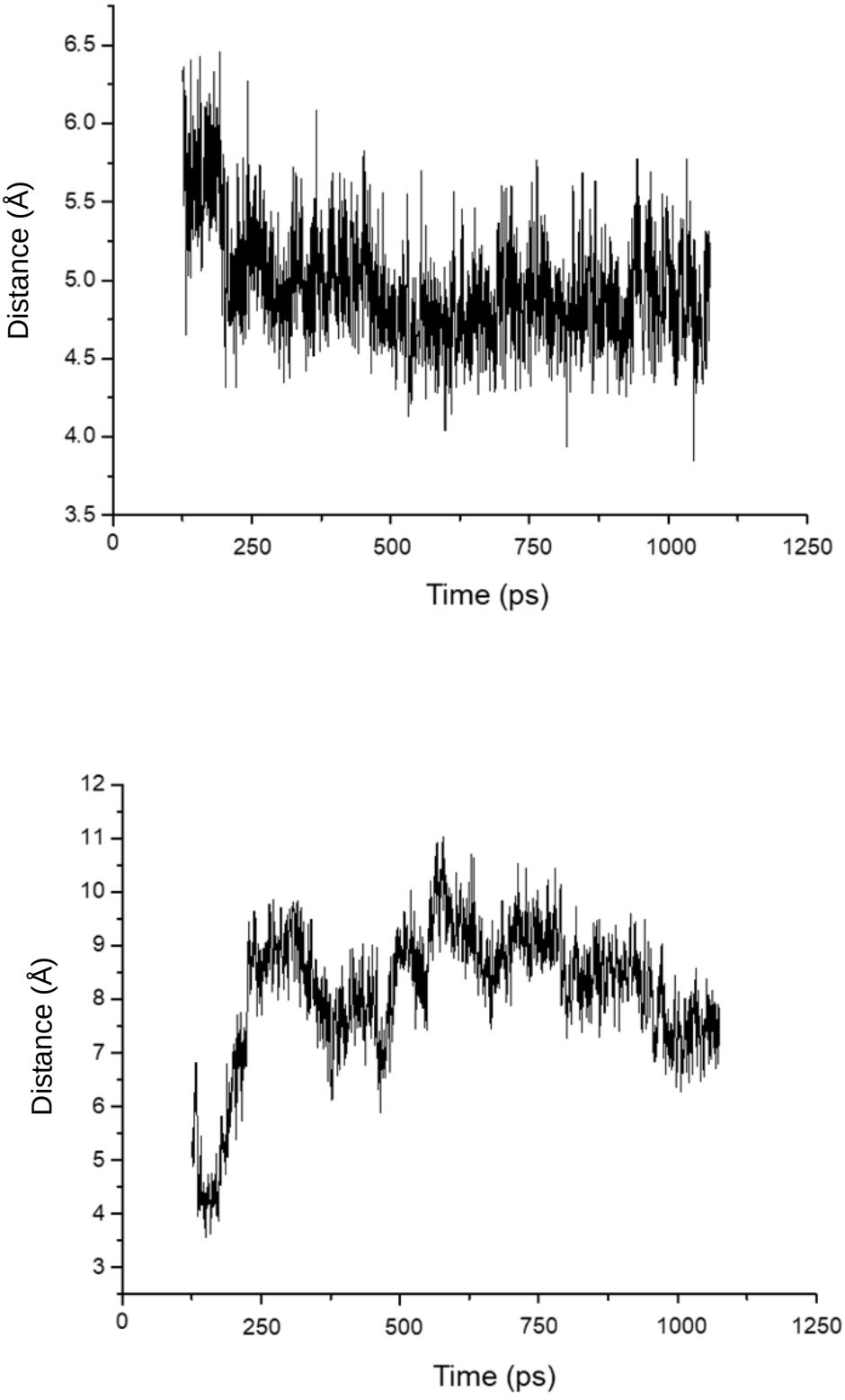

Figure 6.29 - Graphs showing the change in distance between c2-ct atoms throughout the simulation (after equilibration) at 400 K.

Another analysis tool that can be utilised is to calculate the preferred relative angles of the benzene rings (i.e. the angle between the planes of the two rings within the same molecule) in Hydrogenated-DPA and Unhydrogenated-DPA. **Figures 6.30** and **6.31** show which 10-degree interval (*i.e.* 10-20°, 20-30°, *etc.*) the benzene rings prefer to be in. It is noticeable from the histograms that the benzene rings in U-DPA have no real preference in angle except there are few that are very flat, 0-0°. As reported by Thomas *et al.*, the π-orbitals of the alkyne bond are found to sustain a variety of conjugation lengths between the phenyl rings, thereby giving flexibility to the molecule to arrange itself in various conformations.[97] As the energy difference between these conformations is fairly small there is little preference over angles, as observed in the **Figure 6.30**. H-DPA on the other hand seems to strictly prefer the 10-20° conformation at all ratios. The *sp* carbons seen in U-DPA become sp^3 carbons in the H-DPA system which results in a loss of the π-orbitals and thus the conjugation. Also the addition of the 4 hydrogen atoms causes sterical hindrance and so 10-20° conformation is more energetically favourable. At 80-90° for example, the hydrogens of the aliphatic group would clash with those of the benzene ring, which would be energetically unfavourable. These angles are demonstrated in **Figures 6.32** and **6.33**.

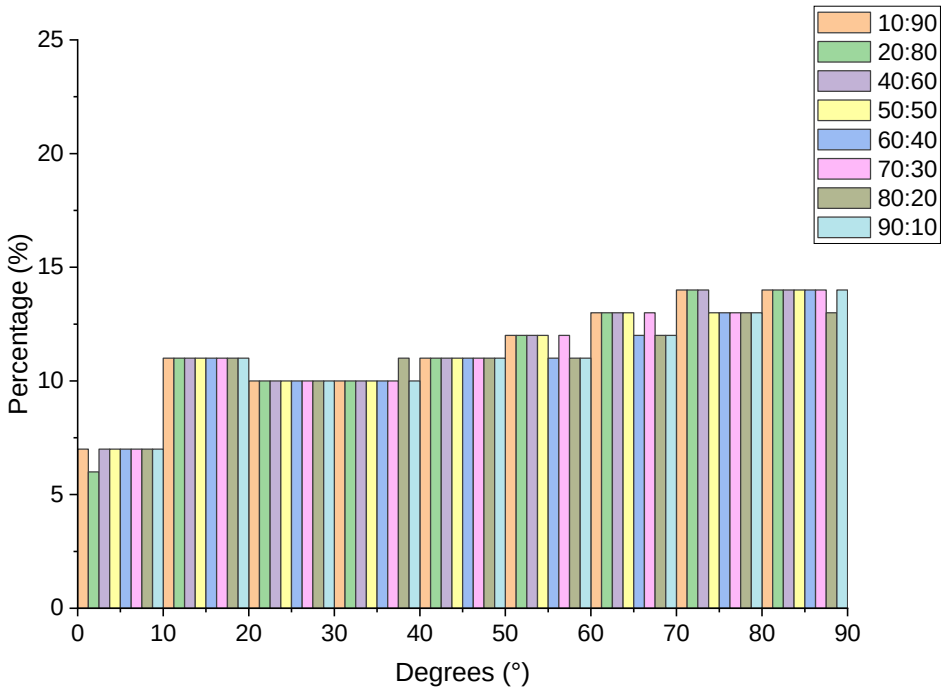

Figure 6.30 – Histogram showing the intramolecular angles for the benzene rings in U-DPA for all various ratios (4H:0H) at 500 K

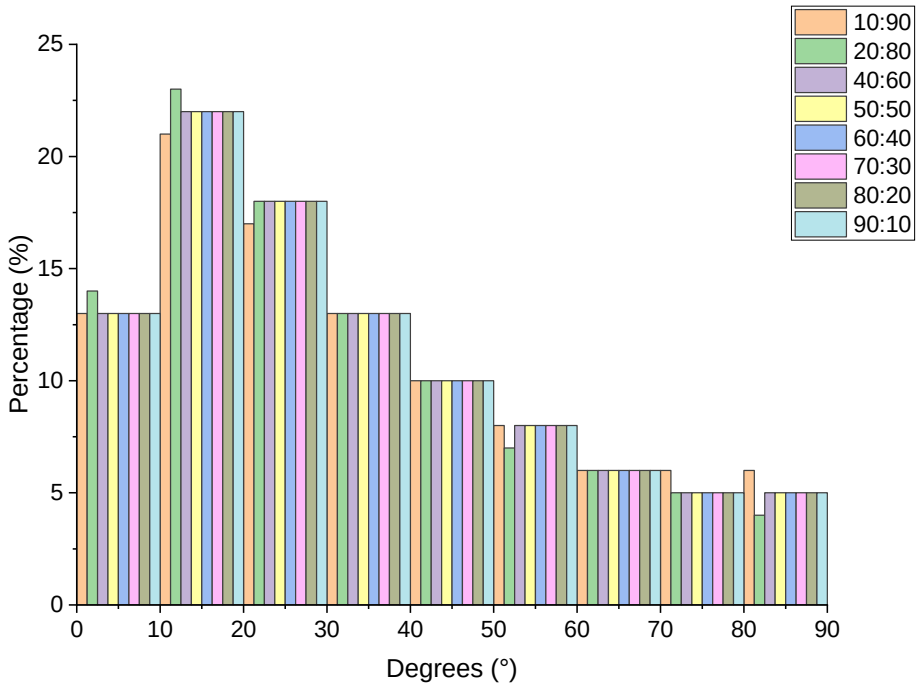

Figure 6.31 – Histogram showing the intramolecular angles for the benzene rings in H-DPA for all various ratios (4H:0H) at 500 K

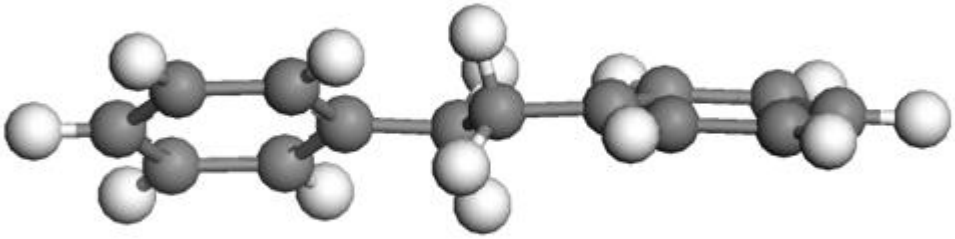

Figure 6.32 – The preferred angle of 10 – 20° for 4H-DPA

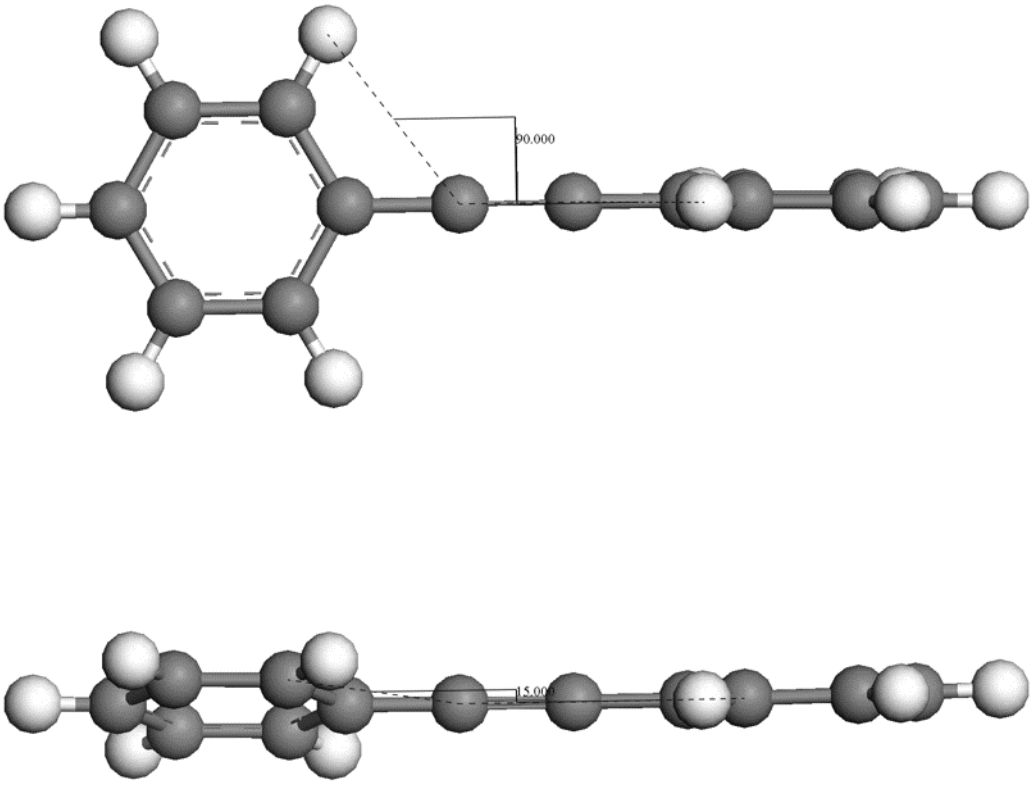

Figure 6.33 - The angles of 80 - 90° (top) and 10 – 20° (bottom) for 0H-DPA

The final piece of useful information to be gained from the study of the mixing of unhydrogenated- and hydrogenated-DPA is diffusion coefficients. These were calculated in the same way that was used for the DEB calculations. As with the DEB diffusion coefficients, the 250 – 750 ps range of

the MSD was used to calculate the value. The ct values have been omitted from the table (**Table 6.1**) as, as in the case of DEB, they are usually lower than their c2 counterparts. The ct values can be found in Appendix C. The same trend from the DEB diffusion coefficients is observed where diffusivity increases as the concentration of c2 and the temperature increases. Interestingly, the values for 4H-DPA are approximately 2.5 – 3 times greater than those seen for the DEB counterpart. This is probably due to the DPA molecule being smaller and thus possessing greater mobility and diffusivity.

Diffusion Coefficients (m^2s^{-1}) [all values are x 10^{-15}]								
Temperature (K)	U10:H90	U20:H80	U30:H70	U40:H60	U50:H50	U60:H40	U80:H20	U90:H10
300	7.54	6.33	6.02	5.99	5.20	5.02	3.52	3.45
350	14.4	12.0	11.1	9.17	8.22	8.08	7.50	7.15
400	28.0	25.7	20.9	18.4	18.2	16.3	16.2	15.5
450	86.4	80.1	67.3	59.8	53.3	51.2	47.6	47.2
500	358	315	296	283	251	180	170	128

Diffusivity increases as temperature increases

Diffusivity increases as concentration of c2 increases (4H-DPA)

Table 6.1 – Table showing the diffusion coefficients for each of the 0H:4H percentages for the 250.5 – 750.5 ps time range of the MSD

The Arrhenius equation, $k = Ae^{\frac{-E_a}{RT}}$, where k is the rate constant, T is the absolute temperature, A is the pre-exponential factor, E_a is the activation energy and R is the universal constant, was rearranged by taking the natural log to create Arrhenius Plots (**Figures 6.34** and **6.35**) for the diffusion coefficients of both atom types. This could be used to calculate activation energies of diffusion for 4H-DPA and 0H-DPA., as plotting lnD vs. 1/T (where D is the diffusion coefficient) gave a slope equal to -Q/R (where Q is the activation energy of diffusion and R is the gas constant). It can be seen from the Arrhenius plots that they are not straight lines and so two activation energies were calculated for each ratio – one between 300 and 400 K and the other between 400 and 500 K. **Table 6.2** shows the calculated activation energies.

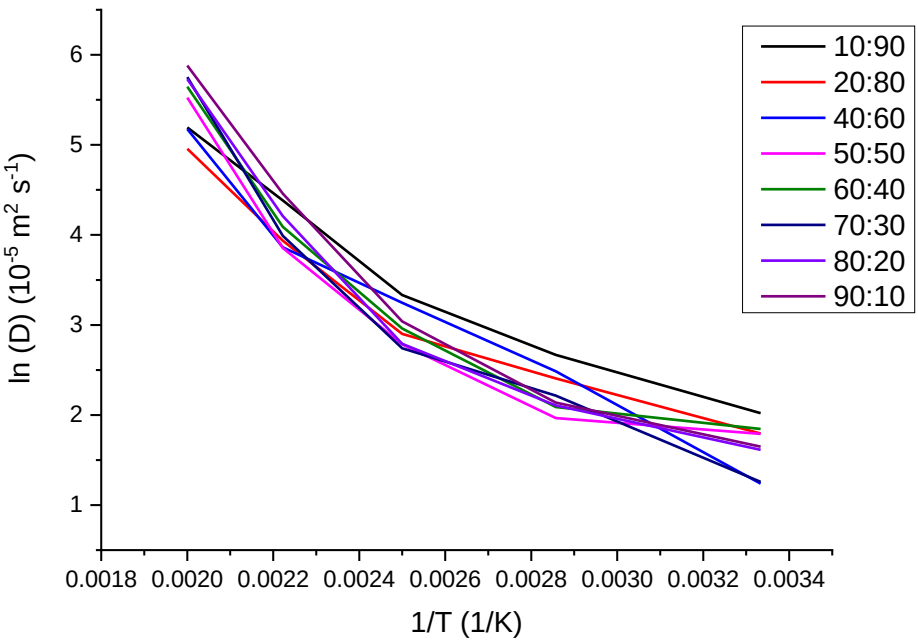

Figure 6.34 – Arrhenius plot for c2 atom type across all 4H:0H ratios

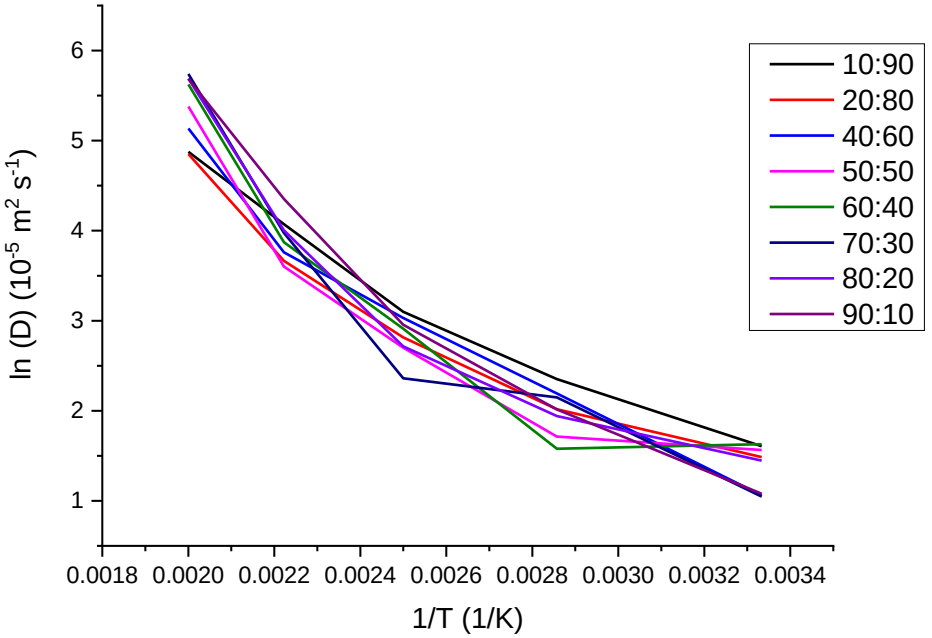

Figure 6.35 - Arrhenius plot for c2 atom type across all 4H:0H ratios

	E_a(c2) (kJ mol^{-1})		E_a(ct) (kJ mol^{-1})	
4H:0H Ratio	*300 - 400 K*	*400 – 500 K*	*300 – 400 K*	*400 – 500 K*
10:90	29.48	13.08	30.91	14.88
20:80	33.83	11.03	34.12	13.25
30:70	32.05	19.62	34.98	20.01
40:60	44.49	9.92	45.52	11.33
50:50	44.60	11.11	45.04	12.79
60:40	50.03	13.09	56.13	14.77
70:30	48.82	11.74	49.43	12.63
80:20	45.38	13.86	47.19	18.7
90:10	29.48	13.08	30.91	14.88

Table 6.2 – Activation energies of diffusion for c2 (4H-DPA) and ct (0H-DPA) across all ratios of 4H:0H.

As mentioned previously, the Arrhenius plots show no linear fitting and hence suggests there is two stages to the diffusion. **Table 6.1** provides further support that the c2 molecules (4H-DPA) have greater mobility than their ct counterparts (8H-DPA), with the ct atom type having a greater activation energy than c2.

6.3 Conclusion

The primary objective was to investigate the melting point 'envelope' and the mobility and diffusivity of the two types of molecule (unhydrogenated- and hydrogenated-DPA) and this has been accomplished. A melting point 'envelope' of 325 – 350 K was established which is in good agreement with the experimental data of 332 K reported by Tkachenko *et al.* [96] Tkachenko *et al.* used adiabatic calorimetry to experimentally calculate this value.

It is clear from the MSDs and the diffusion coefficients calculated from them that the c2 atom type (*i.e*. 4H-DPA) has greater mobility than its 0H-DPA counterpart due to its conformational flexibility. The concentration of each molecule in the system also plays an important role, as the systems with larger concentrations of 4H-DPA provided greater mobility and diffusivity for both types of molecules.

The investigation also provided comparable trends to the ones carried out on DEB. As mentioned throughout the Chapter the trends observed for DEB with regards to the increase of diffusivity as temperature rose are seen with DPA. The major difference is the order of magnitude of DPA's MSDs compared to those of DEB. As previously mentioned, the MSDs of DPA are three to five times larger than those for DEB, due to the smaller nature of the

DPA molecule and the reduction in van der Waals forces. The importance of the mobility of the c2 atom type (*i.e.* 4H-DPA) was highlighted and gave support to the conclusions drawn from the DEB investigation, that the hydrogenated species is faster than the undrogenated species for both systems. Once again, the DPA c2 atom is approximately 2.5 times greater than that of DEB's c2 atom and this is due to DEB being a bulkier molecule and thus mobility is reduced compared to DPA.

Chapter 7 – Concluding Remarks

7.1 Summary and Conclusions

A computer simulation study of the hydrogen getter molecule 1,4-bis(phenylethynyl)benzene (DEB) and related molecules in the solid state has been presented in this thesis, using molecular dynamics (MD) simulations based on interatomic potentials

Firstly, forcefield optimisation has been employed to compare four force fields against each other in order to determine the most suitable candidate to use for MD. This was done by studying the lattice parameters and bond lengths obtained from the lattice dynamics simulations. The cvff force field was found to be the most accurate, which led to its use in the calculation of the thermochemical properties (such as density and enthalpy of vaporization). cvff successfully replicated the density found in literature for both DEB and phenylacetylene. With regards to the enthalpy of vaporization, there were slight discrepancies with the literature values, but this could be ascribed to the variation in conditions under which the calculations were made, compared to those of the experimental determination. In order to obtain a more accurate calculated value, the experimental conditions should be replicated in the calculations. This should be explored in future work.

The crystal minimisation package utilised, GULP, was chosen for the force field validation section of this study due to its ability to apply analytic solutions of dynamics to organic materials whilst supporting various force fields, both of which were important requirements. There are other programs available however the ease of use, with regards to both input and analysis of

output, made GULP the most appropriate choice. These calculations paved the way for the use of molecular dynamics to further study the DEB molecule and its intermediates.

Next, MD techniques were utilised to calculate a melting point 'envelope' for DEB to gain a better understanding of how the system reacts under various temperatures. This was calculated to be between 400.15 K and 473.15 K which was in good agreement with the experimental data which produced a value of 449 K. As discussed during Chapter 4, 2 techniques were used to calculate this envelope, firstly the removal of molecules and then a slab technique. The comparison of these techniques in this thesis produced interesting results. It was determined that the slab technique was more accurate, as it allowed both melting and freezing temperatures to be calculated with more consistency. This method however was more computationally expensive and was therefore not used in Chapter 6. As discussed in Chapter 4, the results from the removal of molecules technique were more open to interpretation. This technique appeared to be influenced by the percentage of molecules removed making the result less reliable and there was also the potential for ambiguity with regards to whether the system had melted or had rather minimised to an amorphous state. This then led into the investigation of the mixture between hydrogenated and unhydrogenated 1,4-bis(phenylethynyl)benzene at various temperatures and concentrations of hydrogenation. MSDs, RDFs and diffusion coefficients were calculated to explore the mixing behaviour of the molecules. The mixing of the molecules was found to be heavily affected by the proportion of the hydrogenated DEB

and the temperature, with diffusivity being greater when there was a higher percentage of fully hydrogenated DEB (8H-DEB) and greater temperatures.

As previously documented at the start of this chapter, molecular dynamics was the chosen simulation technique to be employed for the melting point envelope as it captures the true nature of liquids as opposed to lattice dynamics. DL_POLY was utilised due to its flexibility with regards to number of atoms and number of processors. DL_POLY 4 works well for systems with 10^3 to 10^9 atoms with more than 100 processors[99] and thus was ideal for the study due to the size of the systems being investigated.

Finally, the same techniques used for the melting point 'envelope' and mixing of hydrogenated and unhydrogenated 1,4-bis(phenylethynyl)benzene were applied to diphenylacetylene (DPA) – a closely related molecule – where the melting point 'envelope' was calculated to be between 350 K and 400 K which was not too dissimilar to literature values. Once again, the mixing of the hydrogenated and unhydrogenated DPA was affected by the concentration of hydrogenated DPA present and the temperature of the system.

7.2 Future Work

In summary this thesis has helped advance our current understanding of the behaviour of hydrogenated organic molecules in the solid state under various temperatures through the use of molecular dynamics. This will allow future research to build on the work presented in this thesis and explore different aspects of the investigation in further detail, for example the mobility of both the hydrogenated and unhydrogenated species in both clusters and

on the surface of the DEB pellets. This could include examining the interface between the unhydrogenated/hydrogenated DEB and the carbon support present in the pellet as well as the interface between the mixture and the metal catalyst. This would show what binding is perhaps occurring and the movement of the DEB as hydrogenation increases. As mentioned in Chapter 5, different stages of hydrogenation could also be incorporated into the system to see how that affects the mixing process. The time of the simulation could also be increased to see its affect on the mobility of the different hydrogenated species of DEB. Other computational techniques that were not utilised during this study, for example density functional theory (DFT) could also be used to explore the hydrogenation mechanism in greater detail, by investigating the fundamental binding energetics of the unhydrogenated/hydrogenated species.

As outlined in Chapter 2, PACKMOL was a useful tool in the packing of the molecules into a system to ensure a random order. As discussed, this is not always a simple task due to the size of the individual molecules however future investigations should use this as a building block on which to study the mixture phase of the species. Perhaps future researchers should consider using larger ‘boxes’ and thus pack more molecules into the system as well as using a variety of different hydrogenated species to create this randomized section.

DL_POLY proved very efficient and reliable in its calculations throughout this thesis and should be considered by future researchers. As mentioned previously, DL_POLY 4 is able to be used on systems up to 10^9 atoms and so future researchers continuing this work should be encouraged

to explore larger systems than those used in this study as this would perhaps allow a calculation utilising all 4 hydrogenation levels of DEB (2H-, 4H-, 6H- and 8H-) to be run and examined.

As demonstrated throughout this thesis, the consistent valence force field (cvff) worked well for the molecules and systems investigated, especially when the Morse potential was used. Future researchers should be encouraged to use this force field when utilising molecular dynamic simulations with similar molecules to those studied in this thesis, as it produced accurate and reliable results when compared to literature. The force fields that were compared against each other in Chapter 3 are not an exhaustive list and future researchers may wish to explore other popular options however they should be cautious of the issues identified. This includes what potentials the force field uses, such as Harmonic or Morse, the type of system that the force field was originally designed for, such as biological or liquid, and most importantly how the force field parameters were derived, such as through experimental or computational methods or a mixture of both.

Bibliography

1 R. Hoffmann, *Am. Sci.*, 1998, **86**, 326.

2 E. K. Rideal, *Obit. Not. Fellows R. Soc.*, 1942, **4**, 63–66.

3 The Nobel Prize in Chemistry 1912, http://www.nobelprize.org/nobel_prizes/chemistry/laureates/1912/index.html, (accessed 11 February 2014).

4 J. Halpern, *J. Organomet. Chem.*, 1980, **200**, 133–144.

5 H. Lindlar and R. Dubuis, *Org. Synth.*, 1966, **46**, 89–93.

6 H. Lindlar, *Helv. Chim. Acta*, 1952, **35**, 446–450.

7 S. Akabori, S. Sakurai, Y. Izumi and Y. Fujii, *Nature*, 1956, **178**, 323–324.

8 P. N. Rylander, *Catalytic hydrogenation over platinum metals*, Academic Press, New York, 1967.

9 Y. Nakamura, *Bull. Chem. Soc. Jpn.*, 1941, **16**, 367–370.

10 J. A. Osborn, F. H. Jardine, J. F. Young and G. Wilkinson, *J. Chem. Soc. A Inorganic, Phys. Theor.*, 1966, 1711–1732.

11 L. Horner, H. Siegel and H. Büthe, *Angew. Chemie Int. Ed. English*, 1968, **7**, 942–942.

12 W. S. Knowles and M. J. Sabacky, *Chem. Commun.*, 1968, 1445–1446.

13 R. Murray, US001628190, 1926.

14 T. Harada and Y. Izumi, *Chem. Lett.*, 1978, **7**, 1195–1196.

15 T. Ohta, H. Takaya and R. Noyori, *Tetrahedron Lett.*, 1990, **31**, 7189–7192.

16 A. Miyashita, A. Yasuda, H. Takaya, K. Toriumi, T. Ito, T. Souchi and R. Noyori, *J. Am. Chem. Soc.*, 1980, **102**, 7932–7934.

17 W. S. Mahoney, D. M. Brestensky and J. M. Stryker, *J. Am. Chem. Soc.*, 1988, **110**, 291–293.

18 N. P. Mankad, D. S. Laitar and J. P. Sadighi, *Organometallics*, 2004, **23**, 3369–3371.

19 R. Crabtree, *Acc. Chem. Res.*, 1979, **12**, 331–337.

20 E. L. Muetterties and J. R. Bleeke, *Acc. Chem. Res.*, 1979, **12**, 324–331.

21 R. Courtney and L. Harrah, *J. Mater. Sci.*, 1977, **12**, 175–186.

22 L. N. Dinh, G. A. Cairns, R. Krueger, B. P. Mayer and R. S. Maxwell, *J. Nucl. Mater.*, 2013, **442**, 298–305.

23 L. N. Dinh, M. A. Schildbach, J. L. Herberg, A. P. Saab, J. C. Weigle, S. C. Chinn, R. S. Maxwell and W. McLean, *J. Nucl. Mater.*, 2008, **382**, 51–63.

24 P. J. Nigrey, *An issue paper on the use of hydrogen getters in transportation packaging*, Albuquerque, NM, and Livermore, CA, 2000.

25 A. Maiti, L. N. Dinh, T. F. Baumann, R. S. Maxwell and A. P. Saab, *Chem. Phys. Lett.*, 2009, **475**, 223–226.

26 M. Balooch, W.-E. Wang and J. D. LeMay, *J. Nucl. Mater.*, 1999, **270**,

248–252.

27 M. B. Ibrahim, B. El Ali, I. Malik and M. Fettouhi, *Tetrahedron Lett.*, 2016, **57**, 554–558.

28 K. Sanechika, T. Yamamoto and A. Yamamoto, *Bull. Chem. Soc. Jpn.*, 1984, **57**, 752–755.

29 I. Pri-Bar, S. Pevzner and J. E. Koresh, *J. Mol. Catal. A Chem.*, 2006, **247**, 103–107.

30 R. V. Chaudharl, R. Jaganathan, D. S. Kolhe, G. Emlg and H. Hofmann, *Ind. Eng. Chem. Prod. Res. Dev.*, 1986, **25**, 375–379.

31 I. Pri-Bar and J. E. Koresh, *J. Mol. Catal. A Chem.*, 2003, **206**, 313–318.

32 I. Pri-Bar and J. E. Koresh, *J. Mol. Catal. A Chem.*, 2000, **156**, 173–180.

33 J. J. Stephan, P. L. Franke and V. Ponec, 1976, **365**, 359–365.

34 T. Matsushima, *J. Phys. Chem.*, 1987, **91**, 6192–6197.

35 P. Albers, J. Pietsch and S. F. Parker, *J. Mol. Catal. A Chem.*, 2001, **173**, 275–286.

36 T. Yamada, T. Onishi and K. Tamaru, *Surf. Sci.*, 1983, **133**, 533–546.

37 A. Maiti, R. Gee, R. Maxwell and A. Saab, *J. Phys. Chem. B*, 2006, **110**, 3499–503.

38 H. Sun, *J. Phys. Chem. B*, 1998, **102**, 7338–7364.

39 H. N. Sharma, E. A. Sangalang, C. K. Saw, G. A. Cairns, W. McLean, R. S. Maxwell and L. N. Dinh, *J. Chem. Phys.*, 2017, **147**, 194701.

40 D. Frenkel and B. Smit, in *Understanding Molecular Simulation*, Elsevier, 2002, pp. 63–107.

41 R. Scott, M. P. Allen and D. J. Tildesley, *Math. Comput.*, 1991, **57**, 442.

42 G. H. Grant and W. G. Richards, *Computational Chemistry*, Oxford University Press, 1996.

43 P. Atkins and J. De Paula, *Atkins' Physical Chemistry 9th Edition*, Oxford University Press, 2009.

44 L. Verlet, *Phys. Rev.*, 1967, **159**, 98–103.

45 R. W. Hockney, in *Methods in Computational Physics, Vol. 9*, 1970.

46 H. J. C. Berendsen, J. P. M. Postma, W. F. van Gunsteren, A. DiNola and J. R. Haak, *J. Chem. Phys.*, 1984, **81**, 3684–3690.

47 D. J. Evans and B. L. Holian, *J. Chem. Phys.*, 1985, **83**, 4069–4074.

48 M. Parrinello and A. Rahman, *Phys. Rev. Lett.*, 1980, **45**, 1196–1199.

49 P. M. Morse, *Phys. Rev.*, 1929, **34**, 57–64.

50 J. N. Canongia Lopes and A. A. H. Pádua, *Theor. Chem. Acc.*, 2012, **131**, 1129.

51 J. E. Jones, *Proc. R. Soc. A Math. Phys. Eng. Sci.*, 1924, **106**, 441–462.

52 R. A. Buckingham, *Proc. R. Soc. A Math. Phys. Eng. Sci.*, 1938, **168**, 264–283.

53 Periodic Boundary Conditions, http://isaacs.sourceforge.net/phys/pbc.html, (accessed 19 August 2018).

54 W. Smith and T. R. Forester, *J. Mol. Graph.*, 1996, **14**, 136–141.

55 I. T. Todorov, W. Smith, K. Trachenko and M. T. Dove, *J. Mater. Chem.*, 2006, **16**, 1911.

56 I. J. Bush, I. T. Todorov and W. Smith, *Comput. Phys. Commun.*, 2006, **175**, 323–329.

57 L. Martínez, R. Andrade, E. G. Birgin and J. M. Martínez, *J. Comput. Chem.*, 2009, **30**, 2157–2164.

58 M. J. Martinez and L. Martinez, *J. Comput. Chem.*, 2003, **24**, 819–825.

59 C. W. Yong, *J. Chem. Inf. Model.*, 2016, **56**, 1405–1409.

60 H. Li, D. R. Powell, T. K. Firman and R. West, *Macromolecules*, 1998, **31**, 1093–1098.

61 CVFF forcefield file in new format, converted from original format file shipped with Discover 2.6.0/InsightII 1.1.0/Insight 2.6, September 1990, Biosym Technologies Inc.

62 S. L. Mayo, B. D. Olafson and W. A. Goddard III, 1990, **101**, 8897–8909.

63 W. L. Jorgensen and J. Tirado-rives, *J. Am. Chem. Soc.*, 1988, **110**, 1657–1666.

64 J. Wang, R. M. Wolf, J. W. Caldwell, P. A. Kollman and D. A. Case, *J. Comput. Chem.*, 2004, **25**, 1157–74.

65 J. D. Gale, *J. Chem. Soc. Faraday Trans.*, 1997, **93**, 629–637.

66 J. D. Gale, *Philos. Mag. B*, 1996, **73**, 3–19.

67 J. D. Gale and A. L. Rohl, *Mol. Simul.*, 2003, **29**, 291–341.

68 J. D. Gale, *Zeitschrift für Krist. - Cryst. Mater.*, 2005, **220**, 552–554.

69 J. D. Gale and A. L. Rohl, *Mol. Simul.*, 2007, **33**, 1237–1246.

70 E. R. Cope and M. T. Dove, *J. Appl. Crystallogr.*, 2007, **40**, 589–594.

71 J. D. Gale, P. Raiteri and A. C. T. van Duin, *Phys. Chem. Chem. Phys.*, 2011, **13**, 16666–16679.

72 A. Tkatchenko and M. Scheffler, *Phys. Rev. Lett.*, 2009, **102**, 073005.

73 S. Grimme, *J. Comput. Chem.*, 2004, **25**, 1463–73.

74 S. C. Parker, N. H. de Leeuw, E. Bourova and D. J. Cooke, *Rev. Mineral. Geochemistry*, 2001, **42**, 63–82.

75 J. Wang, W. Wang, P. A. Kollman and D. A. Case, *J. Chem. Inf. Comput. Sci.*, 2001, **222**, U403.

76 R. Thomas, S. Varghese and G. U. Kulkarni, *J. Mater. Chem.*, 2009, **19**, 4401.

77 M. J. McQuaid and B. M. Rice, *Computational Chemistry-Based Enthalpy-of-Formation , Predictions for Azide-Functionalized Compounds*, 2006.

78 J. Nyman, O. S. Pundyke and G. M. Day, *Phys. Chem. Chem. Phys.*, , DOI:10.1039/c6cp02261h.

79 K. Dziubek, M. Podsiadło and A. Katrusiak, *J. Am. Chem. Soc.*, 2007, **129**, 12620–12621.

80 W. V. Steele, R. D. Chirico, S. E. Knipmeyer and a. Nguyen, *J. Chem. Eng. Data*, 2002, **47**, 689–699.

81 S. W. Watt, C. Dai, A. J. Scott, J. M. Burke, R. L. Thomas, J. C. Collings, C. Viney, W. Clegg and T. B. Marder, *Angew. Chemie - Int. Ed.*, 2004, **43**, 3061–3063.

82 P. M. Agrawal, B. M. Rice and D. L. Thompson, *J. Chem. Phys.*, 2003, **118**, 9680–9688.

83 Y. Zhang and E. J. Maginn, *J. Chem. Phys.*, , DOI:10.1063/1.3702587.

84 A. Aesar, 1,4-Bis(phenylethynyl)benzene, 97%, Thermo Scientific™, https://www.fishersci.com/shop/products/1-4-bis-phenylethynyl-benzene-97-3/aah3039506, (accessed 20 January 2016).

85 C. Synthesis, 1,4-bis(phenylethynyl)benzene CAS 1849-27-0, http://www.chemsynthesis.com/base/chemical-structure-33906.html, (accessed 12 April 2018).

86 S. Alavi and D. L. Thompson, *Mol. Simul.*, 2006, **32**, 999–1015.

87 A. Siavosh-Haghighi and D. L. Thompson, *J. Chem. Phys.*, 2006, **125**, 184711.

88 P. Nalakarn, P. Boonnoy, N. Nisoh, M. Karttunen and J. Wong-ekkabut, *Sci. Rep.*, 2019, **9**, 1037.

89 J. Ding, E. Ma, M. Asta and R. O. Ritchie, *Sci. Rep.*, 2015, **5**, 17429.

90 P. Gill, T. T. Moghadam and B. Ranjbar, *J. Biomol. Tech.*, 2010, **21**, 167–93.

91 Mark Stone, Michael Benson, Christopher Orme, Thomas Luther and Eric Peterson, *Improved Hydrogen Gas Getters for TRU Waste -- Final*

Report, 2005.

92 E. S. Tkachenko, R. M. Varushchenko, A. I. Druzhinina, M. D. Reshetova and N. E. Borisova, *J. Chem. Eng. Data*, 2011, **56**, 4700–4709.

93 J. M. Robertson and I. Woodward, *Proc. R. Soc. A Math. Phys. Eng. Sci.*, 1938, **164**, 436–446.

94 R. Thomas, S. Lakshmi, S. K. Pati and G. U. Kulkarni, *J. Phys. Chem. B*, 2006, **110**, 24674–24677.

95 A. C. Cope, D. S. Smith, R. J. Cotter, C. C. Price, T. F. Mckeon, T. F. Mckeon Jr. and T. F. Mckeon, *Org. Synth.*, 1954, **34**, 42.

96 L. I. Smith and M. M. Falkof, *Org. Synth.*, 1942, **22**, 50.

97 R. Thomas, S. Lakshmi, S. K. Pati and G. U. Kulkarni, *J. Phys. Chem. B*, 2006, **110**, 24674–24677.

98 S. V. R. Mastrangelo and R. W. Dornte, *J. Am. Chem. Soc.*, 1955, **77**, 6200–6201.

99 I. T. Todorov, W. Smith and U. K. Cheshire, *DL_POLY_4 User Manual.*, 2006.

Appendix A

cvff (Harmonic)

Atom Types and Charges:

Atom Label	Atom Type	Charge
C1	cp	-0.100
C2	cp	0.085
C3	ct	-0.085
C4	cp	0.028
C5	c2	-0.050
C6	c2	-0.200
C7	c3	-0.300
O	o	-0.178
H	h	0.100

Bond Potentials:

Atom Number 1	Atom Number 2	K2 (kcal $Å^{-2}$)	r0 (Å)
C1 Core	H Core	726.8328	1.0800
C1 Core	C1 Core	960.000	1.3400
C1 Core	C2 Core	960.000	1.3400
C2 Core	C3 Core	702.5054	1.4720
C3 Core	C3 Core	----------	----------

C4 Core	O Core	800.0000	1.3700
C5 Core	O Core	800.0000	1.3700
C5 Core	H Core	681.2350	1.1050
C6 Core	H Core	681.2350	1.1050
C7 Core	H Core	681.2350	1.1050
C1 Core	C4 Core	960.000	1.3400
C2 Core	C4 Core	960.000	1.3400
C5 Core	C6 Core	645.4316	1.5260
C6 Core	C7 Core	645.4316	1.5260

Three-Body Bond Potentials:

Atom Number 1	Atom Number 2	Atom Number 3	k (kcal rad^{-2})	theta0 (°)
C1 Core	C1 Core	H Core	74.0000	120.0000
C1 Core	C1 Core	C2 Core	180.0000	120.0000
C2 Core	C1 Core	C3 Core	69.3598	120.0000
C1 Core	C2 Core	H Core	74.0000	120.0000
C2 Core	C1 Core	C1 Core	180.0000	120.0000
C1 Core	C1 Core	C1 Core	180.0000	120.0000
C1 Core	C4 Core	H Core	74.0000	120.0000
C1 Core	C2 Core	C4 Core	180.0000	120.0000
C2 Core	C3 Core	C4 Core	69.3598	120.0000
O Core	C4 Core	C5 Core	100.0000	109.5000
C4 Core	O Core	C1 Core	120.0000	120.0000
C4 Core	C1 Core	C2 Core	180.0000	120.0000

C5 Core	O Core	H Core	104.0000	109.5000
C5 Core	C6 Core	H Core	88.80000	110.0000
C6 Core	C5 Core	C7 Core	93.2000	110.5000
C6 Core	C5 Core	H Core	88.80000	110.0000
C6 Core	C7 Core	H Core	88.80000	110.0000

Torsion Bond Potentials:

Atom Number 1	Atom Number 2	Atom Number 3	Atom Number 4	k (kcal)	n	phi0 (°)
C3 Core	C2 Core	C1 Core	H Core	12.00	+ 2.00	0.00

Lennard-Jones Parameters:

Atom	A (kcal Å^{12})	B (kcal Å^{6})
C1	2968753.3590	1325.70810
C2	2968753.3590	1325.70810
C3	2968753.3590	1325.70810
C4	2968753.3590	1325.70810
C5	1790340.7240	528.48190
C6	1790340.7240	528.48190
C7	1790340.7240	528.48190
H	7108.4660	32.87076
O	272894.7846	498.87880

cvff (Morse)

Atom Types and Charges:

Atom Label	Atom Type	Charge
C1	cp	-0.100
C2	cp	0.085
C3	ct	-0.085
C4	cp	0.028
C5	c2	-0.050
C6	c2	-0.200
C7	c3	-0.300
O	o	-0.178
H	h	0.100

Bond Potentials:

Atom Number 1	Atom Number 2	De (kcal)	a ($Å^{-1}$)	r0 (Å)
C1 Core	H Core	116.0000	1.7700	1.0800
C1 Core	C1 Core	120.0000	2.0000	1.3400
C1 Core	C2 Core	120.0000	2.0000	1.3400
C2 Core	C3 Core	80.4179	2.0000	1.4720
C3 Core	C3 Core	200.0000	2.0000	1.2040
C4 Core	O Core	68.3000	2.0000	1.3700
C5 Core	O Core	68.3000	2.0000	1.3700

C5 Core	H Core	108.6000	1.7710	1.1050
C6 Core	H Core	108.6000	1.7710	1.1050
C7 Core	H Core	108.6000	1.7710	1.1050
C1 Core	C4 Core	76.0000	1.9300	1.3400
C2 Core	C4 Core	120.000	2.0000	1.3400
C5 Core	C6 Core	88.0000	1.9150	1.5260
C6 Core	C7 Core	88.0000	1.9150	1.5260

Three-Body Bond Potentials:

Atom Number 1	Atom Number 2	Atom Number 3	k (kcal rad^{-2})	theta0 (°)
C1 Core	C1 Core	H Core	74.0000	120.0000
C1 Core	C1 Core	C2 Core	180.0000	120.0000
C2 Core	C1 Core	C3 Core	69.3598	120.0000
C1 Core	C2 Core	H Core	74.0000	120.0000
C2 Core	C1 Core	C1 Core	180.0000	120.0000
C1 Core	C1 Core	C1 Core	180.0000	120.0000
C1 Core	C4 Core	H Core	74.0000	120.0000
C1 Core	C2 Core	C4 Core	180.0000	120.0000
C2 Core	C3 Core	C4 Core	69.3598	120.0000
O Core	C4 Core	C5 Core	100.0000	109.5000
C4 Core	O Core	C1 Core	120.0000	120.0000
C4 Core	C1 Core	C2 Core	180.0000	120.0000
C5 Core	O Core	H Core	104.0000	109.5000
C5 Core	C6 Core	H Core	88.80000	110.0000
C6 Core	C5 Core	C7 Core	93.2000	110.5000

C6 Core	C5 Core	H Core	88.80000	110.0000
C6 Core	C7 Core	H Core	88.80000	110.0000

Torsion Bond Potentials:

Atom Number 1	Atom Number 2	Atom Number 3	Atom Number 4	k (kcal)	n	phi0 (°)
C3 Core	C2 Core	C1 Core	H Core	12.00	+ 2.00	0.00

Lennard-Jones Parameters:

Atom	A (kcal $Å^{12}$)	B (kcal $Å^{6}$)
C1	2968753.3590	1325.70810
C2	2968753.3590	1325.70810
C3	2968753.3590	1325.70810
C4	2968753.3590	1325.70810
C5	1790340.7240	528.48190
C6	1790340.7240	528.48190
C7	1790340.7240	528.48190
H	7108.4660	32.87076
O	272894.7846	498.87880

Dreiding

Atom Types and Charges:

		Charge	
Atom Label	**Atom Type**	**DEB**	**2,5-diproproxyDEB**
C1	C_R	0.0981	- 0.0971
C2	C_R	0.0355	0.0355
C3	C_1	- 0.0365	- 0.0365
C4	C_R	----------	- 0.1040
C5	C_3	----------	0.0000
C6	C_3	----------	0.0000
C7	C_3	----------	0.0000
O	O_R	----------	0.0000
H	H_	0.0984	0.0452

Bond Potentials:

Atom Number 1	**Atom Number 2**	**K2 (kcal Å^{-2})**	**r0 (Å)**
C1 Core	H Core	700.0000	1.0200
C1 Core	C1 Core	1050.000	1.3900
C1 Core	C2 Core	1050.000	1.3900
C2 Core	C3 Core	700.0000	1.2920
C3 Core	C3 Core	2100.000	1.1940
C4 Core	O Core	1050.0000	1.3500
C5 Core	O Core	700.0000	1.4200

C5 Core	H Core	700.0000	1.0900
C6 Core	H Core	700.0000	1.0900
C7 Core	H Core	700.0000	1.0900
C1 Core	C4 Core	1050.0000	1.3900
C2 Core	C4 Core	1050.0000	1.3900
C5 Core	C6 Core	700.0000	1.5300
C6 Core	C7 Core	700.0000	1.5300

Three-body Bond Potentials:

Atom Number 1	Atom Number 2	Atom Number 3	k (kcal rad^{-2})	theta0 (°)
C1 Core	C1 Core	H Core	100.0000	120.0000
C1 Core	C1 Core	C2 Core	100.0000	120.0000
C2 Core	C1 Core	C3 Core	100.0000	120.0000
C1 Core	C2 Core	H Core	100.0000	120.0000
C2 Core	C1 Core	C1 Core	100.0000	120.0000
C1 Core	C1 Core	C1 Core	100.0000	120.0000
C1 Core	C4 Core	H Core	100.0000	120.0000
C1 Core	C2 Core	C4 Core	100.0000	120.0000
C2 Core	C3 Core	C4 Core	100.0000	120.0000
O Core	C4 Core	C5 Core	100.0000	120.0000
C4 Core	O Core	C1 Core	100.0000	120.0000
C4 Core	C1 Core	C2 Core	100.0000	120.0000
C5 Core	O Core	H Core	100.0000	109.4710
C5 Core	C6 Core	H Core	100.0000	109.4710
C6 Core	C5 Core	C7 Core	100.0000	109.4710

C6 Core	C5 Core	H Core	100.0000	109.4710
C6 Core	C7 Core	H Core	100.0000	109.4710

Torsion Bond Potentials:

Atom Number 1	Atom Number 2	Atom Number 3	Atom Number 4	k (kcal)	n	phi0 (°)
C3 Core	C2 Core	C1 Core	H Core	12.50	- 2.00	0.00

Lennard-Jones Parameters:

Atom	ε (kcal mol^{-1})	σ (Å)
C1	0.0951	3.8983
C2	0.0951	3.8983
C3	0.0951	3.8983
C4	0.0951	3.8983
C5	0.0951	3.8983
C6	0.0951	3.8983
C7	0.0951	3.8983
H	0.0152	3.1950
O	0.0957	3.4046

OPLS

Atom Types and Charges:

Atom Label	Atom Type	Charge
C1	CA	-0.1150
C2	CA	0.3950
C3	CZ	-0.3950
C4	CA	-0.1150
C5	CT	0.1400
C6	CT	-0.1200
C7	CT	-0.1800
O	OS	-0.4000
H	HA/HC	0.1150

Bond Potentials:

Atom Number 1	Atom Number 2	K2 (kcal $Å^{-2}$)	r0 (Å)
C1 Core	H Core	734.0000	1.0800
C1 Core	C1 Core	938.0000	1.4000
C1 Core	C2 Core	938.0000	1.4000
C2 Core	C3 Core	800.0000	1.4510
C3 Core	C3 Core	2300.000	1.2100
C4 Core	O Core	900.0000	1.3640
C5 Core	O Core	640.0000	1.4250
C5 Core	H Core	680.0000	1.0900
C6 Core	H Core	680.0000	1.0900
C7 Core	H Core	680.0000	1.0900

C1 Core	C4 Core	938.0000	1.4000
C2 Core	C4 Core	938.0000	1.4000
C5 Core	C6 Core	520.0000	1.5260
C6 Core	C7 Core	520.0000	1.5260

Three-Body Bond Potentials:

Atom Number 1	Atom Number 2	Atom Number 3	k (kcal rad^{-2})	theta0 (°)
C1 Core	C1 Core	H Core	70.0000	120.0000
C1 Core	C1 Core	C2 Core	126.0000	120.0000
C2 Core	C1 Core	C3 Core	140.0000	120.0000
C1 Core	C2 Core	H Core	70.0000	120.0000
C2 Core	C1 Core	C1 Core	126.0000	120.0000
C1 Core	C1 Core	C1 Core	126.0000	120.0000
C1 Core	C4 Core	H Core	70.0000	120.0000
C1 Core	C2 Core	C4 Core	126.0000	120.0000
C2 Core	C3 Core	C4 Core	140.0000	120.0000
O Core	C4 Core	C5 Core	150.0000	111.0000
C4 Core	O Core	C1 Core	140.0000	120.0000
C4 Core	C1 Core	C2 Core	126.0000	120.0000
C5 Core	O Core	H Core	70.0000	109.5000
C5 Core	C6 Core	H Core	75.0000	110.7000
C6 Core	C5 Core	C7 Core	116.7000	112.7000
C6 Core	C5 Core	H Core	75.0000	110.7000
C6 Core	C7 Core	H Core	75.0000	110.7000

Torsion Bond Potentials:

Atom Number 1	Atom Number 2	Atom Number 3	Atom Number 4	k (kcal)	n	phi0 (°)
C3 Core	C2 Core	C1 Core	H Core	7.25	- 2.00	0.00

Lennard-Jones Parameters:

Atom	ε (kcal mol^{-1})	σ (Å)
C1	0.0700	3.5500
C2	0.0700	3.5500
C3	0.1500	3.6500
C4	0.0700	3.5500
C5	0.0660	3.5000
C6	0.0660	3.5000
C7	0.0660	3.5000
H	0.0300	2.4200
O	0.1700	3.000

AMBER (GAFF)

Atom Types and Charges:

		Charge	
Atom Label	**Atom Type**	**DEB**	**2,5-diproproxyDEB**
C1	CA	-0.1168571429	- 0.1273
C2	CA	0.0250	0.0345
C3	C1	- 0.1015	- 0.0925
C4	CA	----------	0.1191
C5	C3	----------	0.1264
C6	C3	----------	- 0.0864
C7	C3	----------	- 0.0941
O	O_R	----------	- 0.3199
H	HA/H1	0.1380	0.0874

Bond Potentials:

Atom Number 1	**Atom Number 2**	**K2 (kcal Å^{-2})**	**r0 (Å)**
C1 Core	H Core	688.6000	1.0870
C1 Core	C1 Core	956.800	1.3870
C1 Core	C2 Core	956.800	1.3870
C2 Core	C3 Core	813.2000	1.4380
C3 Core	C3 Core	1899.000	1.1910
C4 Core	O Core	744.8000	1.3730
C5 Core	O Core	603.0000	1.4390
C5 Core	H Core	671.8000	1.0930

C6 Core	H Core	674.6000	1.0920
C7 Core	H Core	674.6000	1.0920
C1 Core	C4 Core	956.8000	1.3870
C2 Core	C4 Core	956.8000	1.3870
C5 Core	C6 Core	606.2000	1.5350
C6 Core	C7 Core	606.2000	1.5350

Three-Body Bond Potentials:

Atom Number 1	Atom Number 2	Atom Number 3	k (kcal rad^{-2})	theta0 (°)
C1 Core	C1 Core	H Core	48.4600	120.0100
C1 Core	C1 Core	C2 Core	67.1800	119.9700
C2 Core	C1 Core	C3 Core	65.9000	120.0500
C1 Core	C2 Core	H Core	48.4600	120.0100
C2 Core	C1 Core	C1 Core	67.1800	119.9700
C1 Core	C1 Core	C1 Core	67.1800	119.9700
C1 Core	C4 Core	H Core	48.4600	120.0100
C1 Core	C2 Core	C4 Core	67.1800	119.9700
C2 Core	C3 Core	C4 Core	63.8400	120.6300
O Core	C4 Core	C5 Core	62.2700	117.9700
C4 Core	O Core	C1 Core	69.7900	119.2000
C4 Core	C1 Core	C2 Core	67.1800	119.9700
C5 Core	O Core	H Core	46.3600	110.0700
C5 Core	C6 Core	H Core	63.2100	110.6300
C6 Core	C5 Core	C7 Core	46.3700	110.0500
C6 Core	C5 Core	H Core	46.3700	110.0500

C6 Core	C7 Core	H Core	46.3700	110.0500

Torsion Bond Potentials:

Atom Number 1	Atom Number 2	Atom Number 3	Atom Number 4	k (kcal)	n	phi0 (°)
C3 Core	C2 Core	C1 Core	H Core	14.50	+ 2.00	180.00

Lennard-Jones Parameters:

Atom	ε (kcal mol^{-1})	σ (Å)
C1	0.0860	3.8160
C2	0.0860	3.8160
C3	0.2100	3.8160
C4	0.0860	3.8160
C5	0.1094	3.8160
C6	0.1094	3.8160
C7	0.1094	3.8160
H	0.0150	2.9180
O	0.1700	3.3674

Appendix B

RDFs for 0H:8H Mixtures

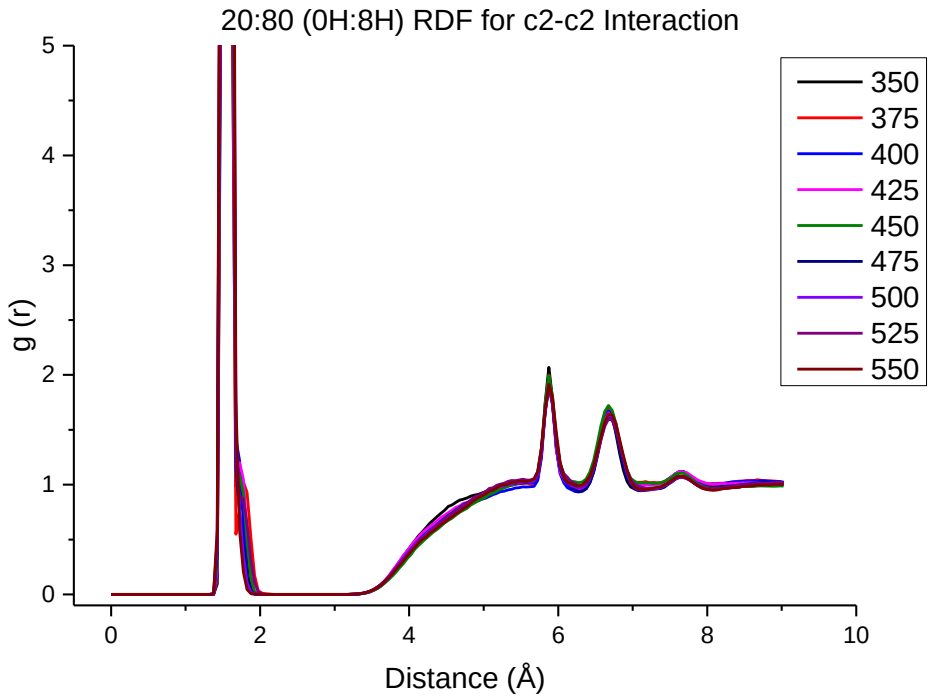

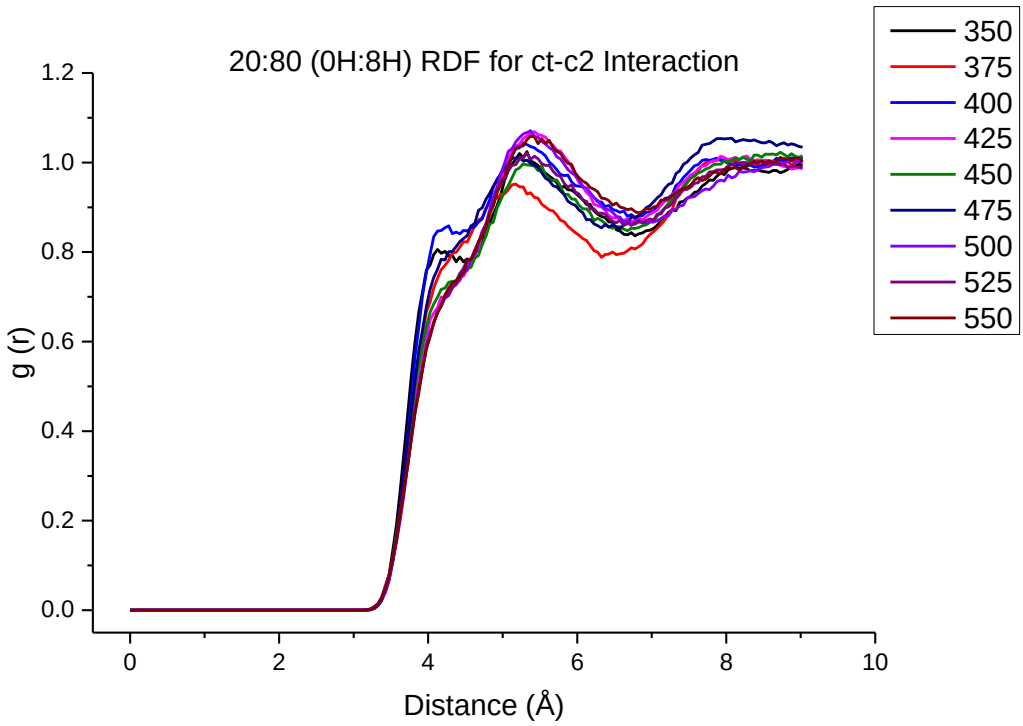

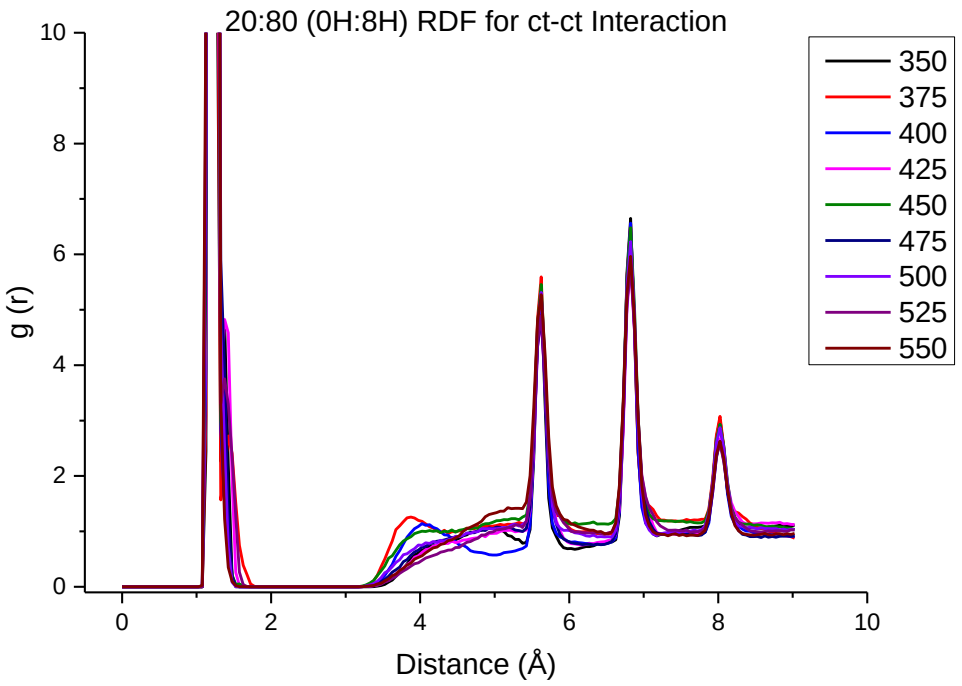
20:80 (0H:8H) RDF for ct-ct Interaction
g (r)
Distance (Å)
350
375
400
425
450
475
500
525
550

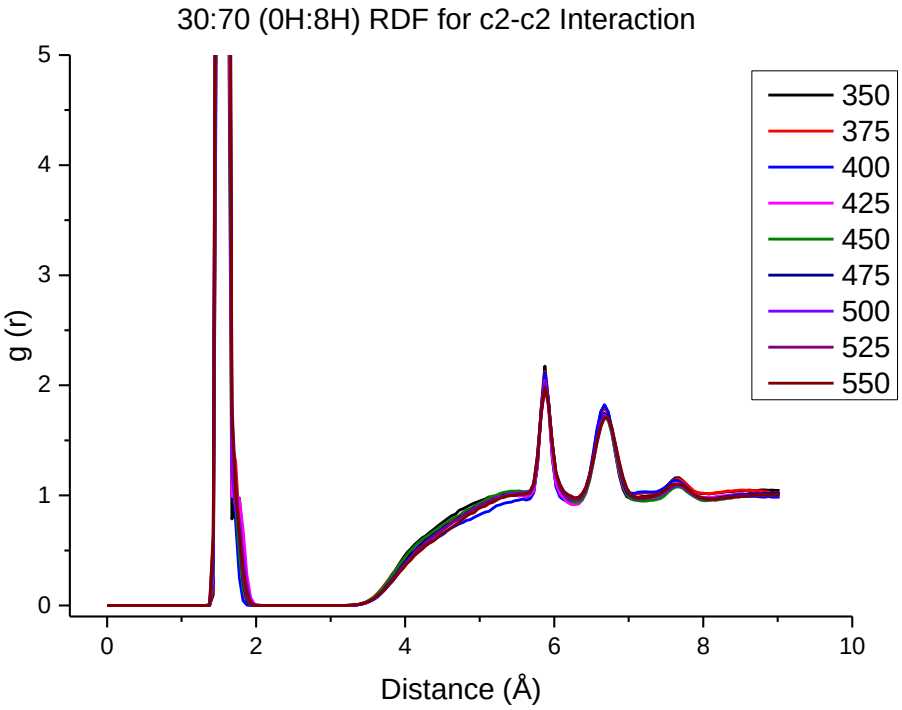
30:70 (0H:8H) RDF for c2-c2 Interaction
g (r)
Distance (Å)
350
375
400
425
450
475
500
525
550

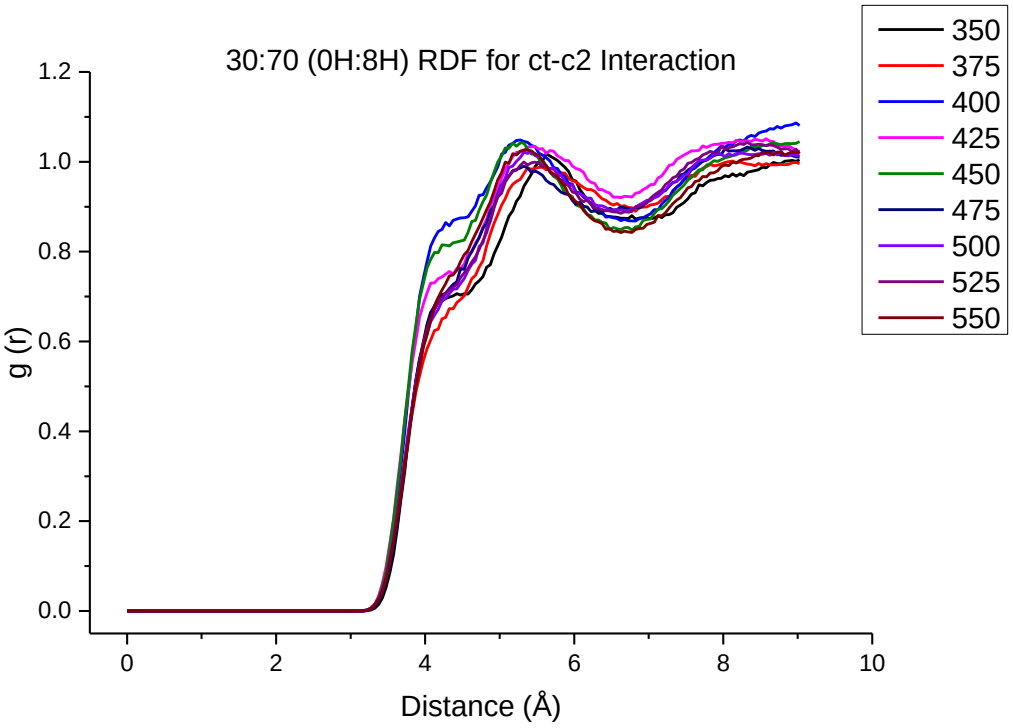
30:70 (0H:8H) RDF for ct-c2 Interaction
g (r)
Distance (Å)
350
375
400
425
450
475
500
525
550

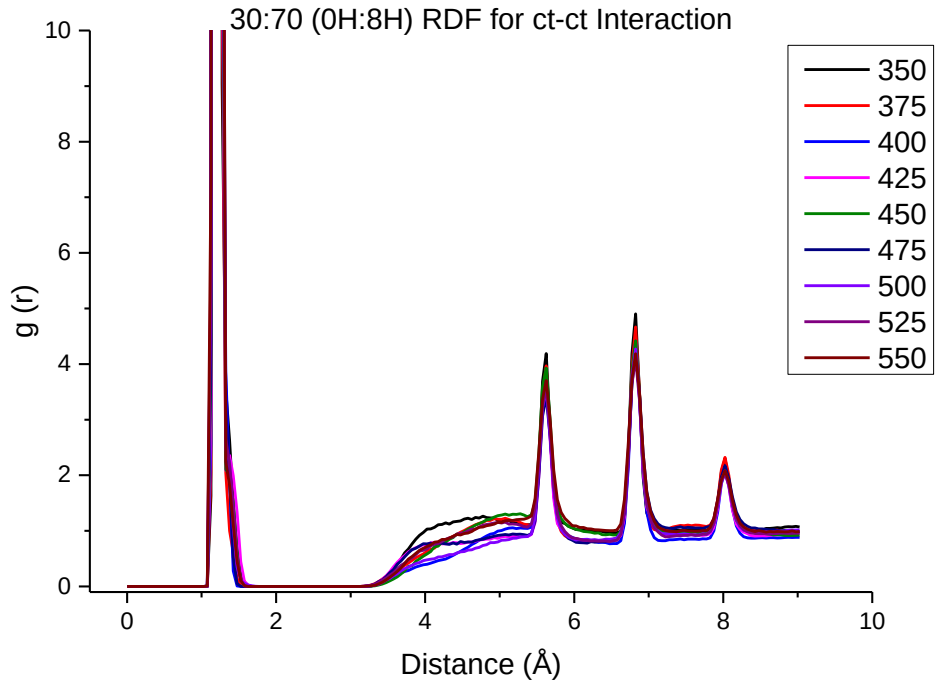
30:70 (0H:8H) RDF for ct-ct Interaction
g (r)
Distance (Å)
350
375
400
425
450
475
500
525
550

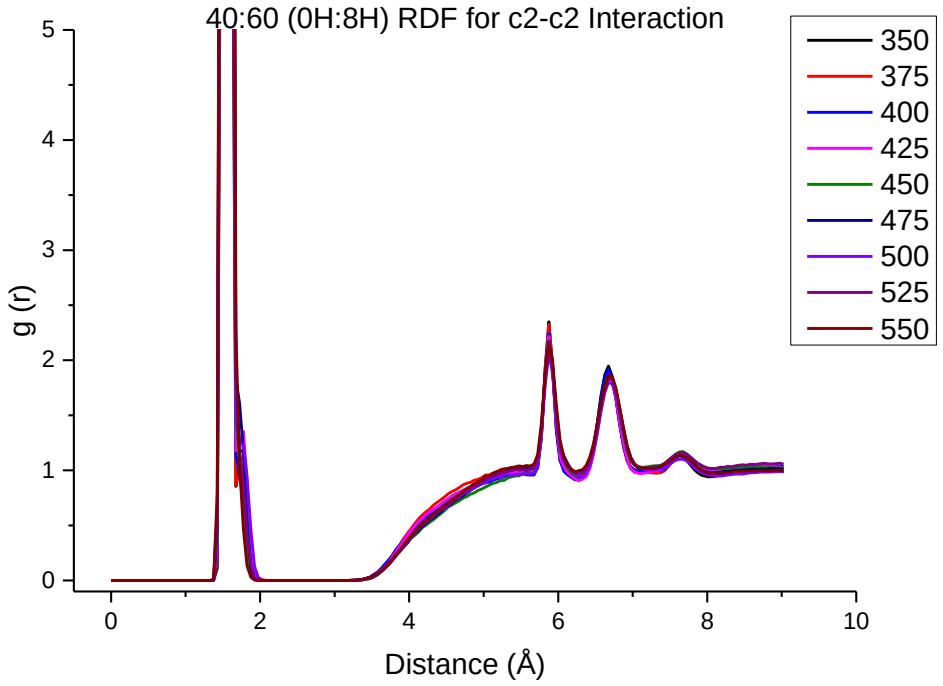
40:60 (0H:8H) RDF for c2-c2 Interaction
g (r)
Distance (Å)
350
375
400
425
450
475
500
525
550

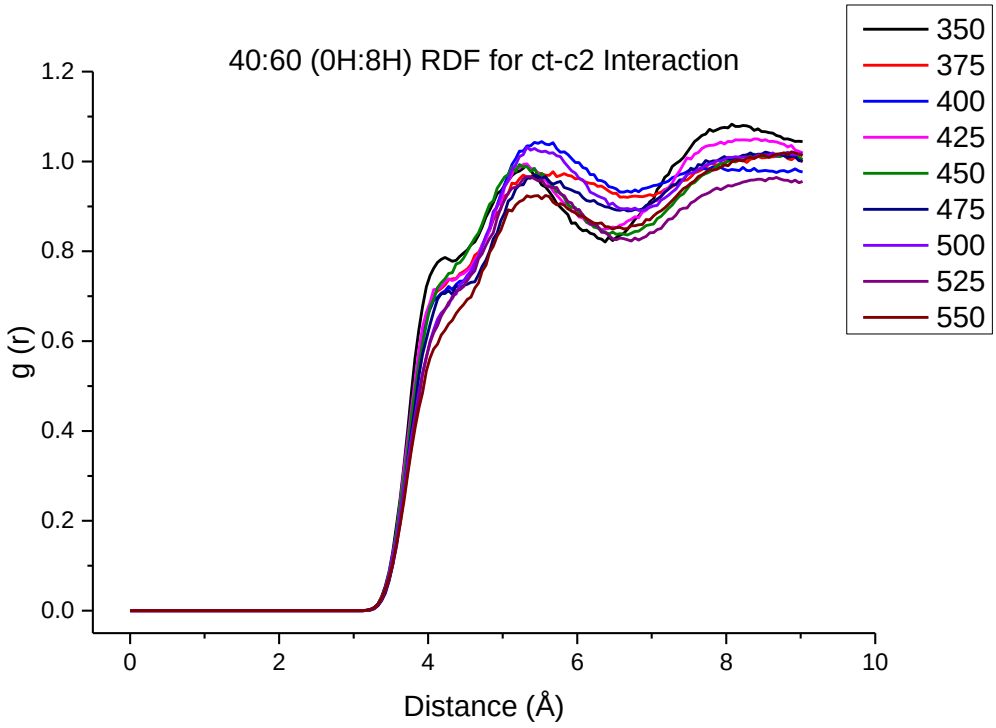
40:60 (0H:8H) RDF for ct-c2 Interaction
g (r)
Distance (Å)
350
375
400
425
450
475
500
525
550

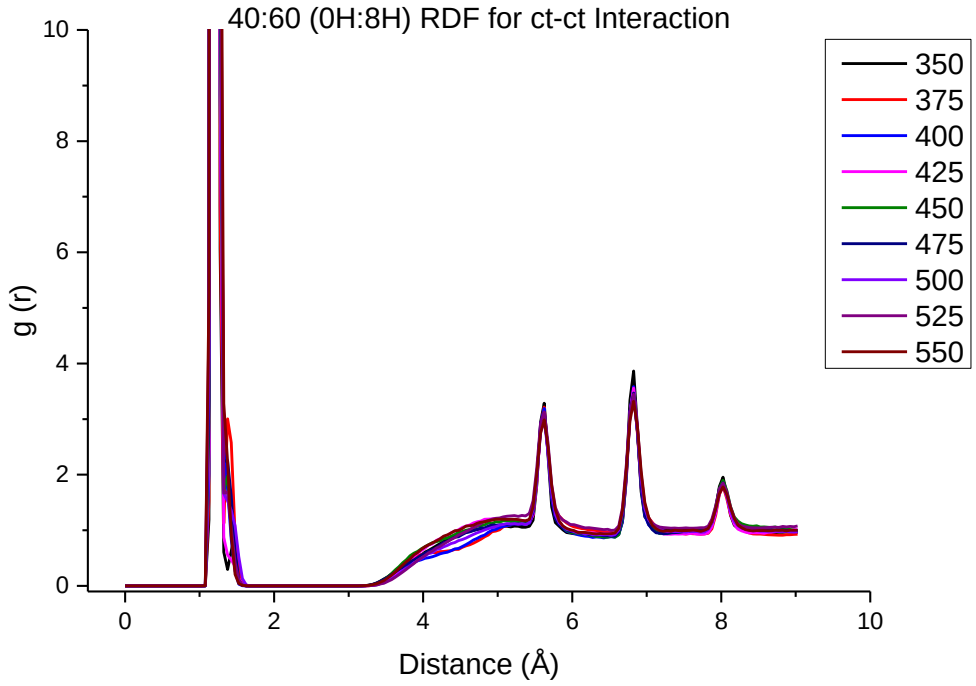
40:60 (0H:8H) RDF for ct-ct Interaction
g (r)
Distance (Å)
350
375
400
425
450
475
500
525
550

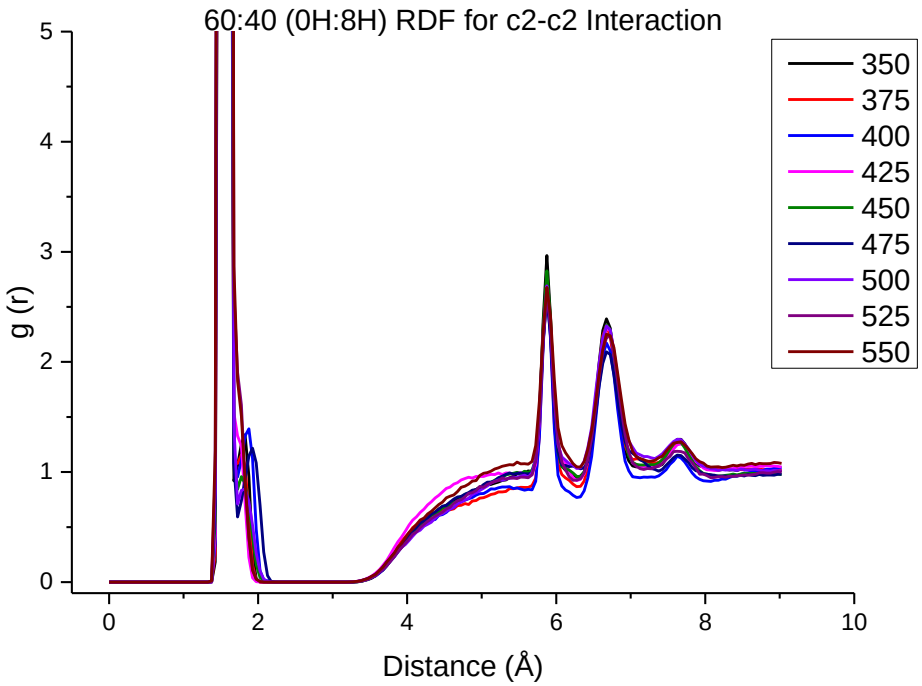
60:40 (0H:8H) RDF for c2-c2 Interaction
g (r)
Distance (Å)
350
375
400
425
450
475
500
525
550

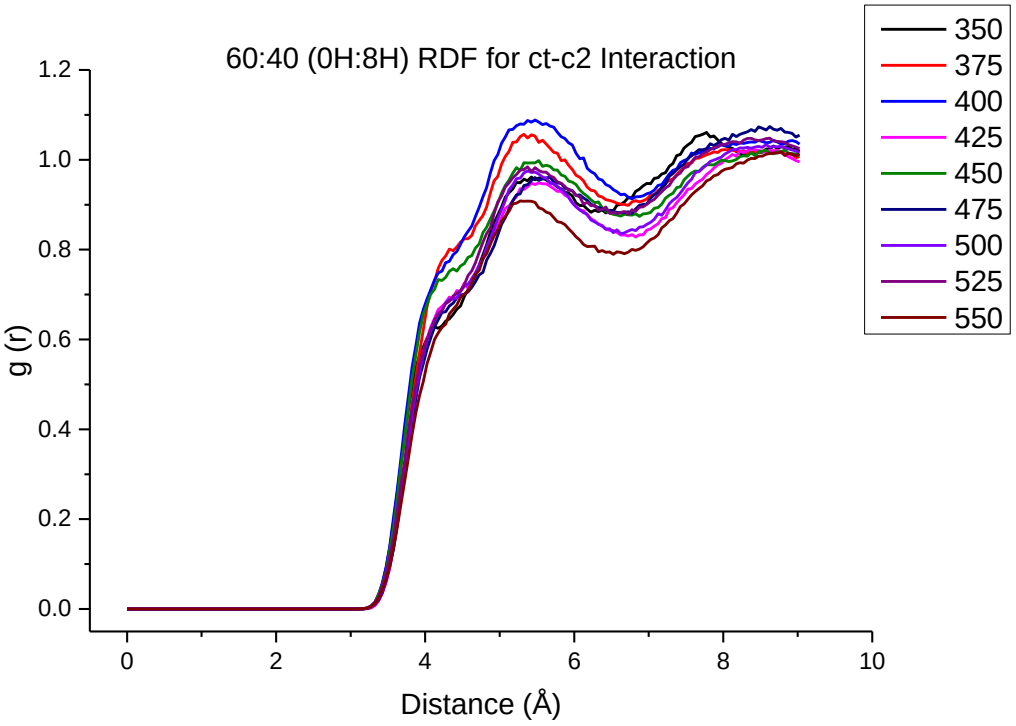
60:40 (0H:8H) RDF for ct-c2 Interaction
g (r)
Distance (Å)
350
375
400
425
450
475
500
525
550

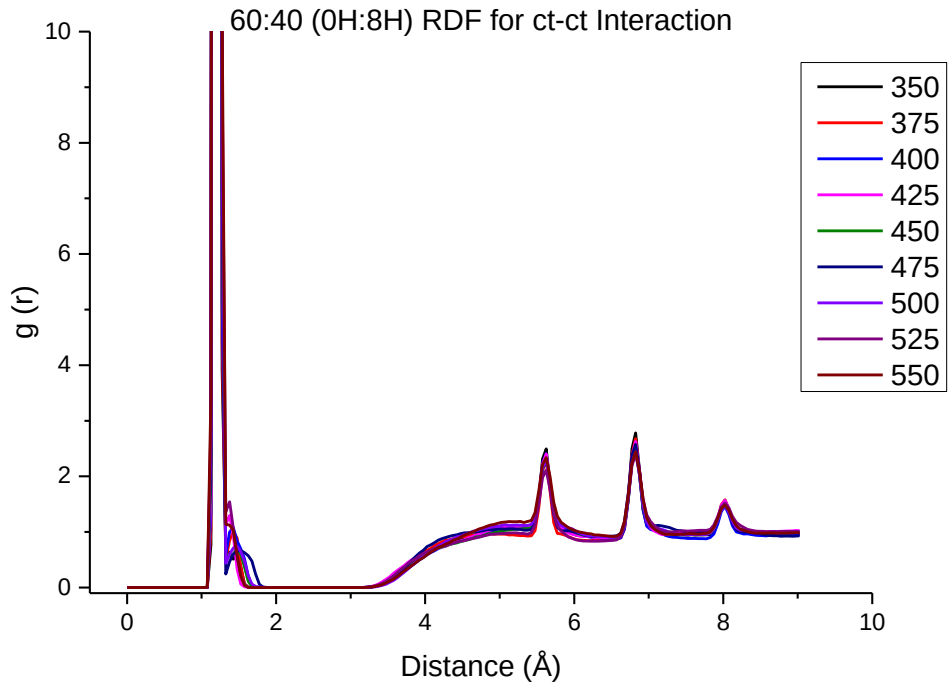
60:40 (0H:8H) RDF for ct-ct Interaction
g (r)
Distance (Å)
350
375
400
425
450
475
500
525
550

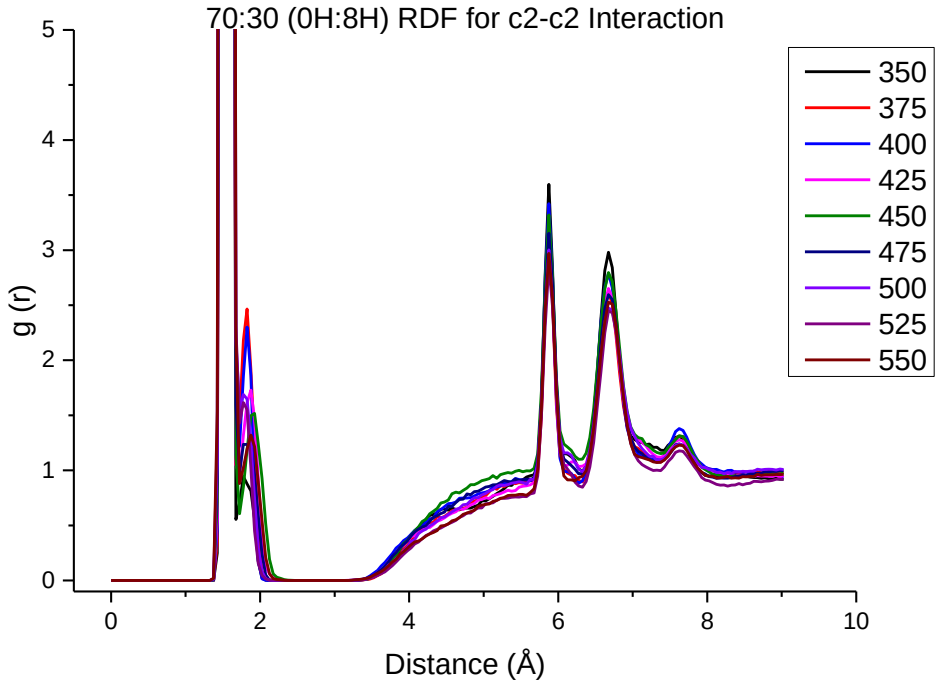
70:30 (0H:8H) RDF for c2-c2 Interaction
g (r)
Distance (Å)
350
375
400
425
450
475
500
525
550

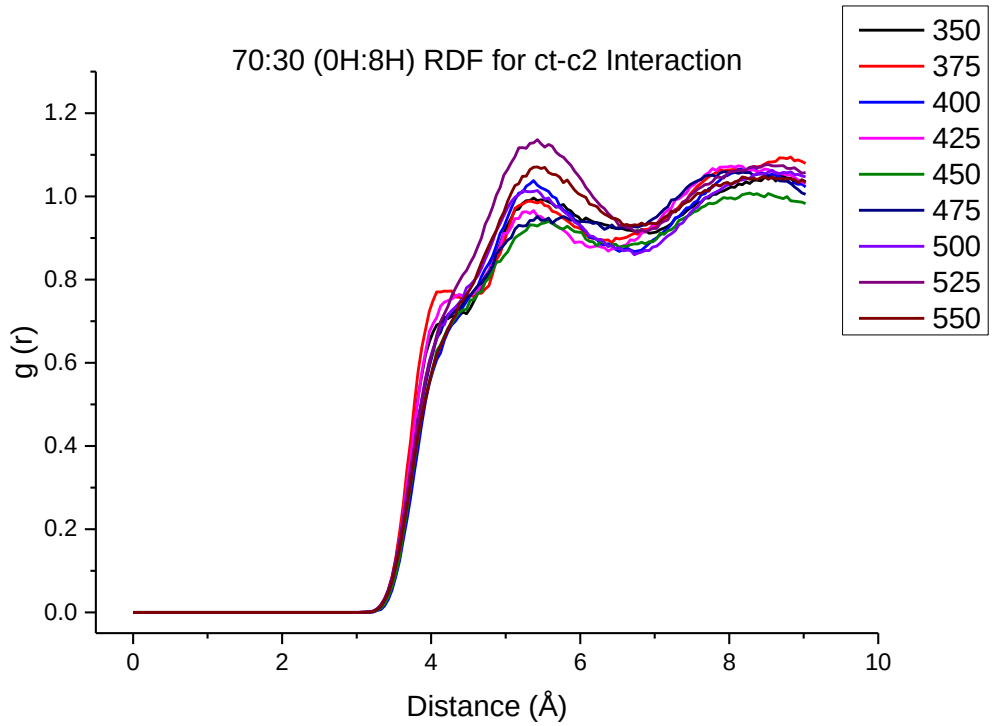
70:30 (0H:8H) RDF for ct-c2 Interaction
g (r)
Distance (Å)
350
375
400
425
450
475
500
525
550

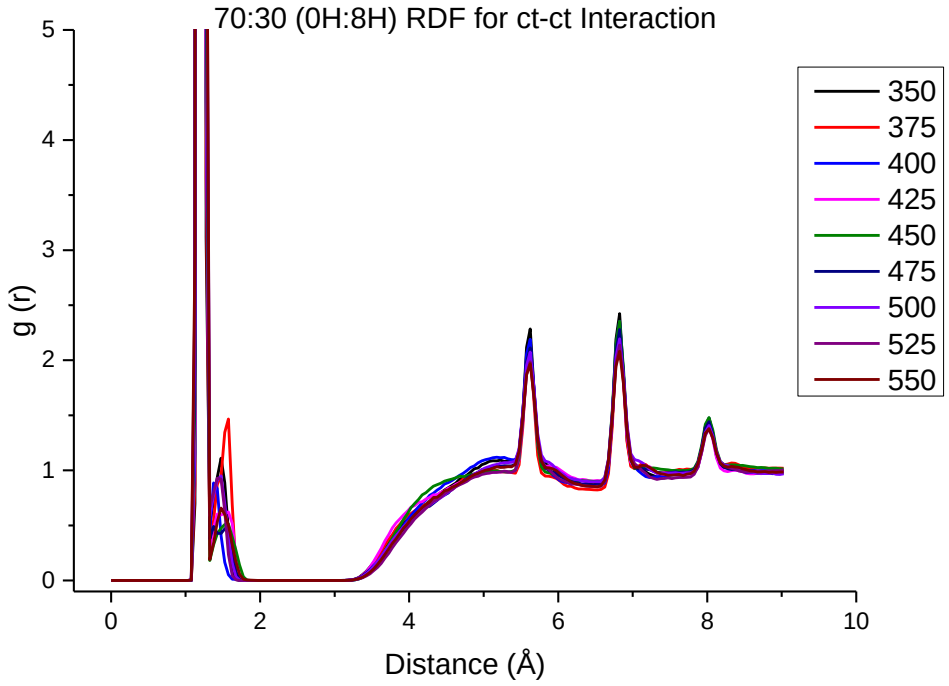
70:30 (0H:8H) RDF for ct-ct Interaction
g (r)
Distance (Å)
350
375
400
425
450
475
500
525
550

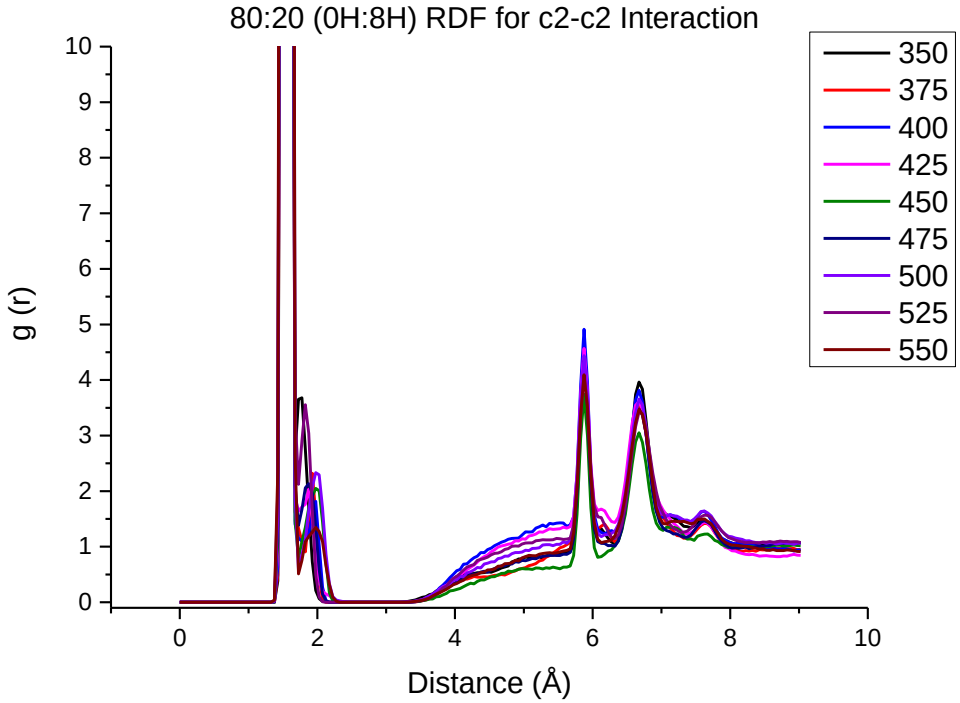
80:20 (0H:8H) RDF for c2-c2 Interaction
g (r)
Distance (Å)
350
375
400
425
450
475
500
525
550

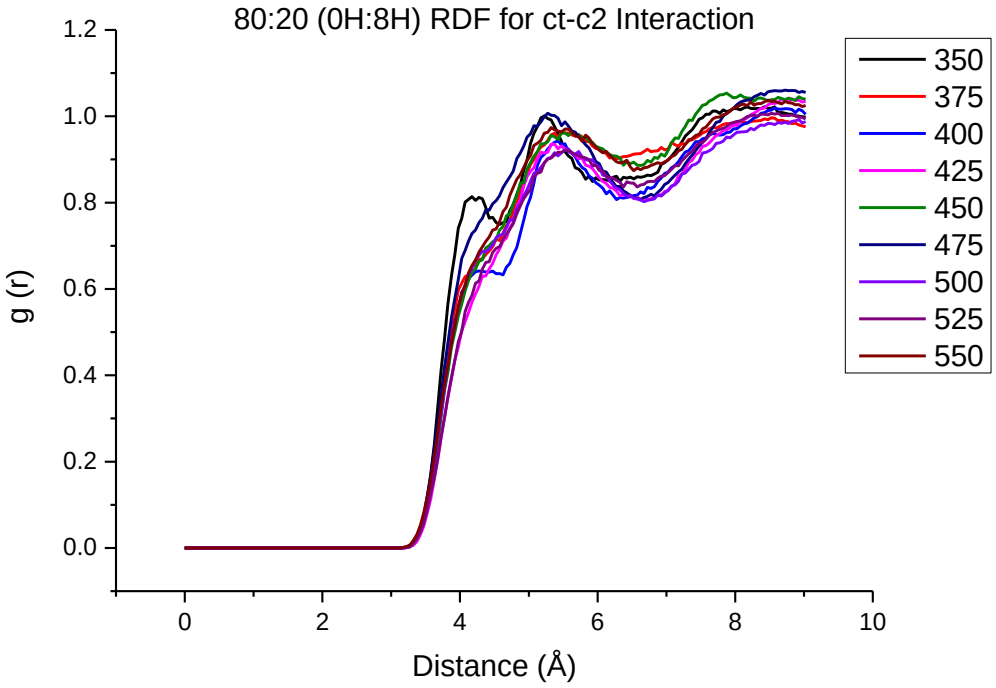
80:20 (0H:8H) RDF for ct-c2 Interaction
g (r)
Distance (Å)
350
375
400
425
450
475
500
525
550

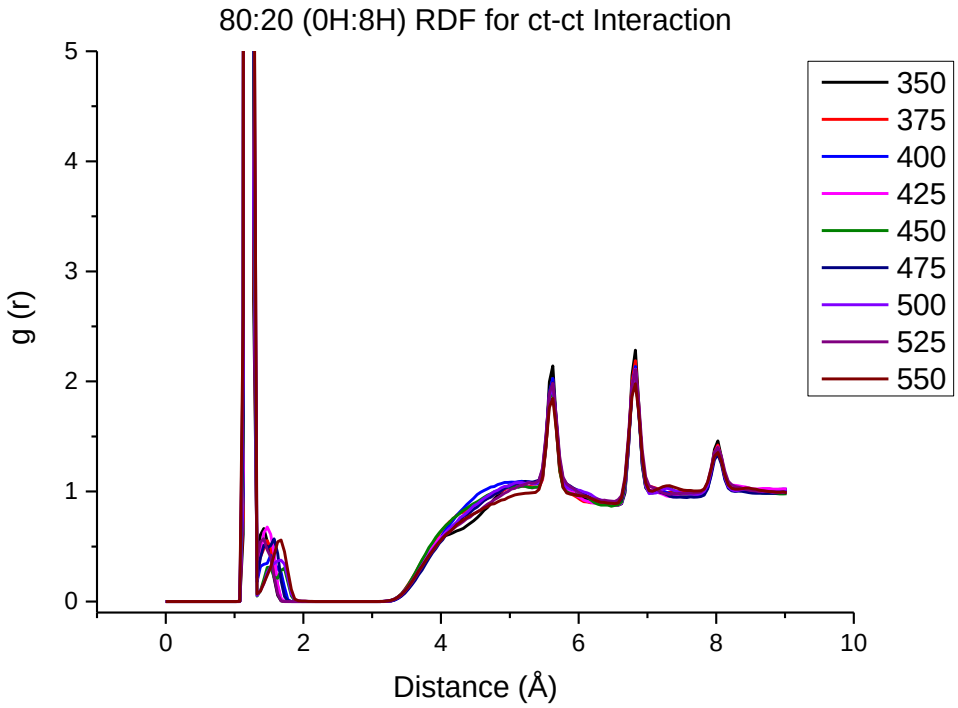
80:20 (0H:8H) RDF for ct-ct Interaction
g (r)
Distance (Å)
350
375
400
425
450
475
500
525
550

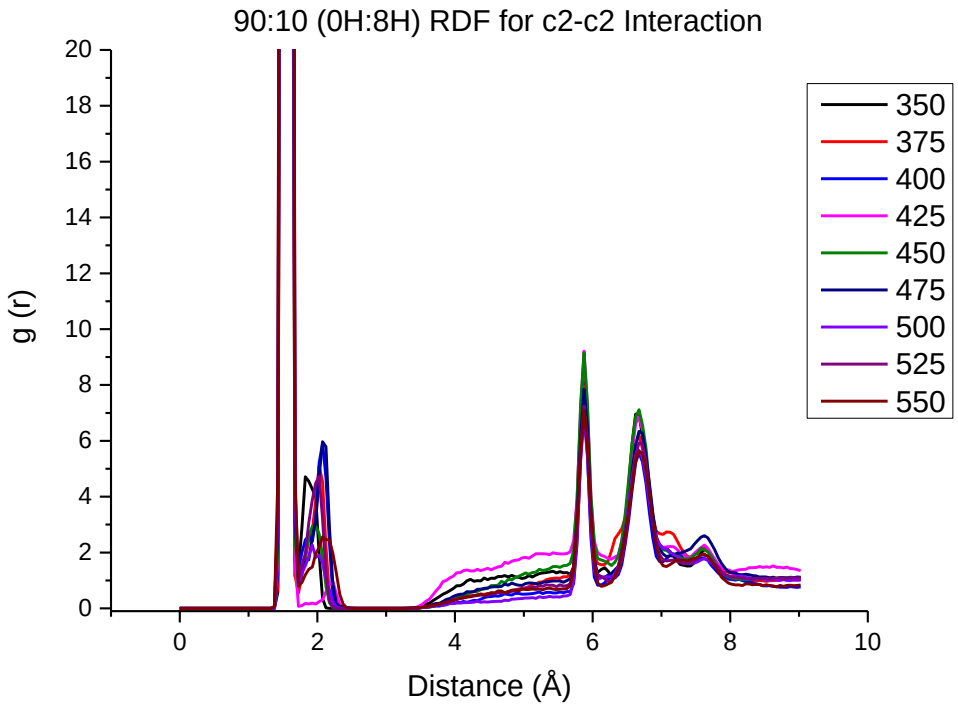
90:10 (0H:8H) RDF for c2-c2 Interaction
g (r)
Distance (Å)
350
375
400
425
450
475
500
525
550

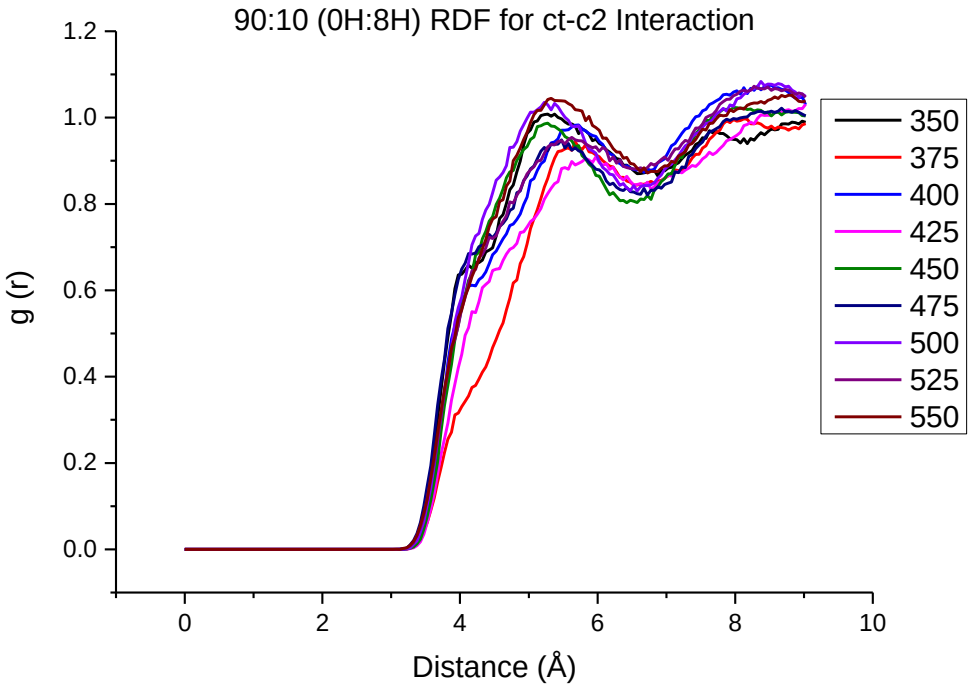
90:10 (0H:8H) RDF for ct-c2 Interaction
g (r)
Distance (Å)
350
375
400
425
450
475
500
525
550

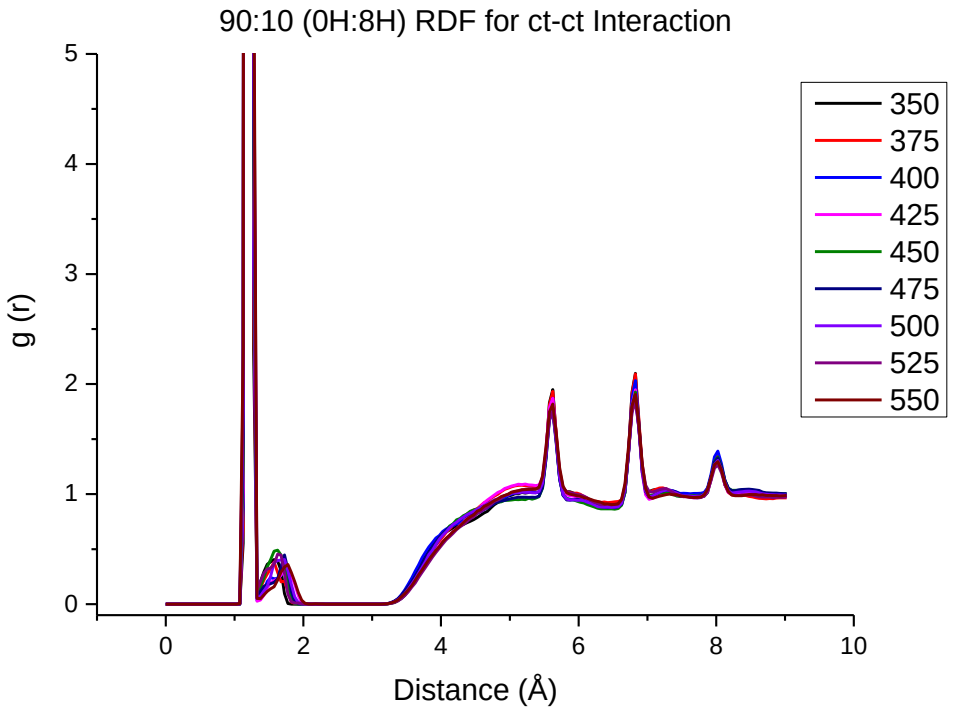

MSDs for 0H:8H Mixtures

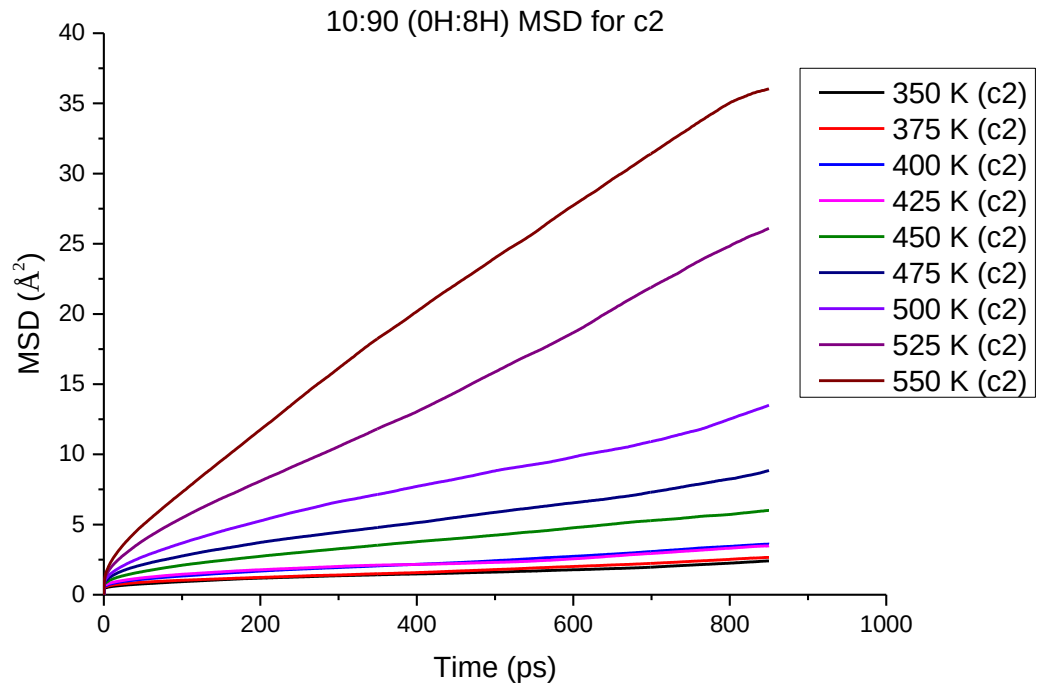

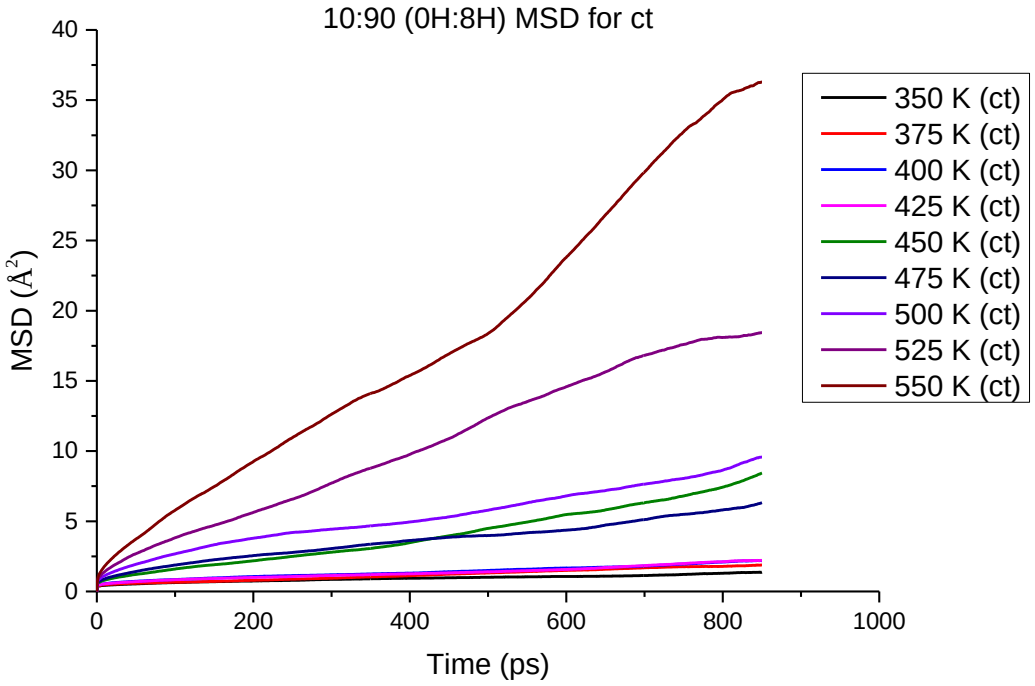
10:90 (0H:8H) MSD for ct
MSD (Å²)
Time (ps)
0
5
10
15
20
25
30
35
40
0
200
400
600
800
1000
350 K (ct)
375 K (ct)
400 K (ct)
425 K (ct)
450 K (ct)
475 K (ct)
500 K (ct)
525 K (ct)
550 K (ct)

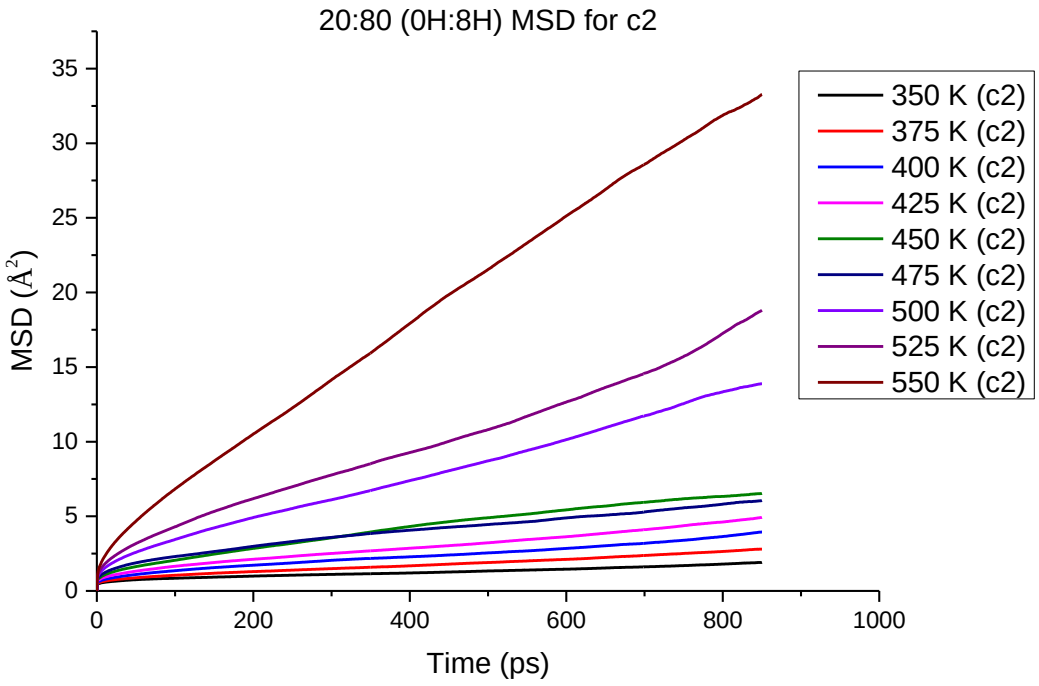
20:80 (0H:8H) MSD for c2
MSD (Å²)
Time (ps)
0
5
10
15
20
25
30
35
0
200
400
600
800
1000
350 K (c2)
375 K (c2)
400 K (c2)
425 K (c2)
450 K (c2)
475 K (c2)
500 K (c2)
525 K (c2)
550 K (c2)

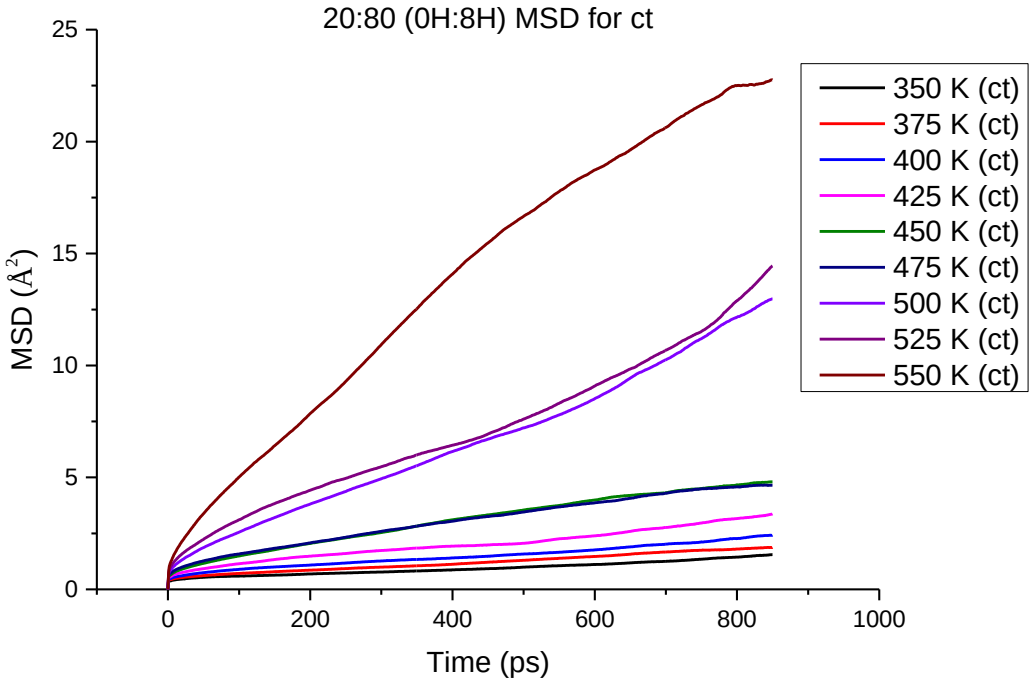
20:80 (0H:8H) MSD for ct
MSD (Å²)
Time (ps)
0
5
10
15
20
25
0
200
400
600
800
1000
350 K (ct)
375 K (ct)
400 K (ct)
425 K (ct)
450 K (ct)
475 K (ct)
500 K (ct)
525 K (ct)
550 K (ct)

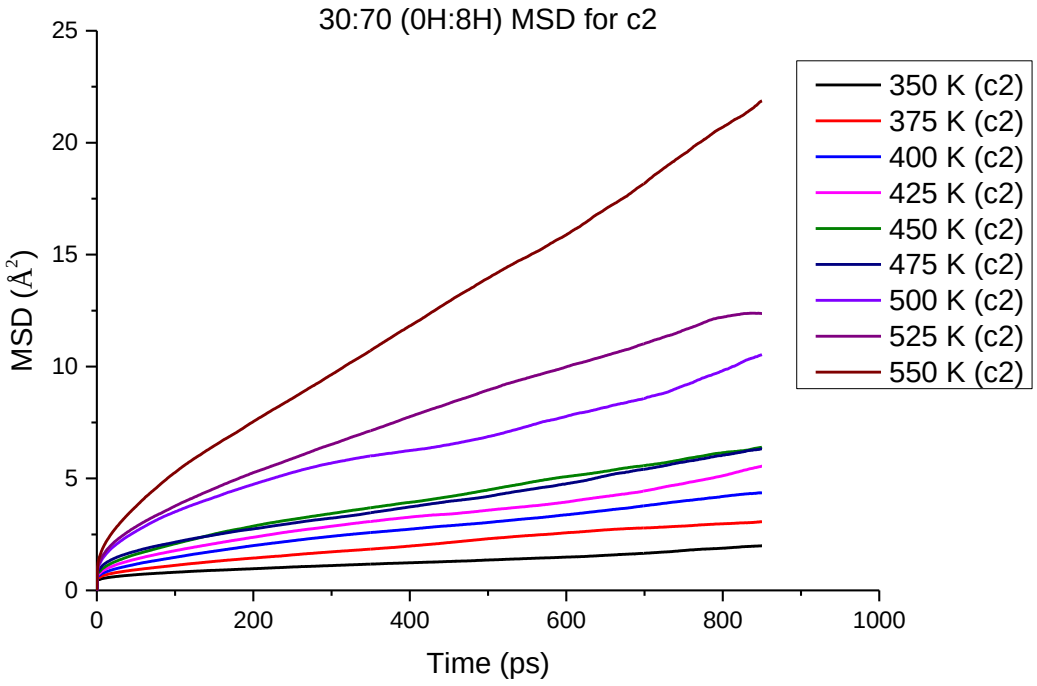
30:70 (0H:8H) MSD for c2
MSD (Å²)
Time (ps)
0
5
10
15
20
25
0
200
400
600
800
1000
350 K (c2)
375 K (c2)
400 K (c2)
425 K (c2)
450 K (c2)
475 K (c2)
500 K (c2)
525 K (c2)
550 K (c2)

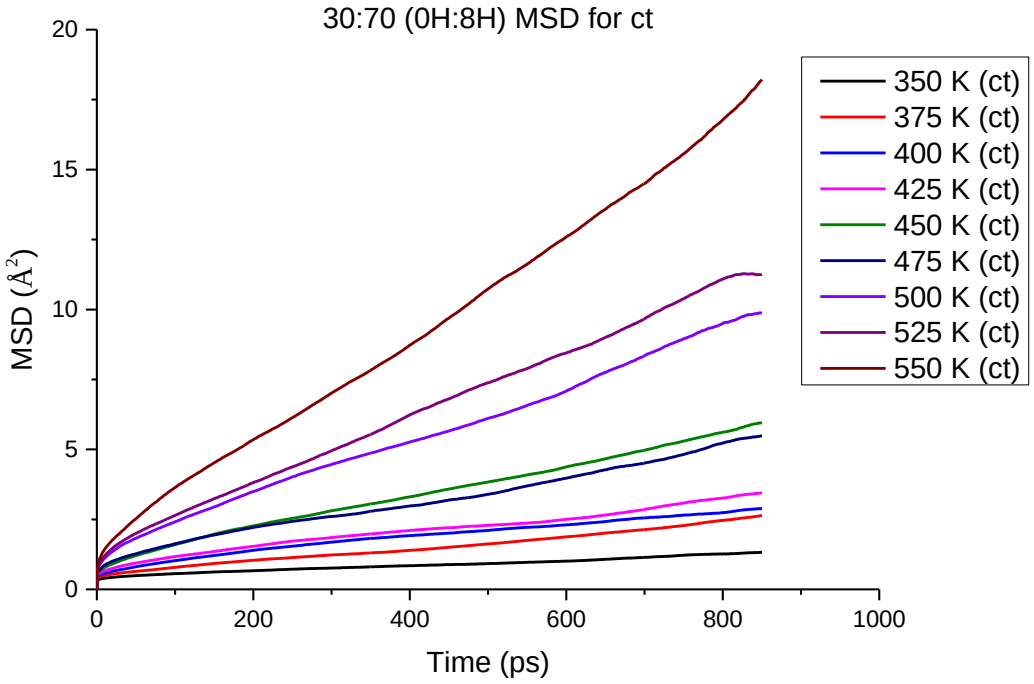
30:70 (0H:8H) MSD for ct
MSD (Å^2)
Time (ps)
0
5
10
15
20
0
200
400
600
800
1000
350 K (ct)
375 K (ct)
400 K (ct)
425 K (ct)
450 K (ct)
475 K (ct)
500 K (ct)
525 K (ct)
550 K (ct)

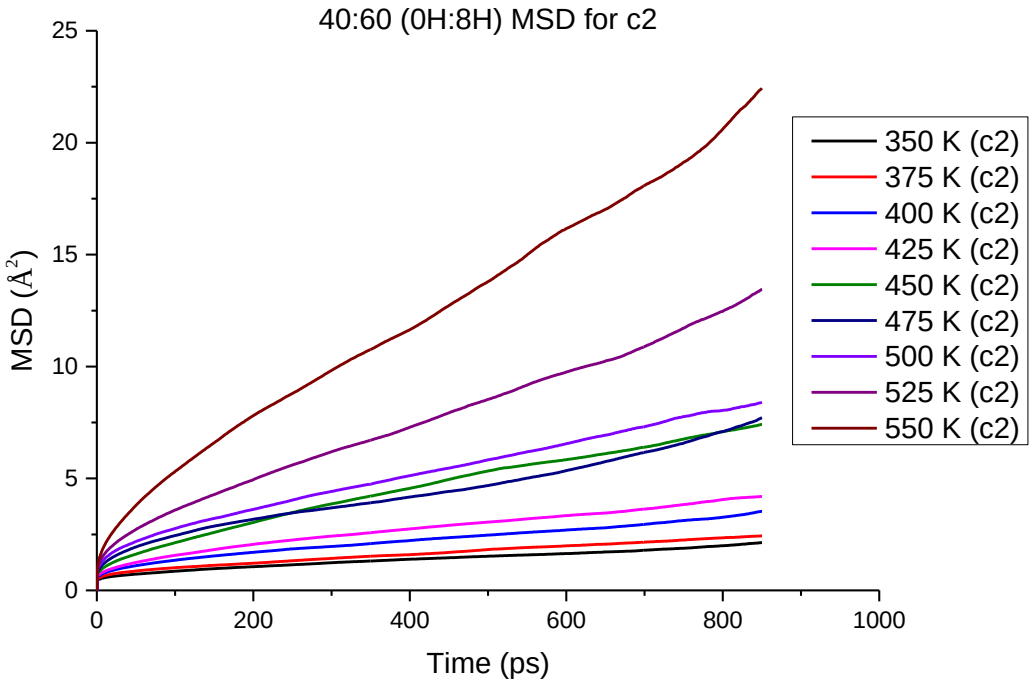
40:60 (0H:8H) MSD for c2
MSD (Å^2)
Time (ps)
0
5
10
15
20
25
0
200
400
600
800
1000
350 K (c2)
375 K (c2)
400 K (c2)
425 K (c2)
450 K (c2)
475 K (c2)
500 K (c2)
525 K (c2)
550 K (c2)

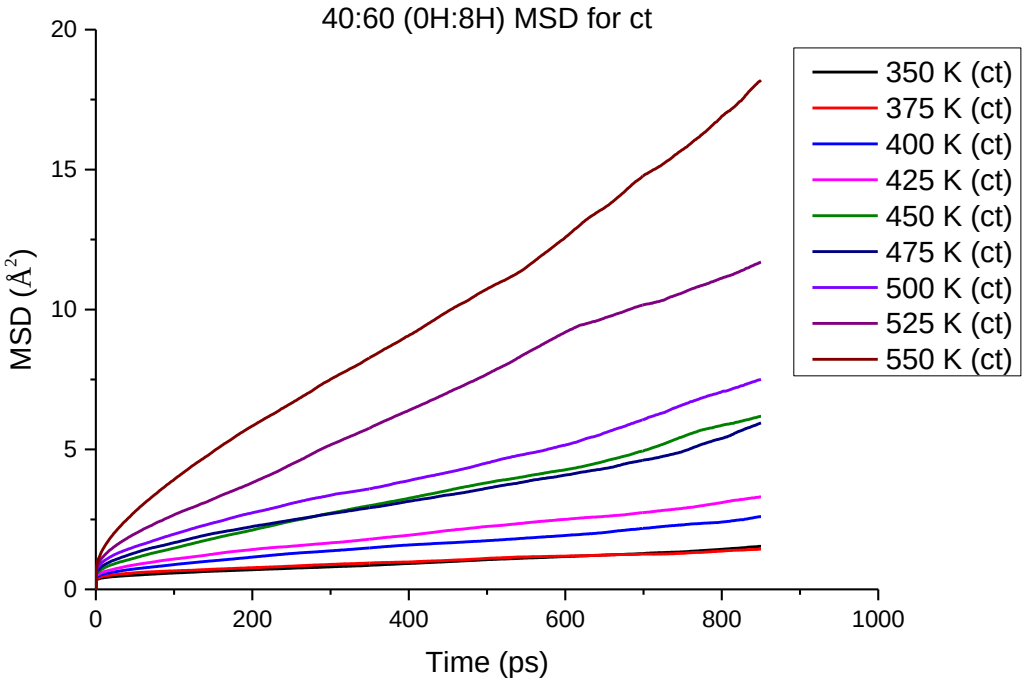
40:60 (0H:8H) MSD for ct
MSD (Å^2)
Time (ps)
0
5
10
15
20
0
200
400
600
800
1000
350 K (ct)
375 K (ct)
400 K (ct)
425 K (ct)
450 K (ct)
475 K (ct)
500 K (ct)
525 K (ct)
550 K (ct)

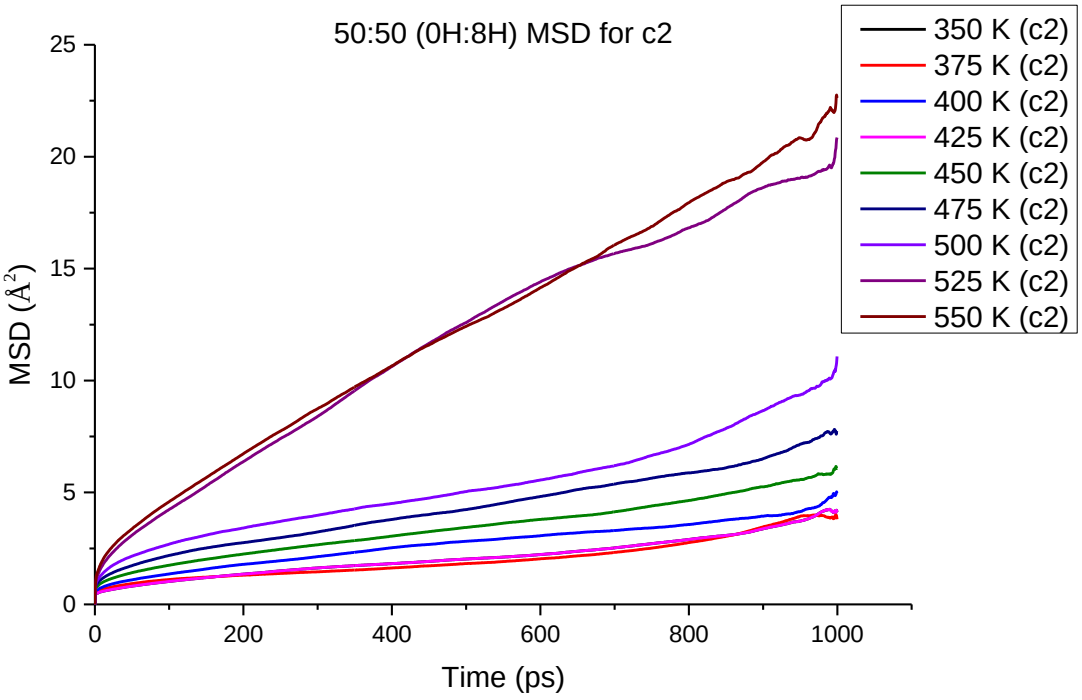
50:50 (0H:8H) MSD for c2
MSD (Å^2)
Time (ps)
0
5
10
15
20
25
0
200
400
600
800
1000
350 K (c2)
375 K (c2)
400 K (c2)
425 K (c2)
450 K (c2)
475 K (c2)
500 K (c2)
525 K (c2)
550 K (c2)

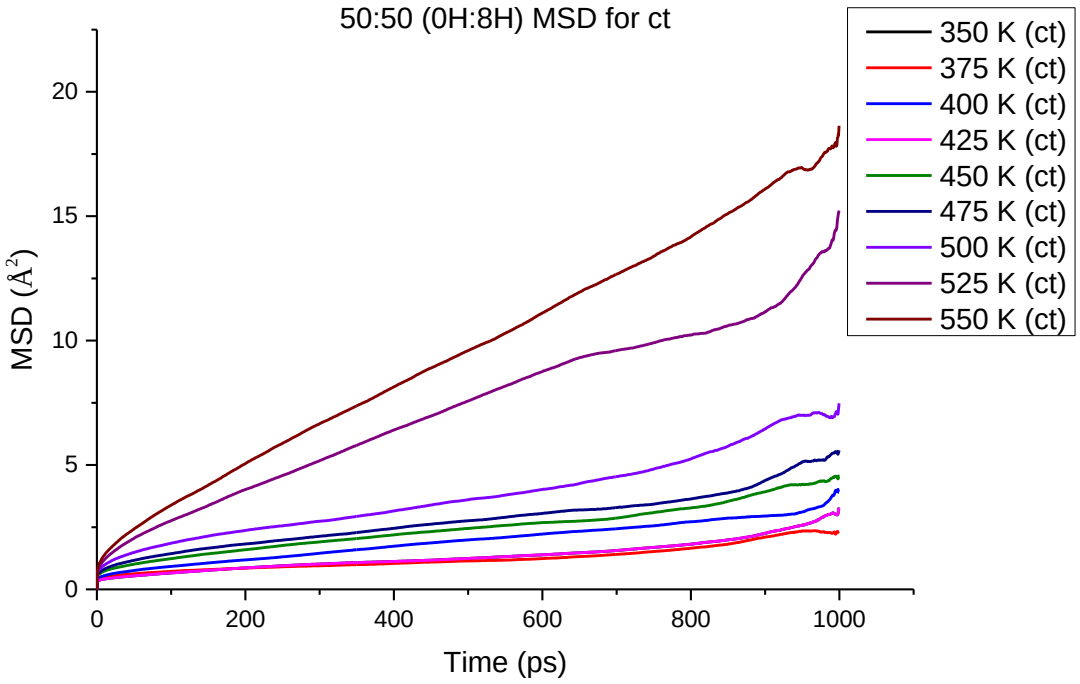
50:50 (0H:8H) MSD for ct
MSD (Å^2)
Time (ps)
0
5
10
15
20
0
200
400
600
800
1000
350 K (ct)
375 K (ct)
400 K (ct)
425 K (ct)
450 K (ct)
475 K (ct)
500 K (ct)
525 K (ct)
550 K (ct)

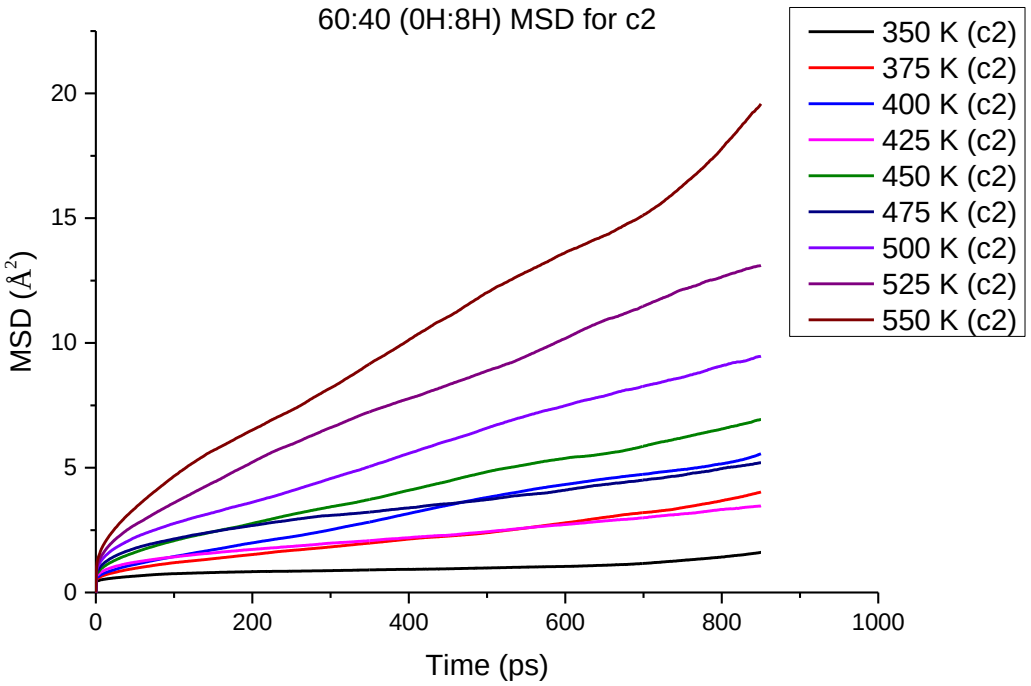
60:40 (0H:8H) MSD for c2
MSD (Å^2)
Time (ps)
0
5
10
15
20
0
200
400
600
800
1000
350 K (c2)
375 K (c2)
400 K (c2)
425 K (c2)
450 K (c2)
475 K (c2)
500 K (c2)
525 K (c2)
550 K (c2)

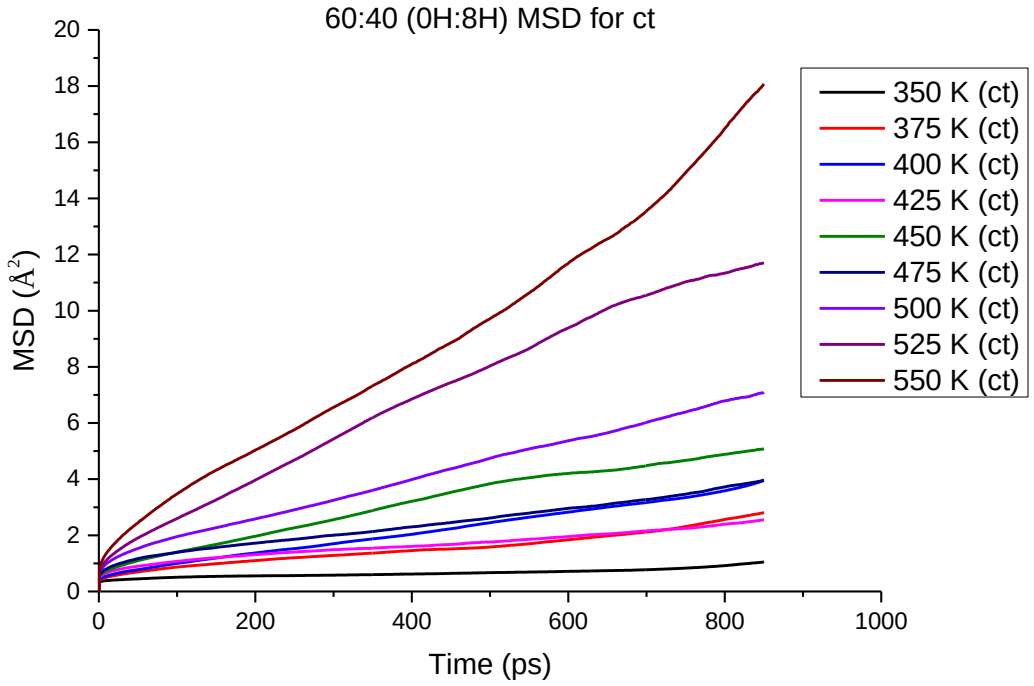
60:40 (0H:8H) MSD for ct
MSD (Å²)
Time (ps)
0
2
4
6
8
10
12
14
16
18
20
0
200
400
600
800
1000
350 K (ct)
375 K (ct)
400 K (ct)
425 K (ct)
450 K (ct)
475 K (ct)
500 K (ct)
525 K (ct)
550 K (ct)

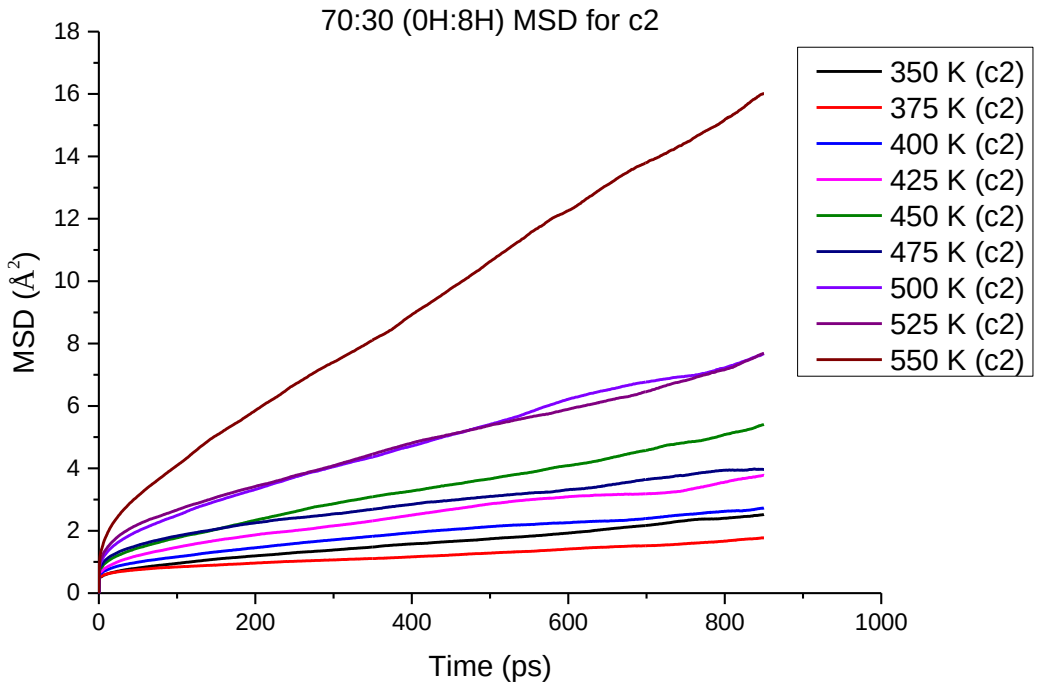
70:30 (0H:8H) MSD for c2
MSD (Å²)
Time (ps)
0
2
4
6
8
10
12
14
16
18
0
200
400
600
800
1000
350 K (c2)
375 K (c2)
400 K (c2)
425 K (c2)
450 K (c2)
475 K (c2)
500 K (c2)
525 K (c2)
550 K (c2)

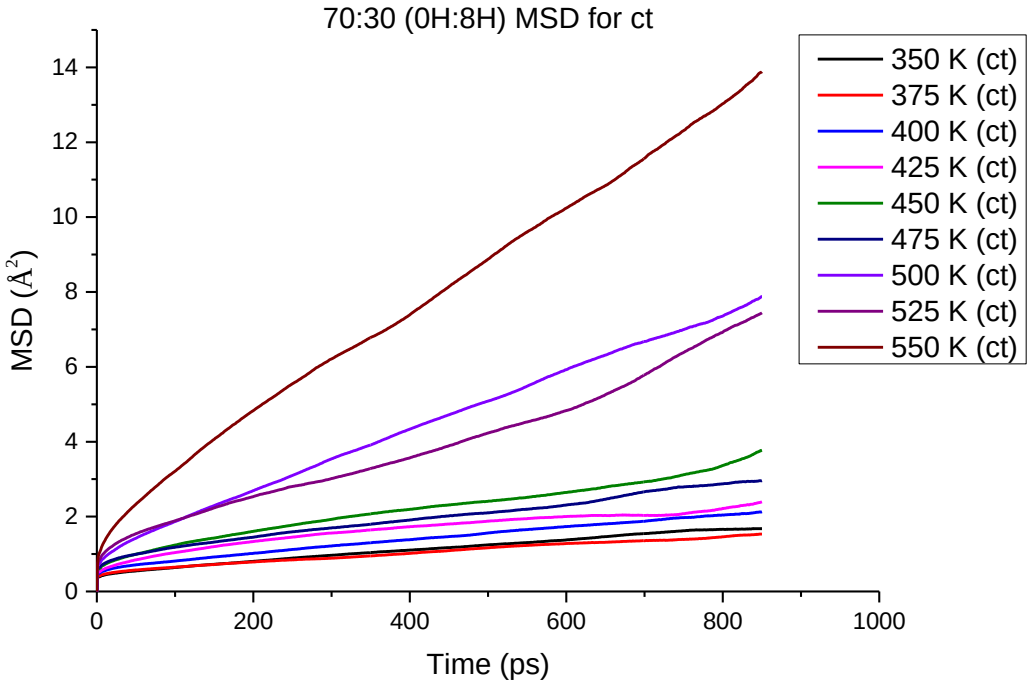
70:30 (0H:8H) MSD for ct
MSD (Å²)
Time (ps)
0
2
4
6
8
10
12
14
0
200
400
600
800
1000
350 K (ct)
375 K (ct)
400 K (ct)
425 K (ct)
450 K (ct)
475 K (ct)
500 K (ct)
525 K (ct)
550 K (ct)

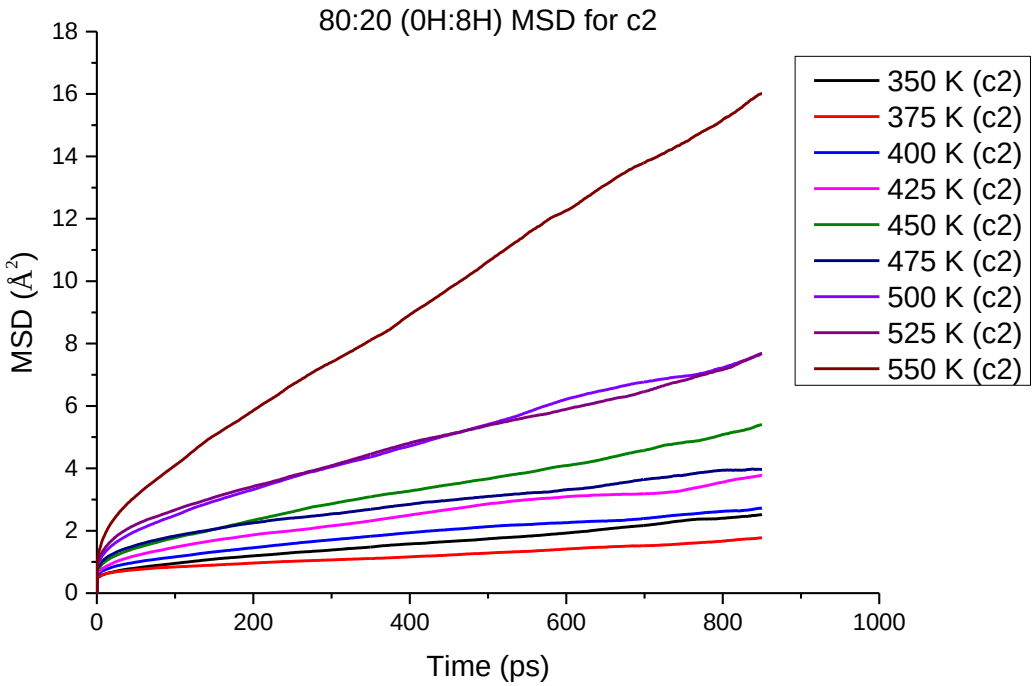
80:20 (0H:8H) MSD for c2
MSD (Å²)
Time (ps)
0
2
4
6
8
10
12
14
16
18
0
200
400
600
800
1000
350 K (c2)
375 K (c2)
400 K (c2)
425 K (c2)
450 K (c2)
475 K (c2)
500 K (c2)
525 K (c2)
550 K (c2)

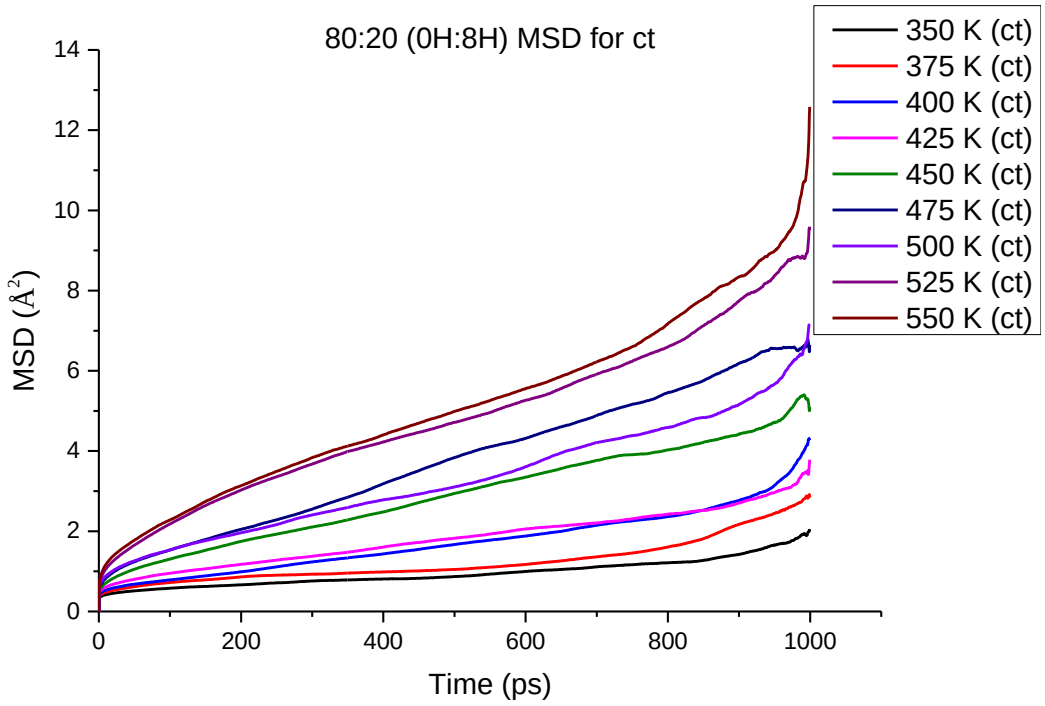
80:20 (0H:8H) MSD for ct
MSD (Å²)
Time (ps)
0
2
4
6
8
10
12
14
0
200
400
600
800
1000
350 K (ct)
375 K (ct)
400 K (ct)
425 K (ct)
450 K (ct)
475 K (ct)
500 K (ct)
525 K (ct)
550 K (ct)

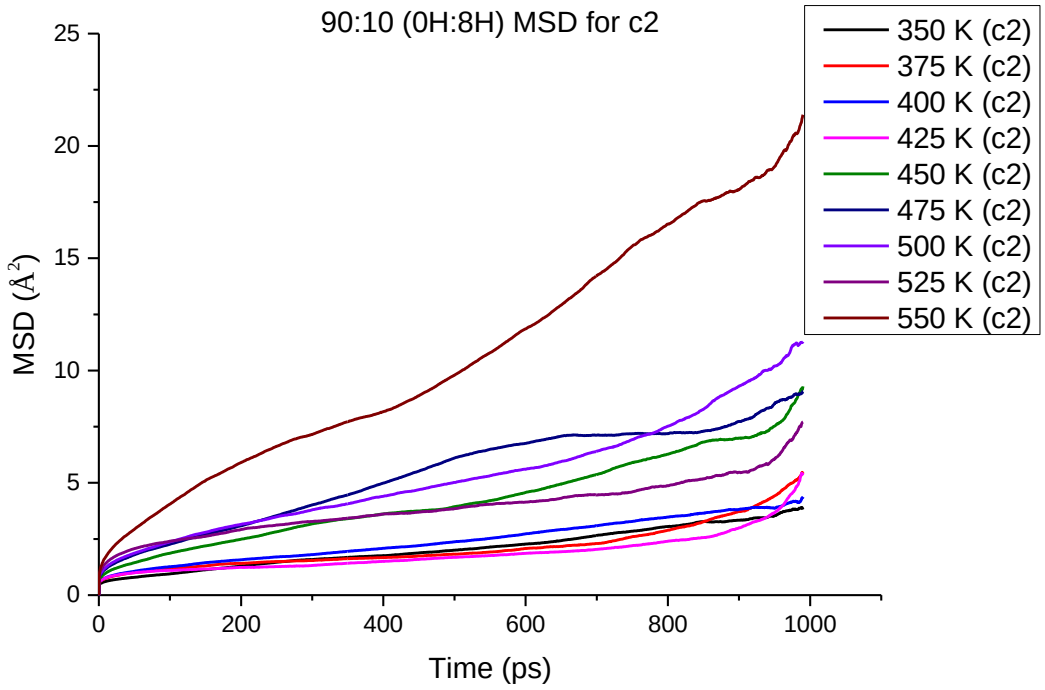
90:10 (0H:8H) MSD for c2
MSD (Å²)
Time (ps)
0
5
10
15
20
25
0
200
400
600
800
1000
350 K (c2)
375 K (c2)
400 K (c2)
425 K (c2)
450 K (c2)
475 K (c2)
500 K (c2)
525 K (c2)
550 K (c2)

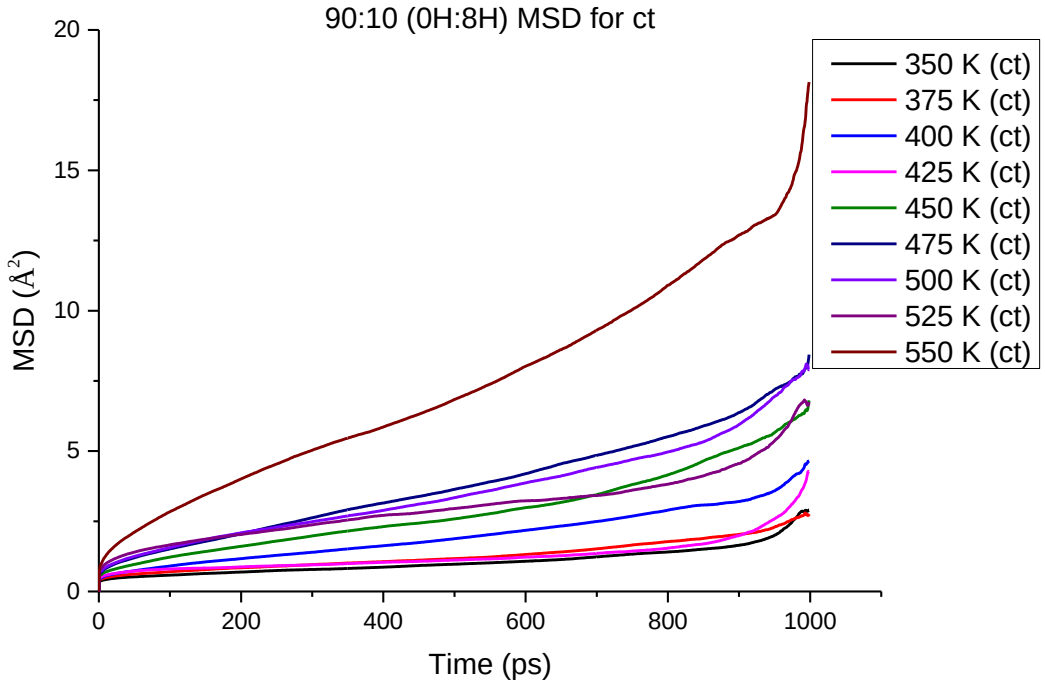

Diffusion Coefficients for all 0H:8H Mixtures

(all values are x 10^{-15} m^2 s^{-1})

10:90 (0H:8H)

Temperature	c2	ct
350	5.18	2.35
375	6.95	6.08
400	9.51	5.42
425	7.56	5.79
450	16.7	29.8
475	23.8	16.4
500	36.0	27.4
525	94.3	76.1
550	127	143

20:80 (0H:8H)

Temperature	c2	ct
350	4.25	4.02
375	7.36	5.64
400	9.65	6.21
425	13.3	8.56
450	19.6	14.9
475	14.2	14.1
500	46.6	43.7
525	56.9	43.5
550	120	80.4

30:70 (0H:8H)

Temperature	c2	ct
350	4.56	3.11
375	9.08	7.70
400	11.3	7.07
425	13.0	8.14
450	18.1	18.1
475	18.1	16.2
500	24.7	32.2
525	37.5	39.1
550	71.0	63.2

40:60 (0H:8H)

Temperature	c2	ct
350	4.63	4.01
375	6.13	3.11
400	8.17	6.49
425	10.1	9.08
450	21.3	18.6
475	20.5	15.9
500	24.3	22.5
525	39.8	42.4
550	69.7	59.9

60:40 (0H:8H)

Temperature	c2	ct
350	2.41	1.63
375	11.3	6.95
400	18.7	12.4
425	8.67	5.64
450	20.5	16.0
475	11.9	10.7
500	31.1	23.1
525	40.7	42.6
550	58.2	59.1

70:30 (0H:8H)

Temperature	c2	ct
350	6.50	4.78
375	3.88	3.92
400	5.73	5.62
425	8.86	4.12
450	14.2	8.25
475	8.87	7.71
500	22.9	26.2
525	19.6	22.8
550	53.7	45.3

80:20 (0H:8H)

Temperature	c2	ct
350	3.59	2.99
375	5.60	3.54
400	7.00	7.57
425	8.46	7.03
450	13.5	13.9
475	32.2	19.4
500	17.3	14.8
525	15.1	18.3
550	44.1	19.9

90:10 (0H:8H)

Temperature	c2	ct
350	8.79	3.71
375	6.54	4.65
400	10.7	9.16
425	5.96	3.32
450	18.4	12.2
475	26.6	18.3
500	21.6	16.1
525	9.83	8.83
550	58.9	35.8

Appendix C

RDFs for 4H:0H Mixtures

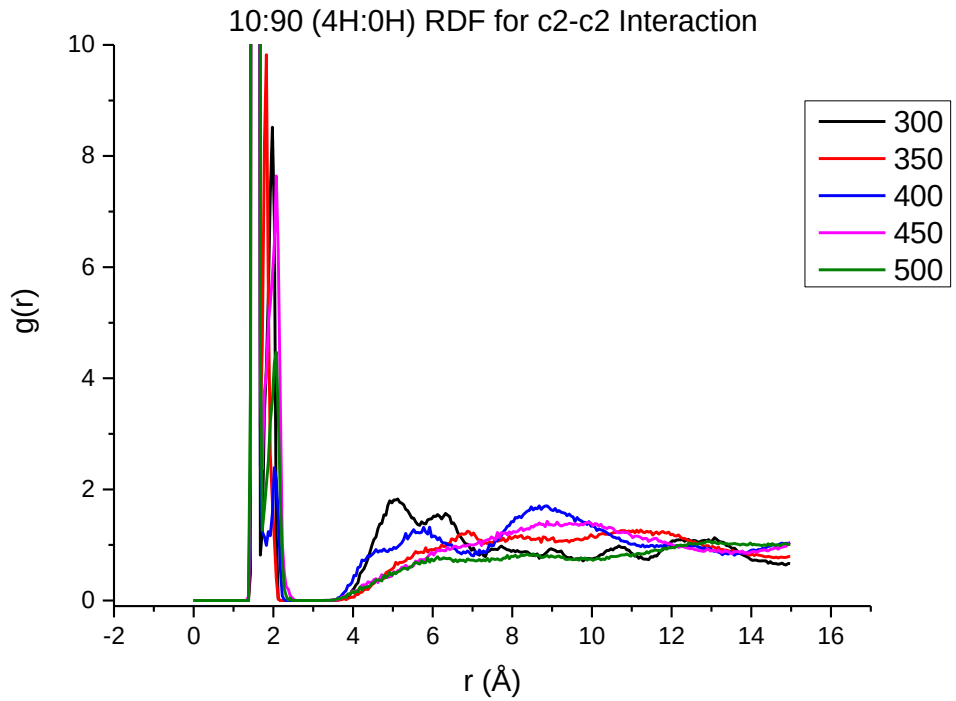

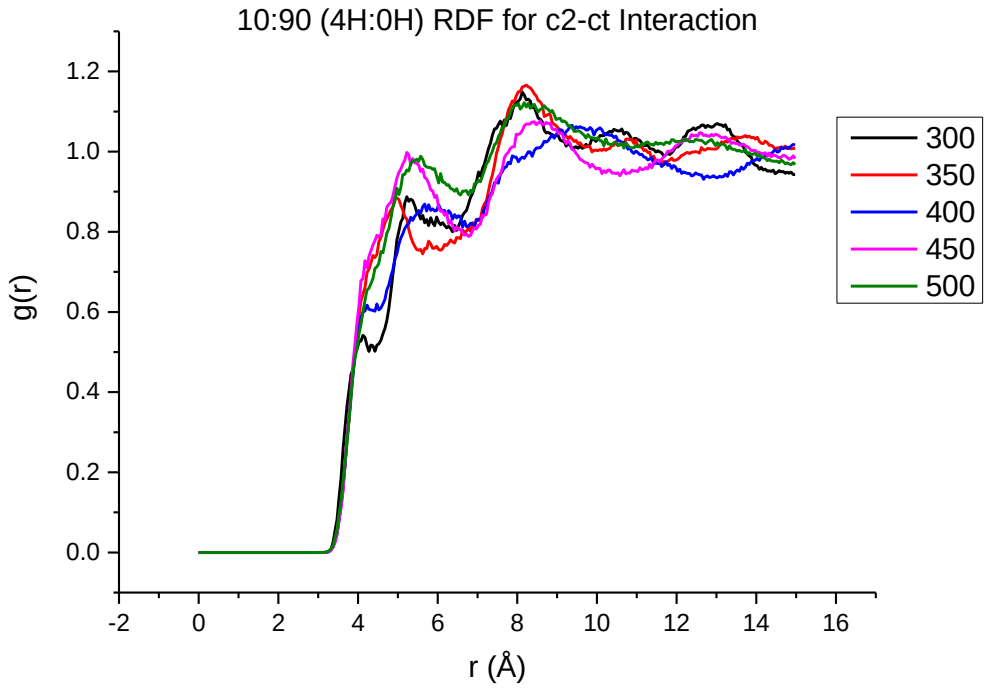

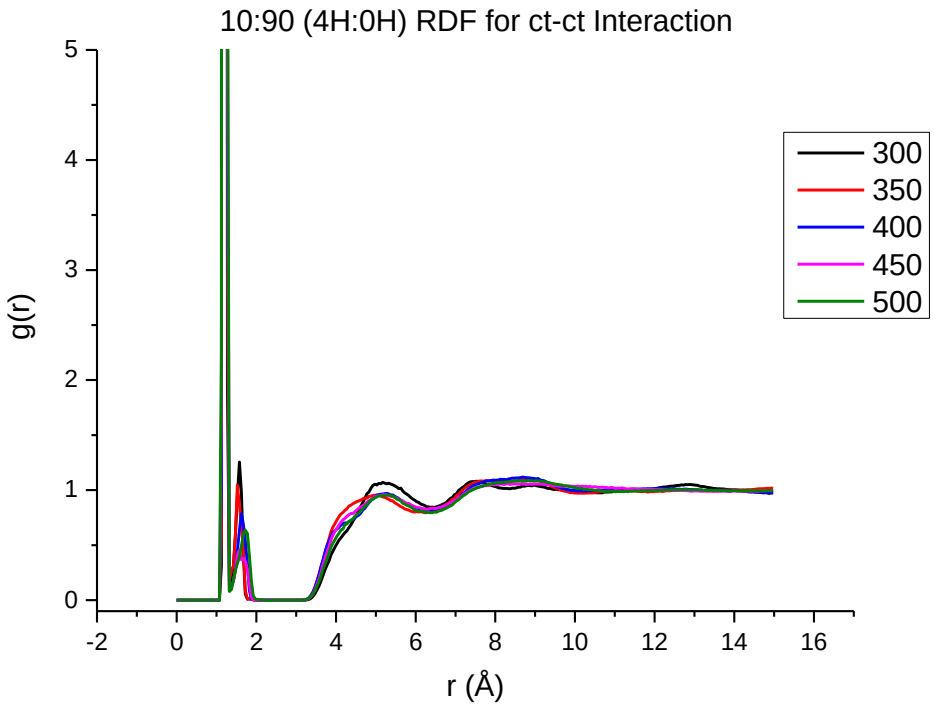
10:90 (4H:0H) RDF for ct-ct Interaction
g(r)
r (Å)
300
350
400
450
500

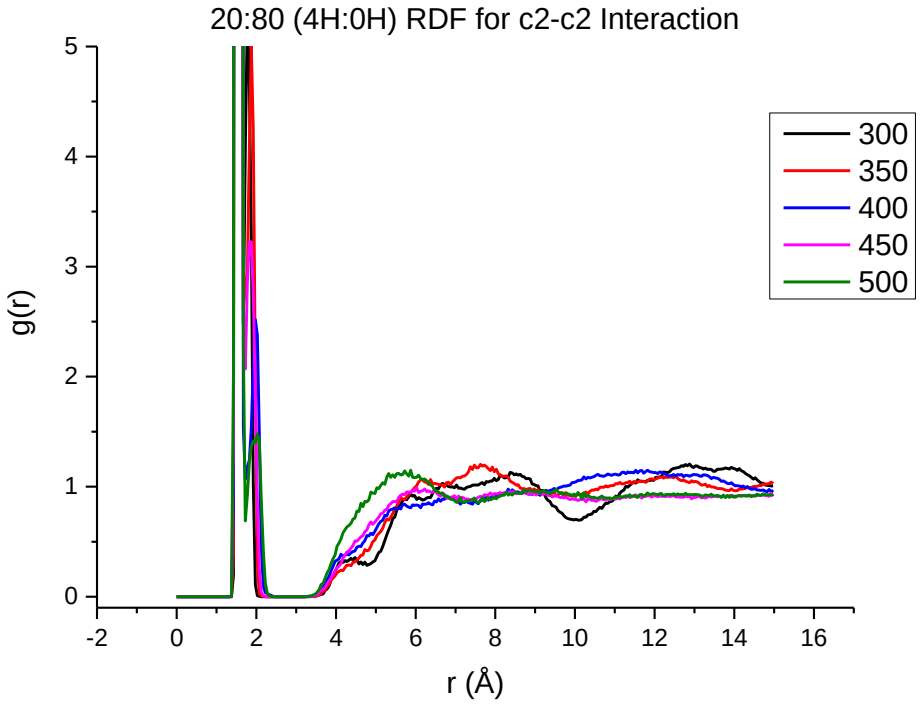
20:80 (4H:0H) RDF for c2-c2 Interaction
g(r)
r (Å)
300
350
400
450
500

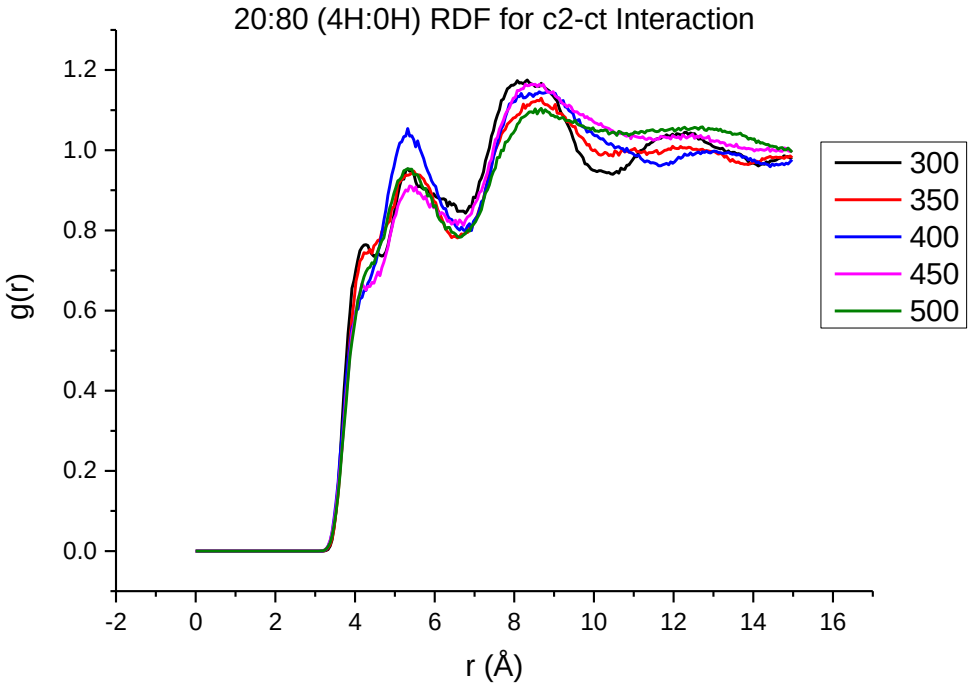
20:80 (4H:0H) RDF for c2-ct Interaction
g(r)
r (Å)
300
350
400
450
500

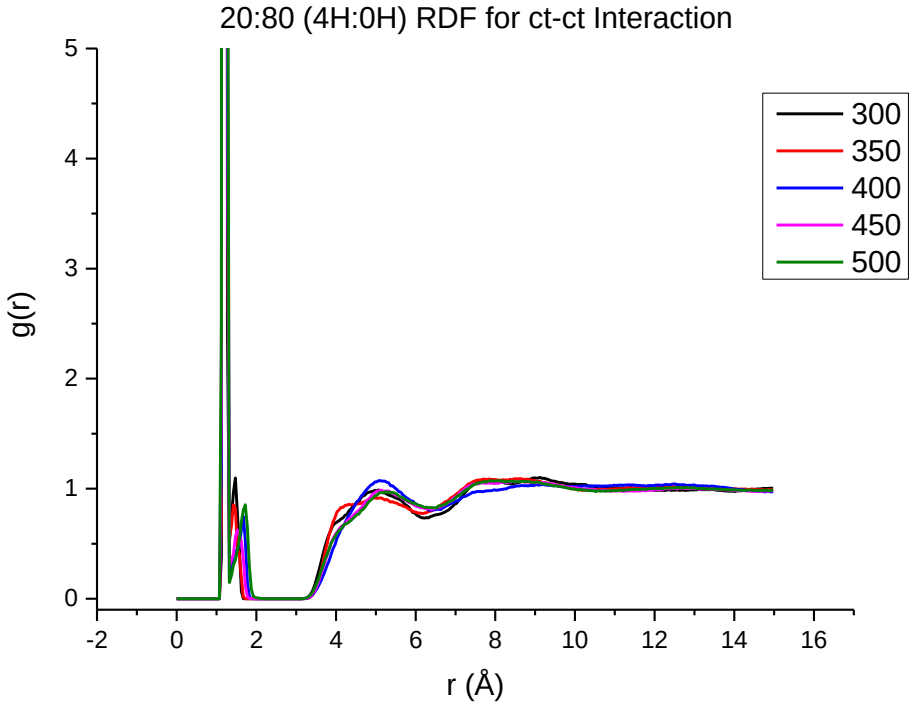
20:80 (4H:0H) RDF for ct-ct Interaction
g(r)
r (Å)
300
350
400
450
500

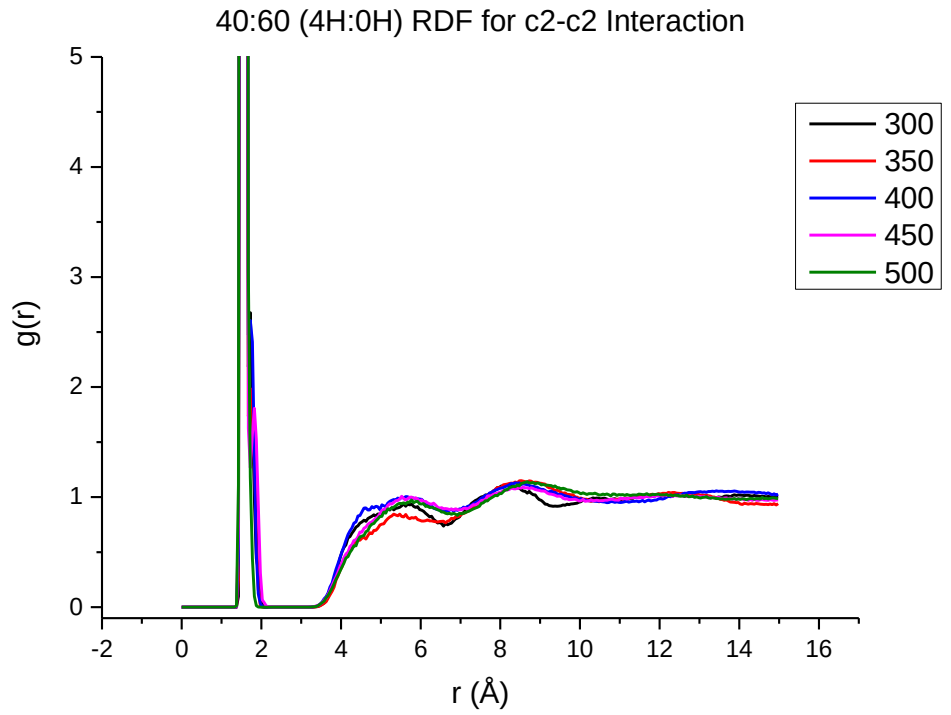
40:60 (4H:0H) RDF for c2-c2 Interaction
g(r)
r (Å)
300
350
400
450
500

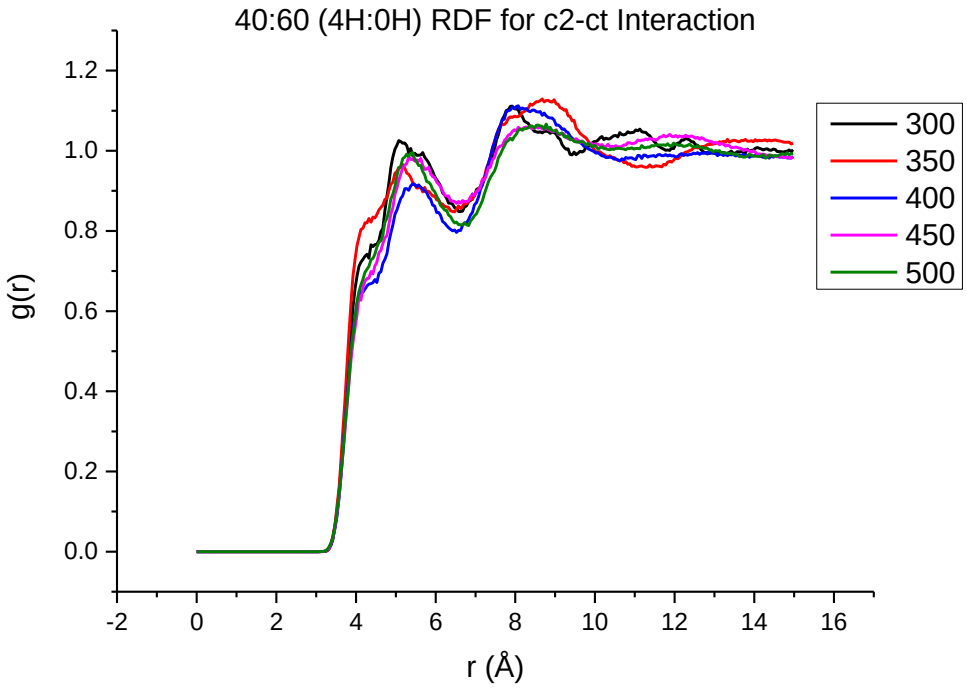
40:60 (4H:0H) RDF for c2-ct Interaction
g(r)
r (Å)
300
350
400
450
500

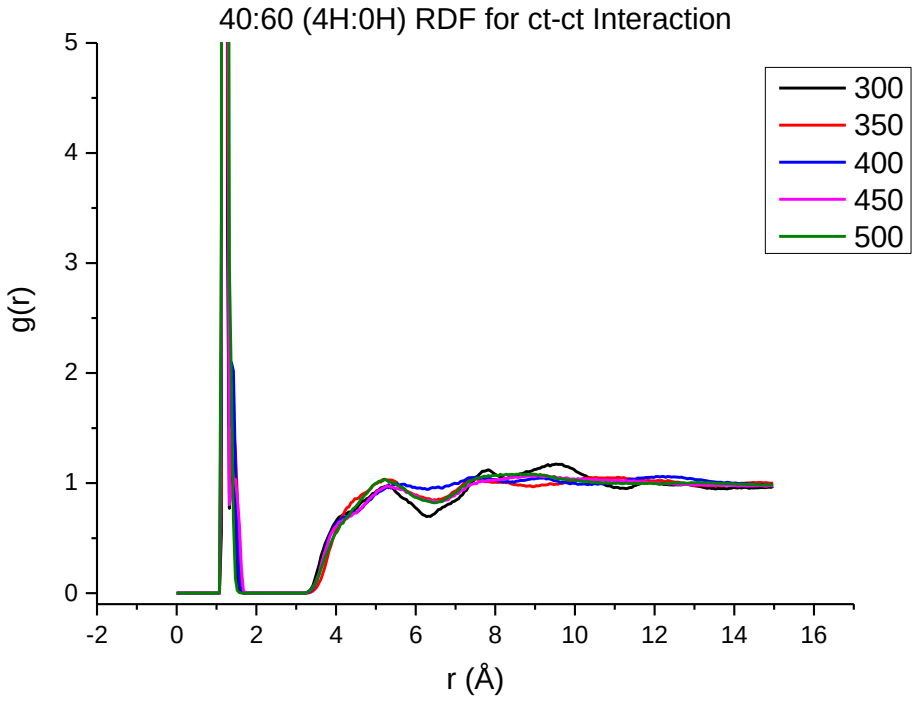
40:60 (4H:0H) RDF for ct-ct Interaction
g(r)
r (Å)
300
350
400
450
500

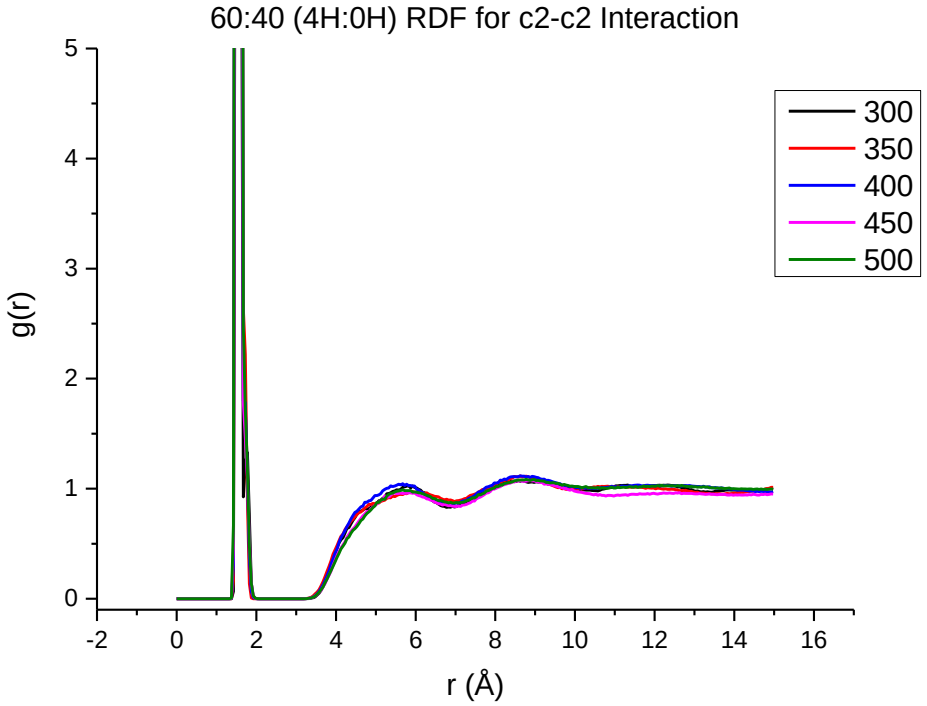
60:40 (4H:0H) RDF for c2-c2 Interaction
g(r)
r (Å)
300
350
400
450
500

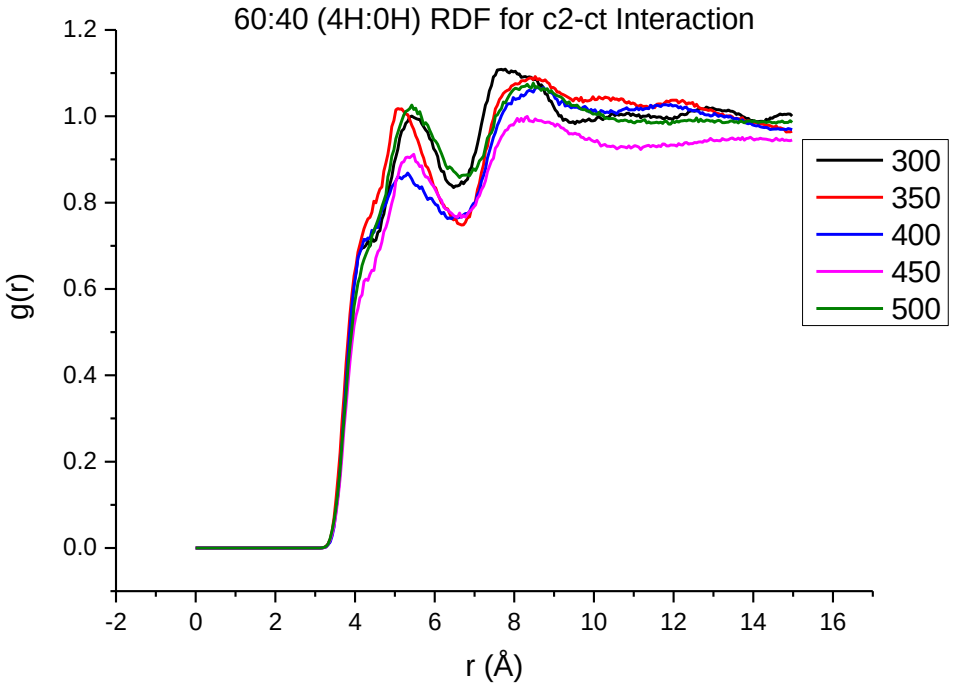
60:40 (4H:0H) RDF for c2-ct Interaction
g(r)
r (Å)
300
350
400
450
500

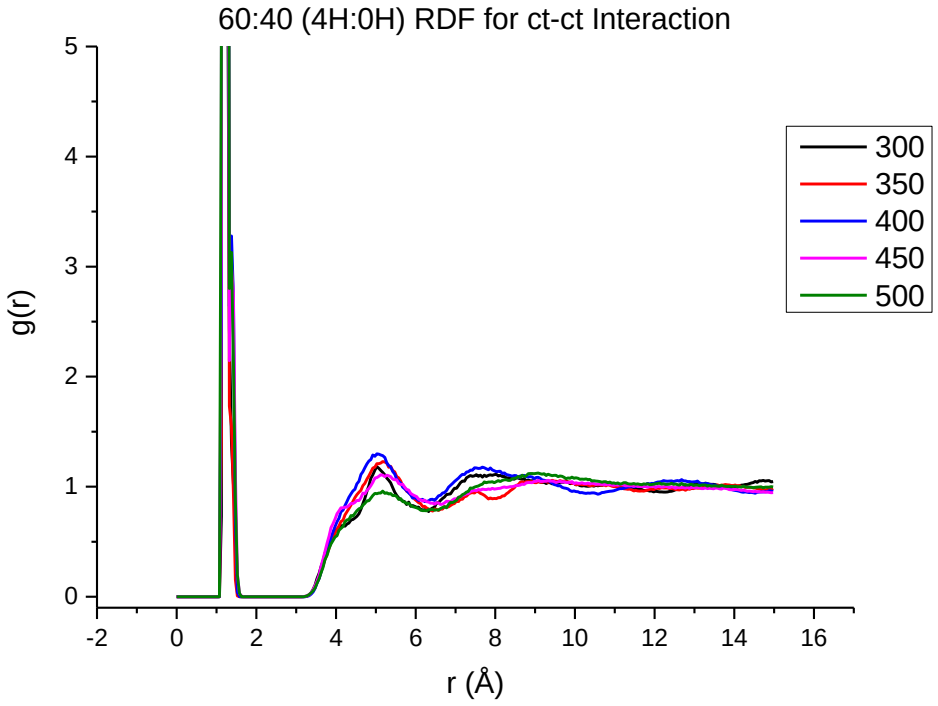
60:40 (4H:0H) RDF for ct-ct Interaction
g(r)
r (Å)
300
350
400
450
500

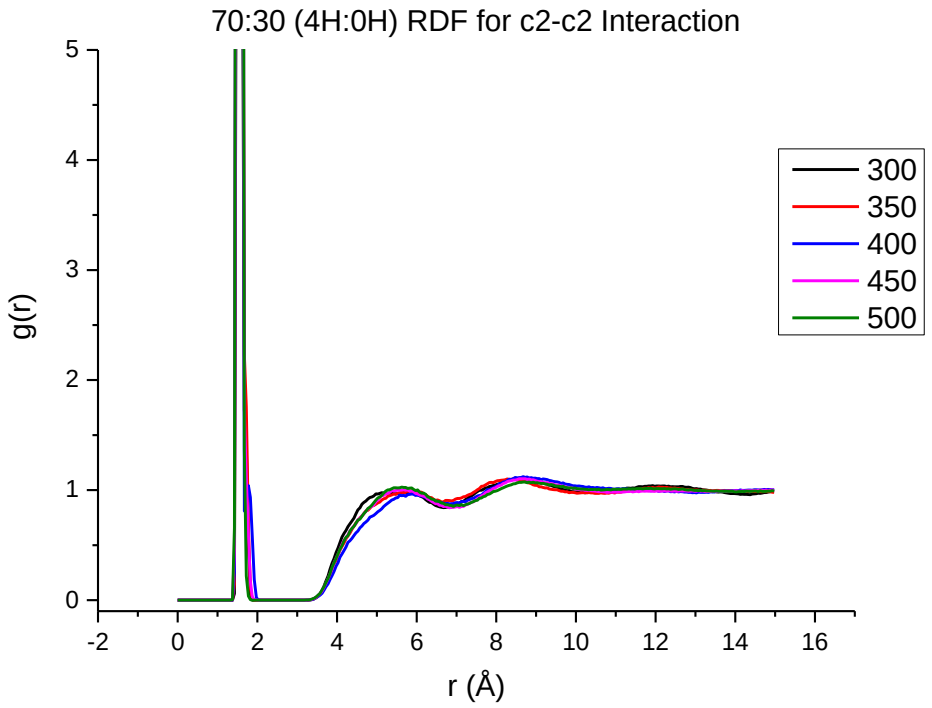
70:30 (4H:0H) RDF for c2-c2 Interaction
g(r)
r (Å)
300
350
400
450
500

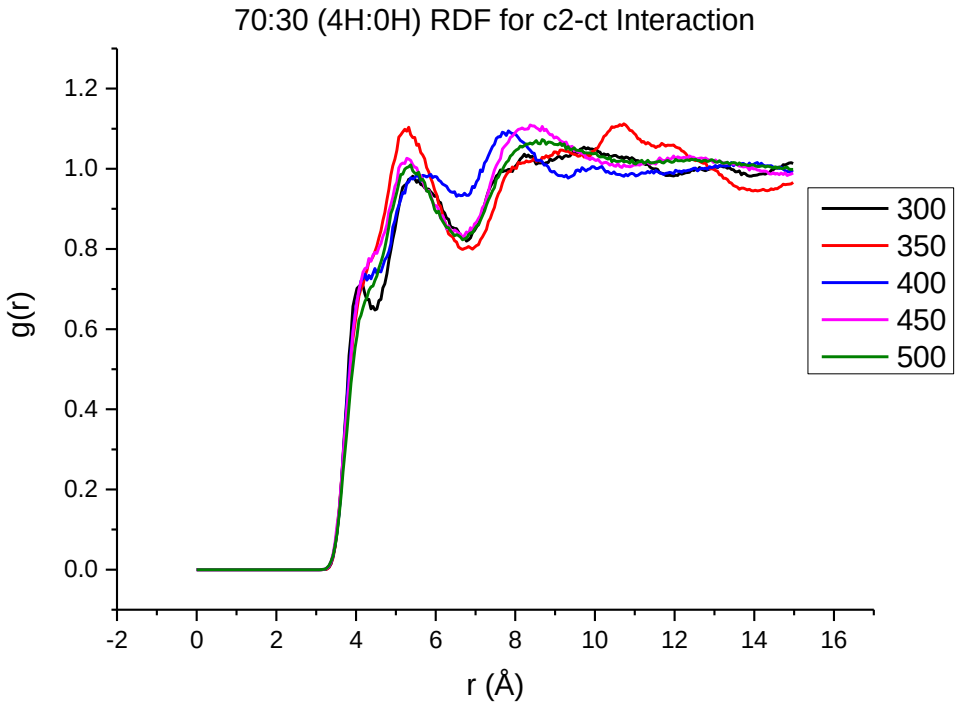
70:30 (4H:0H) RDF for c2-ct Interaction
g(r)
r (Å)
300
350
400
450
500

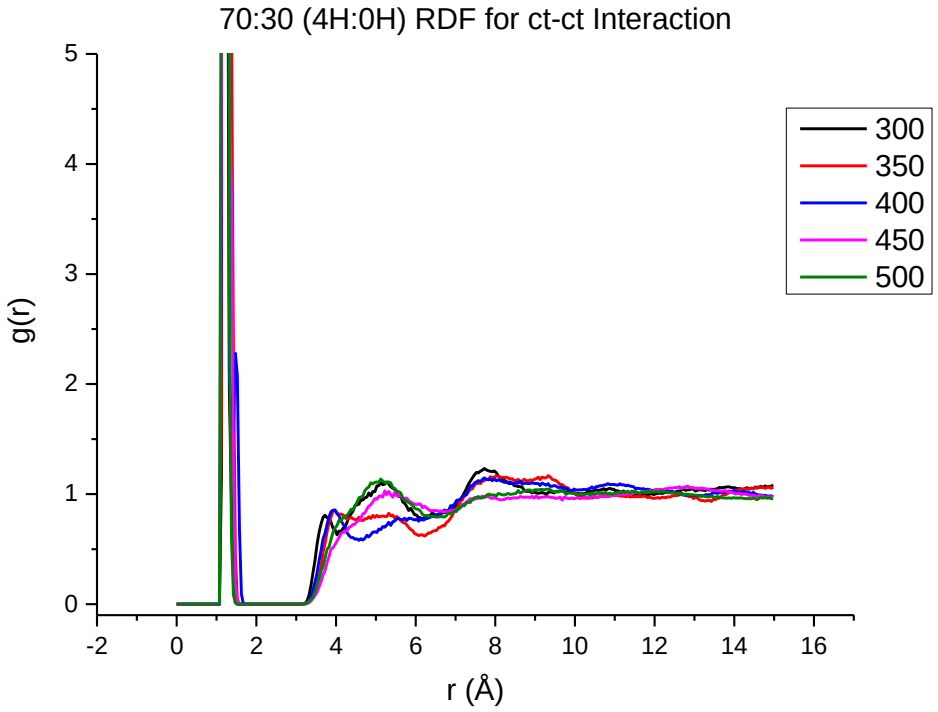
70:30 (4H:0H) RDF for ct-ct Interaction
g(r)
r (Å)
300
350
400
450
500

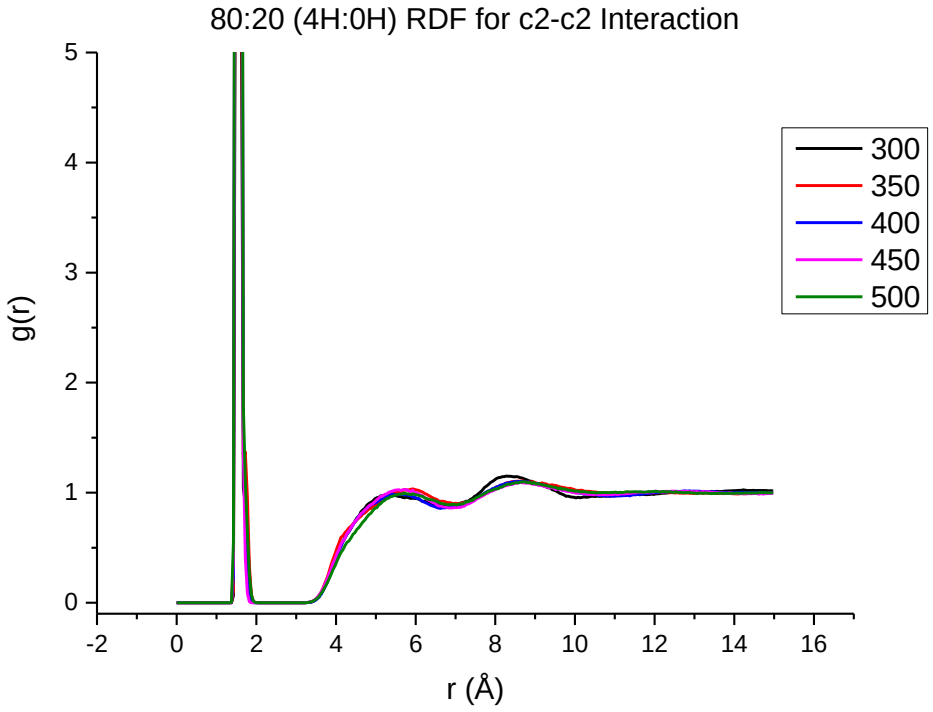
80:20 (4H:0H) RDF for c2-c2 Interaction
g(r)
r (Å)
300
350
400
450
500

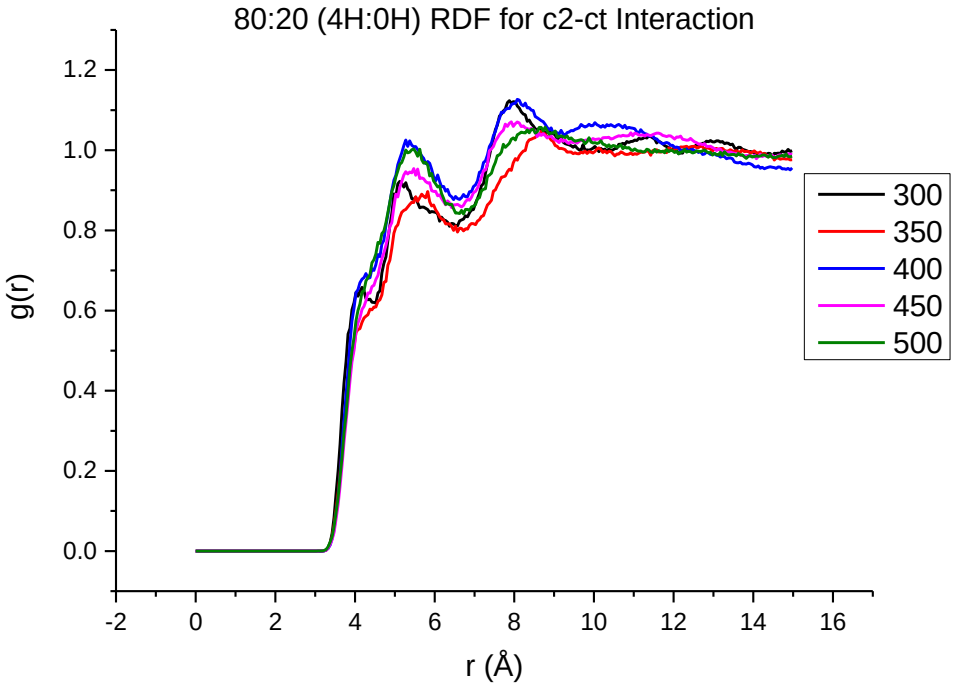
80:20 (4H:0H) RDF for c2-ct Interaction
g(r)
r (Å)
300
350
400
450
500

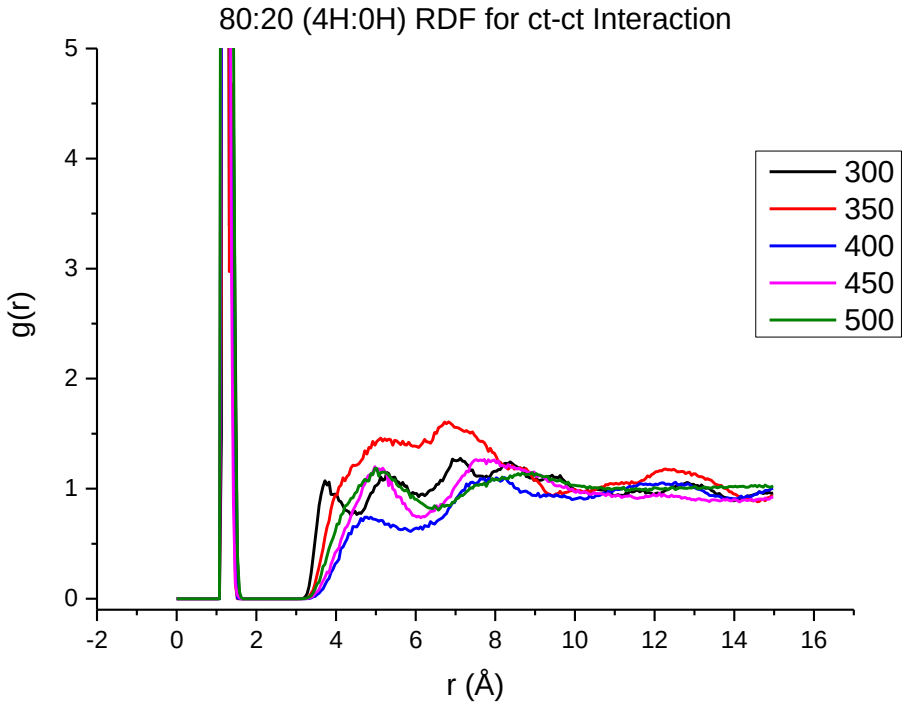
80:20 (4H:0H) RDF for ct-ct Interaction
g(r)
r (Å)
300
350
400
450
500

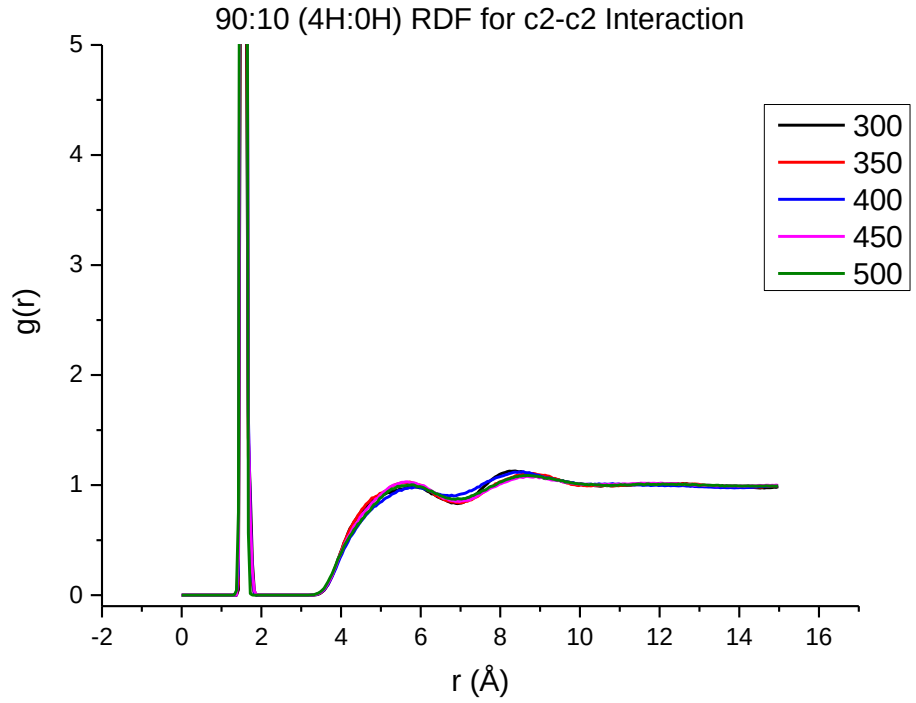
90:10 (4H:0H) RDF for c2-c2 Interaction
g(r)
r (Å)
300
350
400
450
500

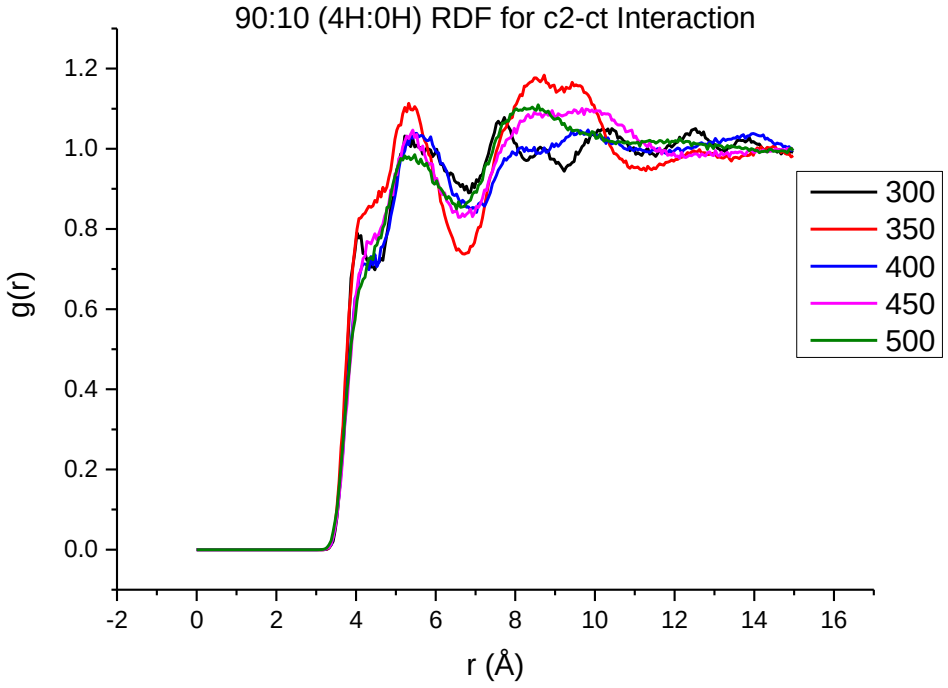
90:10 (4H:0H) RDF for c2-ct Interaction
g(r)
r (Å)
300
350
400
450
500

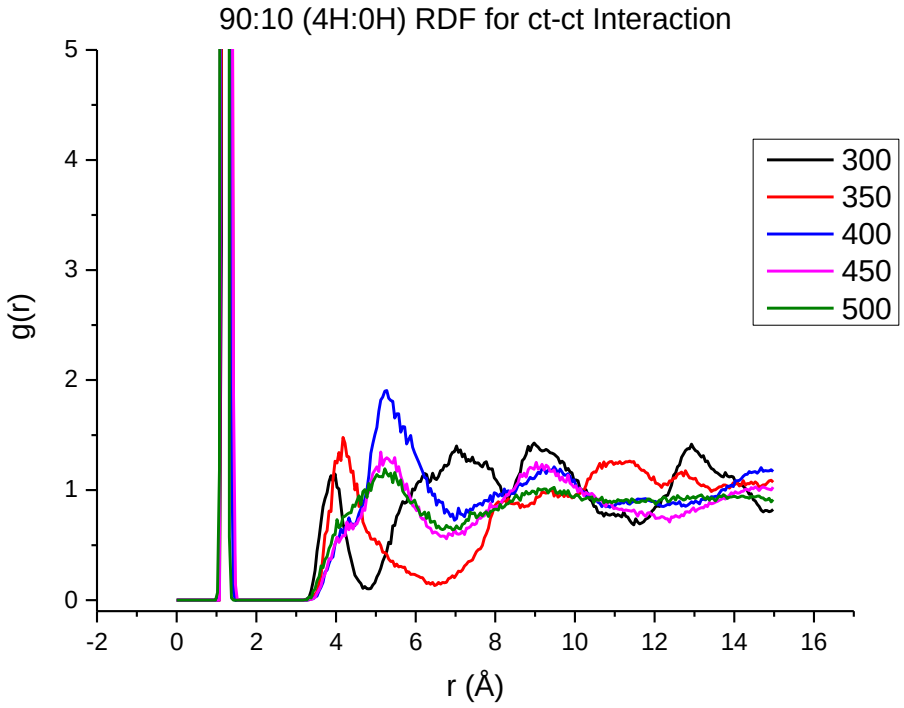

RDFs for 4H:0H Mixtures

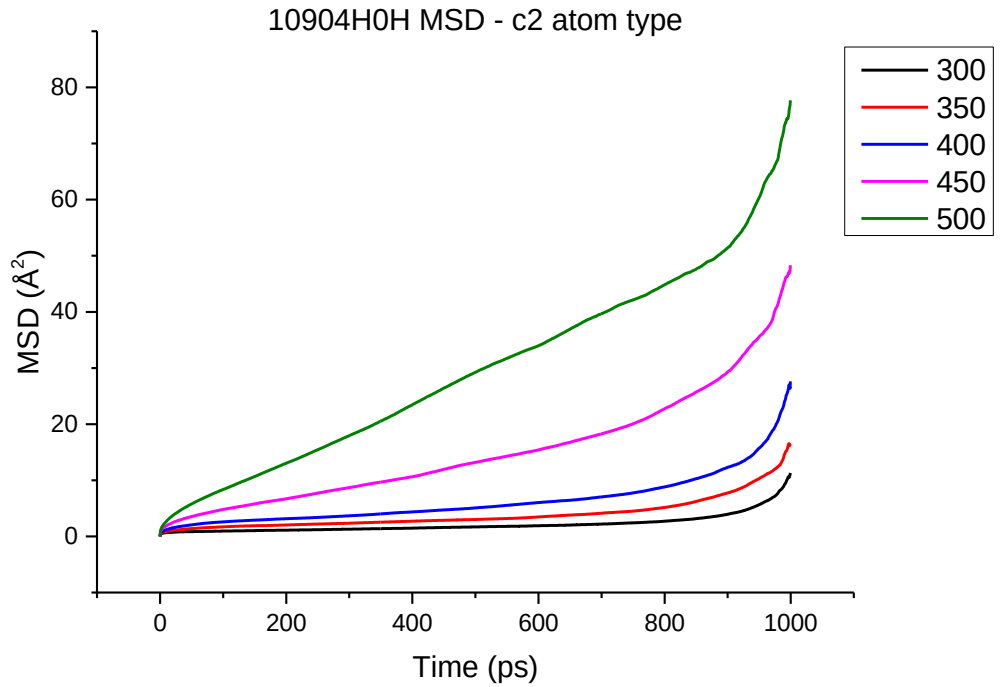

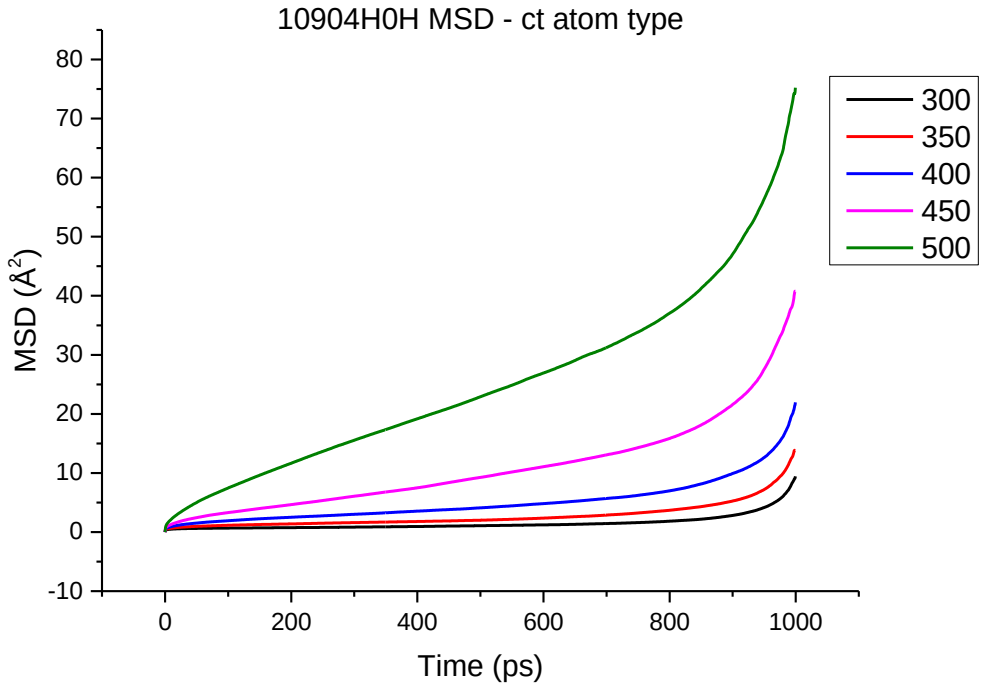
10904H0H MSD - ct atom type
MSD (Å2)
Time (ps)
300
350
400
450
500
80
70
60
50
40
30
20
10
0
-10
0
200
400
600
800
1000

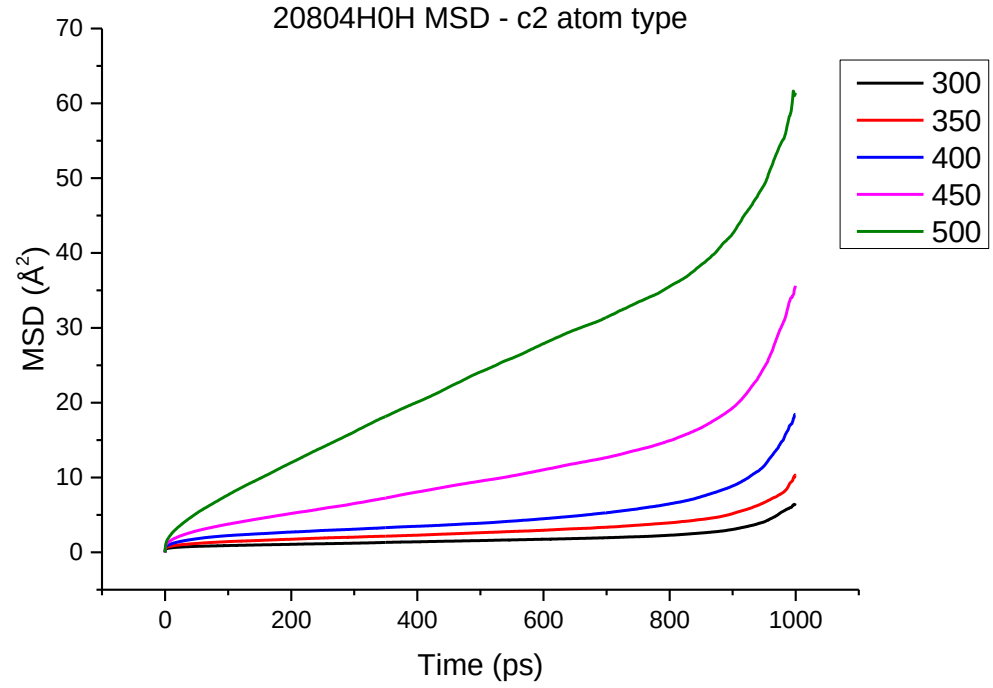
20804H0H MSD - c2 atom type
MSD (Å2)
Time (ps)
300
350
400
450
500
70
60
50
40
30
20
10
0
0
200
400
600
800
1000

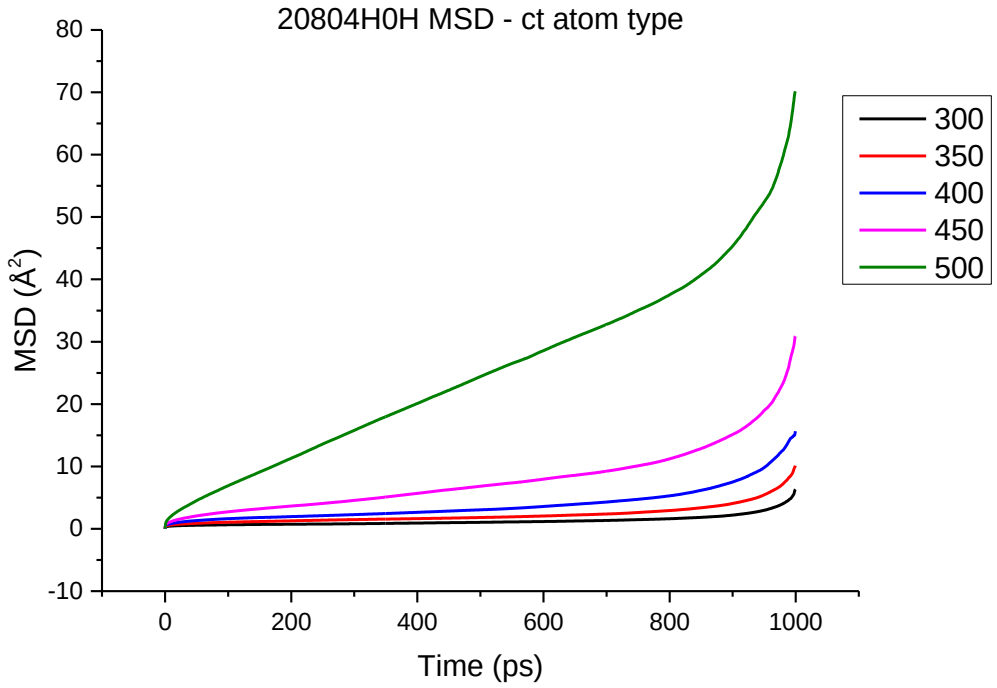
20804H0H MSD - ct atom type
MSD (Å2)
Time (ps)
300
350
400
450
500

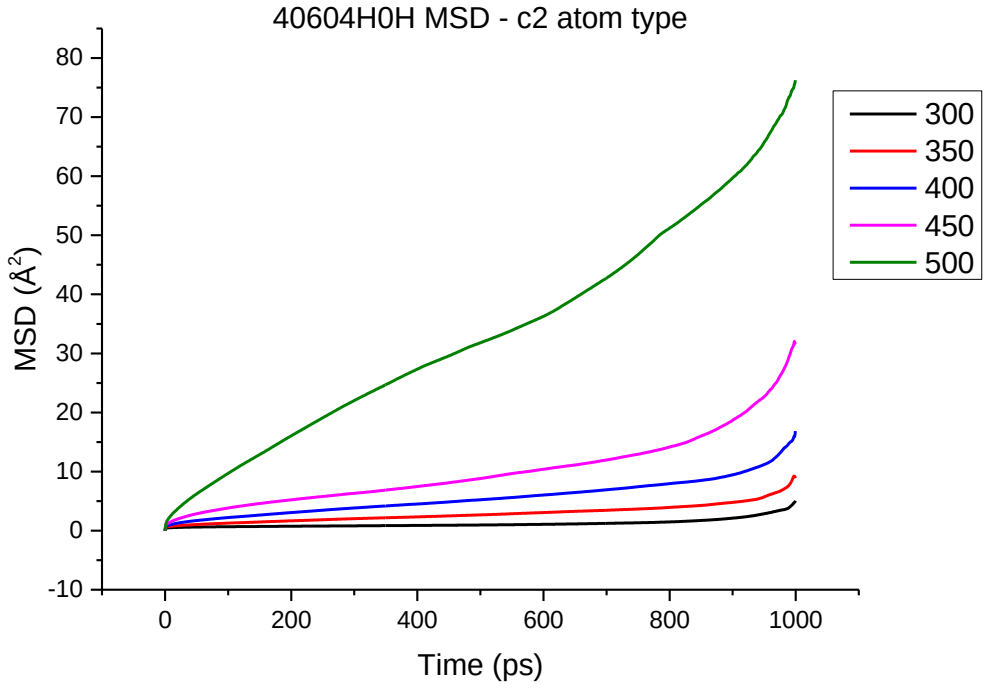
40604H0H MSD - c2 atom type
MSD (Å2)
Time (ps)
300
350
400
450
500

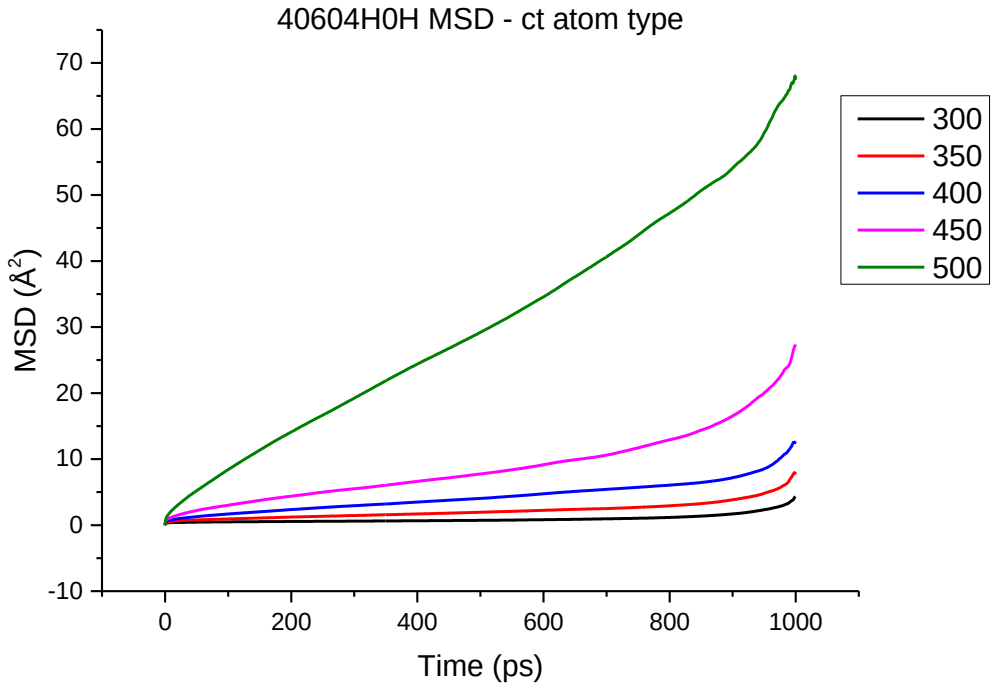
40604H0H MSD - ct atom type
MSD (Å²)
Time (ps)
300
350
400
450
500

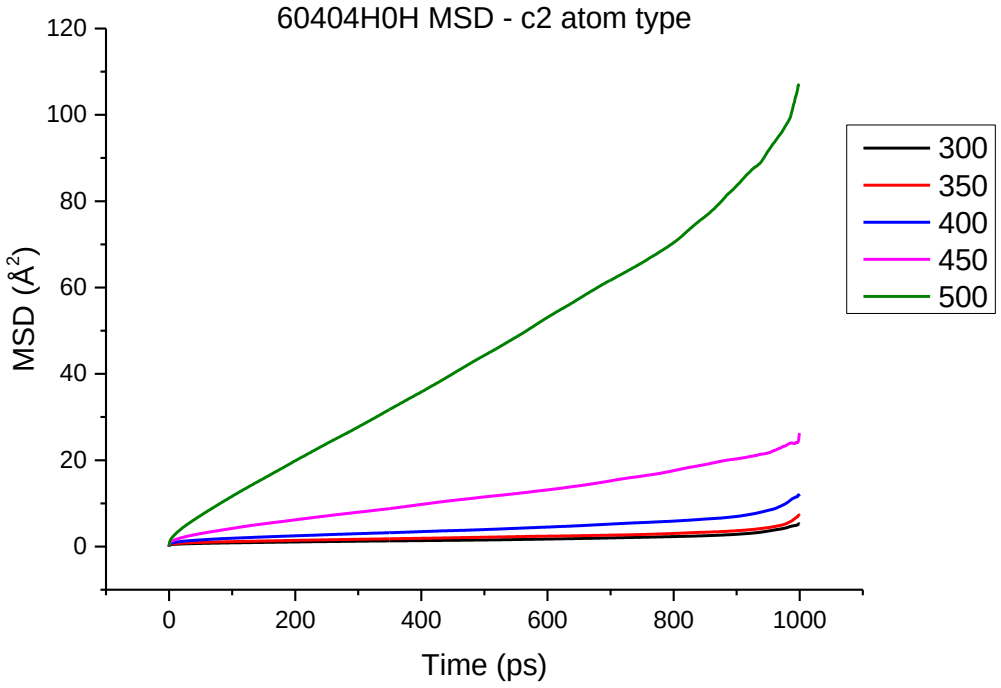
60404H0H MSD - c2 atom type
MSD (Å²)
Time (ps)
300
350
400
450
500

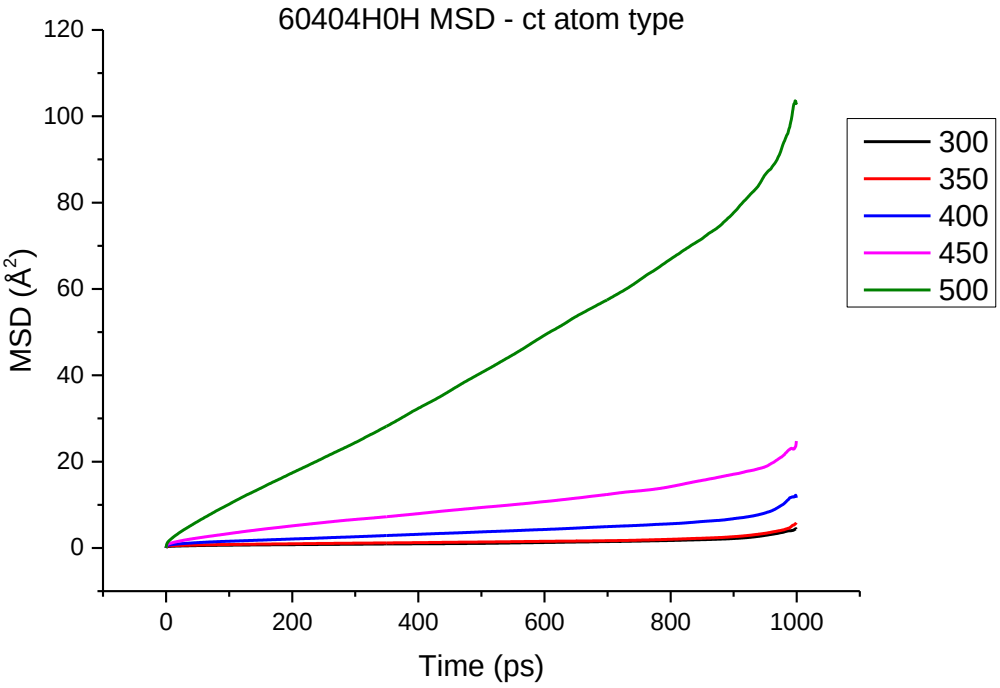
60404H0H MSD - ct atom type
MSD (Å²)
Time (ps)
0
20
40
60
80
100
120
0
200
400
600
800
1000
300
350
400
450
500

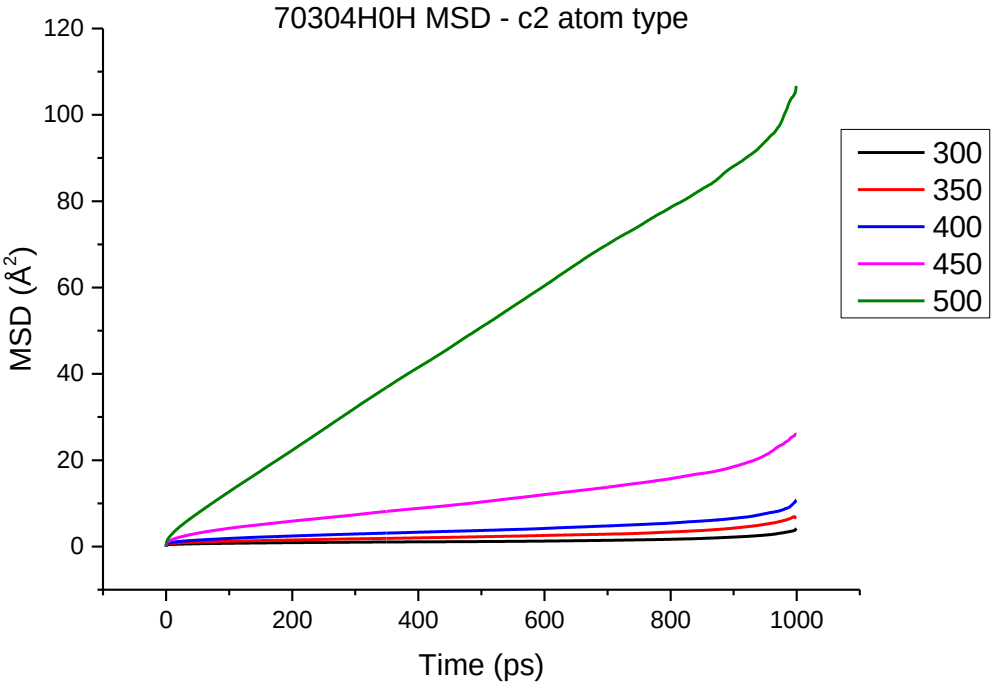
70304H0H MSD - c2 atom type
MSD (Å²)
Time (ps)
0
20
40
60
80
100
120
0
200
400
600
800
1000
300
350
400
450
500

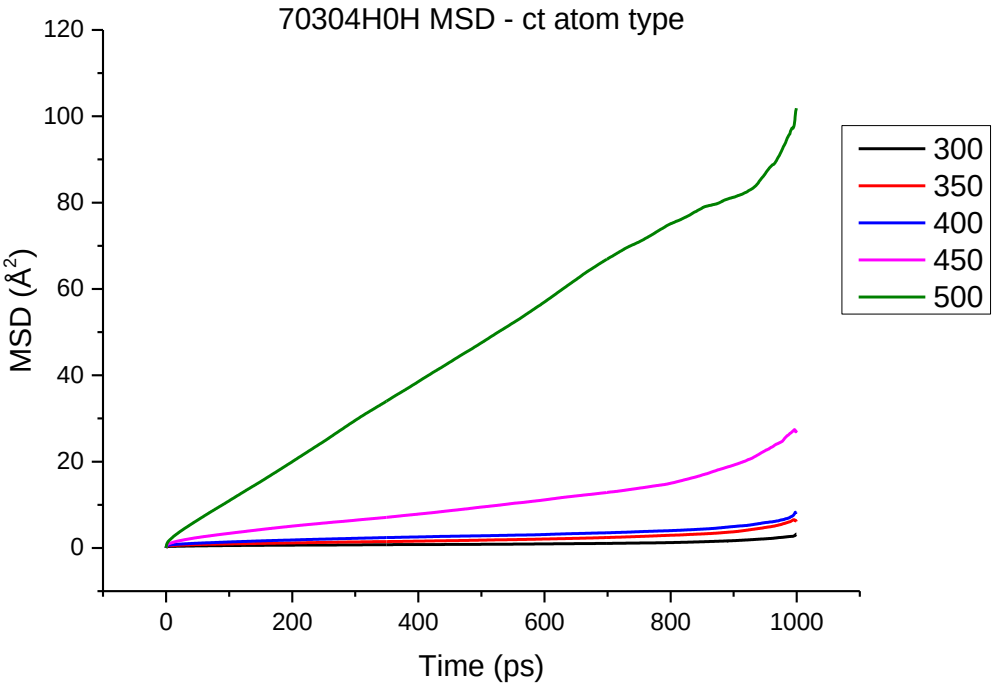
70304H0H MSD - ct atom type
MSD (Å²)
Time (ps)
0
20
40
60
80
100
120
0
200
400
600
800
1000
300
350
400
450
500

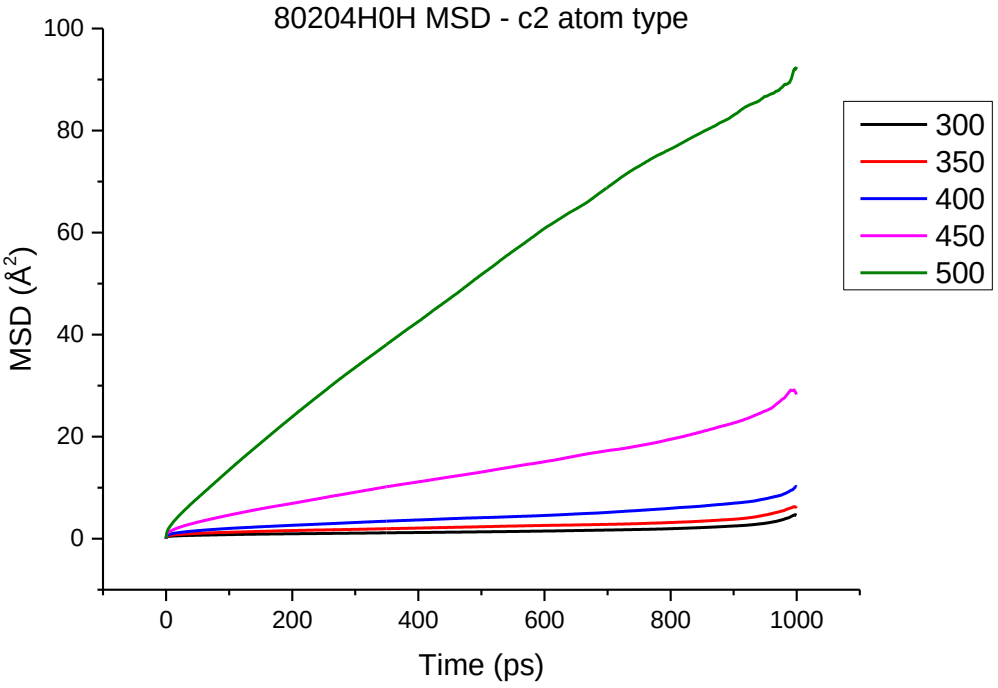
80204H0H MSD - c2 atom type
MSD (Å²)
Time (ps)
0
20
40
60
80
100
0
200
400
600
800
1000
300
350
400
450
500

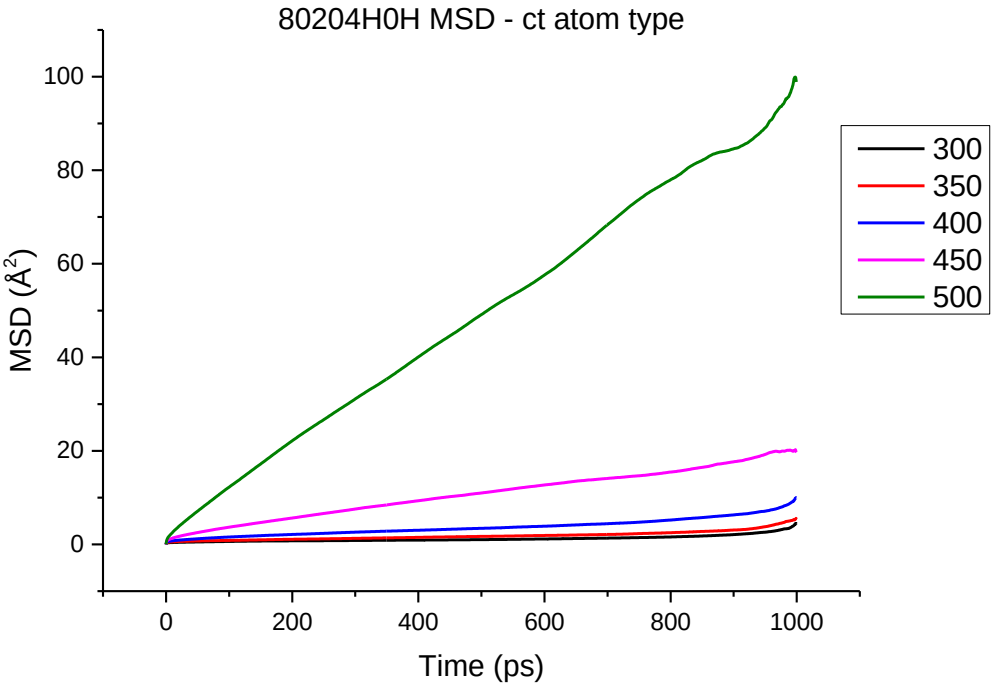
80204H0H MSD - ct atom type
MSD (Å²)
Time (ps)
0
20
40
60
80
100
0
200
400
600
800
1000
300
350
400
450
500

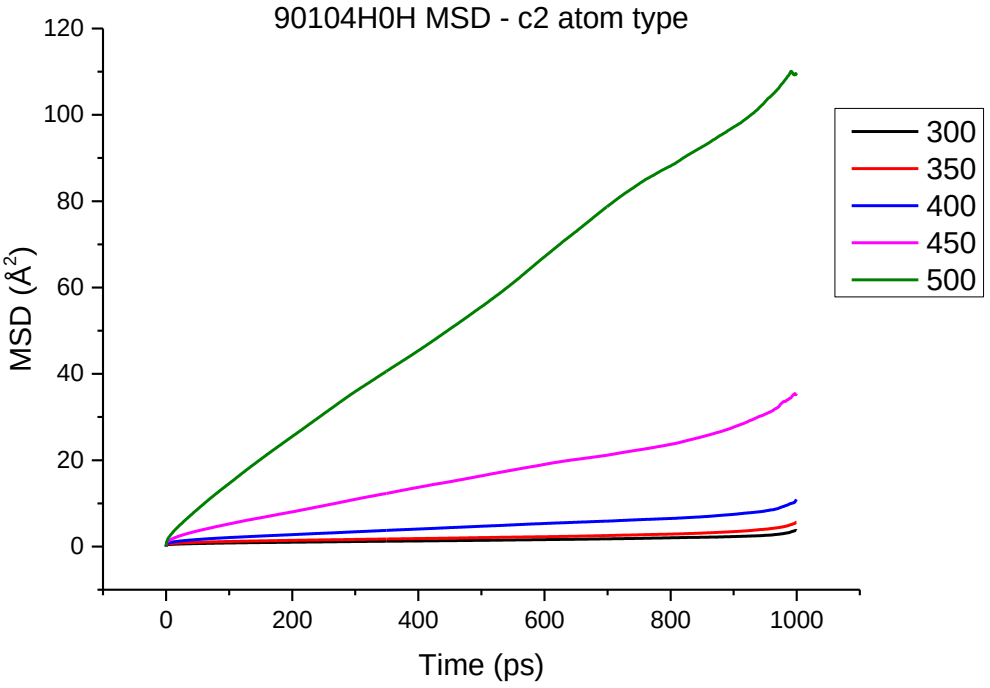
90104H0H MSD - c2 atom type
MSD (Å²)
Time (ps)
0
20
40
60
80
100
120
0
200
400
600
800
1000
300
350
400
450
500

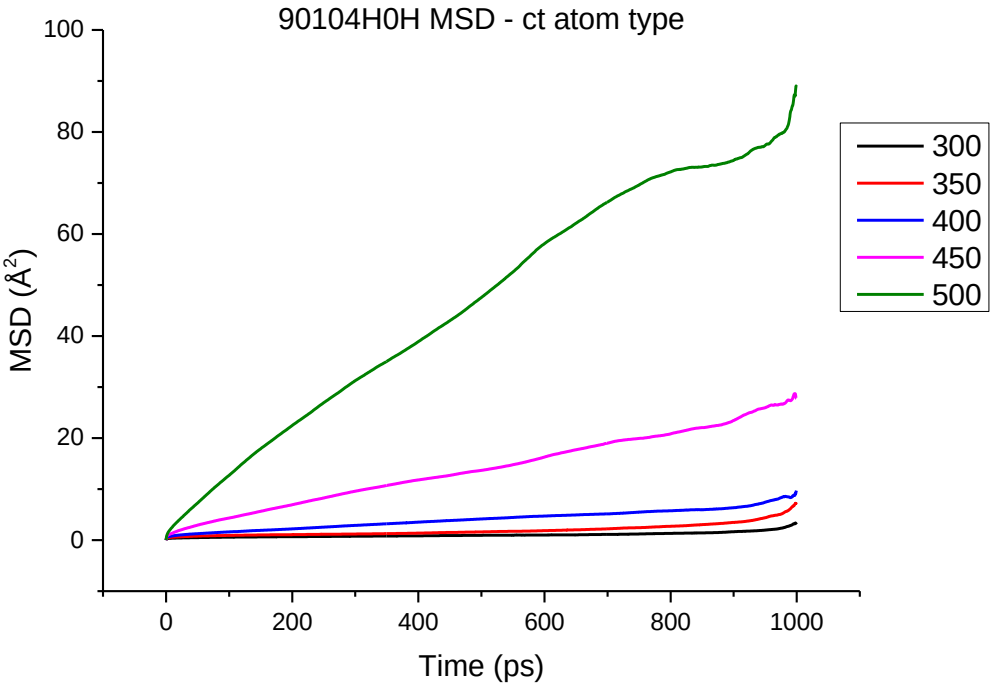

Diffusion Coefficients for all 4H:0H Mixtures

(all values are x 10^{-15} m^2 s^{-1})

10:90 (4H:0H)

Temperature	c2	ct
300	7.54	4.99
350	14.4	10.5
400	28.0	22.2
450	80.1	58.7
500	180	131

20:80 (4H:0H)

Temperature	c2	ct
300	6.02	4.42
350	11.1	7.51
400	18.2	16.7
450	51.2	39.1
500	142	128

40:60 (4H:0H)

Temperature	c2	ct
300	3.45	2.89
350	12.0	8.96
400	25.7	20.7
450	47.6	43.0
500	177	170

50:50 (4H:0H)

Temperature	c2	ct
300	5.99	4.78
350	7.15	5.55
400	16.2	14.9
450	47.2	36.7
500	251	217

60:40 (4H:0H)

Temperature	c2	ct
300	6.33	5.10
350	8.08	4.85
400	19.3	18.4
450	59.8	48.1
500	283	277

70:30 (4H:0H)

Temperature	c2	ct
300	3.52	2.85
350	9.17	8.58
400	15.5	10.6
450	54.1	53.3
500	315	311

80:20 (4H:0H)

Temperature	c2	ct
300	5.02	4.25
350	8.22	6.97
400	16.3	15.1
450	67.3	54.8
500	308	296

90:10 (4H:0H)

Temperature	c2	ct
300	5.20	2.94
350	8.48	7.50
400	20.9	19.2
450	86.4	77.7
500	358	295